

Washington University in St. Louis

Washington University Open Scholarship

Arts & Sciences Electronic Theses and
Dissertations

Arts & Sciences

4-18-2024

Mechanisms of Rod Photoreceptor Metabolism and Function in Health and Disease

Tae Jun Lee

Washington University in St. Louis

Follow this and additional works at: https://openscholarship.wustl.edu/art_sci_etds

Recommended Citation

Lee, Tae Jun, "Mechanisms of Rod Photoreceptor Metabolism and Function in Health and Disease" (2024). *Arts & Sciences Electronic Theses and Dissertations*. 3037.
https://openscholarship.wustl.edu/art_sci_etds/3037

This Dissertation is brought to you for free and open access by the Arts & Sciences at Washington University Open Scholarship. It has been accepted for inclusion in Arts & Sciences Electronic Theses and Dissertations by an authorized administrator of Washington University Open Scholarship. For more information, please contact digital@wumail.wustl.edu.

WASHINGTON UNIVERSITY IN ST. LOUIS
Division of Biology and Biomedical Sciences
Developmental, Regenerative, and Stem Cell Biology

Dissertation Examination Committee:
Rajendra S. Apte, Chair
Jason Held
Philip A. Ruzycki
Yo Sasaki
Philip R. Williams

Mechanisms of Rod Photoreceptor Metabolism and Function in Health and Disease
by
Tae Jun Lee

A dissertation presented to
Washington University in St. Louis
in partial fulfillment of the
requirements for the degree
of Doctor of Philosophy

May 2024
St. Louis, Missouri

© 2024, Tae Jun Lee

Table of Contents

List of Figures.....	vii
Acknowledgments.....	ix
Abstract.....	xiii
Chapter 1: AMPK is a Critical Metabolic Regulator of Rod Photoreceptors through IMPDH1....	1
1.1 Introduction.....	2
1.2 Results.....	5
1.2.1 <i>Prkaa1</i> and <i>Prkaa2</i> expression in the retina.....	5
1.2.2 Expression profiles of AMPK catalytic isoforms are consistent across mouse and human retina.....	6
1.2.3 <i>Prkaa1</i> ^{-Rhod/-Rhod} and <i>Prkaa2</i> ^{-Rhod/-Rhod} express deficient PRKAA1 and PRKAA2 respectively in rod photoreceptors.....	7
1.2.4 <i>Prkaa2</i> ^{-Rhod/-Rhod} rod photoreceptors exhibit disorganized outer segment structures on electron microscopy.....	8
1.2.5 <i>Prkaa2</i> ^{-Rhod/-Rhod} mice demonstrate visual function deficits in vivo.....	9
1.2.6 cGMP, GTP, and ATP levels are elevated in <i>Prkaa2</i> ^{-Rhod/-Rhod} retinas.....	9
1.2.7 <i>Prkaa2</i> ^{-Rhod/-Rhod} retinas demonstrate increased glycolytic flux.....	10
1.2.8 Rod-isolated phosphoproteomics reveal IMPDH as a downstream effector of PRKAA2.....	11

1.2.9 IMPDH activity is aberrantly upregulated in dark adapted <i>Prkaa2^{-Rhod/-Rhod}</i> retinas.....	13
1.2.10 AMPK affecting compounds alter IMPDH activity.....	14
1.2.11 IMPDH is a direct target of PRKAA2 in the retina.....	14
1.2.12 Mycophenolate mofetil treatment improves <i>Prkaa2^{-Rhod/-Rhod}</i> visual function.....	16
1.3 Discussion.....	17
1.4 Materials and Methods.....	20
1.5 Acknowledgments.....	31
1.6 References.....	32
1.7 Figures.....	40
 Chapter 2: NMNAT1 Dysfunction Leads to Rod Photoreceptor Degeneration that can be Prevented by SARM1 Knockout.....	 58
2.1 Introduction.....	59
2.2 Results.....	62
2.3 Discussion.....	69
2.4 Materials and Methods.....	73
2.5 Acknowledgments.....	79
2.6 References.....	79

2.7 Figures.....	91
Chapter 3: Myeloid Knockout of Cholesterol Efflux Transporters, ABCA1 and ABCG1, Results in Rod Photoreceptor Dysfunction as seen in Dry Age-related Macular Degeneration.....	104
3.1 Introduction.....	105
3.2 Results.....	106
3.2.1 Deletion of <i>Abca1</i> and <i>Abcg1</i> in macrophages does not affect the retina at 3 months of age.....	107
3.2.2 <i>Abca1/g1^{-m/-m}</i> mice demonstrate RPE abnormalities, BrM thickening, and impaired dark adaptation at 6 months of age.....	108
3.2.3 Retinal neurodegeneration of <i>Abca1/g1^{-m/-m}</i> mice increases in severity and affects cone photoreceptors at 12 months of age.....	108
3.2.4 Subretinal deposits of <i>Abca1/g1^{-m/-m}</i> mice progressively increase in number with age.....	109
3.2.5 Infiltrating cells in the subretinal space are Iba1- or F4/80- positive monocytic cells.....	109
3.2.6 Aged <i>Abca1/g1^{-m/-m}</i> mice demonstrate lipid accumulation underneath the retina and within RPE.....	110
3.3 Discussion.....	110
3.4 Materials and Methods.....	112
3.5 Acknowledgments.....	118

3.6 References.....	118
3.7 Figures.....	124
Chapter 4: Rod Photoreceptor Knockout of Cholesterol Efflux Transporters, ABCA1 and ABCG1, Results in Rod Photoreceptor and Retinal Pigment Epithelium Dysfunction as seen in Early Dry Age-related Macular Degeneration.....	135
4.1 Introduction.....	136
4.2 Results.....	137
4.2.1 Deletion of <i>Abca1</i> and <i>Abcg1</i> in rod photoreceptors increases retinal cholesterol, but does not affect retinal function in young mice.....	137
4.2.2 Aged <i>Abca1/g1^{-rod/-rod}</i> mice demonstrate lipid accumulation underneath the retina with associated rod neurodegeneration and vision loss.....	137
4.2.3 Retinal neurodegeneration increases in severity and affects cone photoreceptors with increasing age.....	138
4.2.4 Deletion of <i>Abca1</i> and <i>Abcg1</i> in cone photoreceptors does not cause neurodegeneration.....	139
4.2.5 ABCA1 and ABCG1 play vital roles in maintaining retinal function during metabolic stress.....	139
4.3 Discussion.....	140
4.4 Materials and Methods.....	142
4.5 Acknowledgments.....	148

4.6 References.....	149
4.7 Figures.....	154
Chapter 5: ApoM-S1P Ameliorates Retinal Pigment Epithelium Lipotoxicity as seen in Early Dry Age-related Macular Degeneration.....	
	167
5.1 Introduction.....	168
5.2 Results.....	171
5.2.1 Older patients and patients with AMD have lower circulating levels of ApoM.....	171
5.2.2 ApoM plasma transfer ameliorates RPE functional deficits in a dry AMD-like mouse model.....	171
5.2.3 RPE lipid accumulation is reduced with ApoM plasma transfer.....	172
5.2.4 Rod photoreceptor function is improved with ApoM plasma transfer in high fat diet fed <i>AbcA1/gI^{-rod/-rod}</i> mice.....	173
5.2.5 Proper S1P binding of ApoM is necessary for amelioration of RPE lipid accumulation and rod photoreceptor function.....	173
5.2.6 S1PR3 knockout recapitulates features of RPE lipotoxicity.....	174
5.2.7 ApoM overexpression does not rescue high fat diet induced <i>S1pr3^{-/-}</i> RPE lipotoxicity.....	175
5.2.8 ApoM-S1P does not change cholesterol efflux capacity in ARPE-19.....	176

5.2.9 Photoreceptor outer segment treatment of ex vivo RPE recapitulate features of in vivo RPE lipotoxicity.....	176
5.2.10 Lipophagy abrogation recapitulate features of RPE lipotoxicity.....	177
5.3 Discussion.....	179
5.4 Materials and Methods.....	181
5.5 Acknowledgments.....	187
5.6 References.....	188
5.7 Figures.....	196
Chapter 6: Summary and Future Directions.....	210
6.1 Summary.....	211
6.2 Future Directions.....	214

List of Figures

Chapter 1

Figure 1. Both catalytic isoforms of AMPK are appreciably expressed in the retina with consistent expression profiles across human and mouse retinas.....	40
Figure 2. PRKAA2, but not PRKAA1, dysfunction leads to rod photoreceptor structural abnormalities and visual dysfunction.....	42
Figure 3. <i>Prkaa2</i> ^{-Rhod/-Rhod} retinas demonstrate phospho-purine overproduction and increased glycolysis.....	44
Figure 4. PRKAA2 dysfunction leads to wide changes to the phosphoproteome and decreased S416 phosphorylation of IMPDH.....	46
Figure 5. Dysfunctional PRKAA2 cannot regulate IMPDH leading to IMPDH hyperactivity.....	48
Figure 6. Mycophenolate mofetil treatment improves visual function deficits measured by electroretinography in <i>Prkaa2</i> ^{-Rhod/-Rhod}	50
Supplementary Figure 1. <i>Prkaa1</i> and <i>Prkaa2</i> expression levels of isolated rod photoreceptors from <i>Prkaa1</i> ^{-Rhod/-Rhod} and <i>Prkaa2</i> ^{-Rhod/-Rhod}	52
Supplementary Figure 2. Hematoxylin and eosin staining of <i>Prkaa1</i> ^{-Rhod/-Rhod} and <i>Prkaa2</i> ^{-Rhod/-Rhod}	53
Supplementary Figure 3. Metabolomics of <i>Prkaa1</i> ^{-Rhod/-Rhod} retinas.....	54
Supplementary Figure 4. Extracellular flux analyses of <i>Prkaa1</i> ^{-Rhod/-Rhod} retinas.....	55

Supplementary Figure 5. PRKAA2 and IMPDH1/2 are appreciated in the same cellular compartment in *Prkaa2*^{Rhod/-Rhod} inner segments compared to those of *Prkaa2*^{F/F}56

Supplementary Figure 6. Mycophenolate injection does not improve visual function in wild-type mice.....57

Chapter 2

Figure 1. NMNAT1 depletion induces severe retinal degeneration.....91

Figure 2. NMNAT1 induces the loss of photoreceptor cells and retinal function.....93

Figure 3. Photoreceptor-specific depletion of NMNAT1 induces retinal degeneration.....95

Figure 4. Depletion of SARM1 rescues retinal degeneration in the NMNAT1-deficient retina...97

Figure supplement 1. NMNAT1 is ubiquitously expressed in the retina.....99

Figure supplement 2. ERG analysis of NMNAT3-deficient retina.....101

Figure supplement 3. AAV-NMNAT1 partially rescued retinal degeneration in NMNAT1-deficient retinas.....102

Chapter 3

Figure 1. Three-month-old *Abca1/g1*^{-m/-m} retinas do not show functional deficits or morphological abnormalities in the retina and RPE.....124

Figure 2. Six-month-old *Abca1/g1*^{-m/-m} retinas demonstrate decreased scotopic responses and impaired dark adaptation associated with disrupted RPE morphology and Bruch's membrane thickening.....125

Figure 3. Neurodegeneration of aged <i>Abca1/g1^{-m/-m}</i> (12-month-old) retinas increases in severity and extends to photopic dysfunction with significant subretinal deposits.....	127
Figure 4. Subretinal deposits contain lipid globules and degenerative vacuoles.....	128
Figure 5. Infiltrated cells in subretinal space are IBA1 and F4/80 positive.....	129
Figure 6. Lipid analysis of <i>Abca1/g1^{-m/-m}</i> mice eyes at 12 months of age demonstrates focal subretinal and RPE deposits with increased cholesterol metabolites.....	130
Supplementary Figure 1.....	131
Supplementary Figure 2.....	132
Supplementary Figure 3.....	133
Supplementary Figure 4.....	134
 Chapter 4	
Figure 1. Aged (12 months) <i>Abca1/g1^{-rod/-rod}</i> mouse retinas show decreased scotopic responses and accumulation of lipids.....	154
Figure 2. Lipid analysis of <i>Abca1/g1^{-rod/-rod}</i> mouse eyes at 12 months of age demonstrates accumulation of cholesterol metabolites.....	156
Figure 3. <i>Abca1/g1^{-rod/-rod}</i> mouse retinas (aged 18 months) show decreased scotopic and photopic responses and atrophic retinal neurodegeneration.....	157
Figure 4. Deletion of <i>Abca1</i> and <i>Abcg1</i> in cone photoreceptors does not cause detectable neurodegeneration.....	159

Figure 5. A HFD significantly accelerates retinal neurodegeneration in *Abca1/g1^{-rod/-rod}* mice.....161

Supplemental Figure S1. Deletion of *Abca1* and *Abcg1* in rod photoreceptors increases retinal cholesterol but does not affect the retina histopathologically in young mice.....162

Supplemental Figure S2. Comparison of 12-month-old *Abca1/g1^{-rod/-rod}* mice ERG with other controls.....164

Supplemental Figure S3. Comparison of 18-month-old *Abca1/g1^{-rod/-rod}* mice ERG with other controls.....165

Supplemental Figure S4. Deletion of *Abca1* and *Abcg1* in cone photoreceptors in *Abca1/g1^{-cone/-cone}* mice.....166

Chapter 5

Figure 1. ApoM therapy ameliorates a dry AMD-like phenotype.....196

Figure 2. Proper binding of S1P by ApoM is necessary for RPE lipotoxicity amelioration.....198

Figure 3. *Slpr3* knockout is sufficient to provoke a dry AMD-like RPE phenotype.....200

Figure 4. ApoM overexpression does not rescue S1PR3 deficiency induced RPE lipotoxicity..202

Figure 5. ApoM-S1P does not influence cholesterol efflux in ARPE-19.....204

Figure 6. RPE-specific knockout of lipophagy recapitulate features of a dry AMD-like Phenotype.....205

Supplementary Figure 1. *SIPR1* and *SIPR3* are the predominantly expressed S1P receptors in human RPE.....206

Supplementary Figure 2. RPE-specific conditional knockout mice of *Slpr1* do not show retinal deficits.....207

Supplementary Figure 3. ApoM-S1P reduces neutral lipid staining in POS treated ARPE-19 cells.....208

Supplementary Figure 4. Germlines lipophagy knockout results in widespread RPE and retinal dysfunction.....209

Acknowledgments

To all who have accompanied me through this journey, I feel that I am nothing but a conduit of your immeasurable support. Only by the grace of God am I here and able to make any sort of meaningful contribution to those around me and the field of biomedical sciences.

To Raj, I will forever be grateful that I had the opportunity to join your lab. Thank you for constantly cultivating my passion for research and advancing the field of retinal degeneration. I will cherish the innumerable conversations, both scientific and non-scientific, we had and the sincere mentorship that guided me towards my best interest. Thank you to the spectacular co-graduate students in the lab, Joseph, Chas, Jason, and Zelun. Going through the best and worst of graduate school with you all has made it worth it. To the staff and post-docs I have had the pleasure of working with, thank you for the constant support and feedback to help guide me in performing good science, especially Andrea!

To my church family at West Hills, thank you for being a rock through storms. Dan, Varintra, Samuel, Tsehay, Kevin, Sam, Will, Polly... the list goes on and I cannot enumerate all the names! Thank you for always providing spiritual guidance and perspectives to challenging situations, and the community that fostered my spiritual growth.

To my family, thank you for the unwavering support that I feel daily. Even from California, it seems that you all would do anything to show appreciation for what I do. Thank you mom, Jenny, and JR!

Finally, to my amazing wife Mary Morgan, thank you for being by my side through it all. From being a technician while you were in medical school to finishing graduate school as you finish a fellowship in infectious diseases, it has been a joy to experience all of the vicissitudes that come

along with such an arduous journey for both of us. Words cannot describe how much you sincerely mean to me, and I cannot wait to see what lies ahead of us! I love you!

Tae Jun Lee

Washington University in St. Louis, May 2024

For by grace you have been saved through faith. And this is not your own doing; it is a gift of God, not a result of works, so that no one may boast. For we are his workmanship, created in Christ Jesus for good works, which God prepared beforehand, that we should walk in them.

Ephesians 2:8-10 ESV

ABSTRACT OF THE DISSERTATION

Mechanisms of Rod Photoreceptor Metabolism and Function in Health and Disease

by

Tae Jun Lee

Doctor of Philosophy in Biology and Biomedical Sciences

Developmental, Regenerative, and Stem Cell Biology

Washington University in St. Louis, 2024

Professor Rajendra S. Apte, Chair

Over 250 million people globally live with visual acuity loss or blindness as an estimated 7 million people suffer from visual acuity loss in the United States. People in the United States value vision over memory, hearing, or speech and consider losing vision to be among the top four worst outcome to happen to them. The economic cost of major vision problems is estimated to increase to 373 billion dollars by the year 2050. Among the irreparable causes of vision loss, retinal degeneration stands as a chief contributor to catastrophic eye disease.

The retina is a neurosensory tissue located in the back of the eye as part of the central nervous system. Made up of highly specialized neurons and support cells, the retina is the most metabolically active tissue per weight in the human body. Since these neurons are non-proliferative, the cells we have post-differentiation are the ones that we will keep through the entirety of our lifetime. It is thus critical to understand how these neurons function and are supported to best develop therapies and therapeutics to help them function properly for a lifetime. In the vast majority of retinal degeneration cases, the photoreceptor layer is the first

affected layer that directly causes vision loss in patients. The photoreceptor layer in mammals is made up of both rod and cone photoreceptors, with an overwhelming majority made up of rod photoreceptors. In many cases, rod photoreceptors undergo degeneration first which leads to the subsequent loss of cone photoreceptors and visual acuity due to the lack of support from rod photoreceptors. Therefore, there is clear rationale in studying how rod photoreceptors survive and degenerate in order to understand how best to prevent a critical step in the pathogenesis of many forms of retinal degeneration.

Rod photoreceptors are, as a cell type, the most energetically demanding in terms of ATP consumption. AMP-activated protein kinase (AMPK) plays a crucial role in maintaining ATP homeostasis in photoreceptor neurons. AMPK is a heterotrimeric protein consisting of alpha, beta, and gamma subunits. The independent functions of the two isoforms of the catalytic alpha subunit, PRKAA1 and PRKAA2, are uncharacterized in specialized neurons such as photoreceptors. In the following chapter, we demonstrate in mice that rod photoreceptors lacking PRKAA2, but not PRKAA1, show altered levels of cGMP, GTP, and ATP, suggesting isoform-specific regulation of photoreceptor metabolism. Furthermore, PRKAA2 deficient mice display visual functional deficits on electroretinography and photoreceptor outer segment structural abnormalities on transmission electron microscopy consistent with neuronal dysfunction, but not neurodegeneration. Phosphoproteomics identified inosine monophosphate dehydrogenase (IMPDH) as a molecular driver of PRKAA2-specific photoreceptor dysfunction, and inhibition of IMPDH improved visual function in *Prkaa2* rod photoreceptor knockout mice. These findings highlight a novel, therapeutically targetable PRKAA2 isoform-specific function of AMPK in regulating photoreceptor metabolism and function through a previously uncharacterized mechanism affecting IMPDH activity.

Related to ATP metabolism, NAD⁺ metabolism has been shown to be a critical regulator of neuronal function, particularly in rod photoreceptors. Later in this dissertation, we detail a study that investigated a molecular pathway that rescues a phenotype caused by dysregulation of NAD⁺ metabolism. Leber congenital amaurosis type nine is an autosomal recessive retinopathy caused by mutations of the NAD⁺ synthesis enzyme NMNAT1. Despite the ubiquitous expression of NMNAT1, patients do not manifest pathologies other than retinal degeneration. We demonstrate that widespread NMNAT1 depletion in adult mice mirrors the human pathology, with selective loss of photoreceptors highlighting the exquisite vulnerability of these cells to NMNAT1 loss. Conditional deletion demonstrates that NMNAT1 is required within the photoreceptor. Mechanistically, loss of NMNAT1 activates the NADase SARM1, the central executioner of axon degeneration, to trigger photoreceptor death and vision loss. Hence, the essential function of NMNAT1 in photoreceptors is to inhibit SARM1, highlighting an unexpected shared mechanism between axonal degeneration and photoreceptor neurodegeneration. These results define a novel SARM1-dependent photoreceptor cell death pathway and identifies SARM1 as a therapeutic candidate for retinopathies.

Advanced age-related macular degeneration (AMD), the leading cause of blindness among people over 50 years of age, is another form of retinal degeneration characterized by atrophic neurodegeneration of photoreceptors or pathologic angiogenesis. Early AMD is characterized by extracellular cholesterol-rich deposits underneath the retinal pigment epithelium (RPE) called drusen or in the subretinal space called subretinal drusenoid deposits (SDD) that drive disease progression. However, mechanisms of drusen and SDD biogenesis remain poorly understood. Although human AMD is characterized by abnormalities in cholesterol homeostasis and shares phenotypic features with atherosclerosis, it is unclear whether systemic immunity or

local tissue metabolism regulates this homeostasis. Here, we demonstrate that targeted deletion of macrophage cholesterol ABC transporters A1 (ABCA1) and -G1 (ABCG1) leads to age-associated extracellular cholesterol-rich deposits underneath the neurosensory retina similar to SDD seen in early human AMD. These mice also develop impaired dark adaptation, a cardinal feature of RPE cell dysfunction seen in human AMD patients even before central vision is affected. Subretinal deposits in these mice progressively worsen with age, with concomitant accumulation of cholesterol metabolites including several oxysterols and cholesterol esters causing lipotoxicity that manifests as photoreceptor dysfunction and neurodegeneration. These findings suggest that impaired macrophage cholesterol transport initiates several key elements of early human AMD, demonstrating the importance of systemic immunity and aging in promoting disease manifestation. Polymorphisms in genes involved with cholesterol transport and homeostasis are associated with a significantly higher risk of developing AMD, thus making these studies translationally relevant by identifying potential targets for therapy.

Furthermore, we investigated the role of ABCA1 and -G1 in rod photoreceptors. Photoreceptors have high intrinsic metabolic demand and are exquisitely sensitive to metabolic perturbation. In addition, they shed a large portion of their outer segment lipid membranes in a circadian manner, increasing the metabolic burden on the outer retina associated with the resynthesis of cell membranes and disposal of the cellular cargo. Here, we demonstrate that deletion of both ABCA1 and ABCG1 in rod photoreceptors leads to age-related accumulation of cholesterol metabolites in the outer retina, photoreceptor dysfunction, degeneration of rod outer segments, and ultimately blindness. A high-fat diet significantly accelerates rod neurodegeneration and vision loss, further highlighting the role of lipid homeostasis in regulating photoreceptor neurodegeneration and vision.

Lastly, we sought to investigate novel therapeutic pathways that could ameliorate the aforementioned phenotype that predisposes patients to advanced AMD. Cholesterol efflux is the first step in reverse cholesterol transport, and involves the efflux of lipid to apolipoprotein A-I, the main protein constituent of high-density lipoprotein (HDL). However, whether other functions of HDL are involved in the development of AMD is unknown. We tested the novel hypothesis that apolipoprotein M (ApoM) plays an essential role in AMD pathogenesis. ApoM binds a bioactive lipid called sphingosine-1-phosphate (S1P) to regulate diverse processes including inflammation, fibrosis, cell death, and cholesterol efflux. We have discovered that circulating ApoM protein levels are reduced in patients with AMD. Delivery of ApoM-enriched plasma attenuates the development of AMD-like features in mice, but not ApoM knockout plasma or ApoM that cannot bind to S1P does not, suggesting a critical role for the ApoM-S1P interaction in AMD pathogenesis. Knockout of S1P receptor 3 is also sufficient to recapitulate AMD-like phenotypes in mice. Transmission electron microscopy shows that S1P receptor 3 knockout mice exhibit increased lipid droplets in retinal pigment epithelial cells, just like mice with double knockout of cholesterol efflux pumps. Meanwhile, treatment with ApoM decreases the number of lipid droplets, while increasing the numbers of melanosomes. These observations led to the further hypothesis that ApoM and S1P receptor 3 may be stimulating lipophagy, the process of lipid catabolism in the melanosomes of the retinal pigment epithelium. Accordingly, knockout of the key lipophagy enzyme lysosomal acid lipase phenocopied the AMD-like phenotype. Our study revealed an exciting and new therapeutic avenue in the treatment of early AMD where there is a paucity of aggressive therapies available.

Taken together, our collective and collaborative work illuminates the delicate nuances required for rod photoreceptor metabolism and even proper function from supporting cells for

rod photoreceptor function and survival. Future and ongoing work warrants perspicacious consideration of cell-autonomous effects of metabolism in rod photoreceptors as well as the non-cell-autonomous effects from surrounding cells to elucidate therapeutic pathways for rod photoreceptor survival.

Chapter 1: AMPK is a Critical Metabolic Regulator of Rod

Photoreceptors through IMPDH

Adapted from:

Catalytic isoforms of AMP-activated protein kinase differentially regulate IMPDH activity and photoreceptor neuron function

Lee TJ, Sasaki Y, Ruzycki PA, Ban N, Lin JB, Wu H, Santeford A, Apte RS. Catalytic isoforms of AMP-activated protein kinase differentially regulate IMPDH activity and photoreceptor neuron function. JCI Insight. Published online January 16, 2024. doi:10.1172/jci.insight.173707

1.1 Introduction

AMP-activated protein kinase (AMPK) is a crucial regulator of energy homeostasis, and is considered a central player in replenishing low adenosine triphosphate (ATP) levels by initiating catabolic processes (1). Prior studies using both gain and loss of function approaches have investigated the role of AMPK in maintaining the high energy demands of the neurosensory retina in homeostasis and during aging, light- induced oxidative stress, and inflammation (2-4). AMPK has broadly been reported in multiple animal and tissue models to regulate mitochondrial biogenesis, autophagy, glycolysis and gluconeogenesis, beta oxidation and lipogenesis, and protein metabolism (5-9). As a trimeric protein, AMPK has different isoforms for its three subunits (α , β , γ) with gene names beginning with “PRKA” which result in twelve different possible combinations to comprise the complete heterotrimeric enzyme (10). The α subunit, the catalytic subunit, has two isoforms in mammals (PRKAA1 and PRKAA2 also called AMPK α 1 and AMPK α 2 respectively) and is responsible for regulating targets via phosphorylation. The β subunit, a regulatory subunit, has two isoforms in mammals (PRKAB1 and PRKAB2 also called AMPK β 1 and AMPK β 2 respectively) and are necessary for allosteric activation of the α subunit. The γ subunit, a regulatory subunit, has three isoforms in mammals (PRKAG1, PRKAG2, and PRKAG3 also called AMPK γ 1, AMPK γ 2, and AMPK γ 3 respectively) and binds to AMP to initiate allosteric activation of the α subunit. Previous investigations have suggested that PRKAA1 and PRKAA2 are not fully redundant through generation and phenotypic characterization of *Prkaa1* and *Prkaa2* null mutant mice, demonstrating profound effects and embryonic lethality in the case of double *Prkaa1* and *Prkaa2* knockout (11). Other studies have also examined the effects of catalytic isoform-specific null mutant phenotypes, suggesting isoform-specific roles in specific tissues and contexts (12).

However, the specific mechanistic contributions of the individual catalytic isoforms of AMPK in supporting retinal function have not been elucidated. Although some compounds such as AMP analog C2 target a specific catalytic isoform (13), most existing pharmaceuticals that target AMPK such as the widely prescribed type II diabetes drug metformin do so nonspecifically (14-16); they do not specifically target the catalytic subunit. As such, which isoform contributes to therapeutic effects is still unknown. Understanding the potentially unique roles of the catalytic isoforms of AMPK is thus critical to provide molecular mechanistic insight into the pharmacologic effects of AMPK agonists.

A pressing challenge in understanding the molecular roles of AMPK is bridging the heterogeneity and diversity of AMPK targets across different tissue and cell types, especially considering the many heterotrimeric flavors AMPK presents as across tissues (17). However, discerning the functions of PRKAA1 and PRKAA2 within each tissue is difficult to dissect due to biased expression profiles across different tissues, so a molecular investigation to better understand the potentially unique roles of PRKAA1 and PRKAA2 is warranted given the significance of AMPK in regulating energy homeostasis. For example, murine leukocytes predominantly express one of the AMPK catalytic isoforms (*Prkaa1*) over the other making it difficult to investigate the role of individual catalytic isoforms in these cells (18). However, transcriptomic studies of the neurosensory retina have shown appreciable expression of both isoforms, offering the opportunity to investigate the functions of both catalytic isoforms in an energy-demanding, complex neurovascular tissue (19). We hypothesized that the two catalytic isoforms display distinct metabolic roles in regulating photoreceptor function in the retina.

The neurosensory retina is comprised of energy demanding neurons, with roughly 80% of the cell population being rod photoreceptor neurons (20). Photoreceptors are highly metabolically

active; they are essential for vision and especially vulnerable to metabolic perturbations (21). Previous studies have demonstrated that mutations in genes involved in energy homeostasis, the visual cycle, or the phototransduction cascade typically result in photoreceptor dysfunction and loss (22-26). Specialized features of rod photoreceptors predispose them to metabolic vulnerabilities. Known as the Warburg effect (27), photoreceptors heavily rely on aerobic glycolysis to meet the energy demands of both dark current maintenance as well as anabolic generation of new outer segments (21, 22). The dark current is the depolarizing current necessary to appropriately respond to light stimuli while the rod photoreceptor is unstimulated. Although non-proliferative, rod photoreceptors have high anabolic demand due to their diurnal shedding and regeneration of outer segments: specialized organelles rich with membranes holding proteins necessary for phototransduction. Both of these features are unique to rod photoreceptors and are highly dependent on aerobic glycolysis. As such, it is important to investigate the catalytic functions of AMPK that regulate photoreceptor metabolism as impaired AMPK activity leads to photoreceptor dysfunction and subsequent vision loss.

In addition to high ATP demand, photoreceptors require a delicate balance of other metabolites, such as guanosine mono-phosphate (GMP) and cyclic guanosine mono-phosphate (cGMP) for normal phototransduction (28). This is due to their unique reliance on cGMP-gated membrane channels and guanosine triphosphate (GTP)-dependent transducin activation in rod photoreceptor outer segments. The phototransduction cascade is initiated with a light photon activating an opsin protein, eventually leading to active conversion of cGMP to GMP by phosphodiesterase. The resulting decrease in intracellular cGMP concentration forces cGMP-gated channels to be closed, subsequently hyperpolarizing the membrane to initiate the visual transduction cascade to downstream effectors. Reliance on both ATP and GTP homeostasis for critical functions

predispose rod photoreceptors to unique vulnerabilities when phospho-purine homeostasis is impaired. As the de novo purine synthesis pathway intricately connects ATP and GTP homeostasis (29), elucidating the functions of AMPK in rod photoreceptors may offer molecular insights into photoreceptor metabolism and function.

Here, we establish that the AMPK catalytic isoforms PRKAA1 and PRKAA2 have distinct functions in rod photoreceptors and identify a molecular basis of energy regulation and photoreceptor dysfunction in the setting of selective PRKAA2 dysfunction. Abrogation of PRKAA2, but not PRKAA1, function in rod photoreceptors leads to structural abnormalities and visual dysfunction. Furthermore, metabolomic and phosphoproteomic studies reveal PRKAA2 dysfunction causes aberrant inosine monophosphate dehydrogenase (IMPDH) activity, leading to rod photoreceptor dysfunction. We also demonstrate visual function deficits caused by PRKAA2 dysfunction can be improved with an IMPDH antagonist, a finding that has therapeutic possibilities. Taken together, this study mechanistically delineates the functions of PRKAA1 and PRKAA2 in rod photoreceptor neurons, and establishes IMPDH as a target of PRKAA2.

1.2 Results

1.2.1 *Prkaa1* and *Prkaa2* expression in the retina

Delineating the independent functions of PRKAA1 and PRKAA2 in vivo remains challenging due to the biased expression profiles of the catalytic isoforms across different tissue types where the expression of only one isoform often dominates. Using publicly available bulk RNA sequencing data (19), we compared the expression levels of both isoforms in mouse retina and across mouse hepatocytes and macrophages through publicly available bulk RNA sequencing data (Figure 1A-1C) (18, 30). While the retina appreciably expresses both isoforms, hepatocytes

and macrophages demonstrate markedly skewed expression profiles with dominant expression of only one of the catalytic isoforms. As approximately 80% of the mouse retina is comprised of rod photoreceptors that are highly metabolically active, we sought to investigate the functions of PRKAA1 and PRKAA2 in rod photoreceptors (20). Using in-situ hybridization, we were able to visualize the expression of both *Prkaa1* and *Prkaa2* in the outer nuclear layer of retina sections of wild-type mice, which confirmed that both isoforms are expressed in rod photoreceptors (Figure 1D and 1E).

1.2.2 Expression profiles of AMPK catalytic isoforms are consistent across mouse and human retina

We further sought to assess if we could appreciate comparable expression profiles of both isoforms between mouse and human retina. To investigate this, we utilized publicly available single cell RNA sequencing datasets of both mouse and human retina (31, 32). We annotated clusters based on known marker genes, then calculated average normalized expression of PRKAA1 and PRKAA2 within each cell type (Figure 1F and 1G). Both mouse and human data indicate that retina cells express both isoforms above background levels, but suggest some preference for the $\alpha 2$ isoform. Interestingly, a similar pattern of co-expression of both isoforms was also observed across a variety of cell types within the mouse brain (33) (Figure 1H), but is in stark contrast to expression within individual human peripheral blood mononuclear cell types, which demonstrate near complete restriction to PRKAA1 expression (Figure 1I). Taken together, these data justify the study of isoform-specific roles in central nervous system tissues in mice and presents rod photoreceptors as an excellent model.

We also plotted the relative expression of $\alpha 1$ and $\alpha 2$ isoforms within each cell type. Again, this quantitative assessment displays a preference for the $\alpha 2$ isoform within all mouse and human

retinal cell types (Figure 1J). Mouse brain data suggest a split in expression preference between cell types, but closer observation shows more neuronal cell types prefer Prkaa2 expression while immune cells and glia express more Prkaa1. Human PBMC data demonstrate that these cells overwhelmingly express PRKAA1. Taken together, these data support the notion that neuronal cell types express both isoforms, but with some preference for $\alpha 2$. Non-neuronal and immune cells show a strong preference for $\alpha 1$ with little to no appreciable expression of $\alpha 2$. Given the consistent isoform expression profiles across neuronal cell types, including retinal rod photoreceptor neurons, rod cells provide an accessible and important cell type to investigate the functions of the individual isoforms that may have functional implications for other neurons in the central nervous system.

1.2.3 *Prkaa1*^{-Rhod/-Rhod} and *Prkaa2*^{-Rhod/-Rhod} express deficient PRKAA1 and PRKAA2 respectively in rod photoreceptors

We generated Prkaa1 rod photoreceptor specific knockouts (Prkaa1-Rhod/Rhod) with wild-type littermates (Prkaa1F/F) and Prkaa2 rod photoreceptor specific knockouts (Prkaa2-Rhod/-Rhod) with wild-type littermates (Prkaa2F/F) by crossing floxed mice with mice carrying one copy of the rhodopsin-cre transgene. We performed qRT-PCR of magnetically isolated rod photoreceptors to confirm both knockout of the targeted region and lack of any compensatory over-expression of the other catalytic isoform (Supplementary Figure 1) (26). Despite mild decrease in expression of Prkaa2 in Prkaa1-Rhod/-Rhod, we did not observe structural or functional deficits in Prkaa1-Rhod/-Rhod rod photoreceptors (Figure 2C-2F).

Both Prkaa1 and Prkaa2 flox mice have been previously characterized (34). Both protein sequences are highly homologous, with kinase domains and auto-inhibitory sequences of similar size and location (Figure 2A and 2B). The knockout domains were designed to abrogate kinase

function, but preserve overall protein expression. We hypothesized that PRKAA1 and PRKAA2 carry distinct roles in maintaining rod photoreceptor structure and function.

1.2.4 *Prkaa2*^{-Rhod/-Rhod} rod photoreceptors exhibit disorganized outer segment structures on electron microscopy

To structurally characterize the photoreceptors of both *Prkaa1*-Rhod/-Rhod and *Prkaa2*-Rhod/-Rhod mice, we utilized histological techniques. We enucleated eyes from both *Prkaa1*-Rhod/-Rhod and *Prkaa2*-Rhod/-Rhod and processed sagittal sections of the retina and stained with hematoxylin and eosin (H&E). Neither *Prkaa1*-Rhod/-Rhod nor *Prkaa2*-Rhod/-Rhod retina sections exhibited gross anatomical abnormalities in the outer nuclear layer, outer segment, and inner segment layers where rod photoreceptors reside (Supplemental Figure 2). We next evaluated ultrastructural changes that are unappreciable using H&E staining techniques. Using transmission electron microscopy, we were able to consistently observe outer segment changes only in *Prkaa2*-Rhod/-Rhod photoreceptors (Figure 2C and 2D). The structural integrity of the outer segments was visibly compromised with accumulation of granular debris and loss of laminar organization. *Prkaa1*-Rhod/-Rhod outer segments appeared unchanged compared to controls. These data taken together suggest *Prkaa2*-Rhod/-Rhod rod photoreceptors have altered outer segment structural integrity without overt degeneration.

Outer segments of rod photoreceptors are specialized organelles responsible for responding to light photons by converting them into electrical signals (22). These organelles are responsible for the bulk of ATP demand from the cell as maintaining membrane electrochemical sensitivity is ATP intensive. We therefore hypothesized that the lack of outer segment structural integrity in *Prkaa2*-Rhod/-Rhod rod photoreceptors may lead to altered visual function.

1.2.5 *Prkaa2*^{-Rhod/-Rhod} mice demonstrate visual function deficits in vivo

We utilized in vivo full field scotopic electroretinography to assess rod photoreceptor function (35) in both *Prkaa1*-Rhod/-Rhod and *Prkaa2*-Rhod/-Rhod. Dark adapted mice were anesthetized and retinal responses to increasing intensity levels of white light flashes were recorded. Initial hyperpolarized deflections from the baseline were characterized as the scotopic a wave, the putative measurement of rod photoreceptor response, while the trough of the a wave to the crest of the deflection were characterized as the scotopic b wave, the putative measurement of the inner retinal response from rod photoreceptor hyperpolarization. Consistent with ultrastructural photoreceptor outer segment changes, we observed significantly attenuated scotopic a and scotopic b waves in *Prkaa2*-Rhod/-Rhod (Figure 2G and 2H), but not in *Prkaa1*-Rhod/-Rhod (Figure 2E and 2F), suggesting *Prkaa2*-Rhod/-Rhod rod photoreceptors are functionally impaired. These data support that PRKAA2 is the key catalytic AMPK isoform in rod photoreceptors.

1.2.6 cGMP, GTP, and ATP levels are elevated in *Prkaa2*^{-Rhod/-Rhod} retinas

As AMPK is known to modulate the metabolome and cellular energetics (1), we next determined whether differences in phospho-purines such as ATP and GTP might explain the structural and functional deficits observed in the *Prkaa2*-Rhod/-Rhod mice. To investigate this, we utilized whole retina LC-MS/MS based metabolomics to quantify different metabolite levels. AMP, ADP, GMP, GDP, and IMP levels were not significantly changed in *Prkaa2*-Rhod/-Rhod retinas (Figure 3B, 3C, 3E-3G). Surprisingly, we discovered significantly increased levels of ATP (1.723 fold) and GTP (1.927 fold) in *Prkaa2*-Rhod/-Rhod retinas (Figure 3D and 3H). In addition, cGMP also showed an increasing trend (1.42 fold, p=0.055) (Figure 3A). These metabolites were unchanged in *Prkaa1*-Rhod/-Rhod retinas (Supplemental Figure 3). Increased

levels of cGMP and GTP provide insight into potential mechanisms of rod photoreceptor dysfunction as cGMP and GTP homeostasis is critical in the phototransduction cascade and rod dark current maintenance (21, 28). Although AMPK has widely been reported to help modulate catabolic processes contributing to ATP production, these data suggest PRKAA1 or PRKAA2 dysfunction did not negatively impact the steady-state pool of ATP in rod photoreceptors. On the contrary, PRKAA2 dysfunction was associated with increased steady-state ATP levels. These changes could reflect diminished energy consumption. Increased ATP levels can also be driven by de novo AMP synthesis and the ATP salvage pathway through glycolysis, tricarboxylic acid cycle, and the electron transport chain, so we next sought to elucidate the mechanism behind increased ATP production (7, 22, 29).

1.2.7 *Prkaa2*^{-Rhod/-Rhod} retinas demonstrate increased glycolytic flux

Rod photoreceptors primarily use aerobic glycolysis for ATP production to meet their high energy demand (27). To elucidate the metabolic mechanism underlying the increased ATP in *Prkaa2*-Rhod/-Rhod retinas, we performed extracellular flux analyses of retinas to assess both oxidative phosphorylation and glycolytic flux capacity using the Seahorse MitoStress and Glycolytic Stress test kits respectively (36). We did not observe any changes in oxidative phosphorylation flux (Figure 3I); however, we observed a significant increase in glycolytic flux in *Prkaa2*-Rhod/-Rhod (Figure 3J). We did not observe significant changes to extracellular flux capacity in *Prkaa1*-Rhod/-Rhod retinas (Supplemental Figure 4A and 4B). To further corroborate our findings, we extracted retinas and cultured them in Ames' Media for 30 minutes in a 5% CO₂ cell culture incubator to measure excreted lactate levels in the supernatant. We used a colorimetric plate-based assay to measure lactate levels. As lactate is a byproduct of glycolysis and has been reported to be excreted by rod photoreceptors (37), we anticipated an increase of

lactate excretion in Prkaa2-Rhod/-Rhod retinas. Indeed, we observed significantly increased levels of excreted lactate in Prkaa2-Rhod/-Rhod (Figure 3K) but not Prkaa1-Rhod/-Rhod retinas (Supplemental Figure 4C). The constellation of these data support that Prkaa2-Rhod/-Rhod rod photoreceptors demonstrate increased glycolysis whereas Prkaa1-Rhod/-Rhod rods do not. Moreover, these data also suggest that the mechanism behind increased ATP levels in Prkaa2-Rhod/-Rhod is activated glycolysis.

1.2.8 Rod-isolated phosphoproteomics reveal IMPDH as a downstream effector of PRKAA2

We next sought to identify candidate targets of PRKAA2 which mediate the structural and functional phenotype of Prkaa2-Rhod/-Rhod, particularly the mechanism behind the increased cGMP and GTP levels observed through metabolomics. As AMPK phosphorylates downstream targets through its enzymatic activity, we utilized an immuno-magnetic precipitation to isolate rod photoreceptors for unbiased LC/MS-MS phosphoproteomics from both Prkaa1-Rhod/-Rhod and Prkaa2-Rhod/-Rhod (Figure 4A). Phosphoproteomics of Prkaa1-Rhod/-Rhod rod photoreceptors reveal relatively minor changes to the phosphoproteome unrelated to metabolic changes (Figure 4B). However, phosphoproteomics of Prkaa2-Rhod/-Rhod reveal a vastly altered phosphoproteome compared to wild-type controls (Figure 4C).

4,086 unique phosphosites were quantified and 73 phosphosites were found to be significantly changed with <1% false discovery rate with 1.75 fold change and 0.01 p-value cutoffs.

Consistent with diminished visual function on electroretinography, numerous proteins involving the phototransduction cascade and photoreceptor function demonstrated differential phosphorylation including retinitis pigmentosa 1-like 1 protein (RP1L1), phosphodiesterase 6A (PDE6A), phosphodiesterase 6G (PDE6G), interphotoreceptor matrix proteoglycan 2 (IMPG2),

sodium/potassium/calcium exchanger 1 or NCKX1 (SLC24A1), and potassium voltage-gated channel subfamily B member 1 (KCNB1). Other proteins involving synapse function were also differentially phosphorylated such as protein unc-119 homolog A (UNC119), SNARE-associated protein Snapin (SNAPIN), synapsin-2 (SYN2), and disks large-associated protein 1 (DLGAP1). Furthermore, structural and cilia related proteins were also differentially phosphorylated including microtubule-actin cross-linking factor 1 (MACF1), microtubule-associated protein 1B (MAP1B), rootletin (CROCC), kinesin-like protein (KIF3A), spermatogenesis-associated protein 7 homolog (SPATA7), and joubertin (AHI1). Post-translational modifications of these structural or cilia related proteins may lead to the observed outer segment changes seen in Figure 2C and 2D. In addition, phosphoglycerate mutase 1 (PGAM1) and glyceraldehyde-3-phosphate dehydrogenase (GAPDH) which are both essential enzymes involved in glycolysis were differentially phosphorylated in Prkaa2-Rhod⁻/Rhod rod photoreceptors, suggesting a role in the upregulated glycolysis seen in Figure 3. Although AMPK has been described to regulate glycolysis through regulation of 6-phosphofructo-2-kinase (PFKFB) (7), we did not observe any significant changes in phosphorylation status of either PFKFB2 or PFKFB3. We plotted a selection of significantly downregulated phospho-proteins on a heatmap of z-scores to visualize the spread of each sample (Figure 4D).

Closer examination of the phosphoproteomic data identified inosine monophosphate dehydrogenase (IMPDH) as a strong candidate for the phenotype seen in PRKAA2 deficient mice as IMPDH is the rate-limiting enzyme for de novo GMP synthesis. A previous study reported marked changes in retinal ATP and GTP as a result of IMPDH dysfunction (38). The authors also demonstrated that phosphorylation of the S416 moiety downregulates IMPDH activity. Our phosphoproteomics data showed that both IMPDH1 and IMPDH2 have

downregulated phosphorylation at the S416 moiety only in *Prkaa2*-Rhod⁻/Rhod, suggesting aberrant activation of IMPDH as a possible mediator of rod photoreceptor dysfunction in the setting of *Prkaa2* deficiency (Figure 4E and 4F).

1.2.9 IMPDH activity is aberrantly upregulated in dark adapted *Prkaa2*^{-Rhod⁻/Rhod} retinas

Based on previous reports, IMPDH is regulated differently according to light conditions in rod photoreceptors (Figure 5A) (38). IMPDH is allosterically inhibited by increased GTP levels in dark adapted conditions, while IMPDH is activated to produce GMP in light adapted conditions. To ascertain whether IMPDH is aberrantly activated in the *Prkaa2*-Rhod⁻/Rhod rod photoreceptors, we utilized a colorimetric plate-based assay to specifically measure IMPDH activity using dissected and lysed retinas from *Prkaa2*-Rhod⁻/Rhod mice. This assay is based on the reduction of the tetrazolium salt INT in a NADH-coupled reaction to INT-formazan which exhibits a new absorption maximum at 492 nm and allows for sensitive measurement of IMPDH activity (39). When measuring IMPDH activity in ambient light conditions, we detected no significant changes in *Prkaa2*-Rhod⁻/Rhod (Figure 5B). However, we hypothesized that IMPDH activity was constitutively activated in light conditions even in wild-type controls based on previous reports of IMPDH activation in rod photoreceptors (38). Therefore, we sought to investigate IMPDH activity in dark adapted conditions. After overnight dark adaptation, *Prkaa2*-Rhod⁻/Rhod retinas were processed and measured for IMPDH activity. Indeed, the overall absolute values of IMPDH activity were considerably lower than in the light adapted counterparts, and we were able to observe significantly higher levels of IMPDH activity in *Prkaa2*-Rhod⁻/Rhod retinas (Figure 5C). These data suggest that PRKAA2 interacts with and phosphorylates IMPDH1 and IMPDH2 to downregulate their activity, and PRKAA2 dysfunction leads to significant upregulation of IMPDH activity.

1.2.10 AMPK affecting compounds alter IMPDH activity

We next investigated whether metformin, an AMPK activator, suppresses IMPDH activity in retinal lysates (Figure 5D). We measured IMPDH activity from retinal lysates of wild-type mice treated with metformin, and observed a substantial abrogation of IMPDH activity in metformin treated lysates. He et al. also demonstrated that the effect of AMPK activation by metformin in the retina is notably slower than other that of other AMPK activators (40), which corroborates the delay in IMPDH activity inhibition seen in our assay. These results suggest that a potent effect of metformin in the retina is inhibition of IMPDH activity, which could be through activation of AMPK.

We also sought to investigate whether Compound C or dorsomorphin, an AMPK inhibitor, upregulates IMPDH activity in retinal lysate (Figure 5E). Following our hypothesis on IMPDH activity based on dark adaptation, we assumed IMPDH activity is naturally inhibited by AMPK in dark adapted retinas so we sought to test the effect of AMPK inhibition in dark adapted wild-type retinas. Indeed, we detected significantly upregulated IMPDH activity in lysates treated with Compound C. Previous studies have noted 40 μM of Compound C is sufficient for complete inhibition of AMPK activity; however, it is also noted that Compound C can affect numerous other kinases (41). Therefore, we cannot rule out that other kinase inhibition may also affect IMPDH activity in addition to AMPK inhibition.

1.2.11 IMPDH is a direct target of PRKAA2 in the retina

To validate the effect of IMPDH regulation by PRKAA2, we used recombinant human AMPK ($\alpha 2\beta 1\gamma 1$) incubated with recombinant human IMPDH1 or IMPDH2 and measured IMPDH activity. We determined that $\beta 1$ and $\gamma 1$ were the highest expressed isoforms of the other AMPK

subunits based on bulk RNA sequencing data of the retina (19) and hypothesized that AMPK ($\alpha 2\beta 1\gamma 1$) would reduce IMPDH activity compared to IMPDH alone. We observed significantly reduced IMPDH activity in IMPDH incubated with AMPK ($\alpha 2\beta 1\gamma 1$) compared to IMPDH incubated alone (Figure 5F and 5G).

We hypothesized that we could visualize PRKAA2 and IMPDH to be in the same sub-cellular compartment if they interact with each other. To test this, we used immunofluorescence to visualize localization of PRKAA2 and IMPDH in Prkaa2-Rhod^{-/-}Rhod retinal sections (Supplemental Figure 5). The knockout domain of PRKAA2 in Prkaa2-Rhod^{-/-}Rhod is contained within the kinase domain, which allowed us to utilize a PRKAA2 antibody that specifically targets an immunogen outside the kinase domain. Using this targeted approach, we identified that both isoforms of IMPDH are modestly appreciated in the same sub-cellular compartment as PRKAA2 especially in Prkaa2-Rhod^{-/-}Rhod sections compared to Prkaa2^{F/F} sections, particularly in the inner segment layers. These data suggest PRKAA2 may co-localize with IMPDH when the kinase activity is dysfunctional. One potential reason for this may be that PRKAA2 functionally ‘dead kinase’ is actively attempting to inhibit hyperactivated IMPDH in the Prkaa2-Rhod^{-/-}Rhod rod photoreceptors.

We further sought to distinguish whether IMPDH dysregulation was either a direct or indirect manifestation of PRKAA2 abrogation. To elucidate whether IMPDH is a direct target of PRKAA2 in the retina, we performed co-immunoprecipitation experiments (Figure 5H). By co-immunoprecipitating IMPDH1, the predominantly expressed IMPDH isoform in the retina (19, 38), we investigated whether we could detect PRKAA2 bound to IMPDH1 through western blotting. We utilized dark-adapted retinas from wild-type mice based on our hypothesis that PRKAA2 interacts with IMPDH moreso in dark-adapted photoreceptors. Indeed, we were able to

detect PRKAA2 in the IMPDH1 co-immunoprecipitated suspension, suggesting PRKAA2 directly binds to IMPDH1 in the retina (Figure 5I).

1.2.12 Mycophenolate mofetil treatment improves *Prkaa2*^{Rhod/Rhod} visual function

Previous studies have examined the in vivo effect of IMPDH dysregulation using the dual flash paradigm of electroretinography (38, 42). As our previous data have demonstrated IMPDH is dysregulated in *Prkaa2*-Rhod/-Rhod, we hypothesized that *Prkaa2*-Rhod/-Rhod exhibit altered mass rod recovery as measured by the dual flash paradigm due to changed IMPDH activity and potentially changed GTP/cGMP levels. Indeed, using this paradigm, *Prkaa2*-Rhod/-Rhod demonstrated significantly faster rod recovery (Figure 6A-6C). Following these experiments, we next sought to test if these changes were reversible. We utilized mycophenolate mofetil, a known IMPDH inhibitor, injected intravitreally into the eyes of *Prkaa2*-Rhod/-Rhod and assessed the mass rod recovery and full-field scotopic electroretinography function (38). Left eyes were injected with PBS vehicle while right eyes were injected with 1 μ L of 10 mM mycophenolate mofetil to produce an estimated effective concentration of 2 mM in the eye. Mass rod recovery was slower in the mycophenolate injected eyes compared to vehicle injected eyes (Figure 6D-6F). However, the full-field scotopic electroretinography measurements yielded significantly improved scotopic a wave and scotopic b wave amplitudes (Figure 6G and 6H). Furthermore, injection of the same concentration of mycophenolate in wild-type mice did not improve visual function, suggesting the effects of mycophenolate-induced visual function improvement is specific to *Prkaa2*-Rhod/-Rhod (Supplemental Figure 6). These data suggest IMPDH hyperactivity in *Prkaa2*-Rhod/-Rhod is suppressible, and reducing IMPDH hyperactivity improves the function of rod photoreceptors.

1.3 Discussion

Our study suggests that AMPK, specifically through PRKAA2, regulates IMPDH activity in rod photoreceptors. Firstly, we showed that the catalytic subunits of AMPK, PRKAA1 and PRKAA2, are both expressed in the neurosensory retina. In addition, these subunits exhibit distinct roles in that only PRKAA2 plays a unique functional role in rod photoreceptor neuron function during homeostasis as measured by electroretinography. We provide evidence that PRKAA2 directly binds and acts on IMPDH, and that through this interaction, AMPK may regulate the activity of IMPDH, the rate-limiting enzyme for GMP synthesis. Although the phosphorylation site of S416 of IMPDH has been described as a consensus site for AMPK (43), our study is the first to demonstrate that AMPK regulates IMPDH *in vivo* specifically in retinal neurons. Disruption of the AMPK-IMPDH axis with IMPDH hyperactivity contributes to visual function deficits as mycophenolate-induced IMPDH inhibition ameliorates visual function deficits seen in *Prkaa2-Rhod^{-/-}Rhod* mice.

IMPDH inhibition by AMPK suggests AMPK promotes the *de novo* synthesis of AMP by inhibiting *de novo* synthesis of GMP, which would allow more AMP as substrate to produce ATP through glycolysis and oxidative phosphorylation. However, there are likely many intermediate factors that contribute to maintenance of steady-state AMP and GMP levels as *Prkaa2-Rhod^{-/-}Rhod* retinas did not exhibit changes to AMP and GMP levels despite evidence of increased IMPDH activity. Further investigation is warranted to link increased *de novo* production of AMP to increased levels of ATP as AMPK is canonically associated with increasing ATP levels. Additional studies are also necessary to establish the link between the

presumed increased production in GMP and the observed increase in cGMP and GTP levels in Prkaa2-Rhod/-Rhod retinas.

The mass rod recovery electroretinography data from Prkaa2-Rhod/-Rhod may hint at changes to the phototransduction cascade. Lyubarsky and Pugh (42) hypothesized that changes in mass rod recovery through the dual flash paradigm could be attributed to either rare long-lived rhodopsin inactivation or the availability of GTP-bound transducin- α to bind PDE γ . In tandem with Lyubarsky and Pugh's hypothesis, the findings from Plana-Bonamaisó et al. that demonstrate inhibiting de novo GMP synthesis leads to slower mass rod recovery may suggest mass rod recovery is influenced by levels of guanine-phosphate levels. This may potentially be due to availability of GTP-bound transducin- α or cGMP levels. Considering the metabolomics data suggesting increased GTP levels in Prkaa2-Rhod/-Rhod, we speculate that increased GTP or cGMP levels lead to faster mass rod recovery which reflects the opposite phenotype seen in the inhibition of IMPDH (38). Increased levels of cGMP may also contribute to the visual function defects seen in Prkaa2-Rhod/-Rhod. Major players in the phototransduction cascade, such as phosphodiesterase and guanylyl cyclase consume and produce cGMP respectively to delicately regulate cGMP levels and cyclic nucleotide gated (CNG) channels (44). Additional studies are needed to elucidate the mechanism of the potential effect of cGMP levels on visual function in Prkaa2-Rhod/-Rhod as there likely many factors contributing to this effect; however, candidate proteins that may have aberrant activity related to cGMP regulation and closely associated calcium regulation include phosphodiesterase 6A (PDE6A), phosphodiesterase 6G (PDE6G), and sodium/potassium/calcium exchanger 1 or NCKX1 (SLC24A1) as they all have altered phosphorylation based on phosphoproteomics data. Perturbed activity of these enzymes may contribute to disturbed cGMP/GTP homeostasis as seen in Prkaa2-Rhod/-Rhod retinas as

PDE6A and PDE6G directly converts cGMP to GMP and NCKX1 contributes to intracellular calcium levels which affects guanylyl cyclase activity converting GTP to cGMP.

Although AMPK putatively upregulates catabolic processes (1), we observed an increase in glycolysis along with increased ATP levels with loss of PRKAA2 activity. We can therefore speculate that PRKAA2 function is not necessary to upregulate glycolysis. Furthermore, glycolytic upregulation in *Prkaa2-Rhod^{-/-}* may be controlled by PRKAA1 or an AMPK independent pathway. The mechanism of increased glycolysis in *Prkaa2-Rhod^{-/-}* has yet to be elucidated. However, our phosphoproteomics data yielded interesting insights into which glycolysis-related proteins may potentially be affecting the glycolysis phenotype in *Prkaa2-Rhod^{-/-}*. Both phosphoglycerate mutase 1 (PGAM1) and glyceraldehyde-3-phosphate dehydrogenase (GAPDH) had significantly different phosphorylation statuses, suggesting either by direct or indirect effect of *Prkaa2* knockout that PGAM1 and GAPDH may be affecting the glycolysis phenotype. Surprisingly, we did not observe differential phosphorylation status of either PFKFB2 or PFKFB3 despite them being described targets of AMPK for glycolytic regulation (7). These results highlight how despite the thorough characterization of AMPK function in previous studies, the putative targets of AMPK are perhaps regulated according to distinct isoform function and tissue context.

By investigating the *Prkaa1-Rhod^{-/-}* and *Prkaa2-Rhod^{-/-}* models, we have characterized a novel role for the PRKAA2 catalytic isoform of AMPK in regulating IMPDH activity.

Mutations in IMPDH1 in humans are associated with severe forms of inherited blindness, with nine known mutations linked to autosomal dominant retinitis pigmentosa-10 (RP10) (45-49) and two known mutations linked to Lebers Congenital Amaurosis type 11 (LCA11) (46).

Interestingly, RP10 mutations have been suggested to be ‘gain-of-function’ mutations as *Impdh1*

knock-out mice present mild retinopathy (50). Given that Prkaa2-Rhod/-Rhod retinas recapitulate features of Impdh1 ‘gain-of-function’ mutations, these mice could present a suitable model to study and treat RP10 ‘like’ mutations.

The results of our study warrant further investigation into whether PRKAA2 regulates IMPDH activity in other cell types, particularly ones with high energetic demands and those that predominantly express Prkaa2 over Prkaa1. However, it is also possible that the effect of IMPDH activity is more strongly appreciated in rod photoreceptors because they uniquely rely on cGMP and the other guanosine phosphates for phototransduction and dark current maintenance. This study was largely limited to observing the effects of PRKAA2 in homeostasis; therefore, further investigation is necessary to determine the functions of both PRKAA1 and PRKAA2 in disease. Previous studies have described a protective role of AMPK based on both loss-of-function and gain-of-function studies in both endotoxin-induced uveitis and light-induced retinal degeneration models (3, 16), but the role of the individual catalytic subunits in disease is unclear. Future studies that examine specific pathways regulated by either PRKAA1 or PRKAA2 in photoreceptors during disease will illuminate our understanding of how AMPK regulates cellular energy balance and function in disease models.

1.4 Materials and Methods

Sex as a biological variable

Only male mice were used for experiments as interventions not included in the manuscript such as high fat diet and streptozotocin-induced diabetes are more feasible for survival in male mice. Although not included in the manuscript, male mice were continued to be used for consistency. The findings in the manuscript are expected to be relevant to more than one sex.

Animals

All animal experiments were conducted in accordance with the ARVO Statement for the Use of Animals in Ophthalmic and Vision Research and Washington University School of Medicine in St. Louis Animal Care and Use guidelines and after approval by the Institutional Animal Care and Use Committee (IACUC). Male mice between 8 and 12 weeks old (2-3 months of age) were used in this study. Mice were housed in a 12-hour light/dark cycle with free access to food and water. Prkaa1F/F and Prkaa2F/F mice were previously characterized (34) and purchased from Jackson Laboratory (014141 and 014142). These mice were crossed with mice carrying one copy of the rhodopsin-iCre75 (Rhod-cre) transgene, which were provided by Dr. Ching-Kang Jason Chen and have been previously characterized (51) to generate Prkaa1-Rhod/-Rhod and Prkaa2-Rhod/-Rhod. We confirmed that these mice did not carry the Crb1 gene rd8 mutation (data not shown). Mice were fully backcrossed to the inbred C57BL/6J background.

Single cell RNA sequencing analysis

Published datasets were imported into Monocle 3 (v1.3.1) (52) for reanalysis and confirmation of published cell type calls. Count matrix was then exported using the `exprs()` function before normalization of counts to 10K (TP10K) and computation of average expression of genes of interest within each cell type. Nominal 0.01 TP10K pseudocount was added to each average count per cell type before calculation of ratio of PRKAA1 to PRKAA2.

Immunomagnetic rod photoreceptor isolation

To isolate rod photoreceptors from the retina, we utilized the Papain Dissociation System (Worthington Biochemical Corporation) following a previously described modified protocol (26), followed by EasySep Mouse PE and Biotin positive selection kit (Stem Cell Technologies)

following the manufacturer's protocol. We used 2 $\mu\text{g}/\text{mL}$ of PE-conjugated anti-CD73 antibody (Miltenyi Biotec) and 2 $\mu\text{g}/\text{mL}$ of biotin-conjugated anti-rhodopsin antibody (Novus Biologicals) as part of the EasySep protocol.

RNA isolation and qRT-PCR

Total RNA was extracted using RNeasy Micro Plus kit (Qiagen) according to the manufacturer's instructions. To synthesize cDNA, total RNA was added to the High Capacity cDNA Reverse Transcription Kit (Thermo Fisher Scientific) and reverse-transcribed according to the manufacturer's instructions. qRT-PCR was performed in duplicate using the StepOnePlus Real Time PCR system (Thermo Fisher Scientific) using TaqMan Real-Time PCR Assays (Thermo Fisher Scientific), and the mRNA was quantified using the $\Delta\Delta\text{CT}$ method with Gapdh or Actb as the internal control. Custom Taqman probes (Thermo Fisher Scientific) were created and used to specifically measure expression of exon 3 of Prkaa1 and exon 2 of Prkaa2 to confirm knockout in the respective models.

Transmission electron microscopy

We performed transmission electron microscopy as previously described (35). For ultrastructural analyses, eyecups were fixed in 2% paraformaldehyde (PFA)/2.5% glutaraldehyde (Polysciences Inc.) in 100 mM sodium cacodylate buffer, pH 7.2, for 2 hours at room temperature and then overnight at 4°C. Samples were washed in sodium cacodylate buffer at room temperature and postfixed in 1% osmium tetroxide (Polysciences Inc.) for 1 hour. Samples were then rinsed extensively in dH₂O prior to en bloc staining with 1% aqueous uranyl acetate (Ted Pella Inc.) for 1 hour. Following several rinses in dH₂O, samples were dehydrated in a graded series of ethanol and embedded in Eponate 12 resin (Ted Pella Inc.). Sections of 95 nm were cut with a Leica

Ultracut UCT ultramicrotome (Leica Microsystems Inc.), stained with uranyl acetate and lead citrate, and viewed on a JEOL 1200 EX transmission electron microscope (JEOL USA Inc.) equipped with an AMT 8 megapixel digital camera and AMT Image Capture Engine V602 software (Advanced Microscopy Techniques).

Electroretinography (ERG)

Full field scotopic ERG was performed as previously described (35). A UTAS BigShot System (LKC Technologies Inc.) was used. Mice were dark adapted overnight. Under red light illumination, mice were anesthetized with an intraperitoneal injection of 86.9 mg/kg ketamine and 13.4 mg/kg xylazine. Pupils were dilated with 1% tropicamide eye drops. Body temperature was maintained at 37°C with a heating pad. Contact lens electrodes were placed bilaterally with appropriate reference and ground electrodes. The stimulus consisted of a full-field white light flash (10 μ s). Raw data were processed using MATLAB software (MathWorks). The amplitude of the a wave was measured from the average pretrial baseline to the most negative point of the average trace, and the b wave amplitude was measured from that point to the highest positive point.

The mass rod recovery or dual flash paradigm was utilized as previously described (38, 42).

Briefly, mice underwent the same pipeline for full-field scotopic ERG. However, mice were instead exposed to sequential stimuli of a full-field white light flash (10 μ s, 0.977 cd*S/M²) of different inter-stimulus times (IST) per step. The a wave and b wave amplitudes of both the baseline flash and the probe flash were measured for each IST, and the ratio of the response to the probe flash to baseline flash was calculated.

Intravitreal injection

Mice were dark adapted overnight. Under dim red lighting, mice were anesthetized with an intraperitoneal injection of 86.9 mg/kg ketamine and 13.4 mg/kg xylazine. Pupils were dilated with 1% tropicamide eye drops. A 33-gauge Hamilton syringe was used to inject into the vitreous cavity. Left eyes were injected with 1 μ L of PBS vehicle while right eyes were injected with 1 μ L of 10 mM mycophenolate mofetil to produce an effective concentration of 2 mM in the eye. These mice then immediately underwent the ERG pipeline.

Metabolomics measurement

Mice were euthanized and retinas were immediately extracted and frozen in liquid N₂. On the day of extraction, retinal tissues were homogenized in 160 μ l of cold 50% MeOH solution in water using homogenizer (Branson) and then centrifuged (15,000 g, 4°C, 10 min). Clear supernatant was transferred to a new tube containing 100 μ l chloroform and vigorously shaken then centrifuged (15,000 g, 4°C, 10 min). The chloroform extraction was repeated three times. The clear aqueous phase (120 μ l) was transferred to new tube and then lyophilized and stored at -80°C until measurement. Lyophilized samples were reconstituted with 60 μ l of 5 mM ammonium formate (Sigma) and centrifuged at 12,000 x g for 10 min. Cleared supernatant was transferred to a sample tray. Serial dilutions of standards for each metabolite in 5 mM ammonium formate were used to determine the retention time and concentration. Liquid chromatography was performed by HPLC (1290; Agilent) with Atlantis T3 (LC 2.1 \times 150 mm, 3 μ m; Waters) (38). For steady-state metabolite analysis, 20 μ l of samples were injected at a flow rate of 0.7 ml/min with 50 mM ammonium acetate and 5 mM medronic acid for mobile phase A and 100% acetonitrile for mobile phase B. Metabolites were eluted with gradients of 0–0.5 min 80%, 0.5-7.5 min 80-70%, 7.5-8.5 min 70-50%, 8.5-9 min 50%, 9-9.5 min 50-80%, 9.5-11 min 80% of B. The metabolites were detected with a triple quadrupole mass spectrometer (6460,

Agilent) under positive ESI multiple reaction monitoring (MRM) using m/z for AMP 348→136, ATP 508→136, GMP 364→152, GDP 444→152, GTP 524→152, cGMP 346→152, IMP 349→137. Metabolites were quantified by MassHunter quantitative analysis tool (Agilent) with standard curves and normalized by the protein amount in the sample.

Extracellular flux analyses

Oxygen consumption rate (OCR) and extracellular acidification rate (ECAR) measurements were used to evaluate the activity of oxidative phosphorylation and glycolysis respectively in retinas. Performing extracellular flux analyses using 1mm biopsy punches of retinas was previously described (36). Mice were euthanized and retinas were extracted into Seahorse XF DMEM media and maintained on a heating plate set to 37 °C. Three 1 mm biopsy punches (Integra) were isolated from each retina of the central region sparing the optic nerve head. Retina punches were transferred to Seahorse XF24 Islet Capture microplates. Retina punches were then gently placed on the bottom of wells, and mesh inserts were affixed on top of retina punches. Each well contained either a single retina punch or no punches to use as background.

The Seahorse XF24 sensor cartridge was hydrated with Seahorse XF Calibrant solution (1 mL per well) and placed in a non-CO₂ incubator at 37 °C the night before. One hour prior to the experiment, standard medium was removed and replaced with 500uL pre-warmed Seahorse XF DMEM 789 medium supplemented with 1mM sodium pyruvate, 2mM glutamine, and 10mM glucose, pH 7.4, and placed in a non-CO₂ incubator at 37 °C. Chemicals from either the Mito Stress Test kit for OCR or Glycolysis Stress Test kit for ECAR were loaded into the sensor cartridge as previously described. Following calibration of the sensor cartridge in the XFe24 Extracellular Flux Analyzer, the cell plate was inserted. Each cycle consisted of 3 min of mixing and a 2-min pause, followed by a 3-min measurement period. Each cycle repeated 3 times. Total

protein content of each well was measured using Pierce BCA Protein Assay Kit and used to normalize readings.

Retina lactate excretion measurement

Mice were euthanized and retinas were extracted and plated in a 12-well plate with 500 μ L of Ames' Media (prepared from 10 mL dH₂O with 88 mg lyophilized Ames' media, 19 mg sodium bicarbonate, and 20 mg glucose). Retinas were then incubated in a humidified incubator at 37 °C with 5% CO₂ for 30 minutes. The supernatants were then collected and quantified for lactate using a colorimetric assay (Sigma-Aldrich) following the manufacturer's protocol.

Phosphoproteomics

Phosphoproteomics of isolated rod photoreceptors were performed as described previously (53). Mass spectrometric data were collected on an Orbitrap Fusion Lumos mass spectrometer in-line with a Proxeon NanoLC-1200 UHPLC. The 100 μ m capillary column was packed with 35 cm of AccuCore 150 resin (2.6 μ m, 150 Å; ThermoFisher Scientific). Spectra were converted to mzXML using a modified version of ReAdW.exe. Database searching included all entries from the Mouse Genome Database (MGD). This database was concatenated with one composed of all protein sequences in the reversed order. Searches were performed using a 50 ppm precursor ion tolerance for total protein level profiling. The product ion tolerance was set to 0.9 Da. These wide mass-tolerance windows were chosen to maximize sensitivity in conjunction with SEQUEST searches and linear discriminant analysis. TMT tags on lysine residues and peptide N termini (+229.163 Da) and the carbamidomethylation of cysteine residues (+57.021 Da) were set as static modifications, while the oxidation of methionine residues (+15.995 Da) was set as a variable modification. For phosphorylation analysis, deamidation (+0.984) on asparagine and

glutamine and phosphorylation (+79.966) on serine, threonine, and tyrosine were set as variable modifications. Peptide-spectrum matches (PSMs) were adjusted to a 1% false discovery rate (FDR). PSM filtering was performed using a linear discriminant analysis, as described previously, (54) and then assembled further to a final protein-level FDR of 1%. Phosphorylation site localization was determined using the AScore algorithm. AScore is a probability-based approach for high-throughput protein phosphorylation site localization. Specifically, a threshold of 13 corresponded to 95% confidence in site localization. Proteins were quantified by summing reporter ion counts across all matching PSMs, as described previously. Reporter ion intensities were adjusted to correct for the isotopic impurities of the different TMT reagents according to manufacturer specifications. The signal-to-noise (S/N) measurements of peptides assigned to each protein were summed, and these values were normalized so that the sum of the signal for all proteins in each channel was equivalent to account for equal protein loading. Lastly, each protein was scaled such that the summed signal-to-noise for that protein across all channels was greater than 100, thereby generating a relative abundance (RA) measurement.

Immunofluorescent histology

Retinal sections fixed in 4% paraformaldehyde in 1x PBS were deparaffinized, then blocking and hyperpermeabilization were performed through PBS containing 5% bovine serum albumin (BSA) and 0.1% Triton X-100 for 1 hour. Sections were then incubated in blocking buffer with anti-PRKAA2 (R&D Systems, catalog AF2850; 1:100) and either anti-IMPDH1 (Proteintech, catalog 220921AP; 1:100) or anti-IMPDH2 (Proteintech, catalog 12948-1-AP; 1:100) antibodies overnight at 4 °C. The next day, sections were rinsed in PBS and subsequently incubated with Alexa Fluor dyes corresponding to the fluorescence-conjugated secondary antibodies at room

temperature for 1 hour. Nuclei were counterstained with DAPI (Millipore Sigma). Images were taken with the Zeiss LSM 800 Confocal Laser Scanning Microscope.

In situ hybridization

Formalin-fixed and dehydrated slides were pretreated with RNAscope protease reagents (Advanced Cell Diagnostics). Either Prkaa1 or Prkaa2 probes were added on each slide and incubated at 40 °C for 2 hours in a HybEZ Oven (Advanced Cell Diagnostics). Prkaa1 probes were customized to target exon 3 while Prkaa2 probes were customized to target exon 2. Amplification steps and color development using RNAscope 2.5 HD detection reagents (Advanced Cell Diagnostics) were performed in accordance with the manufacturer's instructions. After counterstaining with hematoxylin, coverslips were placed on slides. Images were taken with the Leica DMI8.

IMPDH activity assay

Mice were euthanized and retinas were extracted after either with or without dark adaptation overnight. Each sample was pooled from four retinas. These retinas were then lysed in lysis buffer (Biomedical Research Service and Clinical Application) and the IMPDH activity assay (Biomedical Research Service and Clinical Application) was utilized in accordance with the manufacturer's protocol. The manufacturer's protocol for the IMPDH activity assay can be found here: <https://www.bmrservice.com/impdhassay.html>. Briefly, lysed retina samples were applied in duplicates into a 96-well plate with one replicate serving as a control well and the other a reaction well. Both wells receive IMPDH assay solution, but only the reaction wells receive IMPDH substrate. The combined assay solution is added rapidly to each well containing retinal lysate samples. The plate is kept on ice during the addition of all reagents. The plate is

then swiftly transported to a pre-heated microplate reader at 37°C where the assay begins at time 0 when the plate is inserted and immediately scanned for colorimetric absorption of 492 nm. The microplate reader then measures the same absorption maximum every 10 minutes for 60 minutes. After compiling all of the measurements, enzyme activity is calculated with the difference of absorption measurement between control and reaction wells at each time point. The equation to calculate enzyme activity is as follows: $\Delta O.D. * 1000 * 70 \mu L / (\text{incubation time (minutes)} * 0.5 \text{ cm} * 18 * 20 \mu L) * \mu g = \mu \text{mol} / (\text{L} * \text{min}) * \mu g$. With incubation time being the only changing independent variable at each time point of measurement, a new constant is used at each time point to calculate the enzyme activity. In this assay, activity is measured as a function of absorption difference between the control and reaction wells, so activity can decrease as the difference between the control and reaction wells become smaller. In other words, the absorption measurement increase is not specific to IMPDH activity, so IMPDH activity is calculated relatively with the addition of IMPDH substrate. The assay used in our study uses the principle of measuring a new absorption maximum made through the reduction of tetrazolium salt INT in a NADH-coupled enzymatic reaction to INT-formazan as IMPDH activity reduces NAD⁺ to NADH. The assay was carried out under dim red light with dark adapted samples and were protected from white light throughout the entire assay.

Assays comparing IMPDH activity from retinas of Prkaa2-Rhod^{-/-}-Rhod were performed according to the manufacturer's protocol as described above. Assays assessing the effect of metformin (Millipore Sigma) were performed using ambient light adapted retinas from wild-type mice and added to produce an effective concentration of 5 mM in each well. Assays assessing the effect of Compound C (Millipore Sigma) were performed using overnight dark adapted retinas from wild-type mice and added to produce an effective concentration of 40 μ M in each

well. Assays assessing the effect of recombinant AMPK (Promega) on recombinant IMPDH1 (R&D Systems) or IMPDH2 (R&D Systems) were performed as follows: 500 ng IMPDH1 or 500 ng IMPDH2, 500 μ M dithiothreitol, 1X reaction buffer A (Promega), 100 μ M AMP solution (Promega), and either PBS or 500 ng AMPK and PBS were combined to constitute the initial solution before addition of the IMPDH activity assay constituents.

Co-immunoprecipitation

Co-immunoprecipitation of IMPDH1 from wild-type retinas was performed using the Dynabeads Co-Immunoprecipitation Kit (Thermo Fisher) in accordance with the manufacturer's protocol. 1.5 mg of Dynabeads were used to bind each sample from 6 total lysed retinas. 10 μ g of IMPDH1 antibody (Biolegend) were used for each sample.

Immunoblotting

Resultant samples from co-immunoprecipitation were loaded into lanes for SDS-polyacrylamide gel electrophoresis. 1 μ g of samples were loaded into each lane and one lane of 20 μ g of lysed total retinas were used as control. The proteins were then transferred onto a nitrocellulose membrane (0.22 μ m pore size). Membranes were blocked with 5% bovine serum albumin (BSA) in PBS. Membranes were then incubated with primary antibodies overnight at 4°C, followed by secondary antibodies for one hour at room temperature. IMPDH1 (Proteintech) and PRKAA2 (R&D Systems) were used for primary antibody incubation. Bands were visualized using the dual-channel Odyssey CLx Imaging System and quantified protein bands of interest using Image Studio.

1.5 Acknowledgments

This work was supported by National Institutes of Health (NIH) grants R01 EY019287 (RSA) and P30 EY02687 (Vision Core Grant); The Retina Society (RSA); Jeffrey T. Fort Innovation Fund (RSA); Starr Foundation AMD Research Fund (RSA); Siteman Retina Research Fund (RSA); Carl Marshall and Mildred Almen Reeves Foundation (PAR and RSA); Retina Associates of St. Louis Research Fund (RSA); BrightFocus Foundation (PAR and RSA); a pilot project grant from the Washington University Genome Technology Access Center (PAR and RSA); Research to Prevent Blindness Career Development Award (PAR); an unrestricted grant from Research to Prevent Blindness to the John F. Hardesty, MD Department of Ophthalmology and Visual Sciences at Washington University School of Medicine in St. Louis. TL was supported by NIH Training Grant (1T32GM1397740-1) and Vitreoretinal Surgery Foundation Fellowship (VGR0023118). JBL was supported by the NIH grant F30 DK130282 and the Washington University in St. Louis Medical Scientist Training Program (NIH grant T32 GM07200). YS was supported by NIH grant RF1 AG013730 (to J.M.).

The authors acknowledge Wandy L. Beatty, Molecular Microbiology Imaging Facility in Washington University School of Medicine, for electron microscopy analyses and the Thermo Fisher Scientific Center for Multiplexed Proteomics at Harvard Medical School (<https://tcmp.hms.harvard.edu>) for the phosphoproteomics service and analyses. We also thank Washington University Diabetes Research Center Cores (NIH Grant # 5 P30 DK020579) for the use of XFe24 Extracellular Flux Analyzer. We also thank Alapakkam Sampath, University of California Los Angeles David Geffen School of Medicine, for his advice and expertise on rod photoreceptor physiology.

1.6 References

1. Steinberg GR, Hardie DG. New insights into activation and function of the AMPK. *Nat Rev Mol Cell Biol.* 2023;24(4):255-272. doi:10.1038/s41580-022-00547-x
2. Samuel MA, Voinescu PE, Lilley BN, et al. LKB1 and AMPK regulate synaptic remodeling in old age. *Nat Neurosci.* 2014;17(9):1190-1197. doi:10.1038/nn.3772
3. Xu L, Kong L, Wang J, Ash JD. Stimulation of AMPK prevents degeneration of photoreceptors and the retinal pigment epithelium. *Proc Natl Acad Sci U S A.* 2018;115(41):10475-10480. doi:10.1073/pnas.1802724115
4. Kamoshita M, Ozawa Y, Kubota S, et al. AMPK-NF- κ B Axis in the Photoreceptor Disorder during Retinal Inflammation. Neuhaus SCF, ed. *PLoS ONE.* 2014;9(7):e103013. doi:10.1371/journal.pone.0103013
5. Hoffman NJ, Parker BL, Chaudhuri R, et al. Global Phosphoproteomic Analysis of Human Skeletal Muscle Reveals a Network of Exercise-Regulated Kinases and AMPK Substrates. *Cell Metabolism.* 2015;22(5):922-935. doi:10.1016/j.cmet.2015.09.001
6. Fingar DC, Blenis J. Target of rapamycin (TOR): an integrator of nutrient and growth factor signals and coordinator of cell growth and cell cycle progression. *Oncogene.* 2004;23(18):3151-3171. doi:10.1038/sj.onc.1207542
7. Doménech E, Maestre C, Esteban-Martínez L, et al. AMPK and PFKFB3 mediate glycolysis and survival in response to mitophagy during mitotic arrest. *Nat Cell Biol.* 2015;17(10):1304-1316. doi:10.1038/ncb3231

8. Li Y, Xu S, Mihaylova MM, et al. AMPK phosphorylates and inhibits SREBP activity to attenuate hepatic steatosis and atherosclerosis in diet-induced insulin-resistant mice. *Cell Metab.* 2011;13(4):376-388. doi:10.1016/j.cmet.2011.03.009
9. Inoki K, Zhu T, Guan KL. TSC2 mediates cellular energy response to control cell growth and survival. *Cell.* 2003;115(5):577-590. doi:10.1016/s0092-8674(03)00929-2
10. Li X, Wang L, Zhou XE, et al. Structural basis of AMPK regulation by adenine nucleotides and glycogen. *Cell Res.* 2015;25(1):50-66. doi:10.1038/cr.2014.150
11. Viollet B, Athes Y, Mounier R, et al. AMPK: Lessons from transgenic and knockout animals. *Front Biosci (Landmark Ed).* 2009;14:19-44.
12. Vara-Ciruelos D, Dandapani M, Gray A, Egbani EO, Evans AM, Hardie DG. Genotoxic Damage Activates the AMPK- α 1 Isoform in the Nucleus via Ca²⁺/CaMKK2 Signaling to Enhance Tumor Cell Survival. *Molecular Cancer Research.* 2018;16(2):345-357. doi:10.1158/1541-7786.MCR-17-0323
13. Hunter RW, Foretz M, Bultot L, et al. Mechanism of Action of Compound-13: An α 1-Selective Small Molecule Activator of AMPK. *Chem Biol.* 2014;21(7):866-879. doi:10.1016/j.chembiol.2014.05.014
14. Zhang CS, Li M, Ma T, et al. Metformin Activates AMPK through the Lysosomal Pathway. *Cell Metabolism.* 2016;24(4):521-522. doi:10.1016/j.cmet.2016.09.003
15. Mayor E. Neurotrophic effects of intermittent fasting, calorie restriction and exercise: a review and annotated bibliography. *Front Aging.* 2023;4:1161814. doi:10.3389/fragi.2023.1161814

16. Kamoshita M, Fujinami K, Toda E, Tsubota K, Ozawa Y. Neuroprotective effect of activated 5'-adenosine monophosphate-activated protein kinase on cone system function during retinal inflammation. *BMC Neuroscience*. 2016;17(1). doi:10.1186/s12868-016-0268-5
17. Wu J, Puppala D, Feng X, Monetti M, Lapworth AL, Geoghegan KF. Chemoproteomic Analysis of Intertissue and Interspecies Isoform Diversity of AMP-activated Protein Kinase (AMPK). *J Biol Chem*. 2013;288(50):35904-35912. doi:10.1074/jbc.M113.508747
18. Santeford A, Lee AY, Sene A, et al. Loss of Mir146b with aging contributes to inflammation and mitochondrial dysfunction in thioglycollate-elicited peritoneal macrophages. *eLife*. 2021;10:e66703. doi:10.7554/eLife.66703
19. Wang J, Geisert EE, Struebing FL. RNA sequencing profiling of the retina in C57BL/6J and DBA/2J mice: Enhancing the retinal microarray data sets from GeneNetwork. *Mol Vis*. 2019;25:345-358.
20. Jeon CJ, Strettoi E, Masland RH. The Major Cell Populations of the Mouse Retina. *J Neurosci*. 1998;18(21):8936-8946. doi:10.1523/JNEUROSCI.18-21-08936.1998
21. Okawa H, Sampath AP, Laughlin SB, Fain GL. ATP Consumption by Mammalian Rod Photoreceptors in Darkness and in Light. *Current Biology*. 2008;18(24):1917-1921. doi:10.1016/j.cub.2008.10.029
22. Chinchore Y, Begaj T, Wu D, Drokhlyansky E, Cepko CL. Glycolytic reliance promotes anabolism in photoreceptors. *eLife*. 2017;6:e25946. doi:10.7554/eLife.25946

23. Xue Y, Sun X, Wang SK, Collin GB, Kefalov VJ, Cepko CL. Chromophore supply modulates cone function and survival in retinitis pigmentosa mouse models. *Proc Natl Acad Sci U S A*. 2023;120(23):e2217885120. doi:10.1073/pnas.2217885120
24. Leinonen H, Pham NC, Boyd T, Santoso J, Palczewski K, Vinberg F. Homeostatic plasticity in the retina is associated with maintenance of night vision during retinal degenerative disease. *eLife*. 2020;9:e59422. doi:10.7554/eLife.59422
25. Sasaki Y, Kakita H, Kubota S, et al. SARM1 depletion rescues NMNAT1-dependent photoreceptor cell death and retinal degeneration. *eLife*. 2020;9:1-19.
26. Ban N, Lee TJ, Sene A, et al. Disrupted cholesterol metabolism promotes age-related photoreceptor neurodegeneration. *J Lipid Res*. 2018;59(8):1414-1423. doi:10.1194/jlr.M084442
27. Warburg O. The metabolism of carcinoma cells. *The Journal of Cancer Research*. 1925;9(1):148-163.
28. Laitko U, Hofmann KP. A model for the recovery kinetics of rod phototransduction, based on the enzymatic deactivation of rhodopsin. *Biophys J*. 1998;74(2 Pt 1):803-815.
29. Pareek V, Pedley AM, Benkovic SJ. Human de novo Purine Biosynthesis. *Crit Rev Biochem Mol Biol*. 2021;56(1):1-16. doi:10.1080/10409238.2020.1832438
30. Belicova L, Repnik U, Delpierre J, et al. Anisotropic expansion of hepatocyte lumina enforced by apical bulkheads. *J Cell Biol*. 2021;220(10):e202103003. doi:10.1083/jcb.202103003

31. Heng JS, Rattner A, Stein-O'Brien GL, et al. Hypoxia tolerance in the Norrin-deficient retina and the chronically hypoxic brain studied at single-cell resolution. *Proc Natl Acad Sci U S A*. 2019;116(18):9103-9114. doi:10.1073/pnas.1821122116
32. Orozco LD, Chen HH, Cox C, et al. Integration of eQTL and a Single-Cell Atlas in the Human Eye Identifies Causal Genes for Age-Related Macular Degeneration. *Cell Reports*. 2020;30(4):1246-1259.e6. doi:10.1016/j.celrep.2019.12.082
33. Zeisel A, Hochgerner H, Lönnerberg P, et al. Molecular Architecture of the Mouse Nervous System. *Cell*. 2018;174(4):999-1014.e22. doi:10.1016/j.cell.2018.06.021
34. Nakada D, Saunders TL, Morrison SJ. *Lkb1* regulates cell cycle and energy metabolism in haematopoietic stem cells. *Nature*. 2010;468(7324):653-658. doi:10.1038/nature09571
35. Ban N, Lee TJ, Sene A, et al. Impaired monocyte cholesterol clearance initiates age-related retinal degeneration and vision loss. *JCI Insight*. 2018;3(17). doi:10.1172/jci.insight.120824
36. Millman JR, Doggett T, Oberlin C, Zhang S, Semenkovich CF, Rajagopal R. Measurement of energy metabolism in explanted retinal tissue using extracellular flux analysis. *J Vis Exp*. 2019;(143):10.3791/58626. doi:10.3791/58626
37. Kanow MA, Giarmarco MM, Jankowski CS, et al. Biochemical adaptations of the retina and retinal pigment epithelium support a metabolic ecosystem in the vertebrate eye. *eLife*. 2017;6:e28899. doi:10.7554/eLife.28899

38. Plana-Bonamaisó A, López-Begines S, Fernández-Justel D, et al. Post-translational regulation of retinal IMPDH1 in vivo to adjust GTP synthesis to illumination conditions. *eLife*. 2020;9:e56418. doi:10.7554/eLife.56418
39. Keppeke GD, Chang CC, Peng M, et al. IMP/GTP balance modulates cytoophidium assembly and IMPDH activity. *Cell Div*. 2018;13:5. doi:10.1186/s13008-018-0038-0
40. He J, Yamamoto M, Sumiyama K, et al. Two-photon AMPK and ATP imaging reveals the bias between rods and cones in glycolysis utility. *The FASEB Journal*. 2021;35(9):e21880. doi:10.1096/fj.202101121R
41. Dasgupta B, Seibel W. Compound C/Dorsomorphin: Its Use and Misuse as an AMPK Inhibitor. In: Neumann D, Viollet B, eds. *AMPK: Methods and Protocols*. *Methods in Molecular Biology*. Springer; 2018:195-202. doi:10.1007/978-1-4939-7598-3_12
42. Lyubarsky AL, Pugh EN. Recovery phase of the murine rod photoresponse reconstructed from electroretinographic recordings. *J Neurosci*. 1996;16(2):563-571. doi:10.1523/JNEUROSCI.16-02-00563.1996
43. Hardie DG. AMP-activated protein kinase—an energy sensor that regulates all aspects of cell function. *Genes Dev*. 2011;25(18):1895-1908. doi:10.1101/gad.17420111
44. Leskov IB, Klenchin VA, Handy JW, et al. The Gain of Rod Phototransduction: Reconciliation of Biochemical and Electrophysiological Measurements. *Neuron*. 2000;27(3):525-537. doi:10.1016/S0896-6273(00)00063-5
45. Kennan A, Aherne A, Palfi A, et al. Identification of an IMPDH1 mutation in autosomal dominant retinitis pigmentosa (RP10) revealed following comparative microarray analysis of

transcripts derived from retinas of wild-type and Rho^{-/-} mice. *Human Molecular Genetics*. 2002;11(5):547-558. doi:10.1093/hmg/11.5.547

46. Bowne SJ, Sullivan LS, Blanton SH, et al. Mutations in the inosine monophosphate dehydrogenase 1 gene (IMPDH1) cause the RP10 form of autosomal dominant retinitis pigmentosa. *Hum Mol Genet*. 2002;11(5):559-568.

47. Grover S, Fishman GA, Stone EM. A novel IMPDH1 mutation (Arg231Pro) in a family with a severe form of autosomal dominant retinitis pigmentosa. *Ophthalmology*. 2004;111(10):1910-1916. doi:10.1016/j.ophtha.2004.03.039

48. Wada Y, Tada A, Itabashi T, Kawamura M, Sato H, Tamai M. Screening for Mutations in the IMPDH1 Gene in Japanese Patients With Autosomal Dominant Retinitis Pigmentosa. *American Journal of Ophthalmology*. 2005;140(1):163-165. doi:10.1016/j.ajo.2005.01.017

49. Sullivan LS, Bowne SJ, Reeves MJ, et al. Prevalence of Mutations in eyeGENE Probands With a Diagnosis of Autosomal Dominant Retinitis Pigmentosa. *Invest Ophthalmol Vis Sci*. 2013;54(9):6255-6261. doi:10.1167/iovs.13-12605

50. Aherne A, Kennan A, Kenna PF, et al. On the molecular pathology of neurodegeneration in IMPDH1-based retinitis pigmentosa. *Human Molecular Genetics*. 2004;13(6):641-650. doi:10.1093/hmg/ddh061

51. Li S, Chen D, Sauvé Y, McCandless J, Chen YJ, Chen CK. Rhodopsin-iCre transgenic mouse line for Cre-mediated rod-specific gene targeting. *genesis*. 2005;41(2):73-80. doi:10.1002/gene.20097

52. Trapnell C, Cacchiarelli D, Grimsby J, et al. Pseudo-temporal ordering of individual cells reveals dynamics and regulators of cell fate decisions. *Nat Biotechnol.* 2014;32(4):381-386. doi:10.1038/nbt.2859
53. Navarrete-Perea J, Yu Q, Gygi SP, Paulo JA. Streamlined Tandem Mass Tag (SL-TMT) Protocol: An Efficient Strategy for Quantitative (Phospho)proteome Profiling Using Tandem Mass Tag-Synchronous Precursor Selection-MS3. *J Proteome Res.* 2018;17(6):2226-2236. doi:10.1021/acs.jproteome.8b00217
54. Huttlin EL, Jedrychowski MP, Elias JE, et al. A Tissue-Specific Atlas of Mouse Protein Phosphorylation and Expression. *Cell.* 2010;143(7):1174-1189. doi:10.1016/j.cell.2010.12.001

1.7 Figures

Figure 1

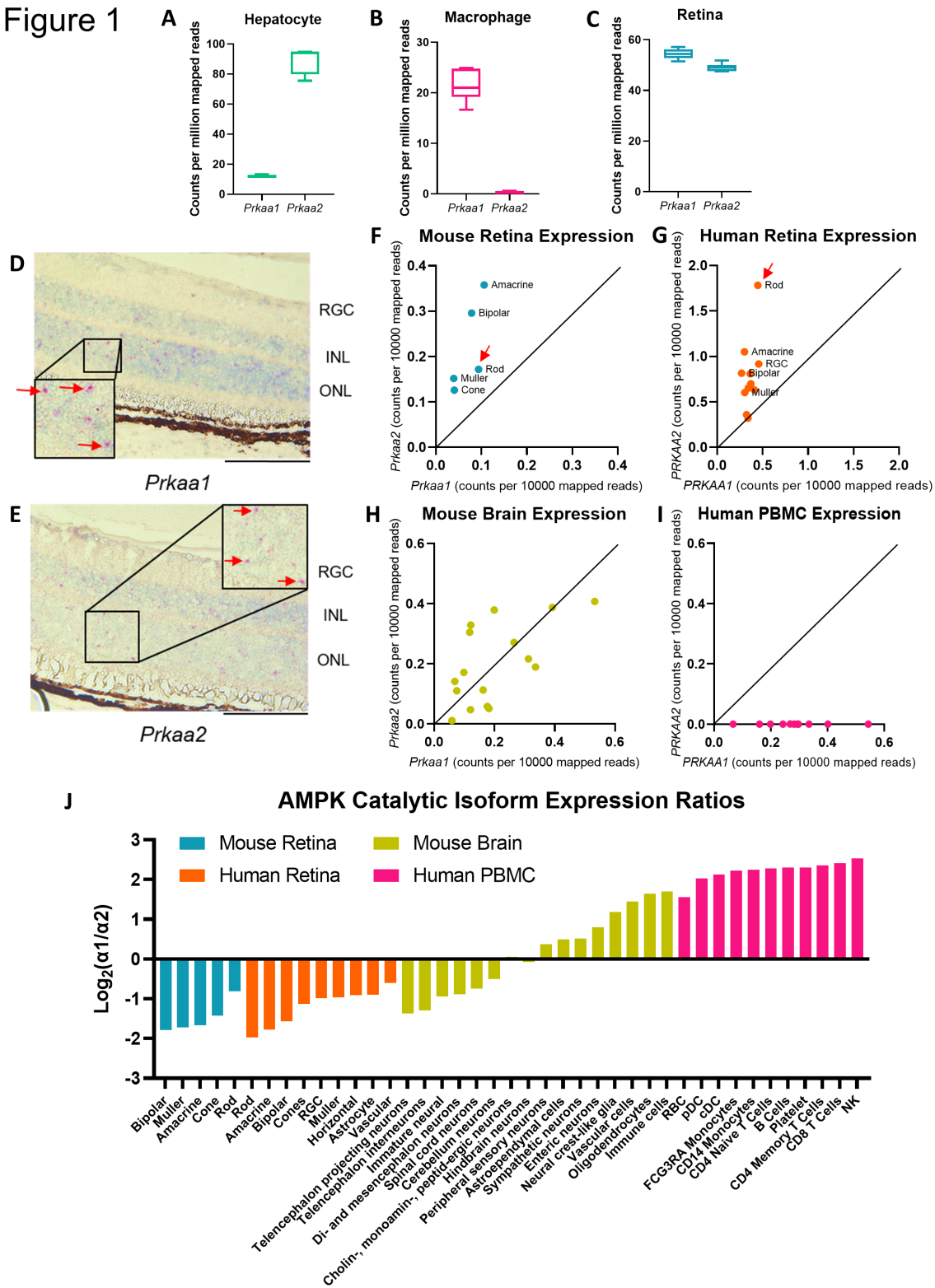


Figure 1. Both catalytic isoforms of AMPK are appreciably expressed in the retina with consistent expression profiles across human and mouse retinas

(A-C) Gene expression of Prkaa1 and Prkaa2 represented in counts per million mapped reads across different mouse tissues. (A) Hepatocytes (n=4) of mice favor Prkaa2 over Prkaa1 expression while (B) macrophages (n=8) of mice favor Prkaa1 over Prkaa2 expression. (C) Retinas of mice demonstrate appreciable expression levels of both Prkaa1 and Prkaa2 (n=6). (D-E) In-situ hybridization of wild-type retina sections confirmed expression of both (D) Prkaa1 and (E) Prkaa2 as seen in the magenta dots within the outer nuclear layer (red arrows) suggesting expression of both isoforms in rod photoreceptors. (F) Scatter plot of Prkaa1 and Prkaa2 expression profiles of mouse retina cell types from single cell RNA sequencing data. The cell types overall show appreciable Prkaa1 and Prkaa2 expression. The rod photoreceptor cluster (red arrow) shows roughly a two-fold expression of Prkaa2 over Prkaa1. (G) Scatter plot of PRKAA1 and PRKAA2 expression profiles of human retina cell types. The cell types overall show appreciable PRKAA1 and PRKAA2 expression. The rod photoreceptor cluster (red arrow) shows roughly a three-fold expression of Prkaa2 over Prkaa1. (H) Scatter plot of Prkaa1 and Prkaa2 expression profiles of mouse brain cell types. Most cell types in the mouse brain demonstrate appreciable expression of both Prkaa1 and Prkaa2. (I) Scatter plot of PRKAA1 and PRKAA2 expression profiles of human peripheral blood mononuclear cell types. These cell types do not appreciably express PRKAA2 unlike the central nervous system tissues. (J) Waterfall graph depicting the expression ratios of both catalytic isoforms across mouse retina, human retina, mouse brain, and human PBMC. The majority of neuronal cell types express the $\alpha 2$ isoform over $\alpha 1$ whereas immune cells overwhelmingly express the $\alpha 1$ isoform over $\alpha 2$. Scale bar represents 100 μm .

Figure 2. PRKAA2, but not PRKAA1, dysfunction leads to rod photoreceptor structural abnormalities and visual dysfunction

(A-B) Schematic representations of the protein sequences in the Prkaa1-Rhod/-Rhod and Prkaa2-Rhod/-Rhod models, respectively. Knockout domains are within the kinase domain to abrogate function but preserve overall expression of the proteins. (A) Schematic representation of the PRKAA1 and (B) PRKAA2 protein sequence. (C) Representative transmission electron microscopy images of magnification 2500x of rod photoreceptors. (Left) Rod photoreceptors of control mice (Prkaa2F/F) demonstrate similar features to those of Prkaa1-Rhod/-Rhod with consistent membrane structure and organization. (Middle) Rod photoreceptors of Prkaa1-Rhod/-Rhod demonstrate intact connections between the outer and inner segments with consistent laminar organization of the outer segment membranes. (Right) Rod photoreceptors of Prkaa2-Rhod/-Rhod consistently demonstrate detachments between the outer and inner segments and occasional outer segment membrane dysmorphisms (red arrow). (D) Representative transmission electron microscopy images of magnification 6000x of the outer segments of rod photoreceptors. (Left) Outer segments from control mice (Prkaa2F/F) show consistent striations and laminar organization resembling Prkaa1-Rhod/-Rhod. (Middle) Prkaa1-Rhod/-Rhod outer segments demonstrated organized and laminar structure indicative of normal wild-type structure. (Right) Prkaa2-Rhod/-Rhod outer segments exhibited disorganized membrane layers and occasional manifestation of granular debris (red arrows). (E-F) Scotopic electroretinography of Prkaa1-Rhod/-Rhod and respective wild-type littermates. (E) Representative traces of 0 dB intensity flashes demonstrate similar waveforms between Prkaa1F/F and Prkaa1-Rhod/-Rhod (n=7). (F) Analyses of scotopic a (left) and scotopic b (right) amplitude measurements reveal no significant changes in Prkaa1-Rhod/-Rhod. (G-H) Scotopic electroretinography of Prkaa2-Rhod/-Rhod and respective wild-type littermates (n=7). (G) Representative traces of 0 dB intensity flashes show a diminutive waveform from Prkaa2-Rhod/-Rhod. (H) Analyses of scotopic a (left) and scotopic b (right) amplitude measurements confirm significant attenuation in Prkaa2-Rhod/-Rhod measurements (****p < 0.0001 by two-way ANOVA with post hoc Bonferroni's multiple comparisons test). Values are mean ± SE. Scale bars represent 2 μm. Representative images selected from 40 images for each group.

Figure 3

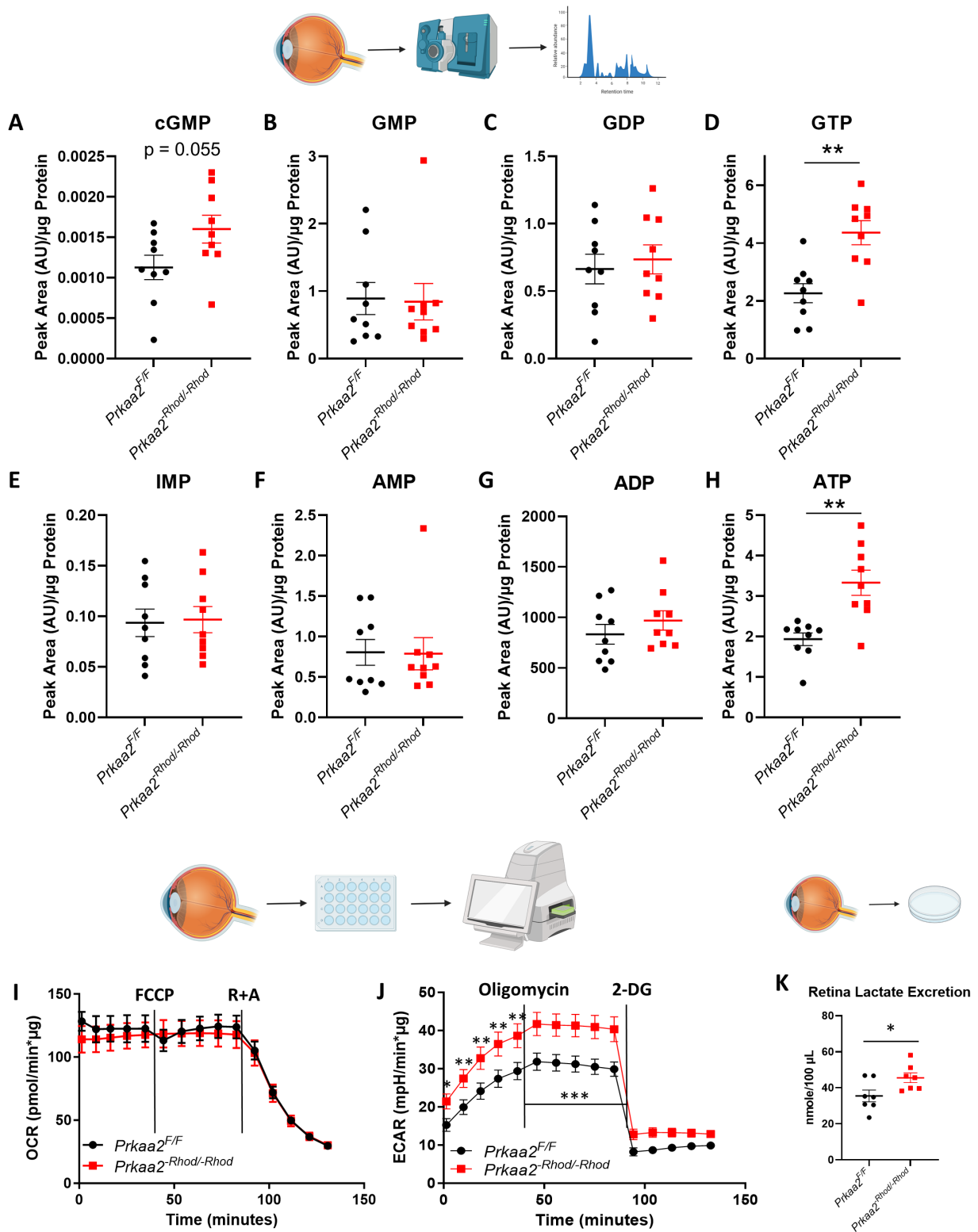


Figure 3. Prkaa2-Rhod/-Rhod retinas demonstrate phospho-purine overproduction and increased glycolysis

(A-H) Metabolomics analyses of different phospho-purines in Prkaa2-Rhod/-Rhod retinas using LC-MS/MS (n = 9). (A) Prkaa2-Rhod/-Rhod retinas demonstrated near significant increase in cGMP levels, a critical regulator of the dark current ($p = 0.056$ by Welch's t-test). (B-C) GMP and GDP levels were not significantly changed in Prkaa2-Rhod/-Rhod. (D) GTP levels were significantly increased in Prkaa2-Rhod/-Rhod (** $p < 0.01$ by Welch's t-test). (E) Levels of IMP, a precursor to GMP, were not significantly changed in Prkaa2-Rhod/-Rhod. (F-G) AMP and ADP levels were not significantly changed in Prkaa2-Rhod/-Rhod. (H) ATP levels were significantly increased in Prkaa2-Rhod/-Rhod (** $p < 0.01$ by Welch's t-test). (I-J) Extracellular flux analyses by retina Seahorse of Prkaa2-Rhod/-Rhod. (I) Oxygen consumption rate as a measure of oxidative phosphorylative flux was not significantly changed in Prkaa2Rhod/-Rhod (n=7). (J) Extracellular acidification rate as a measure of glycolytic flux was significantly increased (**** $p < 0.0001$ by two-way ANOVA). Glycolysis (* $p < 0.05$, ** $p < 0.01$ by post-hoc Bonferroni's multiple comparisons test) and glycolytic capacity (*** $p < 0.001$ by post-hoc Bonferroni's multiple comparisons test) were significantly upregulated in Prkaa2-Rhod/-Rhod (n=8). (K) Excreted retina lactate levels were significantly increased in Prkaa2-Rhod/-Rhod, supporting the increased glycolysis phenotype (n = 7, * $p < 0.05$). Values are mean \pm SE.

Figure 4

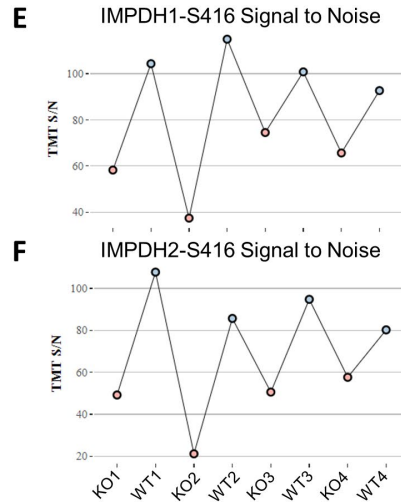
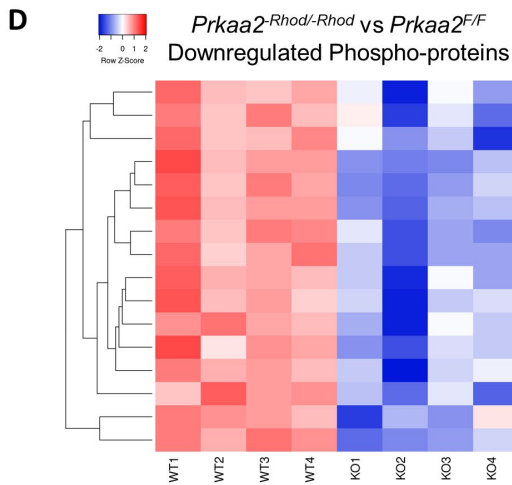
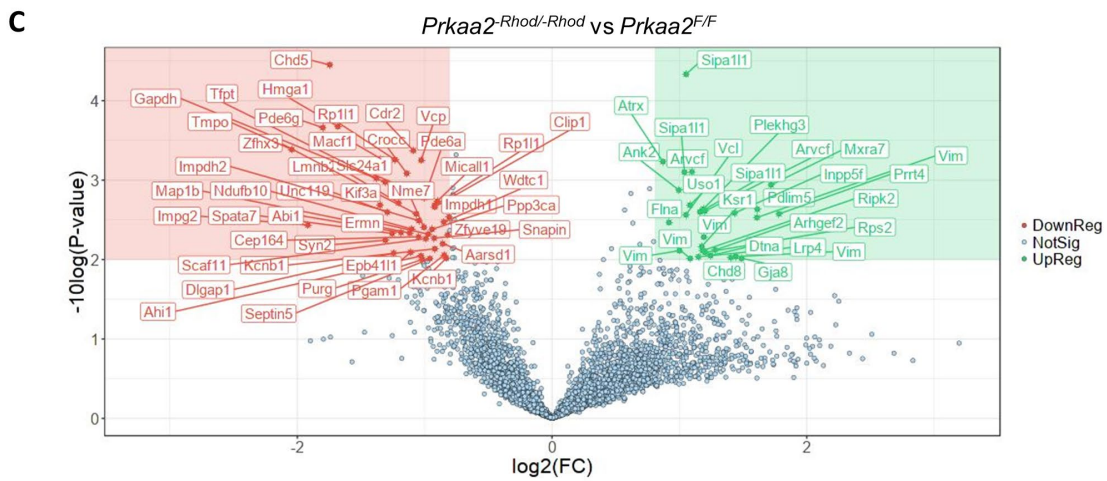
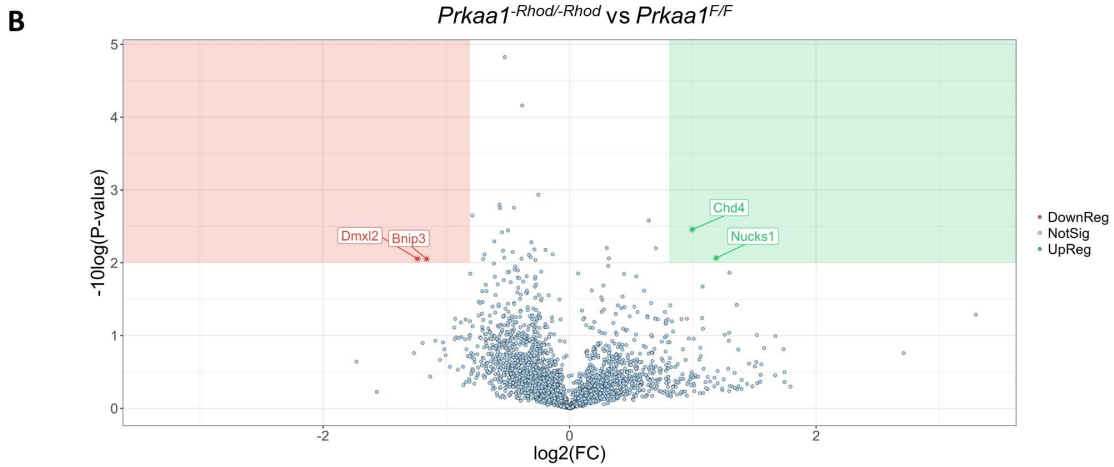
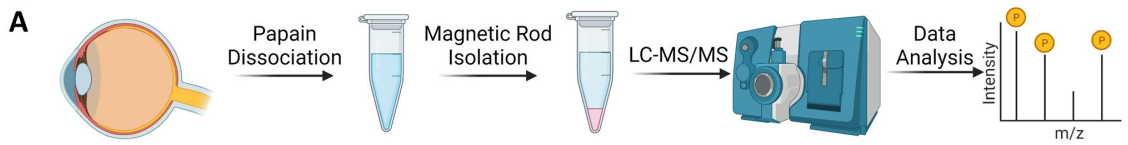


Figure 4. PRKAA2 dysfunction leads to wide changes to the phosphoproteome and decreased S416 phosphorylation of IMPDH

(A) Schematic representation of the workflow to isolate rod photoreceptors to use for phosphoproteomics analysis. Six retinas were dissected per sample and first dissociated using papain digestion. CD73-PE and Rhodopsin-biotin antibodies were used to tag rod photoreceptor inner and outer segments and were isolated using immunomagnetic beads. The cells were then lysed and processed by LC-MS/MS using an unbiased phosphoproteomics pipeline and analyzed. (B-C) Rod photoreceptors from Prkaa1-Rhod/-Rhod and Prkaa2-Rhod/-Rhod were processed for phosphoproteomic analyses (n=4). 1.75 fold change and 0.01 p-value cutoffs with <1% false discovery rate were used to determine significant changes. (B) Prkaa1-Rhod/-Rhod analysis revealed 2 downregulated targets which were unrelated to rod photoreceptor function. (C) Prkaa2-Rhod/-Rhod analysis revealed 45 downregulated targets including species related to the phototransduction cascade and photoreceptor function. (D) A selection of downregulated phospho-proteins from the Prkaa2-Rhod/-Rhod phosphoproteomics dataset were plotted on a heatmap to visualize the spread of individual samples. Samples with higher z-scores are visualized as a deeper red color while samples with lower z-scores are visualized as a deeper blue color. Each row represents a phospho-site of the denoted protein, while each column represents either a sample from Prkaa2F/F (WT) or Prkaa2-Rhod/-Rhod (KO). (E-F) Tandem mass tag signal to noise ratios of IMPDH1-S416 and IMPDH2-S416 from individual Prkaa2F/F (WT) and Prkaa2-Rhod/-Rhod (KO) samples. KO samples are colored as pink dots while WT samples are colored as blue dots. In both IMPDH1-S416 and IMPDH2-S416 measurements, the KO samples overall present lower signal to noise ratios than WT samples.

Figure 5

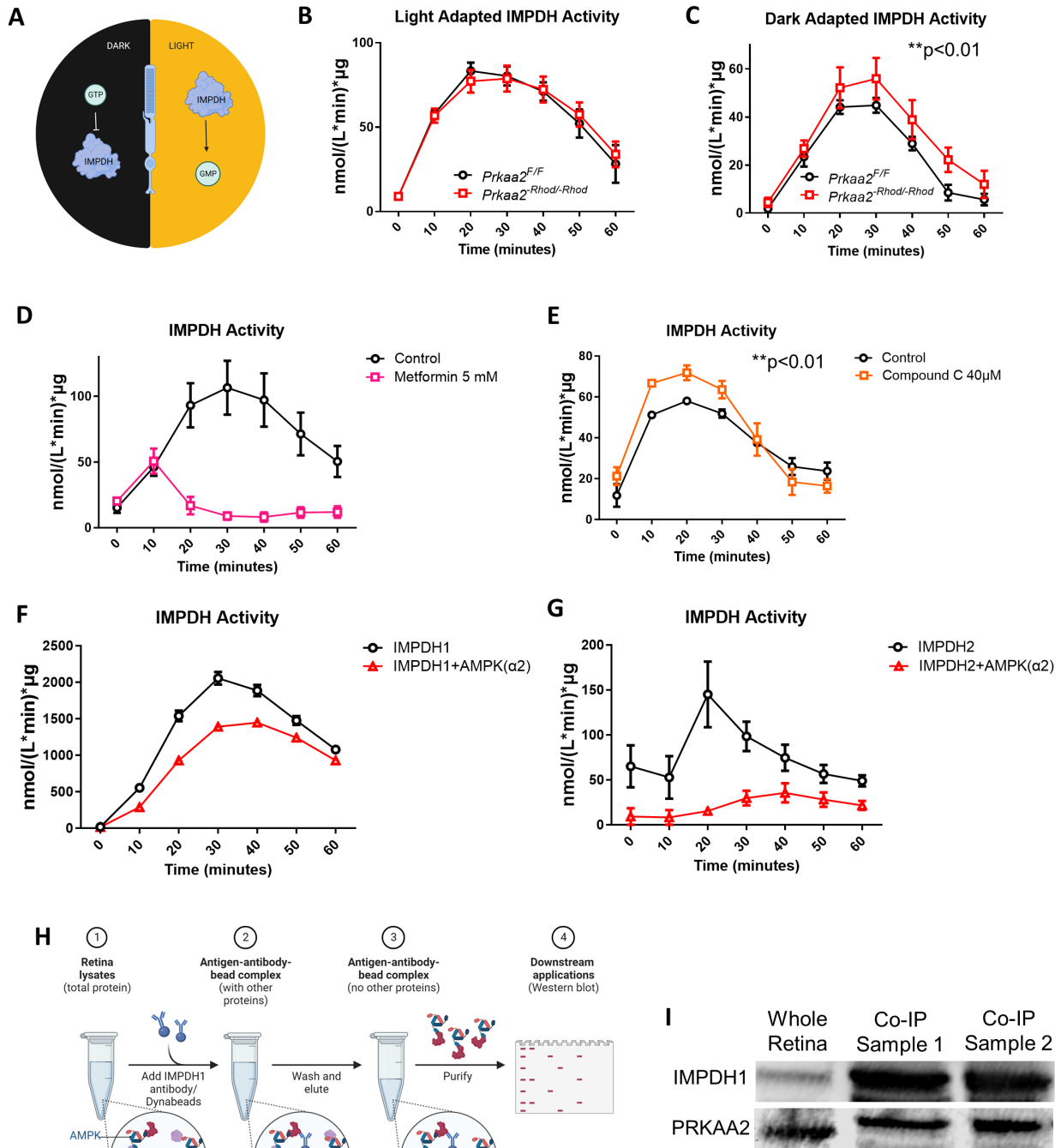


Figure 5. Dysfunctional PRKAA2 cannot regulate IMPDH leading to IMPDH hyperactivity

(A) Schematic representation of IMPDH function in rod photoreceptors according to light exposure. Previous work has shown GTP allosterically inhibits IMPDH in dark adapted conditions while IMPDH is active to produce GMP in light adapted conditions. (B) Ambient light adapted retinas from *Prkaa2-Rhod^{-/-}Rhod* were assessed for IMPDH activity (n=4). No significant changes were detected. (C) Dark adapted retinas from *Prkaa2-Rhod^{-/-}Rhod* showed significantly increased IMPDH activity (n=6; **p<0.01 by Two-way ANOVA). (D) Ambient light adapted wild-type retinas were assessed for IMPDH activity after treatment with 5 mM metformin, an AMPK activator. Metformin is a slower activator of AMPK and metformin treatment inhibits IMPDH activity compared to that of control retinas (n=6, ****p<0.0001 by Two-way ANOVA). (E) Dark adapted wild-type retinas were assessed for IMPDH activity after treatment with 40 μ M Compound C, an AMPK inhibitor. Lysates treated with Compound C exhibited significantly higher IMPDH activity compared to controls (n=4, **p<0.01 by Two-way ANOVA). (F-G) Recombinant human AMPK (α 2 β 1 γ 1) was incubated with recombinant human (F) IMPDH1 or (G) IMPDH2 to assess the effect of AMPK on IMPDH activity. Both IMPDH1 and IMPDH2 when incubated with AMPK had significantly attenuated IMPDH activity compared to IMPDH incubated alone (n=4, ****p>0.0001 by Two-way ANOVA). (F) Schematic workflow of the co-immunoprecipitation protocol of IMPDH1. Six dark-adapted retinas from wild-type mice were dissected and lysed in extraction buffer. Dynabeads coated with IMPDH1 antibody were added to the suspension and allowed to bind to IMPDH1. Attached IMPDH1 along with bound proteins were isolated. The resulting eluant was then used for western blots to detect IMPDH1 and bound protein. (G) The results of western blot detection of co-immunoprecipitation samples are depicted. Clear bands representing IMPDH1 along with PRKAA2 demonstrate PRKAA2 was bound to IMPDH1 in wild-type retinas. Values are mean \pm SE. Scale bars represent 40 μ m.

Figure 6

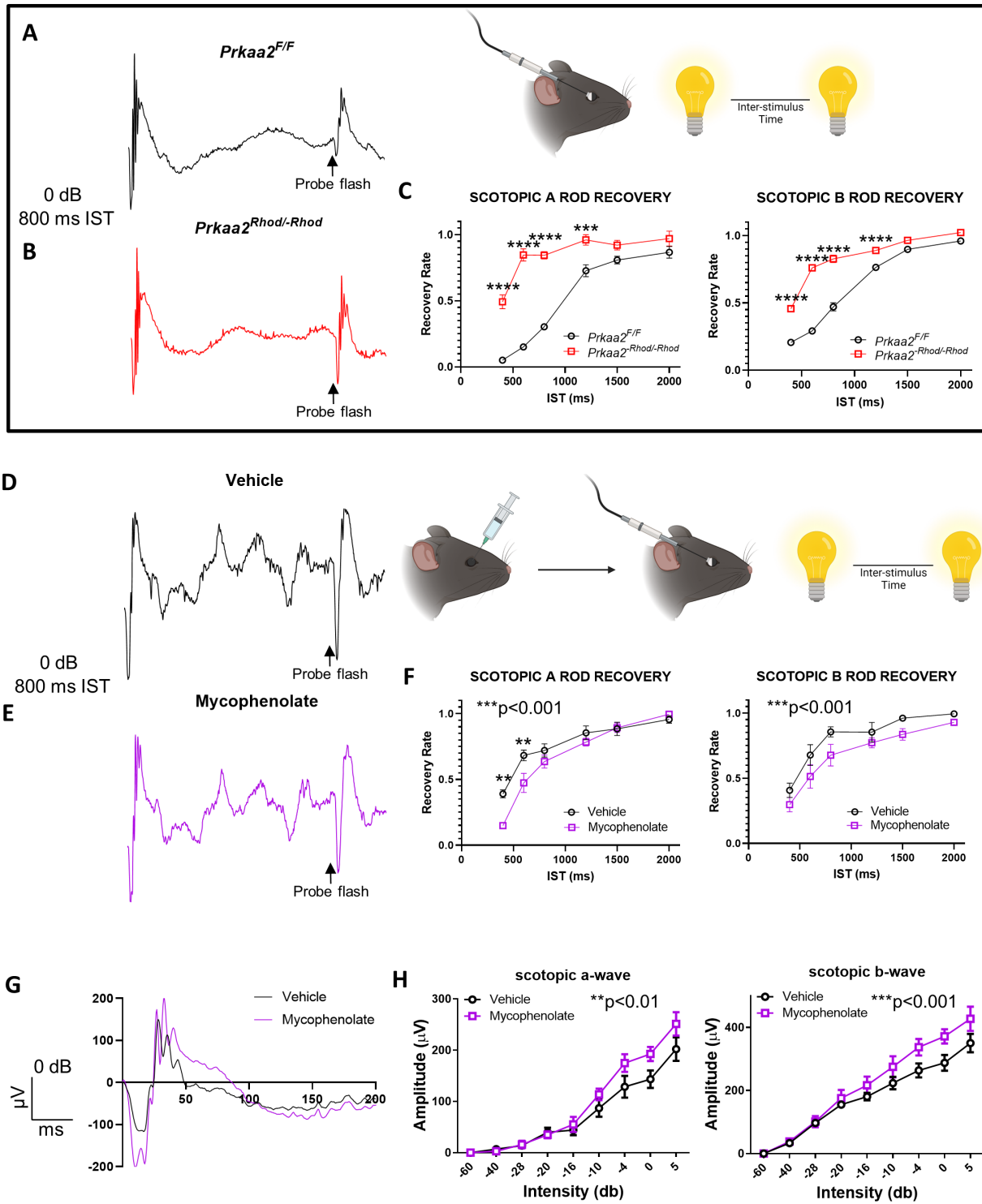
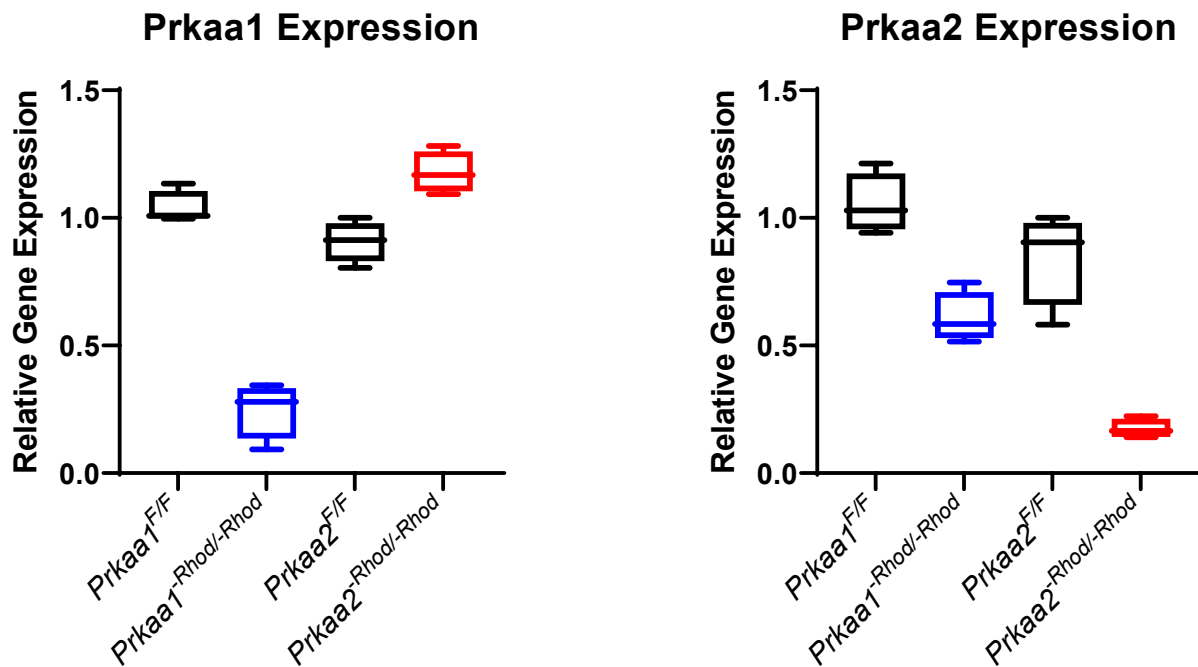
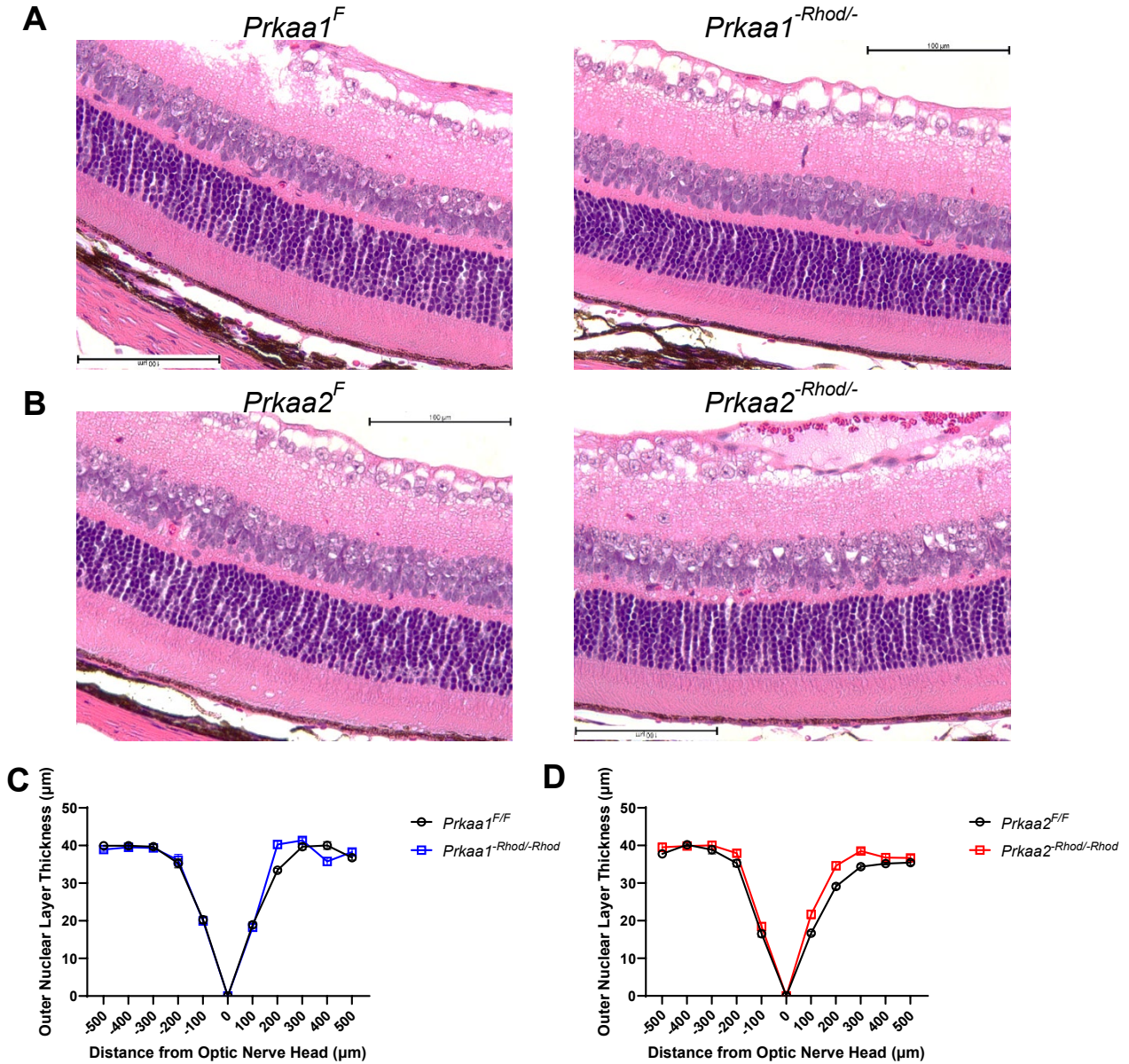


Figure 6. Mycophenolate mofetil treatment improves visual function deficits measured by electroretinography in Prkaa2-Rhod/-Rhod

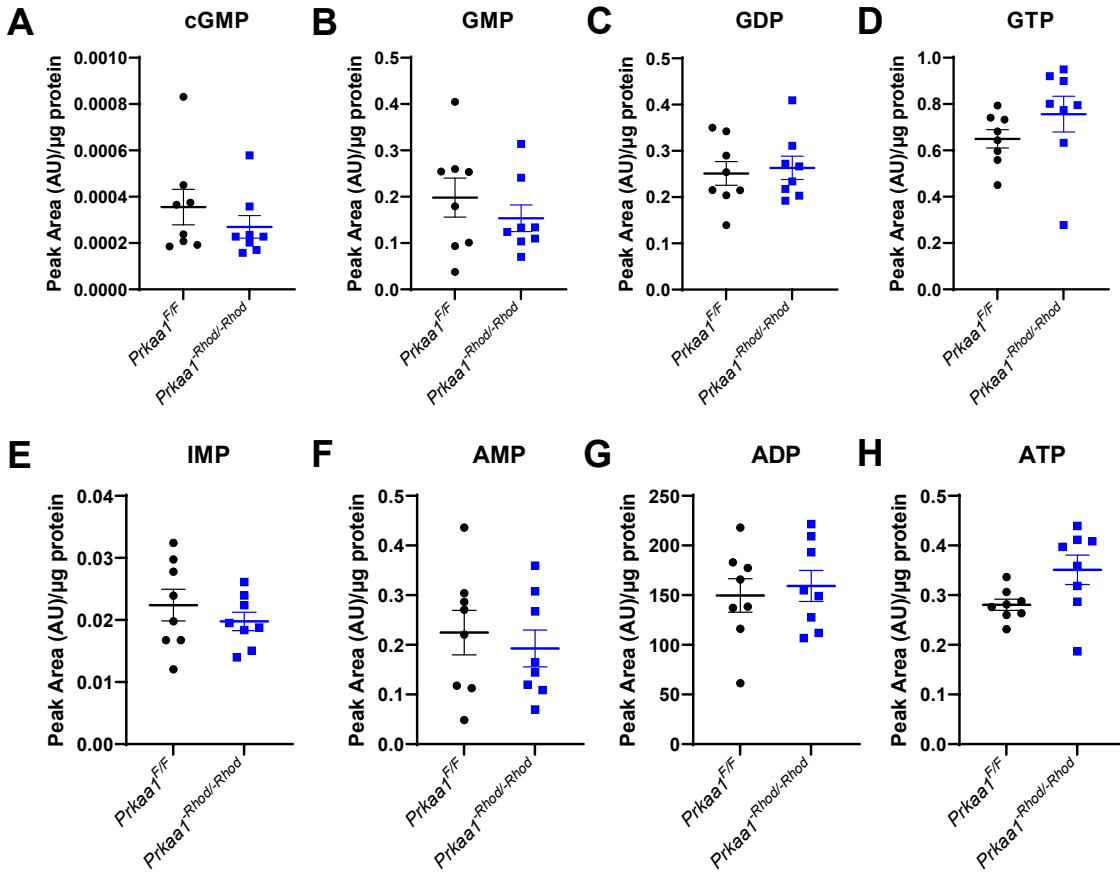
(A-B) Representative electroretinography traces of Prkaa2-Rhod/-Rhod mass rod recovery. A 0 dB flash with 800 millisecond inter-stimulus time is represented. (A) A trace from Prkaa2F/F shows typical attenuated scotopic a and b waves in the test response indicated by the probe flash with 800 ms IST. (B) A trace from Prkaa2-Rhod/-Rhod shows abnormally large scotopic a and b waves with 800 ms IST in the test response indicated by the probe flash. (C) Quantification of scotopic A and scotopic B rod recovery (n=7). Prkaa2-Rhod/-Rhod show significantly faster rod recovery compared to wild-type littermates (**p<0.001, ****p<0.0001 by post-hoc Bonferroni's multiple comparisons test; ****p<0.0001 by Two-way ANOVA). (D-E) Representative electroretinography traces of Prkaa2-Rhod/-Rhod mass rod recovery from eyes treated either with vehicle or mycophenolate mofetil. (D) Vehicle treated eyes demonstrate similar waveform shapes as (E) mycophenolate treated eyes from the probe flash. (F) Quantification of scotopic A and scotopic B rod recovery (n=5). Mycophenolate treated eyes show significantly slower scotopic a and scotopic b rod recovery compared to vehicle treated eyes (**p<0.01 by post-hoc Bonferroni's multiple comparisons test; ***p<0.001 by Two-way ANOVA). (G) Representative traces of full field scotopic electroretinography from vehicle and mycophenolate treated eyes. Although the waveform shape is slightly altered, mycophenolate treatment improves scotopic a and scotopic b wave amplitudes compared to vehicle treatment. (H) Quantification of scotopic a and scotopic b wave amplitudes from full field scotopic electroretinography (n=5). Mycophenolate treated eyes had significantly improved scotopic a and scotopic b wave amplitudes compared to vehicle treated eyes (**p<0.01, ***p<0.001 by Two-way ANOVA). Values are mean \pm SE.



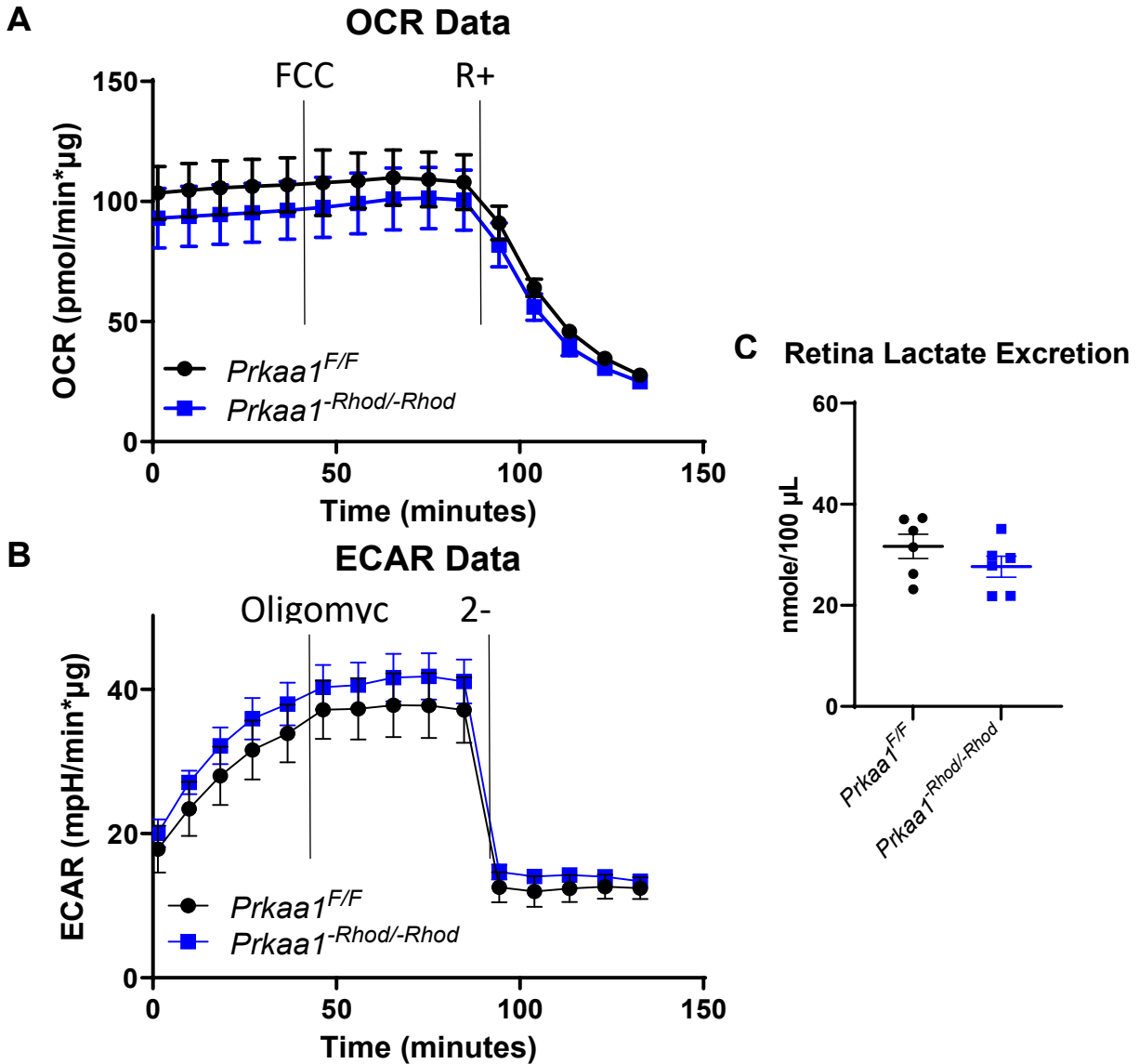
Supplementary Figure 1. *Prkaa1* and *Prkaa2* expression levels of isolated rod photoreceptors from *Prkaa1*^{-Rhod/-Rhod} and *Prkaa2*^{-Rhod/-Rhod}. Knockout model expression levels were normalized to those of their corresponding wild-type cre negative littermates. *Prkaa1* expression was decreased in *Prkaa1*^{-Rhod/-Rhod} compared to wild-type littermates while there were no drastic changes detected in *Prkaa2*^{-Rhod/-Rhod} (n=4). *Prkaa2* expression was decreased in *Prkaa1*^{-Rhod/-Rhod} with roughly 40% decreased expression while it was decreased in *Prkaa2*^{-Rhod/-Rhod} by roughly 80% decreased expression (n=4). Although we see decreased expression of *Prkaa2* in *Prkaa1*^{-Rhod/-Rhod}, we did not observe structural or functional deficits in rod photoreceptors. Values are mean ± SE.



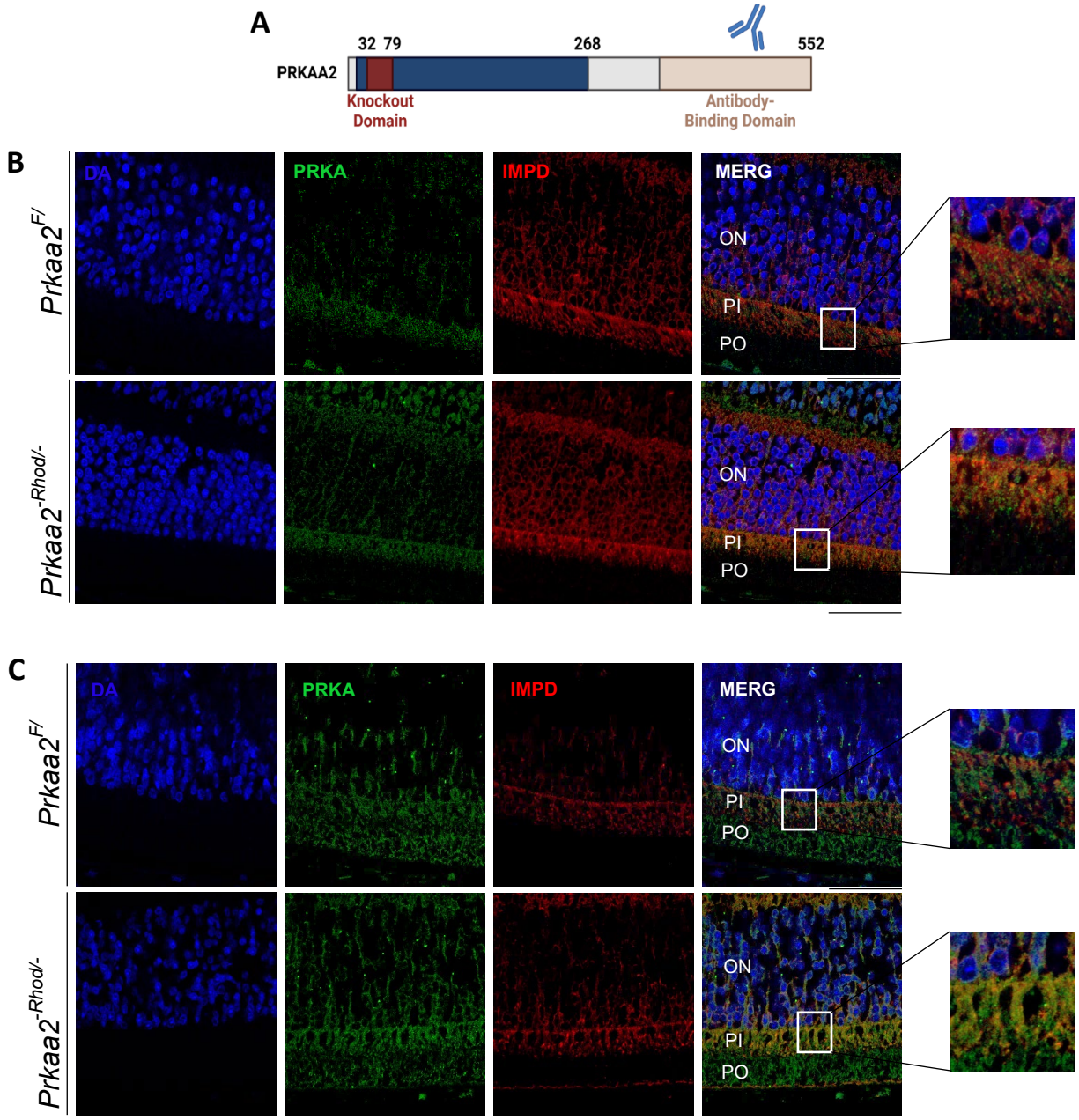
Supplementary Figure 2. Hematoxylin and eosin staining of *Prkaa1^{-Rhod/-Rhod}* and *Prkaa2^{-Rhod/-Rhod}*. No gross anatomical abnormalities were observed in neither (A) *Prkaa1^{-Rhod/-Rhod}* nor (B) *Prkaa2^{-Rhod/-Rhod}* rod photoreceptor layers such as the outer nuclear layer (ONL), photoreceptor inner segment (PIS), and photoreceptor outer segment layers (POS). No overt photoreceptor outer segment thinning was observed in *Prkaa2^{-Rhod/-Rhod}* despite electroretinography changes, suggesting rod photoreceptor dysfunction but not degeneration. (C-D) Butterfly plots quantifying the ONL thickness of both *Prkaa1^{-Rhod/-Rhod}* and *Prkaa2^{-Rhod/-Rhod}* compared to respective wild-type littermates confirm not significant differences in ONL thickness (n=12). Scale bars represent 100 μm . Values are mean \pm SE.



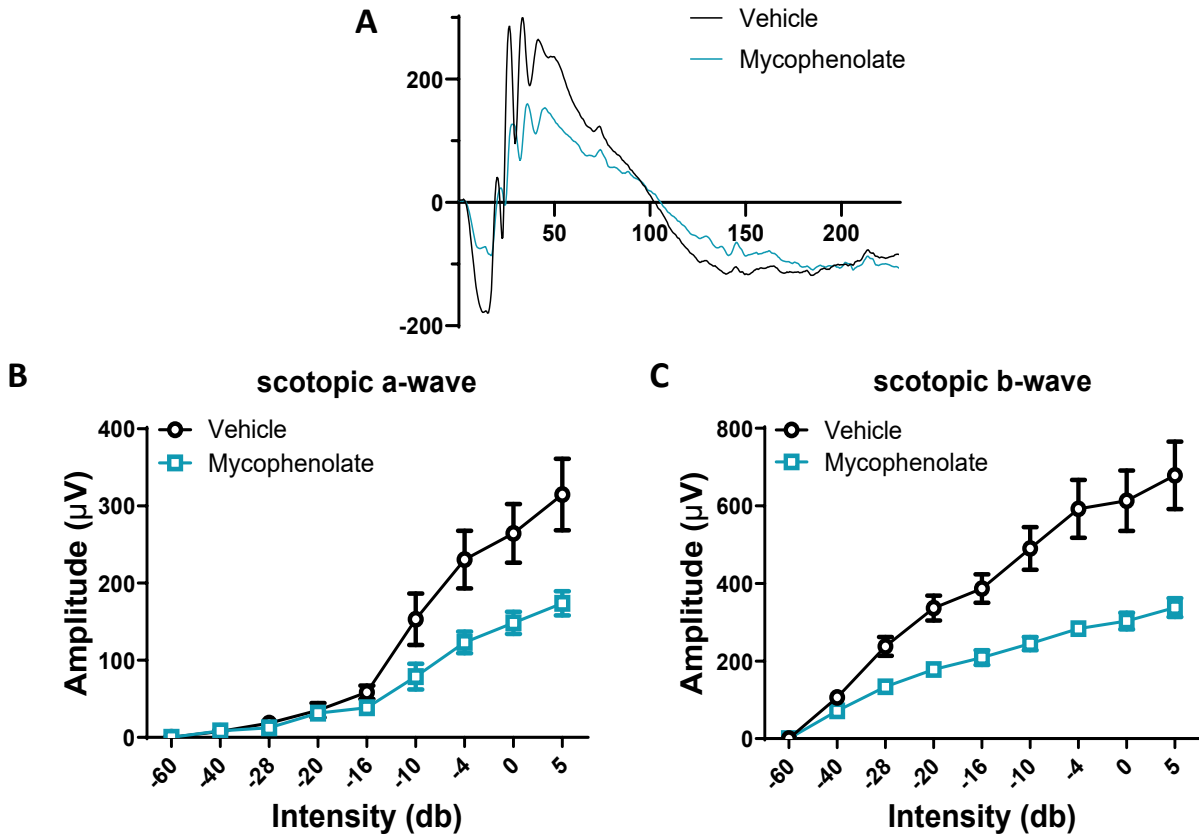
Supplementary Figure 3. Metabolomics of *Prkaa1*^{Rhod/Rhod} retinas. Retinas from *Prkaa1*^{Rhod/Rhod} and wild-type littermates underwent metabolomics measurement of phospho-purine quantities (n=8). No significant changes were observed in each measurement. Welch's t-test was used for each statistical measurement. Values are mean ± SE.



Supplementary Figure 4. Extracellular flux analyses of *Prkaa1^{-Rhod/-Rhod}* retinas. (A-B) Oxidative phosphorylative flux and glycolytic flux were measured through oxygen consumption rate (OCR) (n=8) and extracellular acidification rate (ECAR) (n=7) respectively. No significant differences were detected in neither OCR nor ECAR suggesting *Prkaa1^{-Rhod/-Rhod}* retinas did not exhibit changes in oxidative phosphorylative or glycolytic flux. Two-way ANOVA with post-hoc Bonferroni's multiple comparisons test were used for statistical analyses. **(C)** Lactate excretion measurements are a proxy measurement tool for photoreceptor glycolysis. Lactate measured from the supernatant of cultured retinas from *Prkaa1^{-Rhod/-Rhod}* showed no significant differences compared to that of *Prkaa1^{F/F}* (n=6). Values are mean ± SE.



Supplementary Figure 5. PRKAA2 and IMPDH1/2 are appreciated in the same cellular compartment in *Prkaa2*^{-Rhod/-Rhod} inner segments compared to those of *Prkaa2*^{F/F}. (A) Schematic representation of the protein sequence of PRKAA2. The knockout domain of *Prkaa2*^{Rhod/Rhod} resides within aa 32 – aa 79. Antibodies with an immunogen targeting a separate region than the kinase domain can reliably bind to dysfunctional PRKAA2, such as the one we utilized. (B-C) Immunofluorescent staining of PRKAA2 and IMPDH1/2 of *Prkaa2*^{-Rhod/-Rhod} retina sections suggest PRKAA2 and IMPDH reside in the same cellular compartment. PRKAA2 (green) and IMPDH (red) aggregate in the photoreceptor inner segment layer (PIS), but may have slightly more co-localization (orange) only in *Prkaa2*^{-Rhod/-Rhod} compared to *Prkaa2*^{F/F}. Scale bars represent 40 μ m.



Supplementary Figure 6. Mycophenolate injection does not improve visual function in wild-type mice. (A) A representative ERG trace of mycophenolate and vehicle injected eyes show mycophenolate does not improve visual function as seen in *Prkaa2^{Rhod^{-/-}Rhod}*. (B-C) Quantifications of scotopic a and b waves demonstrate mycophenolate negatively affects visual function, which is the opposite effect seen in *Prkaa2^{Rhod^{-/-}Rhod}* (n=5). Values are mean \pm SE.

Chapter 2: NMNAT1 Dysfunction Leads to Rod
Photoreceptor Degeneration that can be Prevented by
SARM1 Knockout

Adapted from:

SARM1 depletion rescues NMNAT1-dependent photoreceptor cell death and retinal degeneration

Sasaki Y, Kakita H, Kubota S, Sene A, Lee TJ, Ban N, Dong Z, Lin JB, Boye SL, DiAntonio A, Boye SE, Apte RS, Milbrandt J. SARM1 depletion rescues NMNAT1-dependent photoreceptor cell death and retinal degeneration. *eLife*. 2020;9:1-19.

2.1 Introduction

Leber congenital amaurosis (LCA) is a retinal degenerative disease characterized by childhood onset and severe loss of vision. LCA is the most common cause of blindness in children and about 70% of LCA cases are associated with mutations in genes related to the visual cycle, cGMP production, ciliogenesis, or transcription. Recently, more than thirty mutations in the nuclear NAD⁺ biosynthetic enzyme NMNAT1 were identified in patients with autosomal recessive LCA type 9 (LCA9) (Falk et al., 2012; Perrault et al., 2012; Koenekoop et al., 2012; Chiang et al., 2012; Coppieters et al., 2015; Khan et al., 2018). Despite the ubiquitous expression of this key NAD⁺ biosynthesis enzyme, LCA9 patients have no other systemic deficits outside the retina. In many cases, LCA9 associated mutant NMNAT1 proteins retain enzymatic activity and other biochemical functions, but appear to be less stable under conditions associated with cell stress (Sasaki et al., 2015). While it is clear that NAD⁺ deficiency in the retina is an early feature of retinal degenerative disorders in mice (Zabka et al., 2015; Lin et al., 2016), it is not known which cell types and biological pathways are primarily affected in LCA9.

NMNAT1 plays important roles in diverse retinal functions. Overexpression of NMNAT1 in mouse retinal ganglion cells (RGCs) robustly protects against ischemic and glaucomatous loss of the axon and soma (Zhu et al., 2013), while conditional ablation in the developing mouse retina causes severe retinal dystrophy and loss of retinal function (Eblimit et al., 2018; Wang et al., 2017). Mice harboring *Nmnat1* mutations (V9M and D243G) exhibit severe retinal degeneration while the most common LCA9 mutation (E257K), which is not fully penetrant (Siemiatkowska et al., 2014), induces a milder retinal degeneration phenotype (Eblimit et al., 2018; Greenwald et al., 2016). In retinal explants, NMNAT1 promotes the survival of mouse retinal progenitor cells

(Kuribayashi et al., 2018). The requirement for NMNAT in retina is evolutionarily conserved, as the *Drosophila* NMNAT isoform, dNMNAT, is required for the survival of photoreceptor cells after exposure to intense light (Zhai et al., 2006; Zhai et al., 2008).

The selective loss of photoreceptor cells in LCA9 suggests the survival and function of these cells are extremely sensitive to deranged NAD⁺ metabolism. Indeed, many of the enzymes involved in photoreceptor function are dependent on NAD⁺ as a cofactor, and for some of these proteins mutations in their corresponding genes lead to blindness. These include variants in the NAD⁺ or NADPH dependent retinal dehydrogenases like RDH12 that cause LCA13 (Schuster et al., 2007) and the GTP synthesis enzyme IMPDH1 that causes retinitis pigmentosa (Kennan et al., 2002; Bowne et al., 2002). SIRT3, the mitochondrial NAD⁺-dependent deacetylase is also important for photoreceptor homeostasis (Lin et al., 2016; Lin et al., 2019). Together, these observations highlight the importance of cytosolic NAD⁺ dependent pathways in retinal function (Lin et al., 2016; Lin and Apte, 2018); however, the molecular roles of nuclear NAD⁺ and NMNAT1 in the retina are largely unknown.

Multiple enzymatic pathways utilizing distinct metabolic precursors participate in NAD⁺ biosynthesis (Verdin, 2015). However, in each case, these pathways converge at an NMNAT-dependent step that generates either NAD⁺ or its deamidated form NaAD from the precursor NMN or NaMN. Among the three mammalian NMNAT isoforms, NMNAT1 is the only enzyme localized to the nucleus (Berger et al., 2005). However, in photoreceptors NMNAT1 is present in photoreceptor outer segments (Zhao et al., 2016), consistent with an additional, extra-nuclear role of NMNAT1 in photoreceptor cells. This is of particular interest because engineered non-nuclear variants of enzymatically-active NMNAT1 can potently inhibit pathological axon degeneration, which is commonly observed in the early stages of many neurodegenerative

disorders (Walker et al., 2017; Sasaki et al., 2009; Babetto et al., 2010). When NMNAT1 is present in the axon, it can compensate for the injury-induced rapid loss of NMNAT2, the endogenous axonal NMNAT (Gilley and Coleman, 2010). NMNAT2 in turn, inhibits SARM1, an inducible NAD⁺ cleavage enzyme (NADase) that is the central executioner of axon degeneration (Gilley and Coleman, 2010; Gerdts et al., 2015; Sasaki et al., 2016; Gilley et al., 2015; Figley and DiAntonio, 2020). Hence, mutations in NMNAT1 may promote retinal degeneration through the direct impact on NAD⁺ biosynthesis and/or through the regulation of the SARM1-dependent degenerative program.

In this study, we determined the cell types and molecular mechanisms that cause retinal degeneration in LCA9. Using NMNAT1 conditional mutant mice, we showed that photoreceptors degenerate rapidly after the loss of NMNAT1 and that depletion of NMNAT1 in rod or cone cells is necessary and sufficient for the retinal degeneration. The AAV-mediated gene replacement of NMNAT1 in photoreceptors partially rescues the visual impairment caused by loss of NMNAT1. Finally, we determined the mechanism by which loss of NMNAT1 leads to photoreceptor degeneration. Loss of NMNAT1 leads to activation of SARM1 in photoreceptors, much as loss of NMNAT2 leads to SARM1 activation in axons (Gilley and Coleman, 2010). Moreover, photoreceptor degeneration is mediated by SARM1 in the absence of NMNAT1, much as axon degeneration and perinatal lethality is mediated by SARM1 in the absence of NMNAT2 (Gilley and Coleman, 2010; Gilley et al., 2015). Hence, photoreceptor neurodegeneration in LCA9 shares a deep mechanistic similarity to the pathological axon degeneration pathway. Since the SARM1 pathway is likely druggable (DiAntonio, 2019; Krauss et al., 2020), these findings provide a framework for developing new therapeutic strategies for treating patients with LCA9 and potentially other retinal disorders.

2.2 Results

NMNAT1 is a nuclear enzyme that synthesizes NAD⁺, an essential metabolite that is central to all aspects of cellular metabolism. NMNAT1 is indispensable for mouse development (Conforti et al., 2011) and recent studies identified causative mutations in NMNAT1 in patients with Leber congenital amaurosis type 9 (LCA9), a disorder associated with severe, early-onset retinal degeneration and vision loss (Falk et al., 2012; Perrault et al., 2012; Koenekoop et al., 2012; Chiang et al., 2012; Coppieters et al., 2015; Khan et al., 2018). Patients with LCA9 have no systemic involvement outside the eye, suggesting that certain cells within the retina are particularly vulnerable to the loss of NMNAT1 function. Since no specific antibodies exist for immunocytochemical analysis of NMNAT1 localization, we determined its expression pattern in the retina using mice expressing an NMNAT1-lacZ fusion protein without the nuclear localization signal. Mice heterozygous for this mutant allele were viable and were used to map NMNAT1 expression by staining retinal sections with X-gal. LacZ staining was detected in the retinal pigment epithelium (RPE), photoreceptor outer segments (OS), inner segments (IS), outer nuclear layer (ONL), outer plexiform layer (OPL), inner nuclear layer (INL), inner plexiform layer (IPL), and ganglion cell layer (GCL) suggesting the ubiquitous expression of NMNAT1 in retina (Figure 1—figure supplement 1A).

LCA9 patients are mutant for NMNAT1 throughout the body, yet their defects are limited to the eye. In an effort to model this, we generated a global knockout using *Nmnat1* fl/fl: CAG-CreERT2 mice harboring homozygous *Nmnat1* floxed alleles (*Nmnat1* fl/fl) and CAG-CreERT2, which expresses a tamoxifen-activated Cre recombinase from the ubiquitous actin promoter. We chose a conditional approach because NMNAT1 knockout embryos are lethal (Conforti et al.,

2011). We treated 2-month-old *Nmnat1*^{fl/fl}: CAG-CreERT2 and control mice with tamoxifen. We first used RT-PCR to measure *Nmnat1* mRNA in the retina at 21 days after tamoxifen and found that it was significantly decreased in NMNAT1 cKO (*Nmnat1*^{fl/fl}: CAG-CreERT2 + tamoxifen) compared with wild-type (WT) mice (Figure 1—figure supplement 1B). To investigate the metabolic consequence of NMNAT1 deletion, we measured the levels of NMN, the substrate for NMNAT1, and NAD⁺, the product of NMNAT1, in the retina at 25 days after tamoxifen injection. There is a significant increase in levels of NMN, presumably because it cannot be consumed by NMNAT1. There is also a mild decrease in NAD⁺ in NMNAT1 cKO mice, although this is not statistically significant, suggesting that other NMNAT enzymes are an additional source of NAD⁺ (Figure 1A,B). We next evaluated retinal pathology at 4 weeks after *Nmnat1* excision using biomicroscopy. Fundus images showed abnormalities including attenuation of blood vessels (Figure 1C,D arrowhead) and the appearance of a honeycomb structure, suggesting exposure of retinal pigment epithelium (RPE) cells (Figure 1C,D arrow) in the mutant animals. Histopathological examination of the retina with hematoxylin and eosin (HE) stained sections showed severe retinal degeneration as evidenced by the reduction of the retina thickness and the thinning of the outer nuclear layer (ONL) at 4 weeks post tamoxifen treatment (Figure 1E,F). Quantitative analysis demonstrated a significant reduction of retinal thickness, especially of the ONL (Figure 1G,H). Hence, photoreceptor cells are highly vulnerable following the loss of NMNAT1.

To gain insights into the temporal aspects of the retinal degenerative process, we analyzed retinal morphology at seven time points after tamoxifen administration. The loss of nuclei in the ONL layers were evident at 25 days post tamoxifen injection and robust retinal thinning was evident at 33 days post tamoxifen injection (Figure 2A). We measured the loss of photoreceptor cells by

counting the number of ONL cell nuclei. Cell loss was first detected in the ONL around 3 weeks after tamoxifen administration and gradually progressed such that only ~15% of the cells remained at 33 days (Figure 2B).

Next, we evaluated retinal function after NMNAT1 deletion using electroretinogram (ERG). We examined three cohorts of mice: *Nmnat1*fl/fl: CAG-CreERT2 treated with tamoxifen, untreated *Nmnat1*fl/fl: CAG-CreERT2 or *Nmnat1*fl/fl treated with tamoxifen. In mutant animals in which *Nmnat1* was excised, we observed a complete loss of both scotopic (rod-driven responses) and photopic (cone-driven responses) responses, indicating the loss of *Nmnat1* in mature retina causes severe photoreceptor dysfunction (Figure 2C–E). This is consistent with previous reports showing developmental retinal defects in the tissue specific *Nmnat1* knockout mice (Eblimit et al., 2018; Wang et al., 2017). While previous reports show that *Nmnat1* is necessary for appropriate retinal development, our pathological and functional analyses of conditional deletion of NMNAT1 in two-month-old mice demonstrates that NMNAT1 is also necessary for photoreceptor cell maintenance and mature retinal functions.

In addition to NMNAT1, mammalian cells encode two other NMNAT isoforms; NMNAT2 that is localized in the Golgi and cytosol, and NMNAT3 that is localized inside the mitochondria. Since the loss of NMNAT1 induced retinal degeneration, we wished to determine the role of NMNAT2 and 3 in the retinal structure/function. A previous study showed that NMNAT2 knockout mice are perinatally lethal and have truncated optic nerves as well as peripheral axon degeneration (Slivicki et al., 2016). We could not assess the role of NMNAT2 in retinal function due to the lack of conditional knockout mice. On the other hand, NMNAT3 deficient mice (NMNAT3 KO) are viable with splenomegaly and hemolytic anemia (Hikosaka et al., 2014). We generated NMNAT3 KO mice and investigated their retinal function using ERG. Consistent with

the previous report, NMNAT3 KO mice showed splenomegaly (data not shown), however, there were no defects in ERG (Figure 2—figure supplement 1). These results indicate that NMNAT3 is dispensable for retinal function, suggesting NMNAT1 is the functionally dominant isoform controlling retinal phenotype.

Identifying the cells that are vulnerable to NMNAT1 loss is key to understanding LCA9 pathogenesis. The severe loss of the ONL nuclei (Figure 2B) induced by NMNAT1 deletion prompted us to test whether loss of NMNAT1 specifically in photoreceptors would result in their death and recapitulate the phenotype observed using the widely expressed CAG-CreERT2. We therefore generated mice lacking NMNAT1 specifically in rod photoreceptors by crossing the *Nmnat1* fl/fl mice with Rhodopsin-Cre (Rho-Cre) mice (Li et al., 2005). We analyzed the retinas of *Nmnat1* fl/fl:Rho-Cre mice at 6-weeks-of-age. Similar to previous findings using *Crx*-Cre that expresses Cre recombinase in developing photoreceptors as early as E11 (Eblimit et al., 2018; Wang et al., 2017), histological analysis revealed severe thinning of the ONL in these mutant mice (Figure 3A,B). The quantitative analysis showed a significant reduction of the retina and ONL thickness in *Nmnat1* fl/fl:Rho-Cre retina (Figure 3D) as well as a significant reduction in ONL cell number as detected by nuclear counts (Figure 3F). Consistent with the loss of ONL cells, ERG analysis showed a severe reduction in the scotopic a- and -b-waves, representing rod photoreceptor function, in the *Nmnat1* fl/fl:Rho-Cre mice (Figure 3G,H). In addition, we found decreases in cone mediated photoresponses (photopic b-wave signal) (Figure 3I) that is likely secondary to a loss of rod photoreceptor cells due to loss of required rod-derived survival factors (Lin et al., 2016; Aït-Ali et al., 2015).

To explore directly the role of NMNAT1 in cones, we deleted NMNAT1 using the cone-specific OPN1LW-Cre. We crossed *Nmnat1* fl/fl mice with OPN1LW-Cre mice in which Cre

recombinase expression is driven by the human red/green pigment (OPN1LW) promoter starting at P10 (Le et al., 2004). At 6-weeks-of-age we examined these mutant mice histologically, but did not detect any gross abnormalities, presumably due to the low number of cones (only 3% of total photoreceptors) in mice (Figure 3A,C,E). However, ERG analysis showed a complete loss of the photopic b-wave, which is derived from cone photoreceptors. This functional result demonstrates that NMNAT1 activity is vital for cone function (Figure 3I). In summary, these genetic ablation experiments demonstrate the importance of NMNAT1 for proper function and survival of both rods and cones, and indicate that LCA9-associated retinal degeneration is likely due to the direct cell-autonomous effects of NMNAT1 mutations in photoreceptors.

The loss-of-function studies above demonstrate that NMNAT1 is necessary in photoreceptors for proper retinal function. Next we assessed whether viral-mediated expression of NMNAT1 in photoreceptors in an otherwise NMNAT1 deficient animal is sufficient to promote retinal function. First, we developed a system for retinal expression of transgenes. We subretinally delivered AAV8(Y733F) containing the photoreceptor-specific human rhodopsin kinase (hGRK1) promoter driving GFP (Kay et al., 2013; Boye et al., 2013). Virus was injected into the subretinal space of two-month-old wild type mice. Transgene expression was evaluated 4–6 weeks post-injection. AAV-mediated GFP expression was observed in a subset of rhodopsin-positive cells but was weak in the inner nuclear layer (INL) (Figure 3—figure supplement 1A). These results confirm earlier reports that the hGRK1 promoter restricts transgene expression primarily to photoreceptors (Kay et al., 2013). We next asked whether AAV-mediated expression of HA-tagged human NMNAT1 could prevent retinal degeneration caused by *Nmnat1* excision. Two-month-old *Nmnat1*^{fl/fl}; CAG-CreERT2 mice received subretinal

injections of AAV-NMNAT1 in one eye, and control vector (AAV-GFP) in the contralateral eye. We confirmed the expression of NMNAT1-HA in a subset of outer nuclear cells and a minor population of inner nuclear cells (Figure 3—figure supplement 1B,C). Mice that received AAV-NMNAT1 and AAV-GFP were then treated with tamoxifen to deplete endogenous NMNAT1. One month after tamoxifen treatment, we examined retinal function. Despite the expression of NMNAT1 in only a subset of photoreceptors, we observed significantly increased scotopic a-wave amplitudes in AAV-NMNAT1 treated retinas compared with retinas injected with AAV-GFP (Figure 3—figure supplement 1D; Figure 3D). There were also small, but statistically insignificant, increases in the scotopic and photopic b-wave amplitudes between AAV-NMNAT1 and AAV-GFP treated retinas (Figure 3—figure supplement 1E,F). Hence, NMNAT1 gene delivery to photoreceptor cells significantly improved their function in this LCA9 model.

We next sought to determine the molecular mechanisms required for retinal degeneration in the NMNAT1-deficient retina. In injured peripheral nerves, the loss of NMNAT2 induces an increase in NMN that is hypothesized to activate SARM1-dependent axon degeneration (Di Stefano et al., 2015; Zhao et al., 2019). Our metabolomic analysis revealed that NMN is increased in the NMNAT1-deficient retinas (Figure 1B), and previous studies have detected SARM1 in mouse and bovine photoreceptor cells (Zhao et al., 2016; Datta et al., 2015; Menon et al., 2019). These results raised the possibility that the increased retinal NMN activates SARM1 NADase activity, inducing NAD⁺ loss and cellular degeneration in the retina. To test this hypothesis, we crossed *Nmnat1*^{fl/fl}:CAG-CreERT2 mice with SARM1 knockout mice (Szretter et al., 2009) to generate *Nmnat1*^{fl/fl}: CAG-CreERT2:*Sarm1*^{-/-} mice. *Nmnat1* was excised in these mice via tamoxifen administration at 2 months of age (NMNAT1 cKO: SARM1 KO). First, we assessed SARM1 activation via measurement of cADPR, a product of the SARM1

NAD⁺ cleavage enzyme and a biomarker of SARM1 activity as well as NAD⁺ (Sasaki et al., 2020). While the loss of NAD⁺ was not statistically significant at 25 days post tamoxifen injection in NMNAT1 cKO retina (Figure 1A), there was significant loss of NAD⁺ at 29 to 32 days post tamoxifen in NMNAT1 cKO but not in NMNAT1 cKO: SARM1 KO retina (Figure 4A). These data suggest activation of the SARM1 NADase in NMNAT1-deficient retina. Consistent with this idea, we also observed a significant increase of cADPR in NMNAT1 cKO retina in a SARM1-dependent manner (Figure 4B). Hence, SARM1 is activated by the loss of NMNAT1. Next, we assessed retinal degeneration. While there is a dramatic loss of ONL nuclei 32 days post tamoxifen injection in NMNAT1 cKO retina, there was no obvious loss of ONL cells in NMNAT1 cKO: SARM1 KO retina (Figure 4C–E). Quantitative analysis showed no reduction of retinal and ONL thickness in NMNAT1 cKO:SARM1 KO retina compared with WT (Figure 4F,G) in sharp contrast to the dramatic loss of retinal and ONL thickness in the NMNAT1 cKO (Figures 1 and 2). Moreover, there was no detectable loss of ONL nuclei in NMNAT1 cKO:SARM1 KO compared with WT, demonstrating that SARM1 is necessary for photoreceptor cell death induced by the loss of NMNAT1 (Figure 4H). We next examined the functional consequences of NMNAT1 depletion in the presence or absence of SARM1 using ERGs, and again found that loss of SARM1 prevented the severe loss of both scotopic and photopic responses due to NMNAT1 deficiency (Figure 4I–K). Taken together, these findings demonstrate that loss of NMNAT1 leads to the activation of SARM1, and that SARM1 is required for the subsequent photoreceptor degeneration and loss of visual function. Therefore, the essential function of NMNAT1 in photoreceptors is to inhibit SARM1, and inhibition of SARM1 is a candidate therapeutic strategy for the treatment of LCA9.

2.3 Discussion

In this study, we demonstrate that deletion of NMNAT1 in the adult retina causes a dramatic loss of photoreceptors and a concomitant reduction in retinal function. In addition, cell-type specific deletion of NMNAT1 in early postnatal photoreceptors is sufficient to induce retinal degeneration. Hence, NMNAT1 is required for the survival and function of both developing and mature photoreceptors. Using a modified AAV8 vector and the human rhodopsin kinase promoter to express NMNAT1, we demonstrated that a gene replacement strategy can improve retinal function in this model of LCA9. Finally, we defined the molecular mechanism by which NMNAT1 promotes photoreceptor function and survival. In photoreceptors, loss of NMNAT1 leads to activation of the inducible NADase SARM1 and the SARM1-dependent degeneration of photoreceptors. This finding defines a common mechanism operant in both photoreceptor degeneration and pathological axon degeneration. Loss of NMNAT1 in photoreceptors or NMNAT2 in axons leads to the SARM1-induced death of photoreceptors or axons, respectively. This surprising result extends our understanding of both the mechanisms causing retinal degeneration and the potential role of SARM1 in human disease (Figley and DiAntonio, 2020; Coleman and Höke, 2020).

Retinal NAD⁺ homeostasis is crucial for visual function and NAD⁺ decline is a hallmark of many retinal degenerative disease models (Lin et al., 2016). Reduced NAD⁺ induces mitochondrial dysfunction in photoreceptor cells and affects activity of SIRT3, which protects the retina from light-induced and other forms of neurodegeneration. In addition, NAD⁺-dependent enzymes play crucial roles in phototransduction including the regeneration of the photosensitive element, 11-cis-retinal, and the regulation of photoreceptor membrane potential.

Moreover, mutations in the genes encoding some of these enzymes cause retinal degenerative disease. For example, mutations in all-trans-retinal dehydrogenase (RDH12) that is localized to photoreceptor cells are associated with LCA13. Combined deletion of retinal dehydrogenases, RDH12 and RDH8, results in mouse retinal degeneration (Maeda et al., 2009). NAD⁺ is also a cofactor for inosine monophosphate dehydrogenase (IMPDH1), which is the rate limiting enzyme for GTP synthesis and, in turn, is required for cGMP production. cGMP is indispensable for the regulation of photoreceptor membrane potential and calcium concentration upon light stimulation. IMPDH1 mutations cause both a dominant form of retinitis pigmentosa (RP10) and LCA11. These results highlight the central role of NAD⁺ metabolism in the photoreceptor.

NMNAT1 is the only NMNAT enzyme localized to the nucleus in mammals and is crucial for nuclear NAD⁺ synthesis. Despite the broad functions of nuclear NAD⁺ in all cell types, the sole consequence of LCA9-associated NMNAT1 mutations is retinal dysfunction/degeneration without systemic abnormalities. Previous studies, and our results, show early loss of photoreceptor cells in NMNAT1-deficient retina (Eblimit et al., 2018; Wang et al., 2017). In photoreceptors NMNAT1 may localize not only in the nucleus but also outside the nucleus, since a subcellular proteomics study showed the existence and enrichment of NMNAT1 in the photoreceptor outer segments (Zhao et al., 2016). Single-cell transcriptomic RNA analysis also found *Nmnat1* in rods and cones (Menon et al., 2019; Lukowski et al., 2019). Consistent with an extranuclear role for NMNAT1 in photoreceptors, in these studies cytosolic NMNAT2 was either not identified or was found at much lower levels than NMNAT1. NMNAT3 is the mitochondrial NMNAT, and we show here that it is dispensable for retinal homeostasis and function, further highlighting the central requirement for NMNAT1 in photoreceptors.

Having demonstrated that NMNAT1 is required in photoreceptors in this model of LCA9, we showed that viral-mediated gene replacement in photoreceptors is capable of improving retinal function. Adeno-associated virus (AAV) is a naturally occurring, non-pathogenic virus used in gene therapy studies to restore structure and function to diseased cells. Recently, the U.S. FDA approved an AAV-RPE65 vector as a therapeutic reagent for LCA2 and other biallelic RPE65 mutation associated retinal dystrophies (Apte, 2018). Theoretically, LCA9 caused by the loss of NMNAT1 function is a reasonable target for AAV-mediated gene therapy. To achieve expression in photoreceptors, we used an AAV8 variant that is highly efficient for transducing photoreceptors following subretinal injection as well as the hGRK1 promoter that has activity exclusively in rods and cones (Kay et al., 2013; Boye et al., 2013). Delivery of AAV8(Y733F)-hGRK1-NMNAT1 prior to deletion of NMNAT1 resulted in partial improvement of the retinal phenotype, in particular the scotopic a-wave, of mice deficient for NMNAT1. Future studies will assess the efficacy of gene replacement after deletion of NMNAT1 to more closely mimic the human condition.

Since NAD⁺ plays such a central role in photoreceptors, the identification of the NAD⁺ biosynthetic enzyme NMNAT1 as the cause of LCA9 suggests that photoreceptor degeneration in LCA9 is due to the reduction in NAD⁺ synthesis. Surprisingly, we demonstrate here that this is not the essential function for NMNAT1 in photoreceptors. Instead, NMNAT1 is required to restrain the activity of the prodegenerative NADase SARM1. When NMNAT1 is deleted from SARM1 KO photoreceptors, the photoreceptors do not die and but instead maintain their physiological function, demonstrating that these cells do not require NMNAT1 as long as SARM1 is not present. This finding is perfectly analogous to the relationship between NMNAT2 and SARM1 in the axon. NMNAT2 KO mice are perinatal lethal and have dramatic axonal

defects, but NMNAT2, SARM1 double KO mice are viable and have a normal lifespan (Gilley et al., 2015). NMNAT enzymes inhibit the activation of SARM1 (Sasaki et al., 2016), potentially by consuming the NAD⁺ precursor NMN, which is postulated to activate SARM1 (Di Stefano et al., 2015; Zhao et al., 2019). Prior to our current study, loss of NMNAT2 was the only known trigger of SARM1 activation. Our current work suggests that SARM1 is activated by the loss of any NMNAT enzyme whose activity is not redundant with another NMNAT isoform. NMNAT2 is the only cytosolic NMNAT in the axon, and so loss of axonal NMNAT2 leads to localized activation of SARM1 and axon degeneration. In photoreceptors, NMNAT1 is not only nuclear but also likely extranuclear, and NMNAT2 is apparently present at very low levels. Hence, in photoreceptors loss of NMNAT1 triggers activation of SARM1 which consumes NAD⁺ and triggers cell death. As NAD⁺ loss is a common pathology of many retinal diseases, this raises the possibility that SARM1 activation may contribute to a wide range of retinal disorders. In support of this conjecture, recent studies found that SARM1 promotes retinal degeneration in X-linked retinoschisis (Molday et al., 2007) and rhodopsin-deficient mice (Ozaki et al., 2020).

Our identification of SARM1 as the executioner of photoreceptor death in this model of LCA9 opens up new therapeutic possibilities. We previously developed a potent dominant negative SARM1 variant and demonstrated that AAV-mediated expression of dominant negative SARM1 strongly protects injured axons from degeneration in the peripheral nervous system (Geisler et al., 2019) and is also effective in a neuroinflammatory model of glaucoma (Ko et al., 2020).

While NMNAT1 gene replacement is a potential treatment option for LCA9, if SARM1 plays a more general role in retinal degeneration, then using gene therapy to express this dominant negative SARM1 could not only treat LCA9, but also multiple retinal neurodegenerative diseases. In addition, SARM1 is an enzyme and so small molecule enzyme inhibitors would be

another attractive treatment modality (DiAntonio, 2019; Krauss et al., 2020). These findings demonstrate the utility of dissecting the molecular mechanism of degeneration in diseases of retinal neurodegeneration. In the case of LCA9, these studies identified a SARM1-dependent photoreceptor cell death pathway and discovered the heretofore unknown commonality between the mechanism of retinal neurodegeneration and pathological axon degeneration.

2.4 Materials and Methods

Mouse

Animal studies were carried out under approved protocols from animal studies committee at Washington University. NMNAT1 mutant mice (*Nmnat1* FRTgeo;loxP/+) which have FRT sites flanking promoterless LacZ-neomycin phosphotransferase gene (beta Geo) expression cassette located between exon 2 and 3 together with loxP sites flanking exon three was obtained from EUCOMM (*NMNAT*^{tm1a(EUCOMM)}Wtsi, RRID:MGI:5782147). This mouse expresses functionally null truncated NMNAT1 (exon 1 and 2) fused to beta Geo. *Nmnat1* FRTgeo;loxP/+ heterozygote mice were viable and fertile however, in consistent with former results, no whole body knockout (*Nmnat1*FRTgeo;loxP/FRTgeo;loxP) was born (Conforti et al., 2011). Next *Nmnat1* FRTgeo;loxP/+ mice were crossed with FLP recombinase expressing mice in the C57BL/6 J background to remove beta Geo cassette flanked by FRT sites and RD8 mutation that might affect the ocular phenotypes (Mattapallil et al., 2012). The resultant mice (*Nmnat1* fl/+) have two loxP sites flanking the third exon. Then *Nmnat1* fl/+ mice were crossed with mice expressing inducible Cre recombinase under actin promoter (CAG-CreERT2, RRID:IMSR_JAX:004682) and *Nmnat1* fl/fl: CAG-CreERT2 mice were generated. All genotypes were confirmed by genomic PCR. NMNAT1 whole body knockout mice were

generated by injecting 100 µg/g 4-hydroxytamoxifen (Sigma) into 6 to 8 weeks old *Nmnat1* fl/fl: CAG-CreERT2 with IP for total 10 days with 2 days rest after first 5 days injection. The last day of injection was counted as day 0 after tamoxifen injection. Mice expressing Cre recombinase (CAG-CreERT2) were obtained from The Jackson Laboratory. To generate mice lacking *Nmnat1* specifically from rod photoreceptors, we crossed *Nmnat1* fl/fl mice with mice carrying a copy of the Rhodopsin- iCre75 transgene, in which Cre recombinase expression is driven by the rhodopsin promoter starting postnatally at P7, which were provided by Dr. Ching-Kang Jason Chen (Li et al., 2005). To generate mice lacking NMNAT1 specifically from cone photoreceptors, we crossed *Nmnat1* fl/fl mice with mice carrying one copy of the Cre recombinase under human red/green pigment promoter (OPN1LW-Cre, RRID:IMSR_JAX:032911), which were provided by Dr. Yun Le (Le et al., 2004). SARM1 knockout mice were obtained from Dr. Marco Colonna (Szretter et al., 2009). NMNAT3 knockout mice were derived from ES cells (*Nmnat3*tm1(KOMP)Mbp, Knockout Mouse Project (KOMP)) in our facility and crossed with C57BL/6 J mice for at least five generations.

AAV preparation

Plasmids containing the photoreceptor-specific human rhodopsin kinase (hGRK1) promoter upstream of either GFP or HA-tagged NMNAT1 were packaged in AAV8(Y733F) capsid. The detailed methodology of vector production and purification has been previously described (Zolotukhin et al., 2002). Briefly, vectors were packaged using a plasmid based system in HEK293 cells (ATCC CRL-1573, RRID:CVCL_0045) by CaPO₄ transfection. Cells were harvested and lysed by successive freeze thaw cycles. Virus within the lysate was purified by discontinuous iodixanol step gradients followed by further purification via column chromatography on a 5 ml HiTrap Q sepharose column using a Pharmacia AKTA FPLC system

(Amersham Biosciences, Piscataway, NJ, USA). Vectors were then concentrated and buffer exchanged into Alcon BSS (sodium-155.7 mM, potassium- 10.1 mM, calcium- 3.3 mM, m- 1.5 mM, chloride- 128.9 mM, citrate- 5.8 mM, acetate- 28.6 mM, osmolality- 298 mOsm) supplemented with Tween 20 (0.014%). Virus was titered by qPCR relative to a standard and stored at -80°C as previously described (Jacobson et al., 2006). HEK293 cells used for producing AAV were purchased directly from ATCC who applies appropriate quality controls for maintaining and confirming identification of these lines. HEK293 cells were used more than two years ago for viral production and thus could not be authenticated now. HEK293 cells are passaged 50 times before discarding culture and thawing new vial. Short tandem repeat profiling is performed annually to authenticate the cell lines.

Subretinal injections

Mice were anesthetized with a mixture of ketamine (70–80 mg/kg) and xylazine (15 mg/kg) injected intraperitoneally. The pupil was dilated with 1% tropicamide and topical anesthesia (0.5% proparacaine hydrochloride ophthalmic solution) was also applied to the eye. A self-sealing scleral incision was made by using the tip of a 31 G needle with the bevel pointed down. Then a 33G needle on a Hamilton syringe was inserted into the scleral incision and 1 μl of AAV containing solutions were injected in the subretinal space inducing a transient retinal detachment. The needle was slowly removed to prevent reflux and an ophthalmic ointment of neomycin/polymyxin B sulfate/bacitracin zinc was applied to the injected eye.

Fundus microscopy and fluorescent angiography

Digital color fundus photography was performed using the Micron III retinal imaging system (Phoenix Research Laboratories). Prior to fundus imaging, mice were anesthetized with an

intraperitoneal injection of 86.9 mg/kg ketamine and 10 mg/kg xylazine and administered 1.0% tropicamide eye drops (Bausch and Lomb) to dilate the pupils.

Electroretinography (ERG)

ERG was performed as previously described (Hennig et al., 2013) by using the UTAS-E3000 Visual Electrodiagnostic System running EM for Windows (LKC Technologies). Mice were anesthetized by intra peritoneal injection of a mixture of 86.9 mg/kg ketamine and 13.4 mg/kg xylazine. The recording electrode was a platinum loop placed in a drop of methylcellulose on the surface of the cornea; a reference electrode was placed sub-dermally at the vertex of the skull and a ground electrode under the skin of the back or tail. Stimuli were brief white flashes delivered via a Ganzfeld integrating sphere, and signals were recorded with bandpass settings of 0.3 Hz to 500 Hz. After a 10 min stabilization period, a 9-step scotopic intensity series was recorded that included rod-specific/scotopic bright flash responses. After a 5 min light adaptation period on a steady white background, a 7-step cone-specific/photopic intensity series was recorded. Scotopic and photopic b-wave amplitudes and scotopic a-wave amplitudes were recorded for all flash intensities. We extracted quantitative measurements from the ERG waveforms using an existing Microsoft Excel macro that defines the a-wave amplitude as the difference between the average pre-trial baseline and the most negative point of the average trace and defines the b-wave amplitude as the difference between this most negative point to the highest positive point, without subtracting oscillatory potentials.

Quantitative RT-PCR

Mice were euthanized and eyeballs were enucleated and retinas were dissected and immediately freeze in liquid N₂. On the day of preparation, Trizol was directly added to the frozen retina and

tissues were homogenized with Polytron and RNA was extracted using Trizol (Thermo Fisher Scientific) and chloroform (Sigma) phase separation. Quantitative RT-PCR reaction was performed with primers (Nmnat1-forward: AGAACTCACACTGGGTGGAAG, Nmnat1-reverse: CAGGCTTTTCCAGTGCAGGTG, Gapdh-forward: TGCCCCCATGTTTGTGATG, Gapdh-reverse: TGTGGTCATGAGCCCTTCC) with reaction mixture (ThermoFisher, SYBR Green PCR Master Mix) and monitored with Prism 7900HT (ABI) and analyzed with delta-CT method.

Histology

Mice were euthanized and eyeballs were enucleated and fixed in 4% formalin for 8 hr then washed with PBS and then embedded in paraffin. The thickness of the retinal layers or outer nuclear layers was measured using HE stained sections and plotted against the distance from the optic nerve head. The numbers of nuclei in the outer nuclear layer were analyzed using HE stained retinal sections. Outer nuclear layer was visually determined and the number of nucleus in each layer was counted and normalized by the length parallel to each layer of the retina. Data were expressed relative to the total number of nuclei in the WT. For immunostaining of the HA epitope tag, paraffin embedded eye sections were deparaffinized and treated with formic acid (70% in water) for 15 min at room temperature. Sections were rinsed and treated with blocking solution (goat IgG). Primary antibody against HA (Cell Signaling Technology, 3724, 1:400, RRID:AB_1549585) and secondary antibody Jackson Immuno Research Laboratories, AlexaFluo@568, 111-585-003 were used to visualize the HA-tagged NMNAT1. Primary antibody against rhodopsin (Abcam, ab3267, 1:500, RRID:AB_303655) was used to identify the photoreceptor outer segment. Slides were analyzed under the microscope (Nikon, Eclipse 80i) after the nuclear staining with DAPI and mounting (Vector Laboratories, VECTASHIELD with

DAPI, H-1200–10). For X-Gal staining, retina were dissected and fixed in the cold fixation buffer (0.2% Glutaraldehyde, 5 mM EGTA, 2 mM MgCl₂, 0.1M K-phosphate buffer pH7.2) for 1 hr, wash with detergent rinse (0.02% Igepal, 0.01% Sodium Deoxycholate, and 2 mM MgCl₂ in 0.1M phosphate buffer pH 7.3), and incubated with X-Gal solution (1 mg/ml X-Gal, 0.02% Igepal, 0.01% Sodium Deoxycholate, 5 mM Potassium Ferricyanide, 5 mM Potassium Ferrocyanide, and 2 mM MgCl₂, 0.1M phosphate buffer pH 7.3) for 10 hr in the dark at room temperature. Tissues were rinsed with PBS then fix with 4% PFA for 1 hr then paraffin sections were prepared and the sections were analyzed under the microscope (Nikon, Eclipse 80i).

Metabolite measurement

Mice were euthanized and eyeballs were enucleated and retinas were dissected and immediately freeze in liquid N₂. On the day of extraction, retinal tissues were homogenized in 160 µl of cold 50% MeOH solution in water using homogenizer (Branson) and then centrifuged (15,000 g, 4°C, 10 min). Clear supernatant was transferred to new tube containing 100 µl chloroform and vigorously shake then centrifuged (15,000 g, 4°C, 10 min). The chloroform extraction was repeated three times. Clear aqueous phase (120 µl) was transferred to new tube and then lyophilized and stored at –80°C until measurement. Lyophilized samples were reconstituted with 60 µl of 5 mM ammonium formate (Sigma) and centrifuged at 12,000 x g for 10 min. Cleared supernatant was transferred to the sample tray. Serial dilutions of standards for each metabolite in 5 mM ammonium formate were used for calibration. Liquid chromatography was performed by HPLC (1290; Agilent) with Atlantis T3 (LC 2.1 × 150 mm, 3 µm; Waters) (Hikosaka et al., 2014). For steady-state metabolite analysis, 20 µl of samples were injected at a flow rate of 0.15 ml/min with 5 mM ammonium formate for mobile phase A and 100% methanol for mobile phase B. Metabolites were eluted with gradients of 0–10 min, 0–70% B; 10–15 min, 70% B; 16–20

min, 0% B (Hikosaka et al., 2014). The metabolites were detected with a triple quadrupole mass spectrometer (6460, Agilent) under positive ESI multiple reaction monitoring (MRM) using m/z for NAD⁺:664 > 428, NMN:335 > 123, cADPR: 542 > 428, and Nam:123 > 80. Metabolites were quantified by MassHunter quantitative analysis tool (Agilent) with standard curves and normalized by the protein amount in the sample.

Statistical analysis

Sample number (n) was defined as a number of mice or replicates and indicated in the figure legend. Data comparisons were performed using Mann-Whitney U test, Kruskal-Wallis test, one-way ANOVA, or two-way ANOVA using R. F and P values for ANOVA were reported for each comparison in corresponding figure legends. For multiple comparisons, Holm-Bonferroni multiple comparison for one-way-ANOVA and Tukey post-hoc test for two-way-ANOVA were used.

2.5 Acknowledgments

We thank Amy Strickland, Nina Panchenko, Kimberly Kruse, Andrea Santeford, Rachel McClarney, Simburger Kelli, Timothy Fahrner, Neiner Alicia, and Cassidy Menendez for technical assistance.

2.6 References

Aït-Ali N, Fridlich R, Millet-Puel G, Clérin E, Delalande F, Jaillard C, Blond F, Perrocheau L, Reichman S, Byrne LC, Olivier-Bandini A, Bellalou J, Moysse E, Bouillaud F, Nicol X, Dalkara D, van Dorsselaer A, Sahel JA, Lévillard T. Rod-derived cone viability factor promotes cone

survival by stimulating aerobic glycolysis. *Cell*. 2015;161:817–832. doi:
10.1016/j.cell.2015.03.023.

Apte RS. Gene therapy for retinal degeneration. *Cell*. 2018;173:5. doi:
10.1016/j.cell.2018.03.021.

Babetto E, Beirowski B, Janeckova L, Brown R, Gilley J, Thomson D, Ribchester RR, Coleman MP. Targeting NMNAT1 to axons and synapses transforms its neuroprotective potency in vivo. *Journal of Neuroscience*. 2010;30:13291–13304. doi: 10.1523/JNEUROSCI.1189-10.2010.

Berger F, Lau C, Dahlmann M, Ziegler M. Subcellular compartmentation and differential catalytic properties of the three human nicotinamide mononucleotide adenylyltransferase isoforms. *Journal of Biological Chemistry*. 2005;280:36334–36341. doi:
10.1074/jbc.M508660200.

Bowne SJ, Sullivan LS, Blanton SH, Cepko CL, Blackshaw S, Birch DG, Hughbanks-Wheaton D, Heckenlively JR, Daiger SP. Mutations in the inosine monophosphate dehydrogenase 1 gene (IMPDH1) cause the RP10 form of autosomal dominant retinitis pigmentosa. *Human Molecular Genetics*. 2002;11:559–568. doi: 10.1093/hmg/11.5.559.

Boye SL, Peshenko IV, Huang WC, Min SH, McDoom I, Kay CN, Liu X, Dyka FM, Foster TC, Umino Y, Karan S, Jacobson SG, Baehr W, Dizhoor A, Hauswirth WW, Boye SE. AAV-mediated gene therapy in the guanylate cyclase (RetGC1/RetGC2) double knockout mouse model of Leber congenital amaurosis. *Human Gene Therapy*. 2013;24:189–202. doi:
10.1089/hum.2012.193.

Chiang PW, Wang J, Chen Y, Fu Q, Zhong J, Chen Y, Yi X, Wu R, Gan H, Shi Y, Chen Y, Barnett C, Wheaton D, Day M, Sutherland J, Heon E, Weleber RG, Gabriel LA, Cong P, Chuang

K, Ye S, Sallum JM, Qi M. Exome sequencing identifies NMNAT1 mutations as a cause of leber congenital amaurosis. *Nature Genetics*. 2012;44:972–974. doi: 10.1038/ng.2370.

Coleman MP, Höke A. Programmed axon degeneration: from mouse to mechanism to medicine. *Nature Reviews Neuroscience*. 2020;21:183–196. doi: 10.1038/s41583-020-0269-3.

Conforti L, Janeckova L, Wagner D, Mazzola F, Cialabrini L, Di Stefano M, Orsomando G, Magni G, Bendotti C, Smyth N, Coleman M. Reducing expression of NAD⁺ synthesizing enzyme NMNAT1 does not affect the rate of wallerian degeneration. *FEBS Journal*. 2011;278:2666–2679. doi: 10.1111/j.1742-4658.2011.08193.x.

Coppieters F, Todeschini AL, Fujimaki T, Baert A, De Bruyne M, Van Cauwenbergh C, Verdin H, Bauwens M, Ongenaert M, Kondo M, Meire F, Murakami A, Veitia RA, Leroy BP, De Baere E. Hidden genetic variation in LCA9-Associated congenital blindness explained by 5'UTR Mutations and Copy-Number Variations of NMNAT1. *Human Mutation*. 2015;36:1188–1196. doi: 10.1002/humu.22899.

Datta P, Allamargot C, Hudson JS, Andersen EK, Bhattarai S, Drack AV, Sheffield VC, Seo S. Accumulation of non-outer segment proteins in the outer segment underlies photoreceptor degeneration in Bardet-Biedl syndrome. *PNAS*. 2015;112:E4400–E4409. doi: 10.1073/pnas.1510111112.

Di Stefano M, Nascimento-Ferreira I, Orsomando G, Mori V, Gilley J, Brown R, Janeckova L, Vargas ME, Worrell LA, Loreto A, Tickle J, Patrick J, Webster JR, Marangoni M, Carpi FM, Pucciarelli S, Rossi F, Meng W, Sagasti A, Ribchester RR, Magni G, Coleman MP, Conforti L. A rise in NAD precursor nicotinamide mononucleotide (NMN) after injury promotes axon degeneration. *Cell Death & Differentiation*. 2015;22:731–742. doi: 10.1038/cdd.2014.164.

DiAntonio A. Axon degeneration: mechanistic insights lead to therapeutic opportunities for the prevention and treatment of peripheral neuropathy. *Pain*. 2019;160 Suppl 1:S17–S22. doi: 10.1097/j.pain.0000000000001528.

Eblimit A, Zaneveld SA, Liu W, Thomas K, Wang K, Li Y, Mardon G, Chen R. NMNAT1 E257K variant, associated with Leber congenital amaurosis (LCA9), causes a mild retinal degeneration phenotype. *Experimental Eye Research*. 2018;173:32–43. doi: 10.1016/j.exer.2018.04.010.

Falk MJ, Zhang Q, Nakamaru-Ogiso E, Kannabiran C, Fonseca-Kelly Z, Chakarova C, Audo I, Mackay DS, Zeitz C, Borman AD, Staniszewska M, Shukla R, Palavalli L, Mohand-Said S, Waseem NH, Jalali S, Perin JC, Place E, Ostrovsky J, Xiao R, Bhattacharya SS, Consugar M, Webster AR, Sahel J-A, Moore AT, Berson EL, Liu Q, Gai X, Pierce EA. NMNAT1 mutations cause Leber congenital amaurosis. *Nature Genetics*. 2012;44:1040–1045. doi: 10.1038/ng.2361.

Figley MD, DiAntonio A. The SARM1 axon degeneration pathway: control of the NAD⁺ metabolome regulates axon survival in health and disease. *Current Opinion in Neurobiology*. 2020;63:59–66. doi: 10.1016/j.conb.2020.02.012.

Geisler S, Huang SX, Strickland A, Doan RA, Summers DW, Mao X, Park J, DiAntonio A, Milbrandt J. Gene therapy targeting SARM1 blocks pathological axon degeneration in mice. *Journal of Experimental Medicine*. 2019;216:294–303. doi: 10.1084/jem.20181040.

Gerdts J, Brace EJ, Sasaki Y, DiAntonio A, Milbrandt J. SARM1 activation triggers axon degeneration locally via NAD⁺ destruction. *Science*. 2015;348:453–457. doi: 10.1126/science.1258366.

Gilley J, Orsomando G, Nascimento-Ferreira I, Coleman MP. Absence of SARM1 rescues development and survival of NMNAT2-deficient axons. *Cell Reports*. 2015;10:1974–1981. doi: 10.1016/j.celrep.2015.02.060.

Gilley J, Coleman MP. Endogenous Nmnat2 is an essential survival factor for maintenance of healthy axons. *PLOS Biology*. 2010;8:e1000300. doi: 10.1371/journal.pbio.1000300.

Greenwald SH, Charette JR, Staniszewska M, Shi LY, Brown SDM, Stone L, Liu Q, Hicks WL, Collin GB, Bowl MR, Krebs MP, Nishina PM, Pierce EA. Mouse models of NMNAT1-Leber congenital amaurosis (LCA9) Recapitulate key features of the human disease. *The American Journal of Pathology*. 2016;186:1925–1938. doi: 10.1016/j.ajpath.2016.03.013.

Hennig AK, Peng G-H, Chen S. Transcription coactivators p300 and CBP are necessary for Photoreceptor-Specific chromatin organization and gene expression. *PLOS ONE*. 2013;8:e69721. doi: 10.1371/journal.pone.0069721.

Hikosaka K, Ikutani M, Shito M, Kazuma K, Gulshan M, Nagai Y, Takatsu K, Konno K, Tobe K, Kanno H, Nakagawa T. Deficiency of nicotinamide mononucleotide adenylyltransferase 3 (Nmnat3) Causes hemolytic Anemia by altering the glycolytic flow in mature erythrocytes. *The Journal of Biological Chemistry*. 2014;289:14796–14811. doi: 10.1074/jbc.M114.554378.

Jacobson SG, Acland GM, Aguirre GD, Aleman TS, Schwartz SB, Cideciyan AV, Zeiss CJ, Komaromy AM, Kaushal S, Roman AJ, Windsor EA, Sumaroka A, Pearce-Kelling SE, Conlon TJ, Chiodo VA, Boye SL, Flotte TR, Maguire AM, Bennett J, Hauswirth WW. Safety of recombinant adeno-associated virus type 2-RPE65 vector delivered by ocular subretinal injection. *Molecular Therapy*. 2006;13:1074–1084. doi: 10.1016/j.ymthe.2006.03.005.

Kay CN, Ryals RC, Aslanidi GV, Min SH, Ruan Q, Sun J, Dyka FM, Kasuga D, Ayala AE, Van Vliet K, Agbandje-McKenna M, Hauswirth WW, Boye SL, Boye SE. Targeting photoreceptors via intravitreal delivery using novel, capsid-mutated AAV vectors. *PLOS ONE*. 2013;8:e62097. doi: 10.1371/journal.pone.0062097.

Kennan A, Aherne A, Palfi A, Humphries M, McKee A, Stitt A, Simpson DA, Demtroder K, Orntoft T, Ayuso C, Kenna PF, Farrar GJ, Humphries P. Identification of an IMPDH1 mutation in autosomal dominant retinitis pigmentosa (RP10) revealed following comparative microarray analysis of transcripts derived from retinas of wild-type and rho(-/-) mice. *Human Molecular Genetics*. 2002;11:547–558. doi: 10.1093/hmg/11.5.547.

Khan AO, Budde BS, Nürnberg P, Kawalia A, Lenzner S, Bolz HJ. Genome-wide linkage and sequence analysis challenge *CCDC66* as a human retinal dystrophy candidate gene and support a distinct *NMNAT1*-related fundus phenotype. *Clinical Genetics*. 2018;93:149–154. doi: 10.1111/cge.13022.

Ko KW, Milbrandt J, DiAntonio A. *SARM1* acts downstream of neuroinflammatory and necroptotic signaling to induce axon degeneration. *Journal of Cell Biology*. 2020;219:152. doi: 10.1083/jcb.201912047.

Koenekoop RK, Wang H, Majewski J, Wang X, Lopez I, Ren H, Chen Y, Li Y, Fishman GA, Genead M, Schwartzentruber J, Solanki N, Traboulsi EI, Cheng J, Logan CV, McKibbin M, Hayward BE, Parry DA, Johnson CA, Nageeb M, Poulter JA, Mohamed MD, Jafri H, Rashid Y, Taylor GR, Keser V, Mardon G, Xu H, Inglehearn CF, Fu Q, Toomes C, Chen R, Finding of Rare Disease Genes (FORGE) Canada Consortium Mutations in *NMNAT1* cause Leber

congenital amaurosis and identify a new disease pathway for retinal degeneration. *Nature Genetics*. 2012;44:1035–1039. doi: 10.1038/ng.2356.

Krauss R, Bosanac T, Devraj R, Engber T, Hughes RO. Axons matter: the promise of treating neurodegenerative disorders by targeting SARM1-Mediated axonal degeneration. *Trends in Pharmacological Sciences*. 2020;41:281–293. doi: 10.1016/j.tips.2020.01.006.

Kuribayashi H, Baba Y, Iwagawa T, Arai E, Murakami A, Watanabe S. Roles of *Nmnat1* in the survival of retinal progenitors through the regulation of pro-apoptotic gene expression via histone acetylation. *Cell Death & Disease*. 2018;9:0907. doi: 10.1038/s41419-018-0907-0.

Le YZ, Ash JD, Al-Ubaidi MR, Chen Y, Ma JX, Anderson RE. Targeted expression of cre recombinase to cone photoreceptors in transgenic mice. *Molecular Vision*. 2004;10:1011–1018.

Li S, Chen D, Sauvé Y, McCandless J, Chen YJ, Chen CK. Rhodopsin-iCre transgenic mouse line for Cre-mediated rod-specific gene targeting. *Genesis*. 2005;41:73–80. doi: 10.1002/gene.20097.

Lin JB, Kubota S, Ban N, Yoshida M, Santeford A, Sene A, Nakamura R, Zapata N, Kubota M, Tsubota K, Yoshino J, Imai SI, Apte RS. NAMPT-Mediated NAD(+) Biosynthesis is essential for vision in mice. *Cell Reports*. 2016;17:69–85. doi: 10.1016/j.celrep.2016.08.073.

Lin JB, Lin JB, Chen HC, Chen T, Apte RS. Combined SIRT3 and SIRT5 deletion is associated with inner retinal dysfunction in a mouse model of type 1 diabetes. *Scientific Reports*. 2019;9:3799. doi: 10.1038/s41598-019-40177-6.

Lin JB, Apte RS. NAD⁺ and sirtuins in retinal degenerative diseases: a look at future therapies. *Progress in Retinal and Eye Research*. 2018;67:118–129. doi: 10.1016/j.preteyeres.2018.06.002.

Lukowski SW, Lo CY, Sharov AA, Nguyen Q, Fang L, Hung SS, Zhu L, Zhang T, Grünert U, Nguyen T, Senabouth A, Jabbari JS, Welby E, Sowden JC, Waugh HS, Mackey A, Pollock G, Lamb TD, Wang PY, Hewitt AW, Gillies MC, Powell JE, Wong RC. A single-cell transcriptome atlas of the adult human retina. *The EMBO Journal*. 2019;38:e100811. doi: 10.15252/embj.2018100811.

Maeda A, Golczak M, Maeda T, Palczewski K. Limited Roles of Rdh8, Rdh12, and Abca4 in all-trans -Retinal Clearance in Mouse Retina. *Investigative Ophthalmology & Visual Science*. 2009;50:5435–5443. doi: 10.1167/iovs.09-3944.

Mattapallil MJ, Wawrousek EF, Chan C-C, Zhao H, Roychoudhury J, Ferguson TA, Caspi RR. The Rd8 Mutation of the *Crb1* Gene Is Present in Vendor Lines of C57BL/6N Mice and Embryonic Stem Cells, and Confounds Ocular Induced Mutant Phenotypes. *Investigative Ophthalmology & Visual Science*. 2012;53:2921–2927. doi: 10.1167/iovs.12-9662.

Menon M, Mohammadi S, Davila-Velderrain J, Goods BA, Cadwell TD, Xing Y, Stemmer-Rachamimov A, Shalek AK, Love JC, Kellis M, Hafler BP. Single-cell transcriptomic atlas of the human retina identifies cell types associated with age-related macular degeneration. *Nature Communications*. 2019;10:4902–4909. doi: 10.1038/s41467-019-12780-8.

Molday LL, Wu WW, Molday RS. Retinoschisin (RS1), the protein encoded by the X-linked retinoschisis gene, is anchored to the surface of retinal photoreceptor and bipolar cells through its interactions with a Na/K ATPase-SARM1 complex. *Journal of Biological Chemistry*. 2007;282:32792–32801. doi: 10.1074/jbc.M706321200.

Ozaki E, Gibbons L, Neto NG, Kenna P, Carty M, Humphries M, Humphries P, Campbell M, Monaghan M, Bowie A, Doyle SL. SARM1 deficiency promotes rod and cone photoreceptor cell

survival in a model of retinal degeneration. *Life Science Alliance*. 2020;3:e201900618. doi: 10.26508/lsa.201900618.

Perrault I, Hanein S, Zanlonghi X, Serre V, Nicouveau M, Defoort-Delhemmes S, Delphin N, Fares-Taie L, Gerber S, Xerri O, Edelson C, Goldenberg A, Duncombe A, Le Meur G, Hamel C, Silva E, Nitschke P, Calvas P, Munnich A, Roche O, Dollfus H, Kaplan J, Rozet JM. Mutations in NMNAT1 cause Leber congenital amaurosis with early-onset severe macular and optic atrophy. *Nature Genetics*. 2012;44:975–977. doi: 10.1038/ng.2357.

Sasaki Y, Vohra BPS, Baloh RH, Milbrandt J. Transgenic mice expressing the Nmnat1 protein manifest robust delay in axonal degeneration in vivo. *Journal of Neuroscience*. 2009;29:6526–6534. doi: 10.1523/JNEUROSCI.1429-09.2009.

Sasaki Y, Margolin Z, Borgo B, Havranek JJ, Milbrandt J. Characterization of Leber congenital Amaurosis-associated NMNAT1 mutants. *Journal of Biological Chemistry*. 2015;290:17228–17238. doi: 10.1074/jbc.M115.637850.

Sasaki Y, Nakagawa T, Mao X, DiAntonio A, Milbrandt J. NMNAT1 inhibits axon degeneration via blockade of SARM1-mediated NAD⁺ depletion. *eLife*. 2016;5:1010. doi: 10.7554/eLife.19749.

Sasaki Y, Engber TM, Hughes RO, Figley MD, Wu T, Bosanac T, Devraj R, Milbrandt J, Krauss R, DiAntonio A. cADPR is a gene dosage-sensitive biomarker of SARM1 activity in healthy, compromised, and degenerating axons. *Experimental Neurology*. 2020;329:113252. doi: 10.1016/j.expneurol.2020.113252.

Schuster A, Janecke AR, Wilke R, Schmid E, Thompson DA, Utermann G, Wissinger B, Zrenner E, Gal A. The Phenotype of Early-Onset Retinal Degeneration in Persons with RDH12

Mutations. *Investigative Ophthalmology & Visual Science*. 2007;48:1824–1831. doi: 10.1167/iovs.06-0628.

Siemiatkowska AM, Schuurs-Hoeijmakers JH, Bosch DG, Boonstra FN, Riemsdag FC, Ruiter M, de Vries BB, den Hollander AI, Collin RW, Cremers FP. Nonpenetrance of the most frequent autosomal recessive leber congenital amaurosis mutation in *NMNAT1*. *JAMA Ophthalmology*. 2014;132:1002–1004. doi: 10.1001/jamaophthalmol.2014.983.

Slivicki RA, Ali YO, Lu HC, Hohmann AG. Impact of genetic reduction of *NMNAT2* on Chemotherapy-Induced losses in cell viability in vitro and peripheral neuropathy in vivo. *PLOS ONE*. 2016;11:e0147620. doi: 10.1371/journal.pone.0147620.

Szretter KJ, Samuel MA, Gilfillan S, Fuchs A, Colonna M, Diamond MS. The immune adaptor molecule SARM modulates tumor necrosis factor alpha production and microglia activation in the brainstem and restricts west nile virus pathogenesis. *Journal of Virology*. 2009;83:9329–9338. doi: 10.1128/JVI.00836-09.

Verdin E. NAD⁺ in aging, metabolism, and neurodegeneration. *Science*. 2015;350:1208–1213. doi: 10.1126/science.aac4854.

Walker LJ, Summers DW, Sasaki Y, Brace EJ, Milbrandt J, DiAntonio A. MAPK signaling promotes axonal degeneration by speeding the turnover of the axonal maintenance factor *NMNAT2*. *eLife*. 2017;6:e22540. doi: 10.7554/eLife.22540.

Wang X, Fang Y, Liao R, Wang T. Targeted deletion of *Nmnat1* in mouse retina leads to early severe retinal dystrophy. *bioRxiv*. 2017 doi: 10.1101/210757.

Zabka TS, Singh J, Dhawan P, Liederer BM, Oeh J, Kauss MA, Xiao Y, Zak M, Lin T, McCray B, La N, Nguyen T, Beyer J, Farman C, Uppal H, Dragovich PS, O'Brien T, Sampath D, Misner DL. Retinal toxicity, in vivo and in vitro, associated with inhibition of nicotinamide phosphoribosyltransferase. *Toxicological Sciences*. 2015;144:163–172. doi: 10.1093/toxsci/kfu268.

Zhai RG, Cao Y, Hiesinger PR, Zhou Y, Mehta SQ, Schulze KL, Verstreken P, Bellen HJ. *Drosophila* NMNAT maintains neural integrity independent of its NAD synthesis activity. *PLOS Biology*. 2006;4:e416. doi: 10.1371/journal.pbio.0040416.

Zhai RG, Zhang F, Hiesinger PR, Cao Y, Haueter CM, Bellen HJ. NAD synthase NMNAT acts as a chaperone to protect against neurodegeneration. *Nature*. 2008;452:887–891. doi: 10.1038/nature06721.

Zhao L, Chen Y, Bajaj AO, Eblimit A, Xu M, Soens ZT, Wang F, Ge Z, Jung SY, He F, Li Y, Wensel TG, Qin J, Chen R. Integrative subcellular proteomic analysis allows accurate prediction of human disease-causing genes. *Genome Research*. 2016;26:660–669. doi: 10.1101/gr.198911.115.

Zhao ZY, Xie XJ, Li WH, Liu J, Chen Z, Zhang B, Li T, Li SL, Lu JG, Zhang L, Zhang LH, Xu Z, Lee HC, Zhao YJ. A Cell-Permeant mimetic of NMN activates SARM1 to produce cyclic ADP-Ribose and induce Non-apoptotic cell death. *iScience*. 2019;15:452–466. doi: 10.1016/j.isci.2019.05.001.

Zhu Y, Zhang L, Sasaki Y, Milbrandt J, Gidday JM. Protection of mouse retinal ganglion cell axons and soma from glaucomatous and ischemic injury by cytoplasmic overexpression of

Nmnat1. *Investigative Ophthalmology & Visual Science*. 2013;54:25–36. doi: 10.1167/iovs.12-10861.

Zolotukhin S, Potter M, Zolotukhin I, Sakai Y, Loiler S, Fraites TJ, Chiodo VA, Phillipsberg T, Muzyczka N, Hauswirth WW, Flotte TR, Byrne BJ, Snyder RO. Production and purification of serotype 1, 2, and 5 recombinant adeno-associated viral vectors. *Methods*. 2002;28:158–167. doi: 10.1016/s1046-2023(02)00220-7.

2.7 Figures

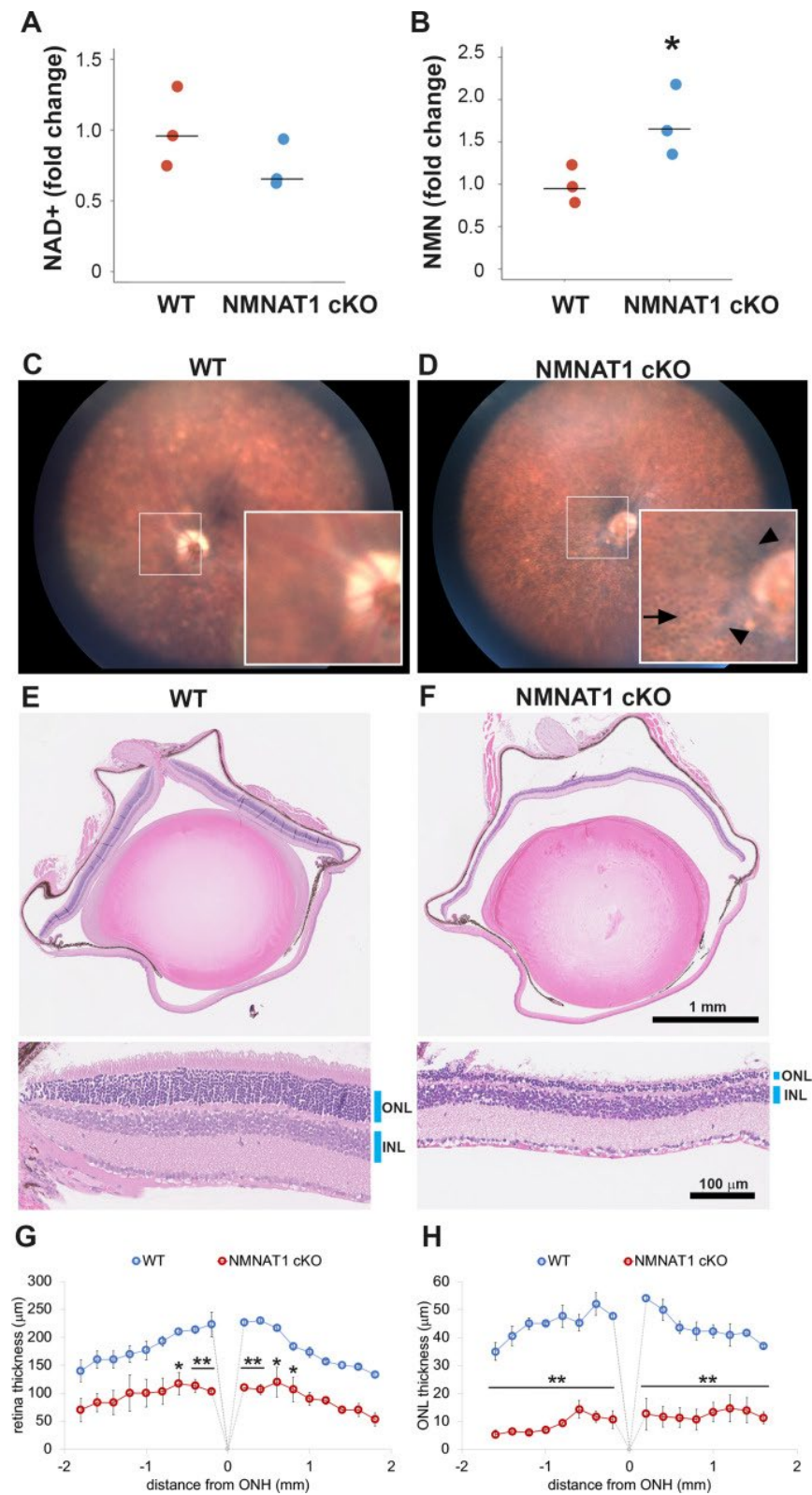


Figure 1. NMNAT1 depletion induces severe retinal degeneration

(A, B) Metabolite analysis by LC-MSMS in retinal tissues from WT or NMNAT1 conditional knockout (Nmnat1fl/fl: CAG-CreERT2 + tamoxifen: NMNAT1 cKO) mice at 25 days post tamoxifen injection. Fold changes of NAD⁺ (A) and NMN (B) concentrations compared with that of WT retinal tissues are shown. *p<0.05 denotes the significant difference from WT with Kruskal-Wallis test (n = 3 mice for WT and n = 3 mice for NMNAT1 cKO). Graphs show the all data points and median (cross bars). (C, D) Fundus biomicroscopy images of the retina from wild type (WT, C) or NMNAT1 conditional knock out (Nmnat1fl/fl: CAG-CreERT2 + tamoxifen: NMNAT1 cKO, D) mice at 4 weeks post tamoxifen injection. (E, F) representative images of hematoxylin and eosin stained eye sections from WT mice (E) or NMNAT1 conditional knockout (Nmnat1fl/fl: CAG-CreERT2 + tamoxifen: NMNAT1 cKO, E) mice at 4 weeks post tamoxifen injection (ONL: outer nuclear layer and INL: inner nuclear layer). The substantial thinning of the ONL was observed in 3 WT and 3 NMNAT1 cKO mice. (G) The quantification of the retina thickness from WT and NMNAT1 conditional knockout (Nmnat1fl/fl: CAG-CreERT2 + tamoxifen: NMNAT1 cKO) mice were shown. Graphs show the average and error bars represent the standard error. Statistical analysis was performed by two-way ANOVA with Tukey post-hoc test (n = 3 mice for WT, n = 3 mice for NMNAT1 cKO (Nmnat1fl/fl: CAG-CreERT2 + tamoxifen at 4 weeks post tamoxifen injection)). F(1, 72)=309, p<1.0×10⁻¹⁶ between WT and NMNAT1 cKO retina. *p<0.05 and **p<0.001 denotes the significant difference compared with WT retina. (H) The quantification of the ONL thickness from WT and NMNAT1 conditional knockout (Nmnat1fl/fl: CAG-CreERT2 + tamoxifen: NMNAT1 cKO) mice were shown. Graphs show the average and error bars represent the standard error. Statistical analysis was performed by two-way ANOVA with Tukey post-hoc test (n = 3 mice for WT and n = 3 mice for NMNAT1 cKO). F(1, 72)=1023, p<1.0×10⁻¹⁶ between WT and NMNAT1 cKO retina. **p<0.001 denotes the significant difference compared WT.

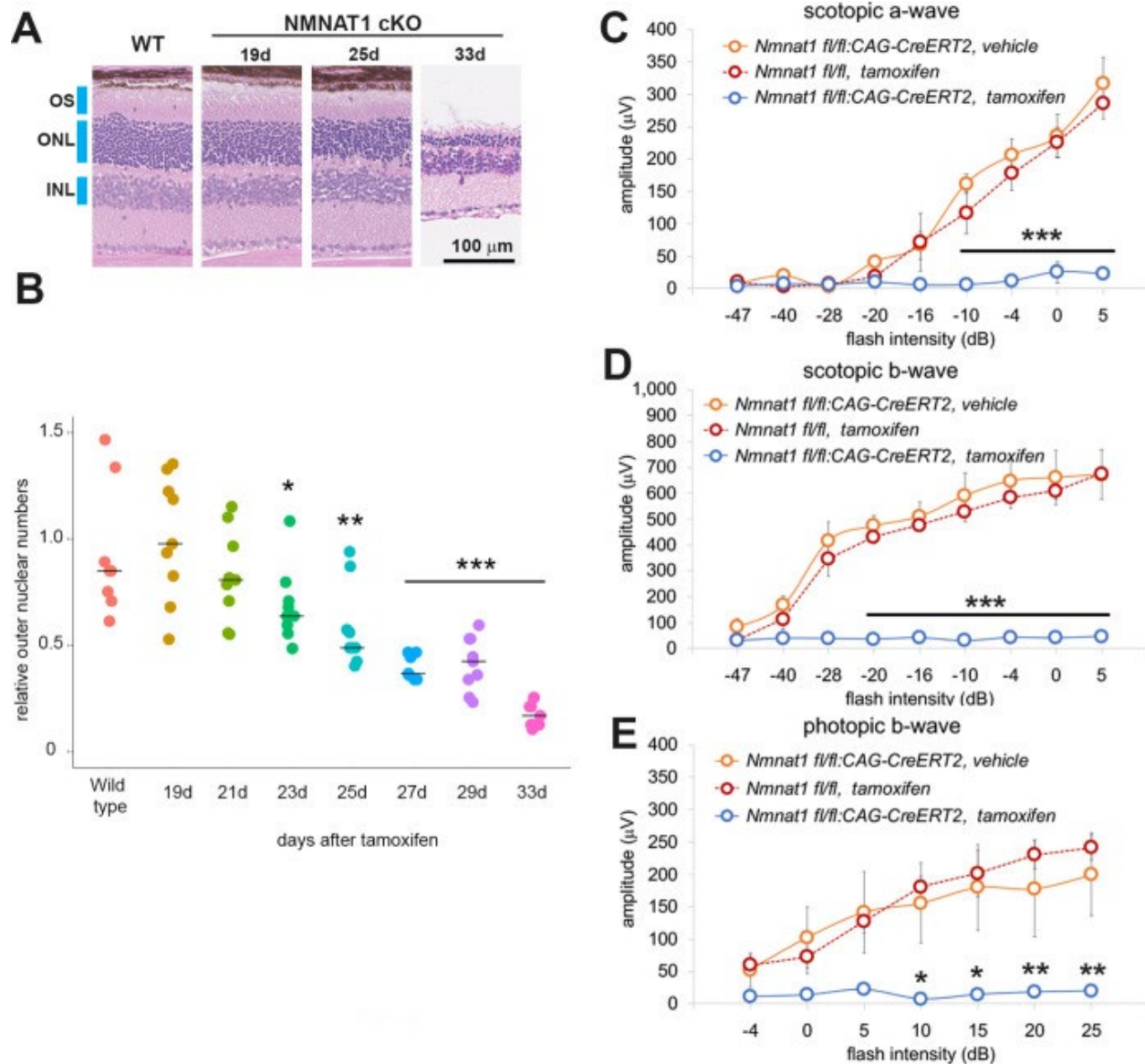


Figure 2. NMNAT1 induces the loss of photoreceptor cells and retinal function

(A) Representative images of hematoxylin and eosin stained sections showing time course of retinal degeneration in NMNAT1 conditional knockout (*Nmnat1* fl/fl; CAG-CreERT2 + tamoxifen: NMNAT1 cKO) mice at 19 to 33 days post tamoxifen injection or littermate wild-type (WT) mice at 33 days post tamoxifen injection (WT). Blue bars indicate outer nuclear layer (ONL), inner nuclear layer (INL), and outer segment (OS). Similar results were obtained from three mice at each time point. (B) Quantification of relative ONL nuclei numbers of NMNAT1 conditional knockout mouse (*Nmnat1* fl/fl; CAG-CreERT2 + tamoxifen: NMNAT1 cKO) compared with WT at various time after tamoxifen injection. The graph shows all data points and median (cross bars). Statistical analysis was performed by one-way ANOVA with Holm-Bonferroni multiple comparison ($n = 3$ mice for each of WT, 19d, 21d, 33d and $n = 4$ mice for each of 25d, 27d). $F(7, 64)=19$, $p=1.9 \times 10^{-13}$. * $p < 0.05$, ** $p < 0.001$, and *** $p < 0.0001$ denotes the significant difference compared with WT. (C, D, E) ERG analysis of controls (*Nmnat1* fl/fl:

CAG-CreERT2 vehicle or Nmnat1fl/fl + tamoxifen) and NMNAT1 conditional knockout (Nmnat1fl/fl: CAG-CreERT2 + tamoxifen: NMNAT1 cKO). Graphs show the average and error bars represent the standard error. Scotopic a-wave (C), scotopic b-wave (D), and photopic b-wave (E) are shown. Statistical analysis was performed by two-way ANOVA with Tukey post-hoc test (n = 3 mice for Nmnat1fl/fl: CAG-CreERT2 with vehicle, n = 3 mice for Nmnat1fl/fl at 33 days post tamoxifen injection, n = 4 mice for Nmnat1fl/fl: CAG-CreERT2 at 33 days post tamoxifen injection). $F(1, 72)=220$, $p<2\times 10^{-16}$ between controls (Nmnat1fl/fl: CAG-CreERT2 with vehicle and Nmnat1fl/fl 33 days post tamoxifen injection) and NMNAT1 cKO for scotopic a-wave, $F(1, 72)=633$, $p<2\times 10^{-16}$ between controls and NMNAT1 cKO for scotopic b-wave, $F(1, 56)=94$, $p=1.3\times 10^{-13}$ between controls and NMNAT1 cKO for photopic b-wave. * $p<0.05$, ** $p<0.001$, and *** $p<0.0001$ denote a significant difference compared with WT.

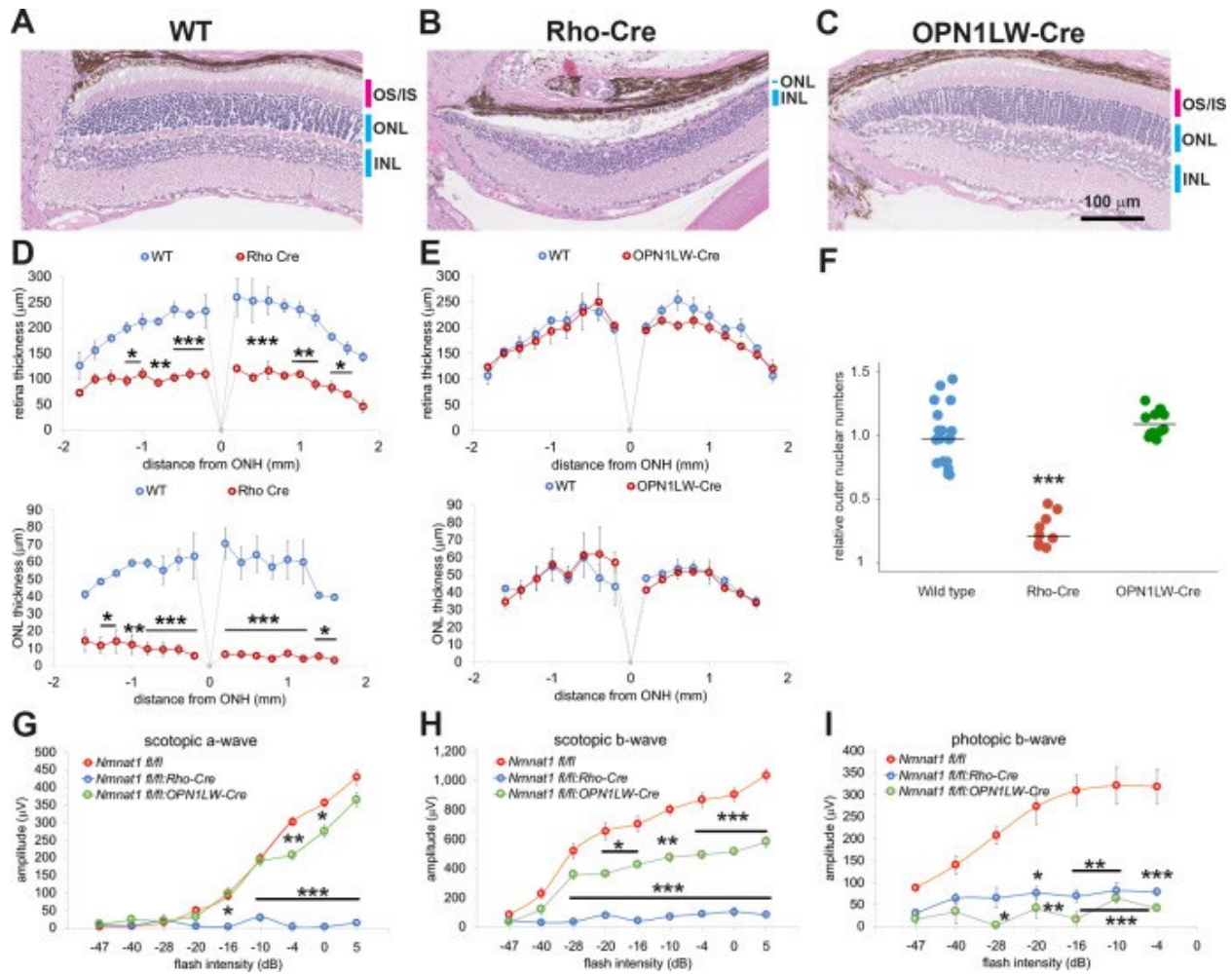


Figure 3. Photoreceptor-specific depletion of NMNAT1 induces retinal degeneration

(A, B, C) Hematoxylin and eosin stained eye sections from 6 week old wild-type (WT, A), rod-specific NMNAT1 KO (*Nmnat1*^{fl/fl};*Rho-Cre*: Rho-Cre, B), or cone-specific NMNAT1 KO (*Nmnat1*^{fl/fl};*OPN1LW-Cre*: OPN1LW-Cre, C) mice. Blue bars indicate outer nuclear layer (ONL) and inner nuclear layer (INL). Red bars indicate the outer segments (OS) and inner segments (IS). Similar results were obtained from three mice for each genotype. (D) Quantification of retina and ONL thickness in WT or rod-specific NMNAT1 KO (Rho-Cre) retinas. The graph shows all data points and median (cross bars). Statistical analysis was performed by two-way ANOVA with Tukey post-hoc test ($n = 3$ mice for WT and $n = 3$ mice for Rho-Cre). $F(1, 72)=428, p<2\times 10^{-16}$ between WT and Rho-Cre retina thickness and $F(1, 64)=530, p<2\times 10^{-16}$ between WT and Rho-Cre ONL thickness. * $p<0.05$, ** $p<0.001$, and *** $p<0.0001$ denote significant differences compared with WT. (E) Quantification of retina and ONL thickness in WT or cone-specific NMNAT1 KO (OPN1LW-Cre) retinas. Graphs show the average and error bars represent the standard error. Statistical analysis was performed by two-way ANOVA with Tukey post-hoc test ($n = 3$ mice for WT and $n = 3$ mice for OPN1LW-Cre). $F(1, 72)=4, p=0.037$ between WT and OPN1LW-Cre retina thickness and $F(1, 64)=0.03, p=0.87$ between WT and OPN1LW-Cre ONL thickness. There are no significant differences in

OPN1LW-Cre retina and ONL thickness compared with WT. (F) Quantification of relative ONL nuclei numbers compared with WT. The graph shows all data points and median (cross bars). Statistical analysis was performed by one-way ANOVA with Holm-Bonferroni multiple comparison (n = 6 mice for WT, n = 3 mice for Rho-Cre, n = 3 mice for OPN1LW-Cre). $F(2, 35)=59$, $p=5.9 \times 10^{-12}$. *** $p < 0.0001$ denotes the significant difference compared WT. (G, H, I) ERG analysis of WT, Rho-Cre, and OPN1LW-Cre mice. Scotopic a-wave (G), scotopic b-wave (H), and photopic b-wave (I) are shown. Graphs show the average and error bars represent the standard error. Statistical analysis was performed by two-way ANOVA with Tukey post-hoc test (n = 6 mice for WT, n = 3 mice for Rho-Cre, n = 3 mice for OPN1LW-Cre). $F(2, 81)=314$, $p < 2.0 \times 10^{-16}$ among genotypes (WT, Rho-Cre, and OPN1LW-Cre) for scotopic a-wave, $F(2, 81)=413$, $p < 2 \times 10^{-16}$ among genotypes for scotopic b-wave, $F(2, 63)=102$, $p < 2 \times 10^{-16}$ among genotypes for photopic b-wave. * $p < 0.05$, ** $p < 0.001$, and *** $p < 0.0001$ denote a significant difference compared with WT.

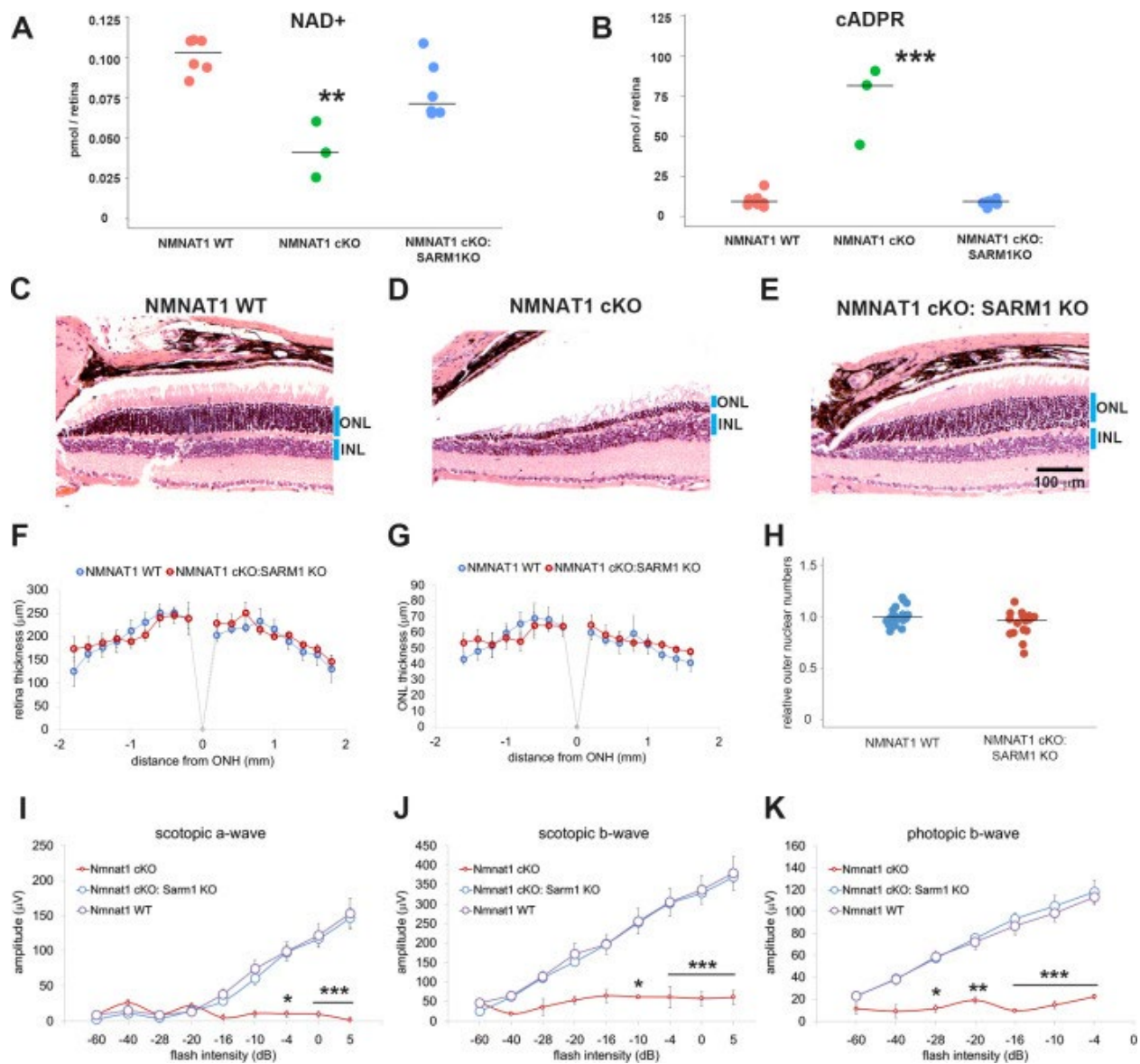


Figure 4. Depletion of SARM1 rescues retinal degeneration in the NMNAT1-deficient retina

(A, B) Metabolite analysis by LC-MSMS in retinal tissues from WT, NMNAT1 conditional knockout (*Nmnat1*^{fl/fl}: CAG-CreERT2 + tamoxifen at 29 to 32 days post tamoxifen injection: NMNAT1 cKO), or NMNAT1 cKO:SARM1 KO mice were shown. Metabolites from whole retina of one eye were analyzed for NAD⁺ (A) and cADPR (B) concentrations and compared with that of WT retinal tissues. Graphs show the all data points and median (cross bars). Statistical analysis was performed by one-way ANOVA with Holm-Bonferroni multiple comparison ($n = 7$ mice for WT, $n = 3$ mice for NMNAT1 cKO, and $n = 6$ mice for NMNAT1 cKO:SARM1 KO). $F(2, 13) = 259$, $p = 3.0 \times 10^{-4}$ for NAD⁺ and $F(2, 13) = 48$, $p = 9.43 \times 10^{-7}$ for cADPR. ** $p < 0.001$ and *** $p < 0.0001$ denote the significant difference compared with WT. (C, D, E) Representative images of hematoxylin and eosin stained eye sections from NMNAT1 WT (*Nmnat1*^{fl/fl}: *Sarm1*^{+/-}, C), NMNAT1 cKO (*Nmnat1*^{fl/fl}: *Sarm1*^{+/-}: CAG-CreERT2 post 32 days tamoxifen injection, D), and NMNAT1 cKO: SARM1 KO (*Nmnat1*^{fl/fl}: *Sarm1*^{-/-}: CAG-

CreERT2 at post 32 days tamoxifen injection, E). Blue bars represent outer nuclear layer (ONL) and inner nuclear layer (INL). Similar results were obtained from three mice for WT, two mice for NMNAT1 cKO, and three mice for NMNAT1cKO:SARM1 KO. (F) The quantification of the retina thickness from NMNAT1 WT and NMNAT1 cKO:SARM1 KO mice were shown. Graphs show the average and error bars represent the standard error. Statistical analysis was performed by two-way ANOVA with Tukey post-hoc test ($n = 3$ mice for NMNAT1 WT, $n = 3$ mice for NMNAT1 cKO:SARM1 dKO). $F(1, 72)=0.8$, $p=0.37$ between NMNAT1 WT and NMNAT1 cKO:SARM1 KO retina. There is no significant difference between NMNAT1 WT and NMNAT1 cKO:SARM1 KO. (G) The quantification of the outer nuclear layer (ONL) thickness from NMNAT1 WT and NMNAT1 cKO:SARM1 KO mice were shown. Graphs show the average and error bars represent the standard error. Statistical analysis was performed by two-way ANOVA with Tukey post-hoc test ($n = 3$ mice for NMNAT1 WT, $n = 3$ mice for NMNAT1 cKO:SARM1 KO). $F(1, 64)=0.43$, $p=0.51$ between NMNAT1 WT and NMNAT1 cKO:SARM1 KO retina. There is no significant difference between NMNAT1 WT and NMNAT1 cKO:SARM1 KO. (H) Quantification of relative ONL nuclei numbers compared with WT. The graph shows all data points and median (cross bars). Statistical analysis was performed by Mann-Whitney U test ($n = 3$ mice for NMNAT1 WT, $n = 3$ mice for NMNAT1 cKO:SARM1 KO). $p=0.10$. There are no statistical differences between NMNAT1 WT and NMNAT1 cKO:SARM1KO. (I, J, K) ERG analysis of NMNAT1 WT (Nmnat1fl/fl: Sarm1+/- or Nmnat1fl/fl: Sarm1-/-), NMNAT1 cKO (Nmnat1fl/fl: CAG-CreERT2 post 29 to 32 days tamoxifen injection), and NMNAT1 cKO: SARM1 KO (Nmnat1fl/fl: SARM1-/-: CAG-CreERT2 post 32 days tamoxifen injection). Graphs show the average and error bars represent the standard error. Statistical analysis was performed by two-way ANOVA with Tukey post-hoc test ($n = 8$ mice for NMNAT1 WT, $n = 3$ mice for NMNAT1 cKO, and $n = 8$ mice for NMNAT1 cKO: SARM1 KO). $F(2, 144)=29$, $p=2.9 \times 10^{-11}$ among genotypes (NMNAT1 WT, NMNAT1 cKO, NMNAT1 cKO:SARM1 KO) for scotopic a-wave, $F(2, 144)=46$, $p < 2.0 \times 10^{-16}$ among genotypes for scotopic b-wave, $F(2, 112)=94$, $p < 2.0 \times 10^{-16}$ among genotypes for photopic b-wave. * $p < 0.05$, ** $p < 0.001$, and *** $p < 0.0001$ denotes the statistical difference between NMNAT1 WT and NMNAT1 cKO or between NMNAT1 cKO:SARM1KO and NMNAT1 cKO. There is no statistical difference between NMNAT1 WT and NMNAT1 cKO: SARM1 KO.

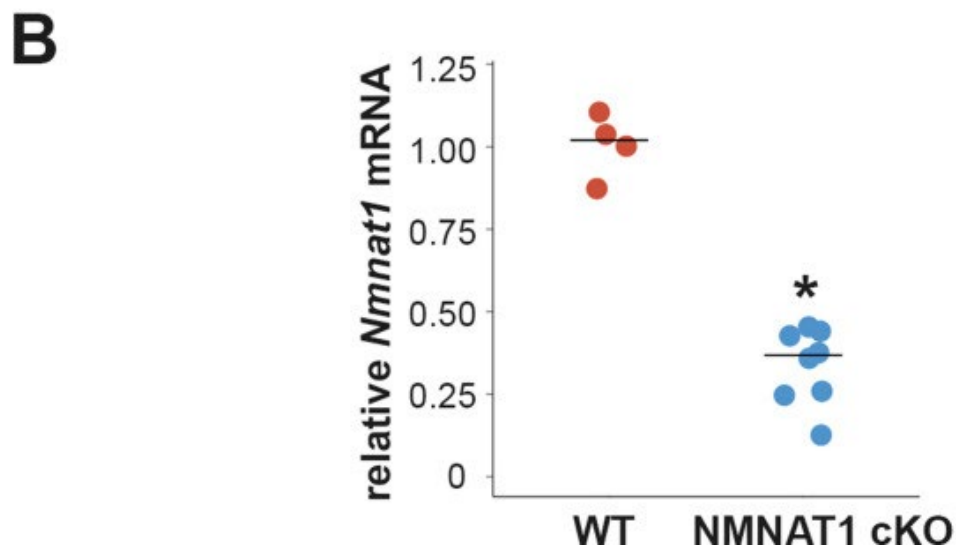
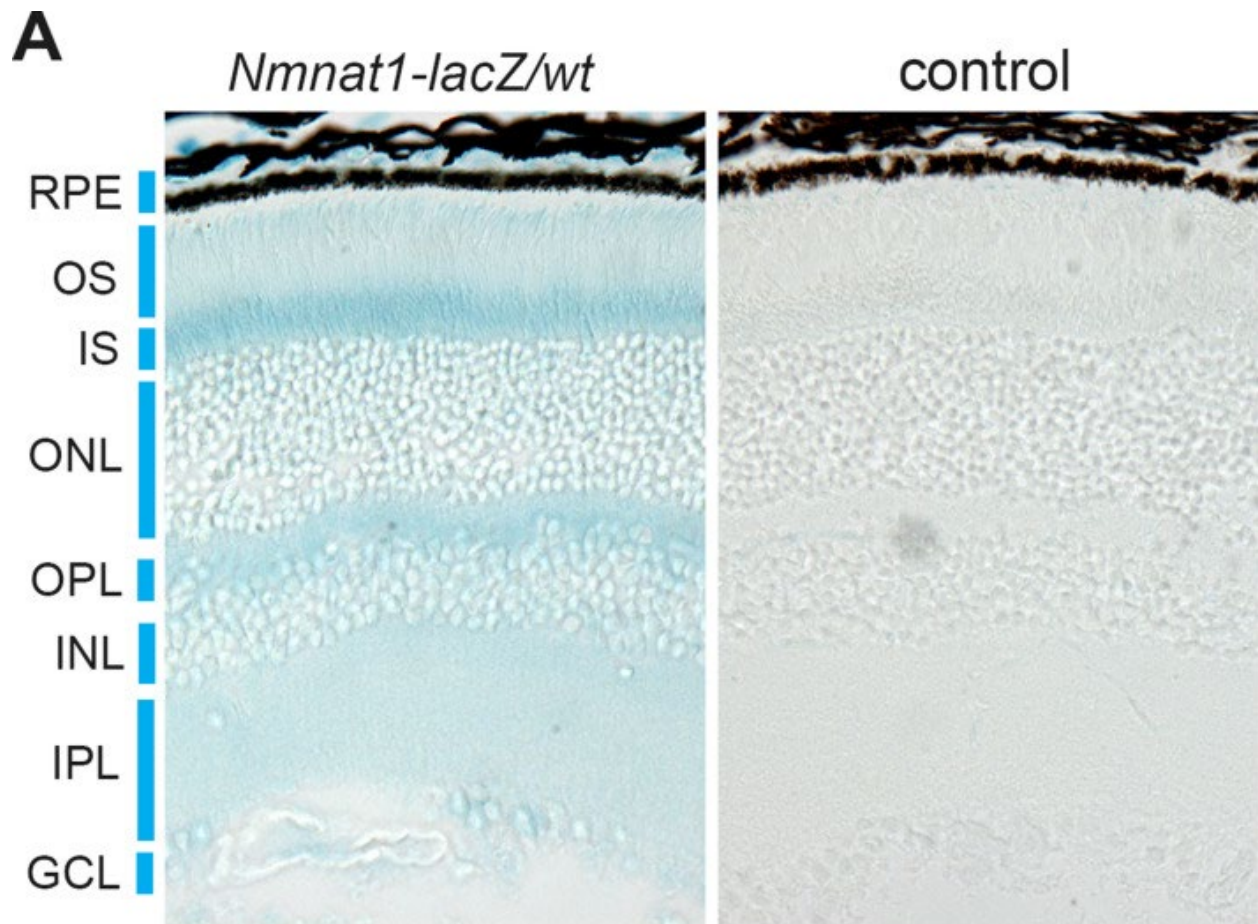


Figure supplement 1. NMNAT1 is ubiquitously expressed in the retina.

(A) X-Gal staining of retinal tissues from mice heterozygous for *Nmnat-lacZ* fusion protein lacking the nuclear localization signal (*Nmnat1-lacZ/wt*) or wild-type (WT) mice (control). (B)

Quantitative RT-PCR analysis of *Nmnat1* mRNA in retinal tissues from WT or *Nmnat1*^{fl/fl}: CAG-CreERT2 mice at 21 days post tamoxifen injection (NMNAT1 cKO) showed significant reduction of *Nmnat1* mRNA compared with WT. * $p < 0.05$ denotes the significant difference from WT with Mann-Whitney U test (n = 4 for WT (two mice) and n = 8 for NMNAT1 cKO (four mice)).

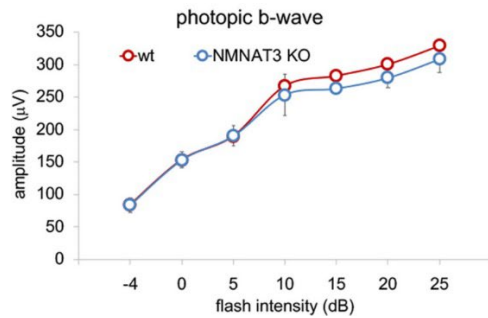
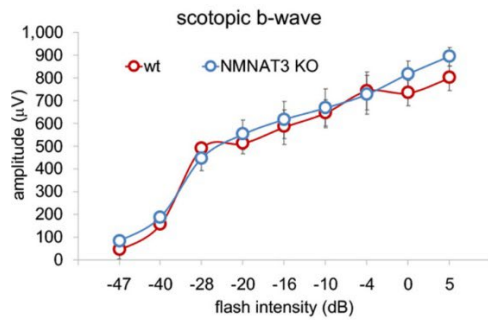
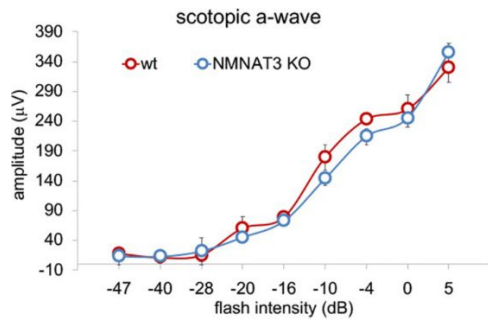


Figure supplement 2. ERG analysis of NMNAT3-deficient retina.

ERG analysis of WT or NMNAT3 knock out mice (NMNAT3 KO). Graphs show the average and error bars represent the standard error. Statistical analysis was performed by one-way ANOVA (n = 3 mice for WT, n = 3 mice for NMNAT3 KO). F (8, 36)=0.78, p=0.623 for scotopic a-wave, F (8, 36)=0.28, p=0.97 for scotopic b-wave, F (6, 28)=0.23, p=0.97 for photopic b-wave and there is no statistical difference between WT and NMNAT3 KO in each flash intensity.

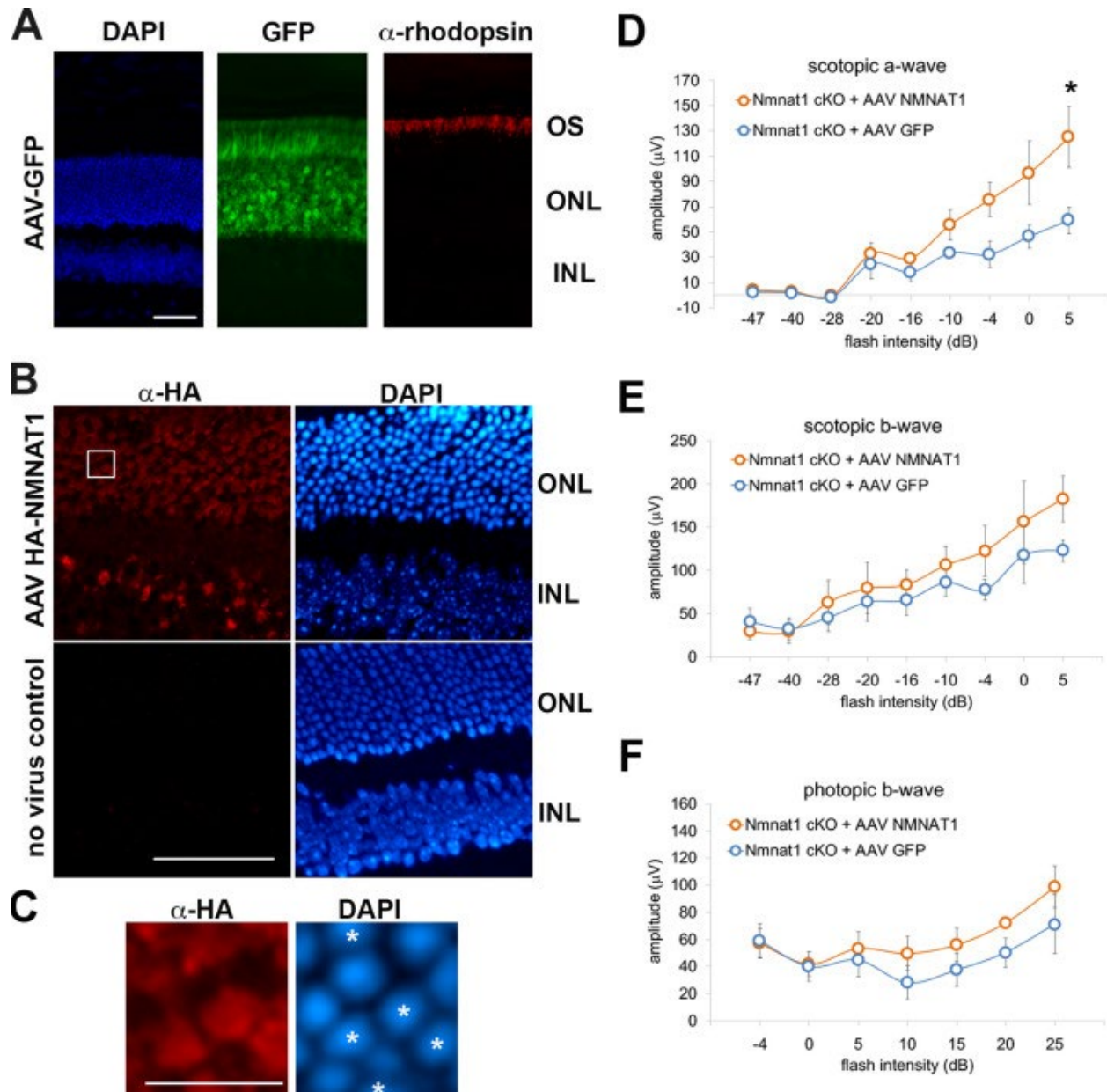


Figure supplement 3. AAV-NMNAT1 partially rescued retinal degeneration in NMNAT1-deficient retinas.

(A) Fluorescent microscope images of the retina after subretinal injection of AAV expressing GFP. The photoreceptor cell layer is identified with immunostaining with antibody against human rhodopsin. Scale bar, 50 μ m. (B) Fluorescent microscope images of the retina after subretinal injection of AAV expressing HA-tagged human NMNAT1. The expression of NMNAT1 is shown by immunohistochemistry with antibody against HA epitope tag and nuclei are visualized with DAPI. Asterisks indicate the cells expressing HA-Nmnat1. Scale bar, 50 μ m. (C) Enlarged images corresponding to the white box in (B), showing the partial expression of NMNAT1 in the cells in the outer nuclear layer. The stars indicate the NMNAT1 expressing cells. Scale bar, 10 μ m. (D, E, F) ERG analysis of AAV-GFP (control) or AAV NMNAT1 (AAV- NMNAT1) administrated NMNAT1 cKO mice. Scotopic a-wave (D), scotopic b-wave

(E), and photopic b-wave amplitudes (F) are shown. Graphs show the average and error bars represent the standard error. Statistical analysis was performed by two-way ANOVA with Tukey post-hoc test (n = 5 for control or AAV- NMNAT1). $F(8, 72)=2.4$, $p=0.022$ between control and AAV-NMNAT1 for scotopic a- wave, $F(8, 72)=0.48$, $p=0.86$ between control and AAV-NMNAT1 for scotopic b- wave, $F(6, 56)=0.39$, $p=0.88$ between controls and AAV-NMNAT1 for photopic b- wave. * $p<0.05$ denotes the statistical difference between WT and AAV-NMNAT1 mice.

**Chapter 3: Myeloid Knockout of Cholesterol Efflux
Transporters, ABCA1 and ABCG1, Results in Rod
Photoreceptor Dysfunction as seen in Dry Age-related
Macular Degeneration**

Adapted from:

Impaired monocyte cholesterol clearance initiates age-related retinal degeneration and vision loss

Ban N, Lee TJ, Sene A, Choudhary M, Lekwuwa M, Dong Z, Santeford A, Lin JB, Malek G, Ory DS, Apte RS. Impaired monocyte cholesterol clearance initiates age-related retinal degeneration and vision loss. JCI insight. 2018;3(17).

3.1 Introduction

Age-related macular degeneration (AMD) is the leading cause of blindness among people over 50 years of age in the industrialized world (1). Early disease is characterized by cholesterol-rich extracellular deposits underneath the retinal pigment epithelium (RPE) called drusen (2-4) or in the sub-retinal space called sub-retinal drusenoid deposits (SDD) (5-7). The composition of these deposits is similar to that of atherosclerotic plaques (3). AMD shares several phenotypic characteristics with atherosclerosis including monocytic inflammation, pathologic angiogenesis and genetic abnormalities in cholesterol homeostasis (4, 8). Although the molecular mechanisms underlying pathological angiogenesis or RPE atrophy in advanced disease are better understood, there is a paucity of animal models that have been able to recapitulate early human disease including anatomic features such as thickening of Bruch's membrane (BrM: an acellular lamina underneath the RPE), drusen or SDD; or functional characteristics such as an association with age, rod photoreceptor dysfunction (9, 10) or impaired dark adaptation (11, 12).

A number of genome wide association studies (GWAS) have linked AMD to polymorphisms in genes involved in many facets of cholesterol homeostasis such as LIPC, ApoE, ABCA1, and CETP (13, 14). In addition, widespread systemic disturbances in cholesterol metabolism as manifested by altered levels of lipoprotein sub-types have also been associated with AMD (15). Despite reports implicating disruptions in cholesterol homeostasis in mouse models and in human AMD pathogenesis, it has not been established whether it is the systemic immune system or local 'eye' cells that regulate cholesterol clearance and the development of the early AMD phenotype. Here we demonstrate that in conditional knockout mice wherein both *Abca1* and *Abcg1* are deleted in macrophages, there is an age-dependent manifestation of several anatomic

and functional AMD disease phenotypes, indicating that cholesterol clearance by macrophages plays a critical role in the early stages of AMD pathogenesis.

Numerous studies have demonstrated that cellular and humoral components of the innate immune system including macrophages, mononuclear phagocytes, and complement proteins contribute to both the development and severity of AMD (16-19). Macrophages not only function as antigen-presenting cells and phagocytic sensors of danger, but are also important in cholesterol regulation by removing cholesterol from peripheral tissues and transporting it back to the liver through the bloodstream. This process is termed cholesterol efflux or reverse cholesterol transport (RCT) (3), and ABCA1 and ABCG1 play crucial roles in macrophage RCT by effluxing cholesterol from cells to extracellular carriers such as ApoA1 and HDL respectively (20). In this study, we generated conditional knockout mice wherein both *Abca1* and *Abcg1* are deleted in macrophages. We evaluated the retinas structurally by biomicroscopy, histology, and electron microscopy at 3-12 months of age. In addition, we evaluated retinal function by electrophysiology.

3.2 Results

3.2.1 Deletion of *Abca1* and *Abcg1* in macrophages does not affect the retina at 3 months of age

We have previously reported that mice selectively deficient in *Abca1* in macrophages (*Abca1*^{fl/fl} LysM-Cre-positive [*Abca1*^{-m/-m}]) demonstrated increased laser-injury induced choroidal neovascularization (CNV), one of the characteristics of advanced AMD (17). However, when we analyzed treatment-naive *Abca1*^{-m/-m} mice retinas up to 24 months of age, we did not detect any functional abnormalities (Supplemental Figure 1, A-F; supplemental material available

online with this article; <https://doi.org/10.1172/jci.insight.120824DS1>) or biomicroscopic defects (Supplemental Figure 1G) compared with littermate controls (*Abca1*fl/fl Cre-negative; *Abca1*F/F) mice. Because *Abca1*-m/-m mice macrophages demonstrated significantly increased *Abcg1* expression (Supplemental Figure 1H), we suspected that ABCG1 might compensate for ABCA1, as both ABCA1 and ABCG1 play crucial roles in macrophage RCT by effluxing cholesterol to extracellular carriers (20). For this reason, and to directly test whether macrophage cholesterol transport regulates the early AMD phenotype, we generated conditional KO mice wherein both *Abca1* and *Abcg1* are deleted in macrophages by crossing *Abca1*fl/fl and *Abcg1*fl/fl mice with *LysM*-Cre mice (17, 21). The deletion of both genes in macrophages of *Abca1*fl/fl and *Abcg1*fl/fl *LysM*-Cre positive (*Abca1/g1*-m/-m) mice was confirmed by quantitative PCR (qPCR) (Supplemental Figure 2A). We also confirmed that these mice did not carry the *Crb1* gene rd8 mutation (22) (data not shown). EM at 3 months of age demonstrated large lipid droplets in *Abca1/g1*-m/-m macrophages but not in macrophages of littermate control (*Abca1*fl/fl and *Abcg1*fl/fl Cre negative; *Abca1/g1*F/F) mice (Supplemental Figure 2B), consistent with decreased cholesterol efflux in *Abca1/g1*-m/-m macrophages and confirming findings from previous studies (17, 23). However, functional analysis at 3 months of age demonstrated that both scotopic and photopic retinal responses (Figure 1, A–C) and dark adaptation curves recorded from *Abca1/g1*-m/-m mice retinas were normal (Figure 1D). In addition, *in vivo* imaging and histological examination of retinal sections of *Abca1/g1*-m/-m mice did not show any substantial differences (Figure 1, E and F). These results suggest that deletion of both ABCA1 and ABCG1 in macrophages does not affect retinal function, vision, or morphology acutely or at a young age.

3.2.2 *Abca1/g1^{-m/-m}* mice demonstrate RPE abnormalities, BrM thickening, and impaired dark adaptation at 6 months of age

In order to simulate the human condition, we aged *Abca1/g1^{-m/-m}* mice and their littermate controls. Upon analysis at 6 months age, we found that scotopic a-waveforms were now slightly attenuated in *Abca1/g1^{-m/-m}* retinas compared with littermate controls, confirming scotopic rod photoreceptor dysfunction (Figure 2, A–C). In addition, 6-month-old *Abca1/g1^{-m/-m}* eyes showed impaired dark adaptation (Figure 2D), consistent with the dysfunction of RPE cells. Notably, this combination of rod photoreceptor dysfunction and impaired dark adaptation is a key feature of early and intermediate AMD (9–12). Ultrastructural histology revealed disrupted RPE structure with accumulation of lipid globules in the eyes of *Abca1/g1^{-m/-m}* mice but not in littermate controls (Figure 2E and Supplemental Figure 3). *Abca1/g1^{-m/-m}* mice RPE also showed increased BrM thickening (Figure 2, F and G), which is another morphological characteristic of human eyes with AMD.

3.2.3 Retinal neurodegeneration of *Abca1/g1^{-m/-m}* mice increases in severity and affects cone photoreceptors at 12 months of age

We next examined whether further aging would recapitulate additional features of human AMD in the mouse eye. At 12 months of age, both scotopic a- and b-waveforms were significantly attenuated in *Abca1/g1^{-m/-m}* retinas compared with littermate controls (Figure 3, A and B), confirming additional rod neurodegeneration. In addition, photopic responses were also significantly attenuated (Figure 3C), suggesting cone photoreceptor dysfunction. Dark adaptation was also further impaired (Figure 3D). Biomicroscopic examination of *Abca1/g1^{-m/-m}* eyes now showed yellowish white lesions scattered throughout the retina (Figure 3E).

3.2.4 Subretinal deposits of *Abca1/g1^{-m/-m}* mice progressively increase in number with age

The yellowish white lesions throughout the retina corresponded to hyperreflective outer retinal focal deposits underneath the neurosensory retina on optical coherence tomography (OCT) imaging (Figure 4A). Quantitative analysis of these SD in *Abca1/g1^{-m/-m}* mice showed progressive increase with age, with a significant number of SD by 12 months of age compared with littermate controls (Figure 4B). EM confirmed that the deposits were subretinal and contained lipid globules, degenerative vacuoles, and cellular debris (Figure 4C). Some SD were associated with infiltration of mononuclear cells (Figure 4C).

3.2.5 Infiltrating cells in the subretinal space are Iba1- or F4/80- positive monocytic cells

To investigate the identity of the cellular component of SD, we performed IHC with a monocyte/microglial marker (Iba1), as well as qPCR of the retina/RPE/choroid complex. The number of Iba1-positive cells in the subretinal space, visualized by IHC, were significantly increased at 12 months of age in *Abca1/g1^{-m/-m}* mice (Figure 5, A and B). Increased Iba1 expression was also confirmed in the retina/RPE/choroid complex of *Abca1/g1^{-m/-m}* mice by qPCR (Figure 5C). IHC with another monocyte/microglial marker (F4/80) also showed increased F4/80-positive cells in the subretinal space (Figure 5, D and E). Increased F4/80 expression was also confirmed in the retina/RPE/choroid complex of *Abca1/g1^{-m/-m}* mice by qPCR (Figure 5F). These results indicate that infiltrating cells in the subretinal space are likely macrophages/microglia. Recent histological analysis of human SDD describes the presence of bloated macrophage clusters in these lesions (7). As such, SD of old *Abca1/g1^{-m/-m}* mice are phenotypically similar to SDD seen in human AMD.

3.2.6 Aged *Abca1/g1^{-m/-m}* mice demonstrate lipid accumulation underneath the retina and within RPE

We further analyzed 12-month-old *Abca1/g1^{-m/-m}* mice for the precise distribution of lipid deposits and for specific composition. Oil Red O (ORO) staining demonstrated focal lipid accumulations within the RPE, as well as in the subretinal space (Figure 6A), consistent with the findings on EM ultrastructural analysis. Analysis of the retina/RPE/choroid complex by liquid chromatography–tandem mass spectrometry (LC-MS/MS) revealed increased free cholesterol and several cholesterol metabolites (3 β ,5 α ,6 β -cholestanetriol [C-triol] and 4 β -hydroxycholesterol [4 β -HC]) (Figure 6B), as well as several cholesterol ester species (Figure 6C). These findings demonstrate that the SD and lipids within RPE are composed of cholesterol and cholesterol esters, as well as cholesterol oxidation products that suggest a highly oxidative environment within the lipid deposits.

3.3 Discussion

Here, we have demonstrated that, in conditional KO mice wherein macrophage cholesterol efflux capacities are disabled (*Abca1/g1^{-m/-m}*), there is an age-dependent manifestation of several early and intermediate anatomic AMD disease phenotypes, including cellular and noncellular SD similar to SDD, increased BrM thickening, and accumulation of free cholesterol, cholesterol metabolites, and cholesteryl esters. In addition, KO mice demonstrate several key features of early functional degradation seen in human AMD, including impaired dark adaptation and rod photoreceptor dysfunction.

Although we generated macrophage-specific conditional KO mice by crossing *Abca1 fl/fl* and *Abcg1 fl/fl* mice with *LysM-Cre* mice, it has been established that *LysM-Cre* promotes

significant deletion not only in macrophages, but also in neutrophils (24). A previous study demonstrated variable deletion of *Abca1* and *Abcg1* in neutrophils (25). Thus, we cannot exclude the possibility that the deletion of *Abca1* and *Abcg1* in neutrophils might also affect the retinal phenotype. However, in addition to the fact that macrophages, but not neutrophils, play crucial roles in RCT from tissues, we demonstrated increased gene expression of macrophage markers *Iba1* and *F4/80*, but not the neutrophil marker *Gr-1*, in the eyes of 12-month-old *Abca1/g1-m/-m* mice (Supplemental Figure 4). For these reasons, we conclude that the retinal phenotypes we observed at 12 months of age are mainly associated with dysfunctional *Abca1*- and *Abcg1*-deficient macrophages, although further study might elucidate this more precisely.

Polymorphisms in genes involved with cholesterol transport and homeostasis are associated with a significantly higher risk of developing AMD (13, 14), thus making these studies translationally relevant by identifying potential targets for therapy. Although there are no previous reports of *ABCG1* polymorphisms associated with increased AMD risk, we found that, in *Abca1-m/-m* mice, *ABCG1* might compensate for the lack of *ABCA1*. As such, we wanted to effectively neutralize the efflux pathway by the deletion of both *Abca1* and *Abcg1* in order to examine its effect on the retinal phenotype with aging.

We are also aware that *ABCA1* polymorphisms associated with AMD risk are HDL elevating (26–30). HDL carrier capacity is not just limited by level but by the size and quality of the particles available at the retinal choroidal interphase. In addition, these findings also suggest that there is a complex interplay between systemic lipid profiles and local lipid profiles in AMD.

Although we are proposing our mouse model as an early-stage AMD model, an important feature of AMD that is lacking in this model is the development of sub-RPE drusen and may represent metabolic differences between the mouse and human retina and RPE. However, although our mouse model (*Abca1/g1-m/-m* mice) does not demonstrate all the features of human disease, age is a key variable here, just as in human AMD that only affects people over the age of 50 years. Thus, these findings suggest that maintenance of cholesterol homeostasis and macrophage-mediated cholesterol efflux may be critical pathways that initiate the development of AMD. These pathways deserve further investigation in order to determine whether pharmacotherapeutic interventions targeting these pathways, either locally or systemically, might prove efficacious in either preventing the development of early AMD or the progression to advanced stages of disease where vision loss is imminent.

3.4 Materials and Methods

Animals.

All mice were housed in a temperature-controlled room under a 12-hour light/dark cycle, with free access to food and water. *Abca1* fl/fl and *Abcg1* fl/fl (*Abca1/g F/F*) mice were previously characterized (23) and were purchased commercially (The Jackson Laboratory). To generate mice lacking both *Abca1* and *Abcg1* specifically from macrophages, we crossed *Abca1/g1F/F* mice with mice carrying 1 copy of the *LysM-Cre* transgene, which were purchased commercially (The Jackson Laboratory) and have been previously characterized (17, 21, 23).

RNA isolation and qPCR.

Total RNA was extracted using RNeasy Micro Plus kit (Qiagen) according to the manufacturer's instructions. To synthesize cDNA, total RNA was added to the High Capacity cDNA Reverse

Transcription Kit (Thermo Fisher Scientific) and reverse-transcribed according to manufacturer's instructions. qPCR was performed in duplicate using the StepOnePlus Real Time PCR system (Thermo Fisher Scientific) using TaqMan Real-Time PCR Assays (Thermo Fisher Scientific), and the mRNA was quantified using the $\Delta\Delta$ CT method with gapdh or bactin as the internal control.

Transmission EM.

We performed transmission EM as previously described (31). Briefly, for ultrastructural analyses, samples were fixed in 2% paraformaldehyde (PFA)/2.5% glutaraldehyde (Polysciences Inc.) in 100 mM sodium cacodylate buffer, pH 7.2, for 2 hours at room temperature and then overnight at 4°C. Samples were washed in sodium cacodylate buffer at room temperature and postfixed in 1% osmium tetroxide (Polysciences Inc.) for 1 hour. Samples were then rinsed extensively in dH₂O prior to en bloc staining with 1% aqueous uranyl acetate (Ted Pella Inc.) for 1 hour. Following several rinses in dH₂O, samples were dehydrated in a graded series of ethanol and embedded in Eponate 12 resin (Ted Pella Inc.). Sections of 95 nm were cut with a Leica Ultracut UCT ultramicrotome (Leica Microsystems Inc.), stained with uranyl acetate and lead citrate, and viewed on a JEOL 1200 EX transmission electron microscope (JEOL USA Inc.) equipped with an AMT 8 megapixel digital camera and AMT Image Capture Engine V602 software (Advanced Microscopy Techniques).

To measure BrM thickness, we used 25,000× EM pictures. We set 5 measurement points that were arranged at equal 500-nm intervals and measured BrM thickness using Adobe Photoshop CS 5.1 (Adobe). We took averages of each picture as representative BrM thickness.

Electroretinography (ERG).

ERG was performed as previously described (32). Briefly, A UTAS BigShot System (LKC Technologies Inc.) was used. Mice were dark adapted overnight. Under red light illumination, mice were anesthetized with an i.p. injection of 86.9 mg/kg ketamine and 13.4 mg/kg xylazine. Pupils were dilated with 1% atropine sulfate eye drops (Bausch & Lomb). Body temperature was maintained at 37°C with a heating pad. Contact lens electrodes were placed bilaterally with appropriate reference and ground electrodes. The stimulus consisted of a full-field white light flash (10 μ s) in darkness or in the presence of dim (30.0 candela [cd]/m²) background illumination after 10-minute adaptation time. Raw data were processed using MATLAB software (MathWorks). The amplitude of the a-wave was measured from the average pretrial baseline to the most negative point of the average trace, and the b-wave amplitude was measured from that point to the highest positive point.

For testing dark adaptation, we modified the protocol as previously described (33). Briefly, we used a UTAS BigShot System (LKC Technologies Inc.) to get scotopic a-waves. A bright LED light (150,000 lux) was applied to both eyes for 15 seconds to photobleach an estimated 90% of the visual pigment. The recovery of the ERG responses was monitored at fixed post-bleach time points within 100 minutes after the bleach. The sensitivity was calculated as the ratio of dim flash response amplitude and the corresponding flash intensity in the linear range of the intensity-response curve. The post-bleach sensitivities were normalized to their dark-adapted prebleach level.

Retinal imaging.

We performed digital color fundus photography and OCT as previously described (21) using the Micron III animal fundus camera equipped with 830 nm OCT (Phoenix Research Labs). Prior to fundus imaging and OCT, we anesthetized mice with an i.p. injection of 86.9 mg/kg ketamine

and 13.4 mg/kg xylazine and administered 1.0% tropicamide eye drops (Bausch & Lomb) to dilate the pupils.

Cryopreservation.

Enucleated posterior poles were fixed in 4% PFA followed by cryopreservation in Tissue-Tek OCT compound (Sakura Finetek). Cryosections (10- μ m thick) were cut and collected on gelatin-coated slides and stored at -20°C until use.

ORO staining.

ORO (0.7%, MilliporeSigma) staining solution was prepared in 100% propylene glycol (MilliporeSigma) by heating the solution to 90°C . The staining protocol was as follows. Slides were rinsed with water and placed in 100% propylene glycol for 5 minutes, followed by staining overnight in preheated (60°C) ORO solution. Slides were next differentiated in 85% propylene glycol for 1 minute at room temperature, followed by 2 rinses in water. Slides were dried at room temperature, mounted in Aqua-Poly/Mount (Polysciences Inc.), and imaged using a ZEISS Axionplan 2 light microscope.

IHC.

Retinal cryosections were incubated with a blocking solution of 10% normal goat serum (NGS) in PBTA (PBS, 0.5% BSA, 0.1% Triton, 0.05% Sodium Azide) for 2 hours at room temperature. After the blocking, sections were probed with either anti-Iba1 (Wako, catalog 019-19741; 1:200 in 10% NGS-PBTA) or anti-F4/80 antibodies (Bio-Rad, catalog MCA497GA; 1:500 in 10% NGS-PBTA) overnight at 4°C . The next day, anti-Iba1 sections were incubated in goat anti-rabbit-568 (Thermo Fisher Scientific, catalog A11011; 1:200 in 5% NGS-PBTA) and anti-F4/80 sections were incubated in goat anti-rat-568 (Thermo Fisher Scientific, catalog A11077; 1:200 in

5% NGS-PBTA), both for 2 hours at room temperature. Nuclei were counterstained with DAPI (MilliporeSigma). All sections were examined under a confocal microscope equipped with a digital camera (C2si confocal microscope, Nikon Corporation). To count Iba1- or F4/80-positive cells in the subretinal space, 3 slides per animal were stained with Iba1 and F4/80, and 3 equidistant fields of view were identified in the nasal, central, and temporal regions, per slide. The number of staining positive cells were counted in each field of view and their mean was taken (n). The n values from 3 slide were averaged as cell counts/field in the subretinal space.

Analyses of oxysterols, free cholesterol, and cholesterol esters in retina/RPE/choroid complex. Each retina/RPE/choroid complex was homogenized with 50-fold excess volume of PBS buffer using Omni Bead Ruptor 24 (Omni International Inc.). All analytes listed above in 50 μ l of the mouse retina homogenate were extracted with 200 μ l of methanol. Prior to the extraction, triol-d7 (2 ng), 7-ketocholesterol-d7 (2 ng), 24-hydroxycholesterol-d7 (24-HC-d7; 2 ng), 27-HC-d5 (2 ng), 4 β -HC-d7 (2 ng), cholesterol esters (18:2)-d7 (CE[18:2]-d7;200 ng), and cholesterol-d7 (1 μ g) were added as the internal standards to the homogenate samples. All oxysterols and cholesterol, as well as their deuterated standards, were derivatized with N,N-dimethylglycine (DMG) to increase the MS sensitivity. Cholesterol esters were not derivatized for the MS analyses.

Oxysterol analysis was performed with a Shimadzu 20AD HPLC system and a Shimadzu SIL 20AC autosampler coupled to a triple quadrupole mass spectrometer (API-6500Qtrap+, Thermo Fisher Scientific) operated in multiple reaction monitoring (MRM) mode. The positive ion electrospray ionization (ESI) mode was used for detection of the DMG derivatized oxysterols. All samples were injected in duplicate for data averaging. Data processing was conducted with Analyst 1.6.3 (Thermo Fisher Scientific).

The analysis of free cholesterol and 2 CEs (CE[16:0] and CE[18:0]) was performed with a Shimadzu 20AD HPLC system: a LeapPAL autosampler coupled to a triple quadrupole mass spectrometer (API 4000) operated with positive ion MRM mode. The data processing was conducted with Analyst 1.5.1 (Thermo Fisher Scientific).

The analysis of the rest of the CEs (CE[16:2], CE[18:1], CE[18:2], and CE[20:4]) was performed with a Shimadzu 10AD HPLC system and a Shimadzu SIL 20AC autosampler coupled to a triple quadrupole mass spectrometer (TSQ Quantum Ultra) operated in MRM mode. The data processing was conducted with XCalibur.

The relative quantification data is reported as peak area ratios of analytes to their internal standards normalized to wet weights (mg) of retina/RPE/choroid complex.

Statistics.

We performed statistical testing with GraphPad Prism (Version 6.0), using the appropriate test for each dataset (2-way ANOVA, 2-way ANOVA with post hoc Bonferroni's multiple comparison test, 2-tailed unpaired t test, or 2-tailed Mann-Whitney U test). We defined statistical significance as a $P < 0.05$. Values are mean \pm SEM.

Study approval.

All animal experiments were reviewed and approved by the IACUC of Washington University in St. Louis and performed in accordance with the Washington University School of Medicine Animal Care and Use guidelines.

3.5 Acknowledgments

We thank Wandy L. Beatty for EM analyses. This work was supported by NIH grants R01 EY019287 (RSA), P30 EY02687 (Vision Core Grant), R01 EY027802 (GM), P30 EY005722 (to the Duke Eye Center); the International Retinal Research Foundation (NB); the Starr Foundation (RSA); the Carl Marshall Reeves and Mildred Almen Reeves Foundation (RSA); the Bill and Emily Kuzma Family Gift for retinal research (RSA); a Physician-Scientist Award and a Nelson Trust Award from Research to Prevent Blindness (RSA); the Jeffrey Fort Innovation Fund (RSA); and the Thome Foundation (RSA). Additional funding came from unrestricted grants to the Department of Ophthalmology and Visual Sciences of Washington University School of Medicine and to the Duke Eye Center, from Research to Prevent Blindness. JBL was supported by the Washington University in St. Louis Medical Scientist Training Program (NIH grant T32 GM07200) and the Washington University in St. Louis Institute of Clinical and Translational Sciences (NIH grants UL1 TR002345, TL1 TR002344). Lipidomics was performed in the Washington University Metabolomics Facility supported by NIH grant P30 DK020579.

3.6 References

1. Friedman, D.S., O'Colmain, B.J., Munoz, B., Tomany, S.C., McCarty, C., de Jong, P.T., Nemesure, B., Mitchell, P., Kempen, J., and Eye Diseases Prevalence Research, G. 2004. Prevalence of age-related macular degeneration in the United States. *Arch Ophthalmol* 122:564-572.
2. Khan, K.N., Mahroo, O.A., Khan, R.S., Mohamed, M.D., McKibbin, M., Bird, A., Michaelides, M., Tufail, A., and Moore, A.T. 2016. Differentiating drusen: Drusen and drusen-

like appearances associated with ageing, age-related macular degeneration, inherited eye disease and other pathological processes. *Prog Retin Eye Res* 53:70-106.

3. Sene, A., and Apte, R.S. 2014. Eyeballing cholesterol efflux and macrophage function in disease pathogenesis. *Trends Endocrinol Metab* 25:107-114.
4. Sene, A., Chin-Yee, D., and Apte, R.S. 2015. Seeing through VEGF: innate and adaptive immunity in pathological angiogenesis in the eye. *Trends Mol Med* 21:43-51.
5. Zweifel, S.A., Spaide, R.F., Curcio, C.A., Malek, G., and Imamura, Y. 2010. Reticular pseudodrusen are subretinal drusenoid deposits. *Ophthalmology* 117:303-312 e301.
6. Curcio, C.A., Messinger, J.D., Sloan, K.R., McGwin, G., Medeiros, N.E., and Spaide, R.F. 2013. Subretinal drusenoid deposits in non-neovascular age-related macular degeneration: morphology, prevalence, topography, and biogenesis model. *Retina* 33:265-276.
7. Greferath, U., Guymer, R.H., Vessey, K.A., Brassington, K., and Fletcher, E.L. 2016. Correlation of Histologic Features with In Vivo Imaging of Reticular Pseudodrusen. *Ophthalmology* 123:1320-1331.
8. Reyes, N.J., O'Koren, E.G., and Saban, D.R. 2017. New insights into mononuclear phagocyte biology from the visual system. *Nat Rev Immunol* 17:322-332.
9. Owsley, C., Jackson, G.R., Cideciyan, A.V., Huang, Y., Fine, S.L., Ho, A.C., Maguire, M.G., Lolley, V., and Jacobson, S.G. 2000. Psychophysical evidence for rod vulnerability in age-related macular degeneration. *Invest Ophthalmol Vis Sci* 41:267-273.
10. Curcio, C.A. 2001. Photoreceptor topography in ageing and age-related maculopathy. *Eye (Lond)* 15:376-383.

11. Haimovici, R., Owens, S.L., Fitzke, F.W., and Bird, A.C. 2002. Dark adaptation in age-related macular degeneration: relationship to the fellow eye. *Graefes Arch Clin Exp Ophthalmol* 240:90-95.
12. Owsley, C., Clark, M.E., and McGwin, G., Jr. 2017. Natural History of Rod-Mediated Dark Adaptation over 2 Years in Intermediate Age-Related Macular Degeneration. *Transl Vis Sci Technol* 6:15.
13. Neale, B.M., Fagerness, J., Reynolds, R., Sobrin, L., Parker, M., Raychaudhuri, S., Tan, P.L., Oh, E.C., Merriam, J.E., Souied, E., et al. 2010. Genome-wide association study of advanced age-related macular degeneration identifies a role of the hepatic lipase gene (LIPC). *Proc Natl Acad Sci U S A* 107:7395-7400.
14. Chen, W., Stambolian, D., Edwards, A.O., Branham, K.E., Othman, M., Jakobsdottir, J., Tosakulwong, N., Pericak-Vance, M.A., Campochiaro, P.A., Klein, M.L., et al. 2010. Genetic variants near TIMP3 and high-density lipoprotein-associated loci influence susceptibility to age-related macular degeneration. *Proc Natl Acad Sci U S A* 107:7401-7406.
15. Cheung, C.M.G., Gan, A., Fan, Q., Chee, M.L., Apte, R.S., Khor, C.C., Yeo, I., Mathur, R., Cheng, C.Y., Wong, T.Y., et al. 2017. Plasma lipoprotein subfraction concentrations are associated with lipid metabolism and age-related macular degeneration. *J Lipid Res* 58:1785-1796.
16. Calippe, B., Augustin, S., Beguier, F., Charles-Messance, H., Poupel, L., Conart, J.B., Hu, S.J., Lavalette, S., Fauvet, A., Rayes, J., et al. 2017. Complement Factor H Inhibits CD47-Mediated Resolution of Inflammation. *Immunity* 46:261-272.

17. Sene, A., Khan, A.A., Cox, D., Nakamura, R.E., Santeford, A., Kim, B.M., Sidhu, R., Onken, M.D., Harbour, J.W., Hagbi-Levi, S., et al. 2013. Impaired cholesterol efflux in senescent macrophages promotes age-related macular degeneration. *Cell Metab* 17:549-561.
18. Espinosa-Heidmann, D.G., Suner, I.J., Hernandez, E.P., Monroy, D., Csaky, K.G., and Cousins, S.W. 2003. Macrophage depletion diminishes lesion size and severity in experimental choroidal neovascularization. *Invest Ophthalmol Vis Sci* 44:3586-3592.
19. Edwards, A.O., Ritter, R., 3rd, Abel, K.J., Manning, A., Panhuysen, C., and Farrer, L.A. 2005. Complement factor H polymorphism and age-related macular degeneration. *Science* 308:421-424.
20. Wang, X., Collins, H.L., Ranalletta, M., Fuki, I.V., Billheimer, J.T., Rothblat, G.H., Tall, A.R., and Rader, D.J. 2007. Macrophage ABCA1 and ABCG1, but not SR-BI, promote macrophage reverse cholesterol transport in vivo. *J Clin Invest* 117:2216-2224.
21. Santeford, A., Wiley, L.A., Park, S., Bamba, S., Nakamura, R., Gdoura, A., Ferguson, T.A., Rao, P.K., Guan, J.L., Saitoh, T., et al. 2016. Impaired autophagy in macrophages promotes inflammatory eye disease. *Autophagy* 12:1876-1885.
22. Mattapallil, M.J., Wawrousek, E.F., Chan, C.C., Zhao, H., Roychoudhury, J., Ferguson, T.A., and Caspi, R.R. 2012. The Rd8 mutation of the *Crb1* gene is present in vendor lines of C57BL/6N mice and embryonic stem cells, and confounds ocular induced mutant phenotypes. *Invest Ophthalmol Vis Sci* 53:2921-2927.
23. Westerterp, M., Murphy, A.J., Wang, M., Pagler, T.A., Vengrenyuk, Y., Kappus, M.S., Gorman, D.J., Nagareddy, P.R., Zhu, X., Abramowicz, S., et al. 2013. Deficiency of ATP-

binding cassette transporters A1 and G1 in macrophages increases inflammation and accelerates atherosclerosis in mice. *Circ Res* 112:1456-1465.

24. Clausen, B. E., Burkhardt, C., Reith, W., Renkawitz, R., and Förster, I. 1999. Conditional Gene Targeting in Macrophages and Granulocytes Using LysMcre Mice. *Transgenic Research* 8, no. 4 (August 1, 1999): 265–77.

25. Abram, C.L., Roberge, G.L., Hu, Y., and Lowell, C.A. 2014. Comparative analysis of the efficiency and specificity of myeloid-Cre deleting strains using ROSA-EYFP reporter mice. *J Immunol Methods* 408:89-100.

26. Klein, R., Klein, B.E., and Franke, T. 1993. The relationship of cardiovascular disease and its risk factors to age-related maculopathy. The Beaver Dam Eye Study. *Ophthalmology* 100:406-414.

27. Klein, R., Klein, B.E., and Jensen, S.C. 1997. The relation of cardiovascular disease and its risk factors to the 5-year incidence of age-related maculopathy: the Beaver Dam Eye Study. *Ophthalmology* 104:1804-1812.

28. Delcourt, C., Michel, F., Colvez, A., Lacroux, A., Delage, M., and Vernet, M.H. 2001. Associations of cardiovascular disease and its risk factors with age-related macular degeneration: the POLA study. *Ophthalmic Epidemiol* 8:237-249.

29. Klein, R., Klein, B.E., Tomany, S.C., and Cruickshanks, K.J. 2003. The association of cardiovascular disease with the long-term incidence of age-related maculopathy: the Beaver Dam Eye Study. *Ophthalmology* 110:1273-1280.

30. Paun, C.C., Ersoy, L., Schick, T., Groenewoud, J.M., Lechanteur, Y.T., Fauser, S., Hoyng, C.B., de Jong, E.K., and den Hollander, A.I. 2015. Genetic Variants and Systemic Complement Activation Levels Are Associated With Serum Lipoprotein Levels in Age-Related Macular Degeneration. *Invest Ophthalmol Vis Sci* 56:7766-7773.
31. Lin JB, et al. NAMPT-Mediated NAD(+) Biosynthesis Is Essential for Vision In Mice. *Cell Rep.* 2016;17(1):69–85. doi: 10.1016/j.celrep.2016.08.073.
32. Rajagopal R, Bligard GW, Zhang S, Yin L, Lukasiewicz P, Semenkovich CF. Functional Deficits Precede Structural Lesions in Mice With High-Fat Diet-Induced Diabetic Retinopathy. *Diabetes.* 2016;65(4):1072–1084. doi: 10.2337/db15-1255.
33. Xue Y, Shen SQ, Corbo JC, Kefalov VJ. Circadian and light-driven regulation of rod dark adaptation. *Sci Rep.* 2015;5:17616.

3.7 Figures

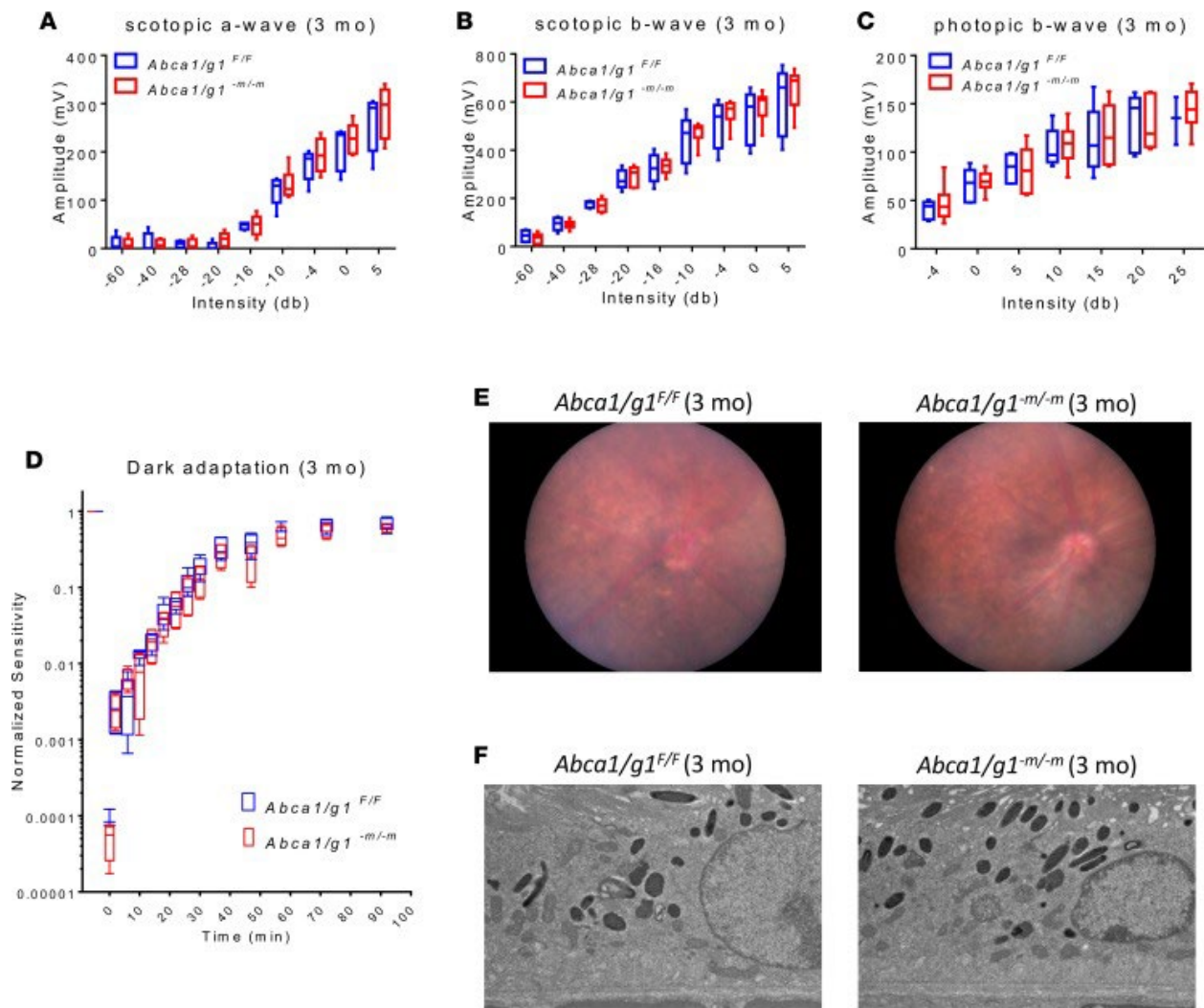


Figure 1. Three-month-old *Abca1/g1^{-m/-m}* retinas do not show functional deficits or morphological abnormalities in the retina and RPE.

(A–C) Electretinography (ERG) of 3-month-old *Abca1/g1^{F/F}* (n = 5) and *Abca1/g1^{-m/-m}* mice (n = 6). (A) Scotopic a-wave amplitude. (B) Scotopic b-wave amplitude. (C) Photopic b-wave amplitude. No significant difference was detected by 2-way ANOVA. (D) Dark adaptation curves of 3-month-old *Abca1/g1^{F/F}* (n = 5) and *Abca1/g1^{-m/-m}* mice (n = 4). No significant difference was detected by 2-way ANOVA. (E) Representative fundus images of 3-month-old *Abca1/g1^{F/F}* and *Abca1/g1^{-m/-m}* mice. (F) Representative electron microscopy images of 3-month-old *Abca1/g1^{F/F}* and *Abca1/g1^{-m/-m}* mice retinal pigmented epithelium (RPE). Scale bar: 1 μ m. Values are mean \pm SEM.

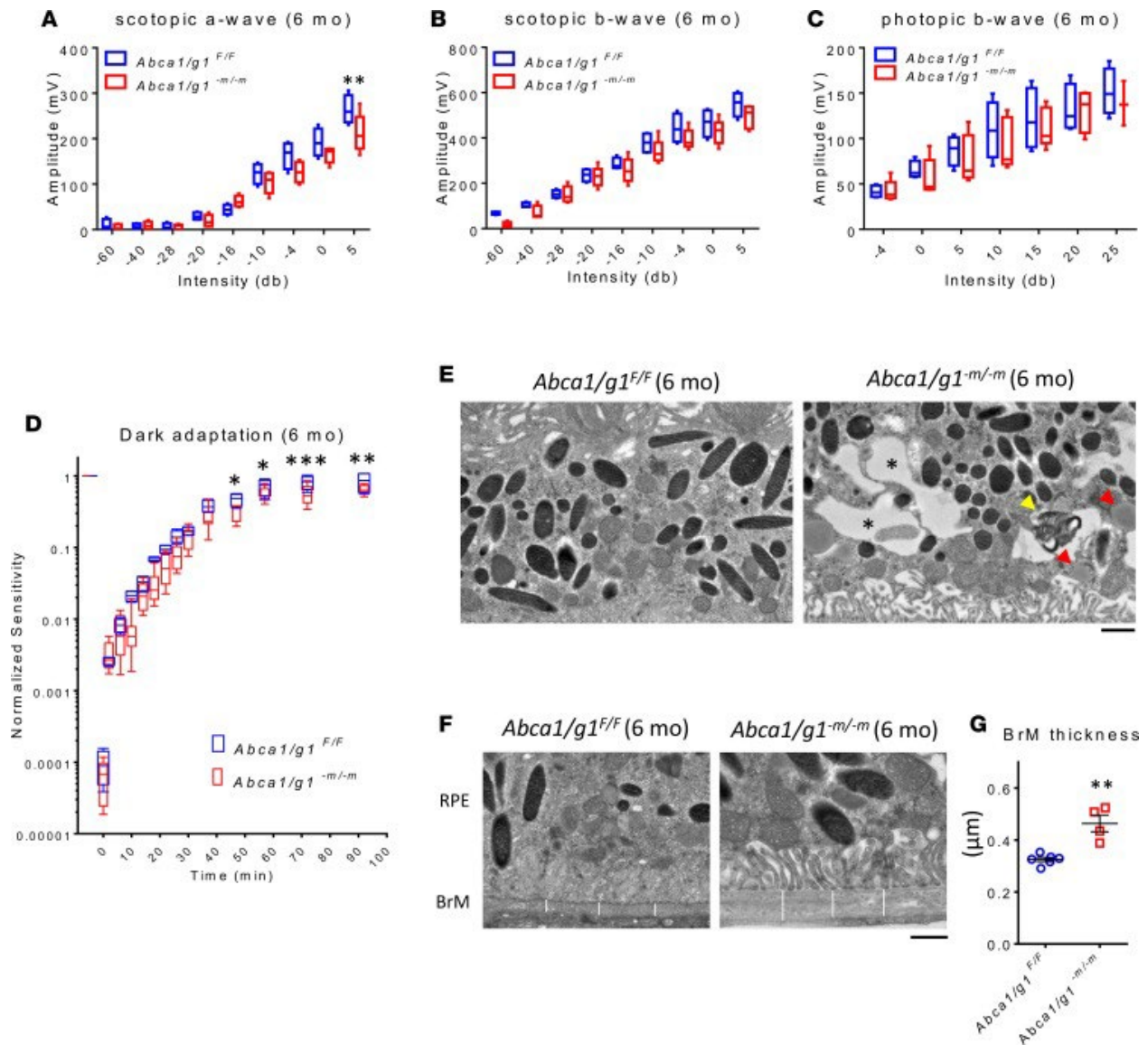


Figure 2. Six-month-old *Abca1/g1^{-m/-m}* retinas demonstrate decreased scotopic responses and impaired dark adaptation associated with disrupted RPE morphology and Bruch's membrane thickening.

(A–C) ERG of 6-month-old *Abca1/g1^{F/F}* ($n = 4$) and *Abca1/g1^{-m/-m}* mice ($n = 5$). (A) Scotopic a-wave amplitude. (B) Scotopic b-wave amplitude. (C) Photopic b-wave amplitude. $**P < 0.01$ by 2-way ANOVA with post hoc Bonferroni's multiple comparison test. (D) Dark adaptation curves of 6-month-old *Abca1/g1^{F/F}* ($n = 4$) and *Abca1/g1^{-m/-m}* mice ($n = 8$). $*P < 0.05$, $**P < 0.01$, and $***P < 0.001$ by 2-way ANOVA with post hoc Bonferroni's multiple comparison test. (E and F) Representative electron microscopy images of 6-month-old *Abca1/g1^{F/F}* and *Abca1/g1^{-m/-m}* mice retinal pigmented epithelium (RPE). (E) Illustration of dysmorphic changes in 6-month-old *Abca1/g1^{F/F}* and *Abca1/g1^{-m/-m}* mice RPE. Note the vacuoles (asterisks), photoreceptor disk fragments (yellow arrowhead), and lipid droplets (red arrowheads) in *Abca1/g1^{-m/-m}* mice RPE. Scale bar: 1 μm . (F) Thickness change of 6-month-

old Abca1/g1F/F (n = 6) and Abca1/g1-m/-m (n = 4) mice Bruch's membrane (BrM). Note the white bars, which represent BrM thickness. Scale bar: 1 μ m. (G) Quantification of BrM thickness. **P < 0.01 by 2-tailed unpaired t test. Values are mean \pm SEM.

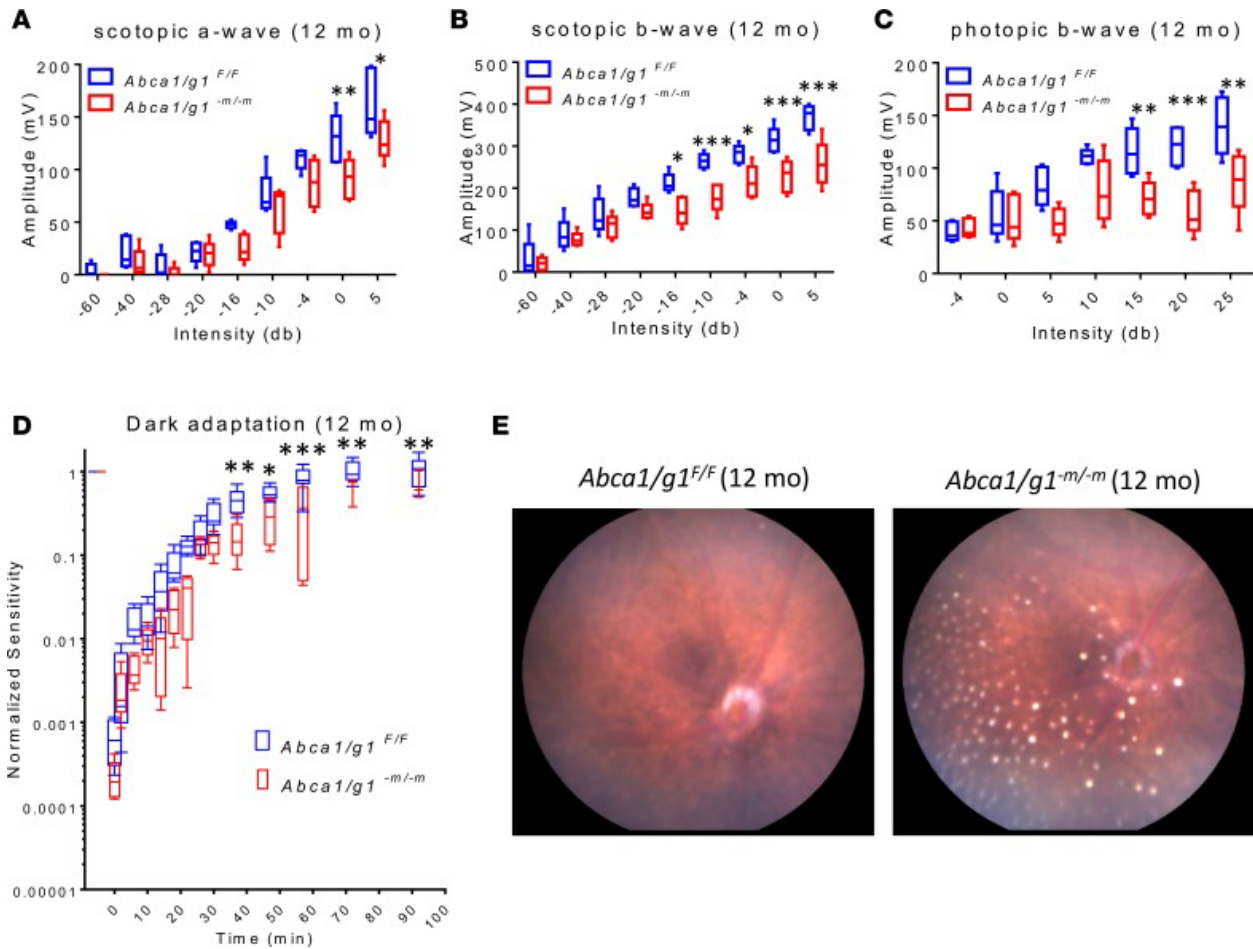


Figure 3. Neurodegeneration of aged *Abca1/g1*^{-m/-m} (12-month-old) retinas increases in severity and extends to photopic dysfunction with significant subretinal deposits.

(A–C) Electroretinography (ERG) of 12-month-old *Abca1/g1*^{F/F} ($n = 5$) and *Abca1/g1*^{-m/-m} mice ($n = 5$). (A) Scotopic a-wave amplitude. (B) Scotopic b-wave amplitude. (C) Photopic b-wave amplitude. * $P < 0.05$, ** $P < 0.01$, and *** $P < 0.001$ by 2-way ANOVA with post hoc Bonferroni's multiple comparison test. (D) Dark adaptation curves of 12-month-old *Abca1/g1*^{F/F} ($n = 8$) and *Abca1/g1*^{-m/-m} ($n = 5$). * $P < 0.05$, ** $P < 0.01$, and *** $P < 0.001$ by 2-way ANOVA with post hoc Bonferroni's multiple comparison test. (E) Representative fundus images of 12-month-old *Abca1/g1*^{F/F} and *Abca1/g1*^{-m/-m} mice retinas. Note the white yellowish dots of *Abca1/g1*^{-m/-m} mice retinas.

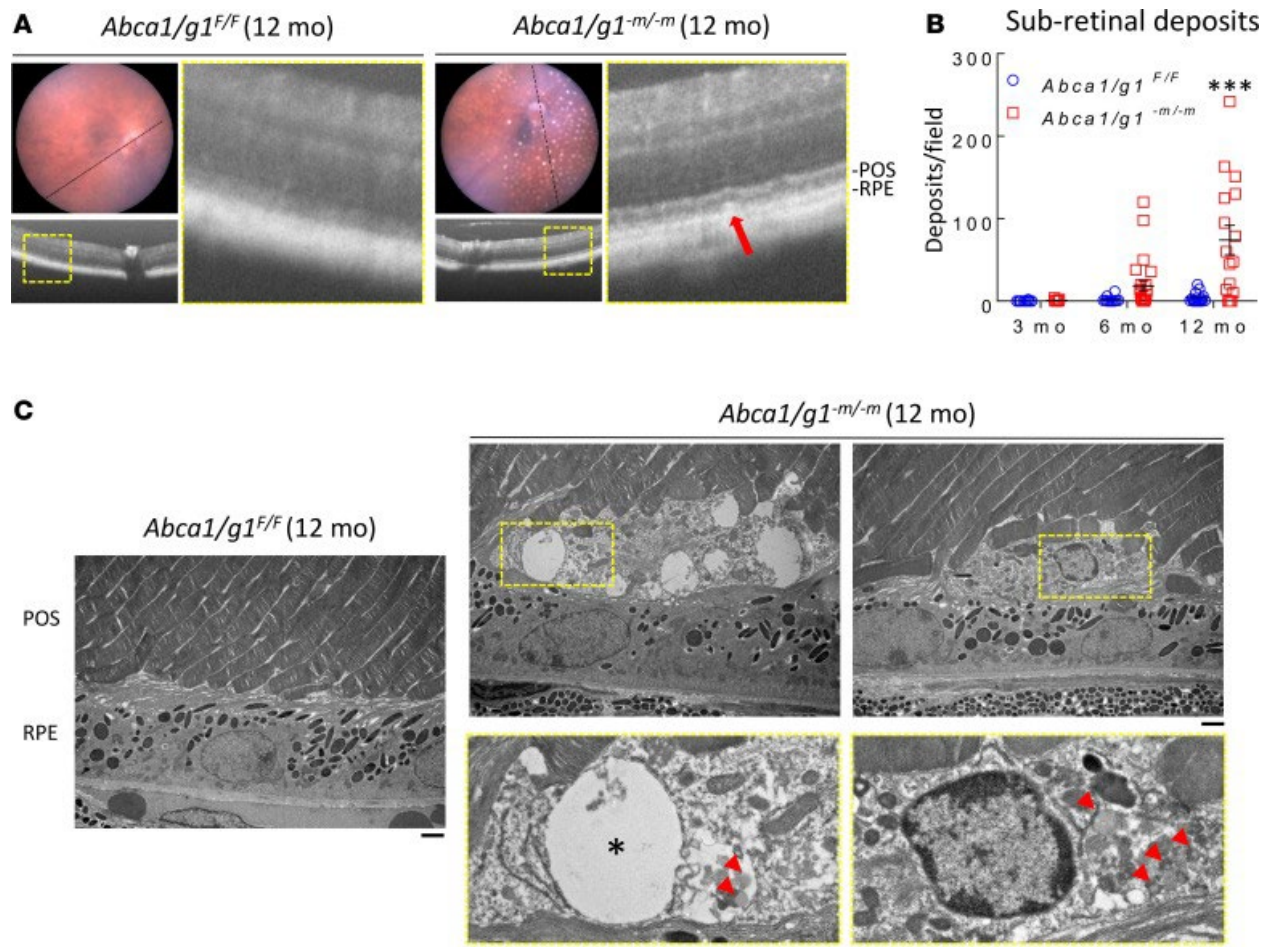


Figure 4. Subretinal deposits contain lipid globules and degenerative vacuoles.

(A) Representative optical coherence tomography (OCT) images of 12-month-old *Abca1/g1^{F/F}* and *Abca1/g1^{-m/-m}* mice retinas. Note the subretinal hyperreflective deposits in *Abca1/g1^{-m/-m}* mice retinas (red arrow) corresponding to fundus yellowish white dots. POS, photoreceptor outer segment. (B) Quantification of subretinal deposits in 3-, 6-, and 12-month-old *Abca1/g1^{F/F}* and *Abca1/g1^{-m/-m}* mice retinas. *Abca1/g1^{F/F}*, n = 10, 10, and 15; *Abca1/g1^{-m/-m}*, n = 13, 24, and 16, respectively. ***P < 0.001 by 2-way ANOVA with post hoc Bonferroni's multiple comparison test. (C) Representative electron microscopy images of 12-month-old *Abca1/g1^{F/F}* and *Abca1/g1^{-m/-m}* mice retinas. Note the vacuoles (asterisk) and lipid globules (red arrowheads) within the subretinal deposit in *Abca1/g1^{-m/-m}* mice retinas. Scale bar: 1 μ m. Values are mean \pm SEM.

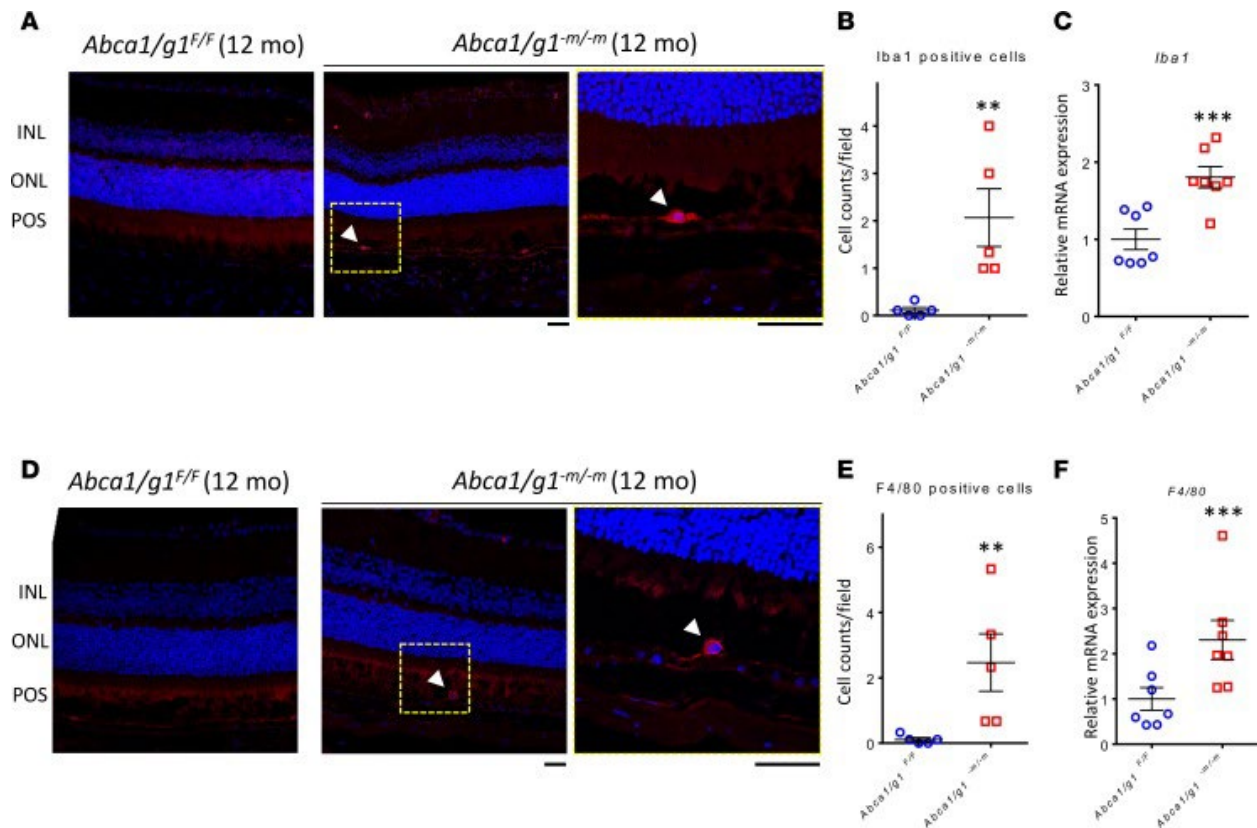


Figure 5. Infiltrated cells in subretinal space are IBA1 and F4/80 positive.

(A) Representative Iba1 IHC staining of 12-month-old *Abca1/g1^{F/F}* and *Abca1/g1^{-m/-m}* mice retinas. Red, Iba1; blue, DAPI. Scale bar: 50 μ m. INL, inner nuclear layer; ONL, outer nuclear layer; POS, photoreceptor outer segment. (B) Quantification of Iba1-positive cells in subretinal space. *Abca1/g1^{F/F}*, n = 5; *Abca1/g1^{-m/-m}*, n = 5. **P < 0.01 by 2-tailed Mann-Whitney U test. (C) qPCR quantification of Iba1 expressions in the retina/RPE/choroid complex. *Abca1/g1^{F/F}*, n = 7; *Abca1/g1^{-m/-m}*, n = 7. ***P < 0.001 and by 2-tailed unpaired t test. (D) Representative IHC staining of 12-month-old *Abca1/g1^{F/F}* and *Abca1/g1^{-m/-m}* mice retinas. Red, F4/80; blue, DAPI. Scale bar: 50 μ m. (E) Quantification of F4/80-positive cells in the subretinal space. *Abca1/g1^{F/F}*, n = 5; *Abca1/g1^{-m/-m}*, n = 5. **P < 0.01 and by 2-tailed Mann-Whitney test. (F) qPCR quantification of F4/80 expressions in the retina/RPE/choroid complex. *Abca1/g1^{F/F}*, n = 7; *Abca1/g1^{-m/-m}*, n = 7. ***P < 0.001 and by 2-tailed unpaired t test. Values are mean \pm SEM.

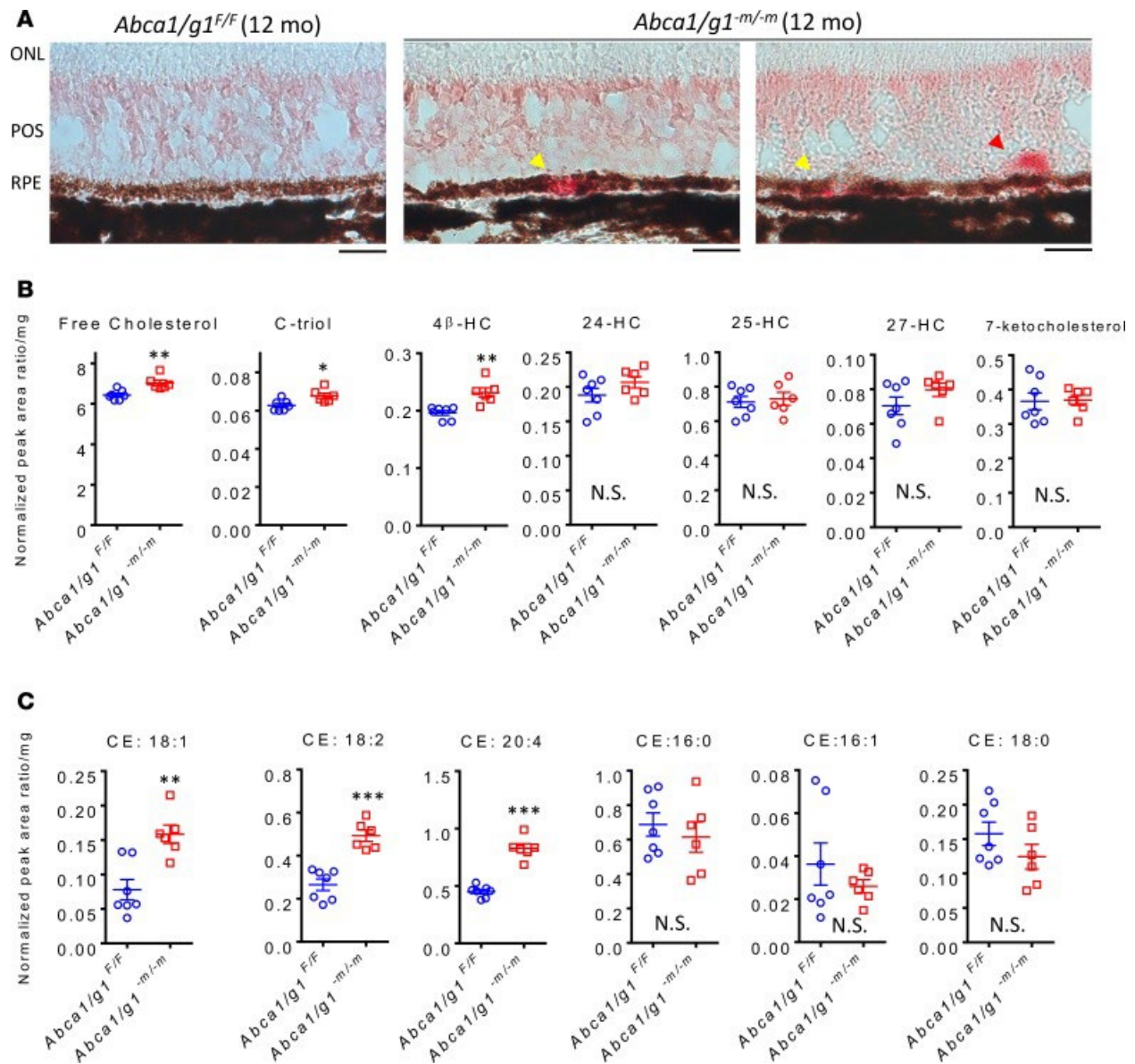
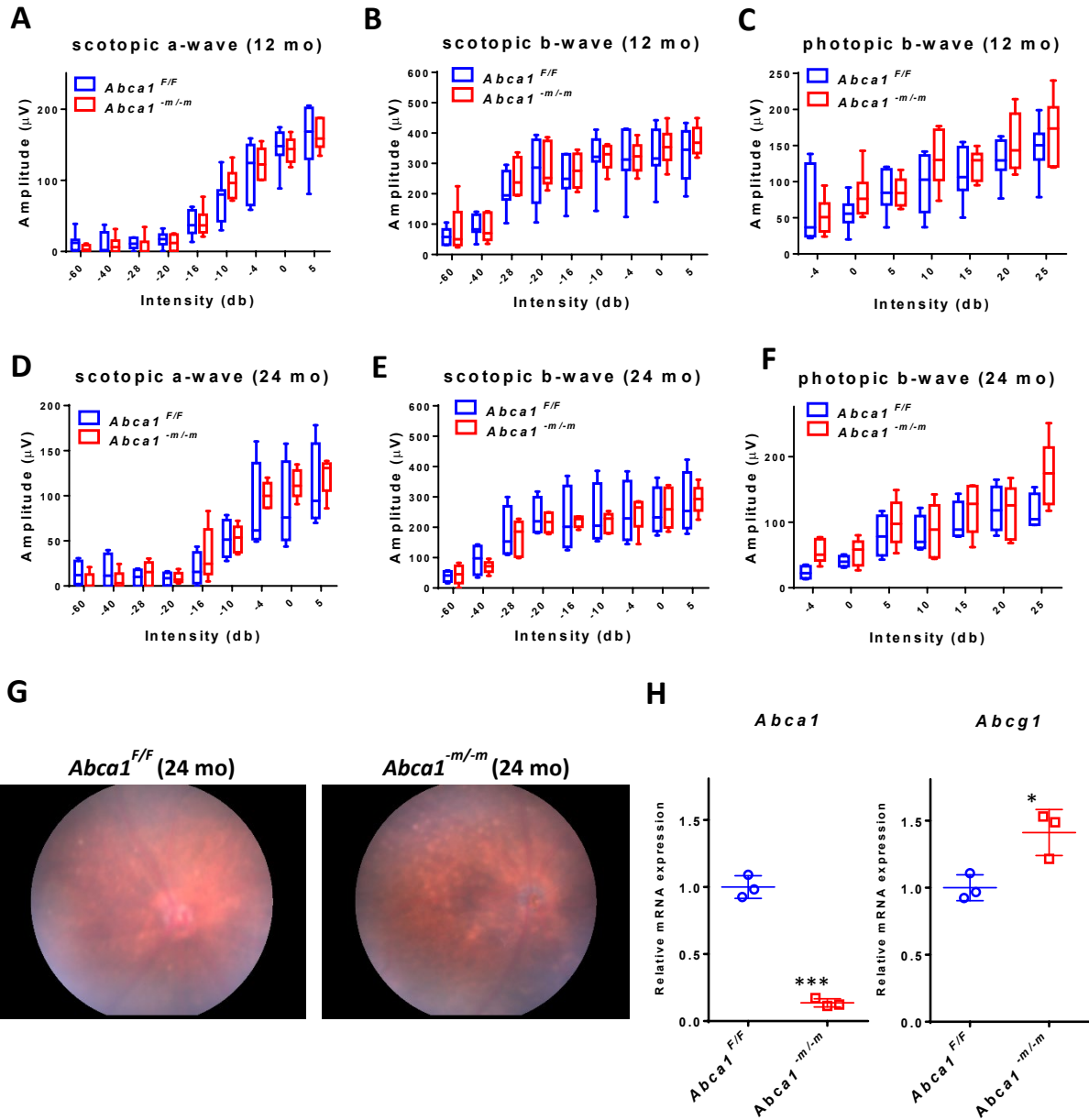


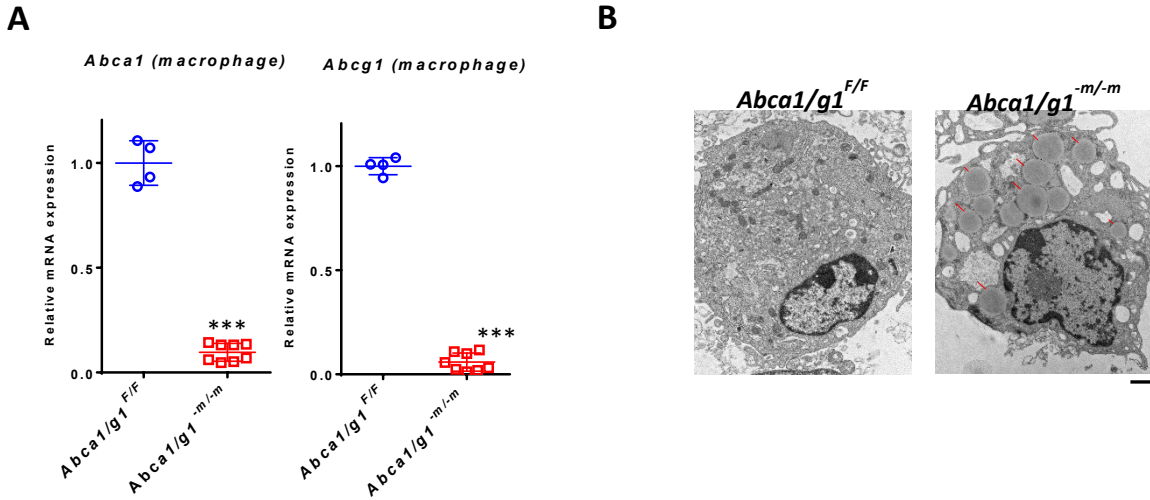
Figure 6. Lipid analysis of *Abca1/g1^{-/-}* mice eyes at 12 months of age demonstrates focal subretinal and RPE deposits with increased cholesterol metabolites.

(A) Representative Oil Red O staining of 12-month-old *Abca1/g1^{F/F}* and *Abca1/g1^{-/-}* mice retinas. Note the lipid deposits within the RPE (yellow arrowheads) or subretinal space (red arrowhead). Scale bar: 20 μ m. (B) Analyses of free cholesterol, 3 β ,5 α ,6 β -cholestanetriol (C-triol), 4 β -hydroxycholesterol (4 β -HC), 24-hydroxycholesterol (24-HC), 25-HC, 27-HC, and 7-ketocholesterol in retina/RPE/choroid complex at 12 months of age (normalized peak area ratio/mg wet tissue weight). *Abca1/g1^{F/F}*, n = 7; *Abca1/g1^{-/-}*, n = 6. *P < 0.05 and **P < 0.01 by 2-tailed unpaired t test. (C) Analyses of cholesterol esters (CE) in retina/RPE/choroid complex at 12 months of age (normalized peak area ratio/mg wet tissue weight). *Abca1/g1^{F/F}*, n = 7; *Abca1/g1^{-/-}*, n = 6. **P < 0.01 and ***P < 0.001 by 2-tailed unpaired t test. Values are mean \pm SEM.



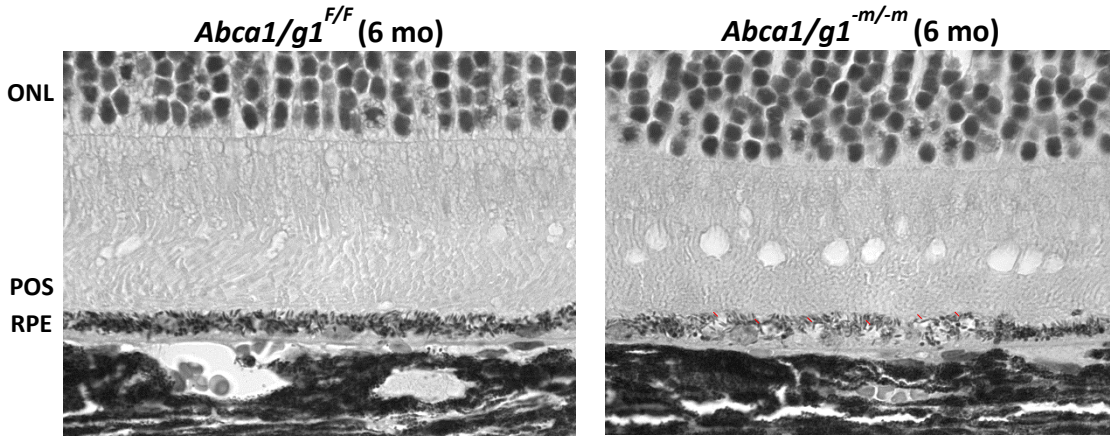
Supplementary Figure 1

(A-C) Electroretinography (ERG) of 12-month-old *Abca1*^{F/F} (n=5) and *Abca1*^{-m/-m} mice (n=6) (A) Scotopic a-wave amplitude. (B) Scotopic b-wave amplitude. (C) Photopic b-wave amplitude. No significant difference was detected by two-way ANOVA. (D-F) ERG of 24-month-old *Abca1*^{F/F} (n=4) and *Abca1*^{-m/-m} mice (n=5) (D) Scotopic a-wave amplitude. (E) Scotopic b-wave amplitude. (F) Photopic b-wave amplitude. No significant difference was detected by two-way ANOVA. (G) Representative fundus images of 12-month-old *Abca1*^{F/F} and *Abca1*^{-m/-m} mice retinas. (H) *Abca1* and *Abcg1* expression in peritoneal macrophages from 3-month-old *Abca1*^{F/F} (n=3) and *Abca1*^{-m/-m} mice (n=3). *p<0.05 and ***p<0.001 by two-tailed unpaired t-test. Values are mean ± SE.



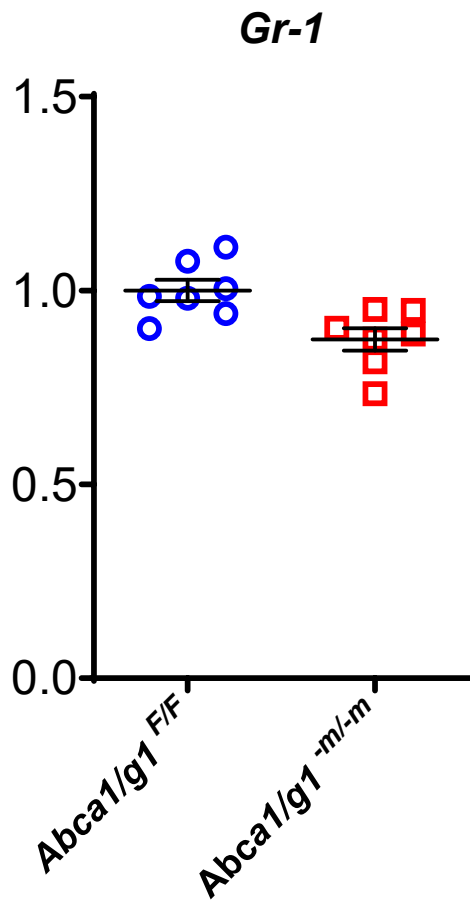
Supplementary Figure 2

(A) *Abca1* and *Abcg1* expression in peritoneal macrophages from 3-month-old *Abca1/g1*^{F/F} (n=4) and *Abca1/g1*^{-m/-m} mice (n=8). ***p<0.001 by two-tailed unpaired t-test. (B) Representative electron microscopy images of peritoneal macrophages of 3-month-old *Abca1/g1*^{F/F} and *Abca1/g1*^{-m/-m} mice. Note the lipid droplets in macrophages of *Abca1/g1*^{-m/-m} mice (red arrowheads). Scale bar: 1 μ m. Values are mean \pm SE.



Supplementary Figure 3

Representative H and E images of 6-month-old *Abca1/g1^{F/F}* and *Abca1/g1^{m/m}* mice retinas. Note the vacuoles in the RPE of *Abca1/g1^{m/m}* mice (red arrowheads). ONL: outer nuclear layer. POS: photoreceptor outer segment. Scale bar: 10 μ m.



Supplementary Figure 4

qPCR quantification of *Gr-1* expression in the retina/RPE/choroid complex at 12 months of age; *Abca1/g1^{F/F}*: n=7, *Abca1/g1^{-m/-m}*: n=7. No significant difference was detected by two-tailed unpaired t-test.

**Chapter 4: Rod Photoreceptor Knockout of Cholesterol
Efflux Transporters, ABCA1 and ABCG1, Results in Rod
Photoreceptor and Retinal Pigment Epithelium Dysfunction
as seen in Early Dry Age-related Macular Degeneration**

Adapted from:

Disrupted cholesterol metabolism promotes age-related photoreceptor neurodegeneration

Ban N, Lee TJ, Sene A, Dong Z, Santeford A, Lin JB, Ory DS, Apte RS. Disrupted cholesterol metabolism promotes age-related photoreceptor neurodegeneration. *Journal of Lipid Research*. 2018;59(8).

4.1 Introduction

Metabolic neurodegeneration is a central feature of diverse age-related pathologies such as Alzheimer's disease (1) and retinal degeneration (2). The neurosensory retina, an extension of the CNS, is a complex neurovascular tissue whose primary function is to process light and color perceived by photoreceptor neurons and transmit this information to the visual cortex for further processing in order to generate a precise visual image. In the neurosensory retina, photoreceptor degeneration causes blindness in diseases such as retinitis pigmentosa (3) and age-related macular degeneration (AMD) (4).

The retina is also the most metabolically active tissue in the body (5, 6) and is exquisitely sensitive to metabolic flux (7). A significant portion of this metabolic demand is related to the circadian shedding of about ten percent of photoreceptor lipid bilayer membranes (7, 8).

Photoreceptor outer segments once shed have to be regenerated, placing a very high biochemical burden on these cells. In addition, the lipid-rich shed outer segments have to be processed by the retinal pigment epithelium (RPE) underneath the neurosensory retina (9).

These cholesterol-containing lipids are then packaged onto carrier lipoproteins for transport from the eye to the bloodstream using a well-characterized process called reverse cholesterol transport or cholesterol efflux (7, 10). ABCA1 and ABCG1 play a central role in coordinating reverse cholesterol transport by packaging cholesterol and other lipids onto apolipoprotein carriers, such as ApoA1 and HDL, for transport through the blood stream to the liver (10, 11). For these reasons, we hypothesized that maintaining physiologic cholesterol homeostasis by ABCA1 and ABCG1 would play a key role in photoreceptor function and survival. In the retina, there are two types of photoreceptors: rods responsible for dim vision and cones responsible for color and

daytime vision. Although ABCA1 and ABCG1 have been reported to be expressed in the retina, including in photoreceptors (12, 13), their function in photoreceptor physiology is largely unknown. In order to assess the functions of ABCA1 and ABCG1 in photoreceptors, we generated mice lacking both *Abca1* and *Abcg1* specifically from either rods (14, 15) or cones (15, 16). Retinas were structurally evaluated by biomicroscopy, histology, and electron microscopy at 3–18 months of age. In addition, retinal function and vision were evaluated by electrophysiology.

4.2 Results

4.2.1 Deletion of *Abca1* and *Abcg1* in rod photoreceptors increases retinal cholesterol, but does not affect retinal function in young mice

The deletion of both *Abca1* and *Abcg1* in *Abca1/g1^{-rod/-rod}* mouse rod photoreceptors was confirmed by quantitative (q)PCR (supplemental Fig. S1A). Total cholesterol levels were higher in the neurosensory retinas of *Abca1/g1^{-rod/-rod}* mice compared with littermate controls (*Abca1/g1^{F/F}*) (supplemental Fig. S1B). However, *Abca1/g1^{-rod/-rod}* retinas were functionally and histopathologically normal at 3 months of age (Fig. 1A–C; supplemental Fig. S1C, D). Serum levels of HDL, LDL/VLDL, and ApoA-1 also did not show any differences (supplemental Fig. S1E–G).

4.2.2 Aged *Abca1/g1^{-rod/-rod}* mice demonstrate lipid accumulation underneath the retina with associated rod neurodegeneration and vision loss

Although young *Abca1/g1^{-rod/-rod}* mice did not demonstrate a functional phenotype at 3 months of age, upon analysis at 12 months of age, both scotopic a- and b-waveforms were significantly attenuated in *Abca1/g1^{-rod/-rod}* mouse retinas compared with littermate controls

(Fig. 1D, E) and other controls (supplemental Fig. S2A, B), confirming rod photoreceptor dysfunction and vision loss. In contrast, photopic responses, a measure of cone function, were normal in *Abca1/g1-rod/-rod* mouse retinas (Fig. 1F, supplemental Fig. S2C). Although fundus biomicroscopy at 12 months showed no gross abnormalities (Fig. 1G), electron microscopy demonstrated attenuation of normal vesicular structures at the rod inner and outer segment junction (25) in *Abca1/g1-rod/-rod* mouse retinas (Fig. 1H). In addition, photoreceptor degeneration characterized by outer segment dysmorphic changes was identified in *Abca1/g1-rod/-rod* mouse retinas, while littermate controls were normal (Fig. 1I). These structural changes were also associated with accumulation of large lipid droplets within the RPE (Fig. 1J). Further analysis by LC-MS/MS confirmed an increase in the levels of free cholesterol and several cholesterol metabolites underneath the neurosensory retina in the RPE complex (Fig. 2A) with no increase in any of the CEs analyzed (Fig. 2B).

4.2.3 Retinal neurodegeneration increases in severity and affects cone photoreceptors with increasing age

We kept *Abca1/g1-rod/-rod* mice up to 18 months to check to determine whether further aging might affect the neurodegenerative phenotype. At 18 months of age, vision loss was more severe with further degradation of scotopic rod responses on electrophysiology in *Abca1/g1-rod/-rod* mice compared with littermate controls (Fig. 3A, B) and other controls (supplemental Fig. S3A, B, D, E). A secondary decline in photopic cone responses was also observed (Fig. 3C; supplemental Fig. S3C, F). These findings recapitulate human diseases where rods are required for cone survival and where cone loss occurs after significant rod degeneration (26). At 18 months, photoreceptor neurodegeneration was identifiable on biomicroscopy, as seen by the atrophic areas within the retina (Fig. 3D, E). These atrophic areas corresponded to hyper-

reflective outer retinal foci at and above the level of the RPE on optical coherence tomography imaging (Fig. 3F). Electron microscopy demonstrated degenerative vacuolization at the junction of the RPE and the retina, confirming the biomicroscopy and optical coherence tomography findings (Fig. 3G). On histology, degenerative vacuolization of the outer retina was clearly identifiable (Fig. 3H, I). The RPE also showed structural disruption including accumulation of lipid globules, undigested photoreceptor disk fragments, and vacuoles (Fig. 3J).

4.2.4 Deletion of *Abca1* and *Abcg1* in cone photoreceptors does not cause neurodegeneration

In addition to *Abca1/g1-rod/-rod* mice, we also generated *Abca1/g1-cone/-cone* mice to reveal the function of ABCA1 and ABCG1 in cone photoreceptors and analyzed them up to 18 months. The deletion of both *Abca1* and *Abcg1* in *Abca1/g1-cone/-cone* mouse cone photoreceptors was confirmed by qPCR (supplemental Fig. S4). Similar to the phenotype seen in young *Abca1/g1-rod/-rod* mouse retinas, young *Abca1/g1-cone/-cone* mouse retinas did not show any neurodegenerative phenotype at 3 months old of age (Fig. 4A–C). However, in distinct contrast to old *Abca1/g1-rod/-rod* mouse retinas, *Abca1/g1-cone/-cone* mouse retinas were functionally (Fig. 4D–) and histopathologically (Fig. 4J–L) normal even at 18 months of age.

4.2.5 ABCA1 and ABCG1 play vital roles in maintaining retinal function during metabolic stress

In order to test whether this neurodegenerative phenotype was directly related to cholesterol uptake from the blood stream and associated metabolic stress, we placed *Abca1/g1-rod/-rod* mice on a HFD. *Abca1/g1-rod/-rod* mice placed on a HFD showed significant neurodegeneration and vision loss at 3 months compared with littermate controls on a HFD (Fig.

5A–C). Electron microscopy demonstrated rod outer segment degeneration (Fig. 5D), accumulation of lipid globules, and undigested photoreceptor disk fragments in the RPE (Fig. 5E) in *Abca1/g1-rod/-rod* mice on a HFD, which is similar to the findings seen at 12–18 months of age in *Abca1/g1-rod/-rod* mice placed on a normal diet.

4.3 Discussion

In this study, we hypothesized that maintaining physiologic cholesterol homeostasis in photoreceptors by ABCA1 and ABCG1 would play a key role in retinal function. In support of this hypothesis, we demonstrated that deletion of both *Abca1* and *Abcg1* in rod photoreceptors leads to age-related accumulation of cholesterol metabolites in the outer retina and retinal neurodegeneration. In addition, metabolic stress induced by a HFD significantly accelerated this neurodegenerative phenotype.

We generated *Abca1/g1-rod/-rod* mice to reveal the function of ABCA1 and ABCG1 in rod photoreceptors. As expected, total cholesterol levels were significantly increased in *Abca1/g1-rod/-rod* mouse retinas, whereas systemic lipoprotein levels were not changed. However, young *Abca1/g1-rod/-rod* retinas were functionally and histopathologically normal, suggesting that increased cholesterol levels in rod photoreceptors did not have acute effects on retinal structure and function. We were interested in examining the effects of aging on the retinal phenotype, as a number of neurodegenerative disease phenotypes, such as in AMD, occur with aging. As such, we aged *Abca1/g1-rod/-rod* mice and their littermate controls to 18 months of age and were able to demonstrate rod and subsequent cone photoreceptor degeneration and vision loss. In addition, we demonstrated that lipid droplets accumulated in the RPE of eyes from *Abca1/g1-rod/-rod* mice, but not in neurosensory retina, a finding consistent with the fact that

one of the major functions of the RPE is phagocytosis of lipid-rich photoreceptor outer segments shed in a circadian manner. In addition, we examined the RPE complex for free cholesterol and cholesterol metabolites by LC-MS. The results confirmed increased levels of free cholesterol and several cholesterol metabolites in the RPE complex, without an increase in any of the CEs analyzed. These findings are in contrast to retinas from mice deficient in cytochrome P450 (CYP) enzymes, which showed an increase mainly in esterified cholesterols (27).

The majority of photoreceptors in murine retinas are rods, with only about 3% being cones. The ratio of rod and cone photoreceptors in human retinas is also very similar, but the distribution is different. Although aged *Abca1/g1-rod/-rod* mice showed significant retinal neurodegeneration, *Abca1/g1-cone/-cone* mouse retinas did not show any neurodegenerative phenotype, even at 18 months. These data suggest that either deletion of *Abca1* and *Abcg1* in a small percentage of photoreceptors does not impact visual function or that ABCA1 and ABCG1 are not important for normal cone function.

Finally, we tested to determine whether increased cholesterol uptake from the blood stream could affect the neurodegenerative phenotype of *Abca1/g1-rod/-rod* mouse retinas. In fact, cellular and tissue cholesterol level is regulated by a complex interplay between uptake and de novo biosynthesis of cholesterol, both responsible for cholesterol input and enzymatic elimination and efflux of cholesterol, which are responsible for cholesterol output. Remarkably, although short-term HFD feeding usually does not cause any retinal dysfunction in mice (21), even short-term HFD feeding to young *Abca1/g1-rod/-rod* mice accelerated photoreceptor neurodegeneration and vision loss, recapitulating the phenotype of aged *Abca1/g1-rod/-rod* mice on a normal diet. These results indicate that ABCA1 and ABCG1 play vital roles in maintaining cholesterol homeostasis in rod photoreceptors and retinal function during metabolic stress. Even in human

studies, it is still controversial whether high serum cholesterol causes retinal neurodegeneration or cholesterol-lowering drugs prevent disease progression. For example, although the hallmark feature of AMD is accumulation of lipid-rich deposits underneath the RPE (called drusen), most previous studies failed to demonstrate the efficacy of cholesterol-lowering drugs, such as statins, to prevent disease progression (28, 29). Our study clearly revealed that, in the limited condition of disrupted cholesterol metabolism in rod photoreceptors, HFD caused retinal neurodegeneration. This fact might give us a new insight into the relationship between HFD or serum cholesterol and retinal neurodegenerative diseases such as AMD.

In summary, this study identifies cholesterol homeostasis as a critical regulator of age-related rod photoreceptor neurodegeneration and provides a unifying metabolic mechanism of vision loss in diverse retinal degenerative diseases. Accumulation of cholesterol and its metabolites in the outer retina may be a danger signal that leads to chronic lipotoxicity and neurodegeneration. These findings have potential translational relevance, as multiple genome-wide association studies have identified polymorphisms in genes involved in cholesterol metabolism, in general, and ABC transporters, in particular, in diseases such as AMD (30, 31) and Stargardts disease (32, 33) that are characterized by lipoprotein deposition and retinal neurodegeneration. In addition, these findings have potential implications beyond the eye, as recent studies also demonstrate a role for cholesterol clearance in regulating myelination of the CNS (34). Targeted metabolic interventions that regulate ABCA1 and ABCG1 in the retina may thus provide potential therapeutic avenues and prevent vision loss.

4.4 Materials and Methods

Animals

All animal experiments were conducted in accordance with Washington University in St. Louis School of Medicine Animal Care and Use guidelines after approval by the Animal Studies Committee. All mice were housed in a temperature-controlled room under a 12 h light/dark cycle, with free access to food and water. All mouse species used in the experiments are summarized in Table 1. *Abca1*/gF/F mice were previously characterized (17, 18) and were purchased commercially (Jackson Laboratory, Bar Harbor, ME). To generate mice lacking both *Abca1* and *Abcg1* specifically from rod photoreceptors, we crossed *Abca1*/g1F/F mice with mice carrying one copy of the rhodopsin-*iCre*⁷⁵ (*Rhod-iCre*) transgene, which were provided by Dr. Ching-Kang Jason Chen and have been previously characterized (14, 15). To generate mice lacking both *Abca1* and *Abcg1* specifically from cone photoreceptors, we crossed *Abca1*/g1F/F mice with mice carrying one copy of the human red/green pigment-*Cre* (*HRGP-Cre*) transgene, which were provided by Dr. Yun Le and have been previously characterized (15, 16, 19). We confirmed that these mice did not carry the *Crb1* gene rd8 mutation (20) (data not shown). For high-fat diet (HFD) feeding experiments, only male *Abca1*/g1F/F and *Abca1*/g1-rod/-rod mice were used. We used an adjusted-calorie diet (42% from fat, 43% kcal from carbohydrate, and 15% kcal from protein; TD.88137; ENVIGO, Indianapolis, IN) (21) as a HFD, starting from 6 weeks old to the target age of analysis. We used Purina 4043 chow (13% kcal from fat, 62% kcal from carbohydrate, 25% kcal from protein) as the normal diet (21).

Isolation of rod or cone photoreceptors from the retina

To isolate rod or cone photoreceptors from the retina, we used the Papain Dissociation System (Worthington Biochemical Corporation, Lakewood, NJ) following a previously described modified protocol (22), followed by EasySep Mouse PE or FITC positive selection kit (Stem Cell Technologies, Vancouver, Canada), respectively, following the manufacturer's protocol. We

used 1 µg/ml of PE-conjugated anti-CD73 antibodies (Miltenyi Biotec, Bergisch Gladbach, Germany) (15) for rod photoreceptors and 5 µg/ml of fluorescein peanut agglutinin (Vector Laboratories, Burlingame, CA) (23) for cone photoreceptors, respectively.

RNA isolation and quantitative PCR

Total RNA was extracted using an RNeasy Micro Plus kit (Qiagen, Hilden, Germany) according to the manufacturer's instructions. To synthesize cDNA, total RNA was added to the high-capacity cDNA reverse transcription kits (Thermo Fisher Scientific, Waltham, MA) and reverse-transcribed according to manufacturer's instructions. Quantitative (q)PCR was performed in duplicate using the StepOnePlus real-time PCR system (Thermo Fisher Scientific) using TaqMan real-time PCR assays (Thermo Fisher Scientific), and the mRNA was quantified using the $\Delta\Delta\text{CT}$ method with Gapdh or Actb as the internal control.

Electroretinography

Electroretinography (ERG) was performed as previously described (21). A UTAS BigShot system (LKC Technologies, Inc., Gaithersburg, MD) was used. Mice were dark adapted overnight. Under red light illumination, mice were anesthetized with an intraperitoneal injection of 86.9 mg/kg ketamine and 13.4 mg/kg xylazine. Pupils were dilated with 1% atropine sulfate eye drops (Bausch and Lomb, Rochester, NY). Body temperature was maintained at 37°C with a heating pad. Contact lens electrodes were placed bilaterally with appropriate reference and ground electrodes. The stimuli consisted of a full-field white light flash (10 µs) in darkness or in the presence of dim [30.0 candela (cd)/m²] background illumination after 10 min adaptation time. Raw data were processed using MATLAB software (MathWorks, Natick, MA). The amplitude of the a-wave was measured from the average pretrial baseline to the most negative

point of the average trace, and the b-wave amplitude was measured from that point to the highest positive point.

Retinal imaging

We performed digital color fundus photography and optical coherence tomography, as previously described (15, 24), using the Micron III animal fundus camera equipped with 830 nm optical coherence tomography (Phoenix Research Labs, Pleasanton, CA). Prior to fundus imaging and optical coherence tomography, we anesthetized mice with an intraperitoneal injection of 86.9 mg/kg ketamine and 13.4 mg/kg xylazine and administered 1.0% tropicamide eye drops (Bausch and Lomb) to dilate the pupils.

Transmission electron microscopy

We performed transmission electron microscopy analysis as previously described (15). For ultrastructural analyses, samples were fixed in 2% paraformaldehyde/2.5% glutaraldehyde (Polysciences Inc., Warrington, PA) in 100 mM sodium cacodylate buffer (pH 7.2) for 2 h at room temperature and then overnight at 4°C. Samples were washed in sodium cacodylate buffer at room temperature and postfixed in 1% osmium tetroxide (Polysciences Inc.) for 1 h. Samples were then rinsed extensively in dH₂O prior to en bloc staining with 1% aqueous uranyl acetate (Ted Pella Inc., Redding, CA) for 1 h. Following several rinses in dH₂O, samples were dehydrated in a graded series of ethanol and embedded in Eponate 12 resin (Ted Pella Inc.). Sections of 95 nm were cut with a Leica Ultracut UCT ultramicrotome (Leica Microsystems Inc., Bannockburn, IL), stained with uranyl acetate and lead citrate, and viewed on a JEOL 1200 EX transmission electron microscope (JEOL USA Inc., Peabody, MA) equipped with an AMT 8

megapixel digital camera and AMT Image Capture Engine V602 software (Advanced Microscopy Techniques, Woburn, MA).

Analysis of total cholesterol in the neurosensory retina

We used Amplex Red cholesterol assay kits (Thermo Fisher Scientific) to measure total cholesterol in the neurosensory retina following the manufacturer's protocol. Each neurosensory retina was homogenized with RIPA buffer (Thermo Fisher Scientific). Cholesterol concentrations were normalized to wet weights of the neurosensory retina (milligrams).

Analyses of HDL, LDL/VLDL, and ApoA-1 in serum

We collected blood samples from facial veins after overnight fasting. Blood samples were centrifuged at 800 g for 15 min, and then serum samples were collected. HDL and LDL/VLDL in serum were measured using HDL and LDL/VLDL quantitation kits (Sigma, St. Louis, MO) following the manufacturer's protocol. ApoA-1 in serum was measured using an ApoA1 ELISA kit (LifeSpan BioSciences, Seattle, WA) following the manufacturer's protocol.

Analyses of oxysterols, free cholesterol, and cholesteryl esters in RPE complex

To prepare RPE/choroid/sclera samples, we dissected the eyeballs to remove the anterior parts, including cornea, lens, and iris. After removing neurosensory retina, RPE/choroid/sclera samples were flash-frozen with liquid nitrogen and then stored at -80°C until the analyses. This RPE/choroid/sclera sample was named the RPE complex.

Each RPE complex was homogenized with 50-fold excess volume of PBS buffer using Omni Bead Ruptor 24 (Omni International Inc., Kennesaw, GA). All of the analytes listed above in 50 μl of the mouse retina homogenate were extracted with 200 μl of methanol. Prior to the

extraction, triol-d7 (2 ng), 7-ketocholesterol-d7 (2 ng), 24-hydroxycholesterol (HC)-d7 (2 ng), 27-HC-d5 (2 ng), 4 β -HC-d7 (2 ng), cholesteryl esters (CEs) (18:2)-d7 (200 ng), and cholesterol-d7 (1 μ g) were added as the internal standards to the homogenate samples. All oxysterols and cholesterol, as well as their deuterated standards, were derivatized with N,N-dimethylglycine to increase the MS sensitivity. Cholesteryl esters were not derivatized for the MS analyses.

The analysis of oxysterols and free cholesterol was performed with a Shimadzu 20AD HPLC system and a Shimadzu SIL 20AC autosampler coupled to a triple quadrupole mass spectrometer (API-6500Qtrap+ Thermo Fisher Scientific) operated in MRM mode. The positive ion ESI mode was used for detection of the N,N-dimethylglycine-derivatized oxysterols and free cholesterol. An Agilent Eclips XDB-C18 HPLC column (3.0 \times 100 mm, 3.5 μ m) was used for separation of all oxysterols. Mobile phase (a) 1% formic acid in water and mobile phase (b) 1% formic acid in 1:1 methanol/acetonitrile were programmed from 60% (b) to 99% in 4 min at a flow rate of 0.9 ml/min. All samples were injected in duplicate for data averaging. Data processing was conducted with Analyst 1.6.3 (Thermo Fisher Scientific).

The analysis of two cholesteryl esters [CE(16:0) and CE(18:0)] was performed with a Shimadzu 20AD HPLC system, a LeapPAL autosampler coupled to a triple quadrupole mass spectrometer (API 4000; Thermo Fisher Scientific) operated with positive ion MRM mode. An Agilent Eclips XDB-C8 HPLC column (4.6 \times 100 mm, 3.5 μ m) was used for these cholesteryl esters. The mobile phases, (a) 10 mmol ammonium acetate in 3:7 acetonitrile/water and (b) 10 mmol ammonium acetate in 1:1 methanol/isopropanol, were programmed from 80% (b) to 99% in 4 min and held for 2 min at a flow rate of 1.2 ml/min. The data processing was conducted with Analyst 1.5.1 (Thermo Fisher Scientific).

The analysis of the rest of the cholesteryl esters [CE(16:2), CE(18:1), CE(18:2), and CE(20:4)] was performed with a Shimadzu 10AD HPLC system and a Shimadzu SIL 20AC autosampler coupled to a triple quadrupole mass spectrometer (TSQ Quantum Ultra; Thermo Fisher Scientific) operated in MRM mode. A Thermo-Keystone betasil C18 HPLC column (2.0 × 100 mm, 5 μm) was used for the cholesteryl esters. The identical mobile phases [(a) and (b) listed above] were also used with an isocratic condition at 97% (b) for 12 min at a flow rate of 0.4 ml/min. The data processing was conducted with XCalibur (Thermo-Fisher Scientific).

The relative quantification data is reported as peak area ratios of analytes to their internal standards normalized to wet weights (milligrams) of RPE complex.

Statistics

We performed statistical testing with GraphPad Prism (Version 6.0), using the appropriate test for each dataset. We defined statistical significance as a $P < 0.05$. Values are mean ± SE.

4.5 Acknowledgments

The authors thank Wandy L. Beatty for electron microscopy analyses. This work was supported by National Institutes of Health Grants R01 EY019287; (R.S.A.) and P30 EY02687 (Vision Core Grant), the International Retinal Research Foundation (N.B.), the Starr Foundation (R.S.A.); the Carl Marshall and Mildred Almen Reeves Foundation (R.S.A.); the Bill and Emily Kuzma Family Gift for Retinal Research (R.S.A.), Research to Prevent Blindness Physician-Scientist and Nelson Trust Awards (R.S.A.), the Jeffrey Fort Innovation Fund (R.S.A.); the Glenn Foundation for Medical Research, and the Thome Memorial Foundation (R.S.A.). Additional support was provided by an unrestricted Research to Prevent Blindness Grant to the Department of Ophthalmology and Visual Sciences of Washington University School of Medicine. J.B.L.

was supported by the Washington University in St. Louis Medical Scientist Training Program (National Institutes of Health Grant T32 GM07200), the Washington University in St. Louis Institute of Clinical and Translational Sciences (National Institutes of Health Grants UL1 TR002345; and TL1 TR002344), and the VitreoRetinal Surgery Foundation. The content is solely the responsibility of the authors and does not necessarily represent the official views of the National Institutes of Health. The authors declare that they have no conflict of interest.

4.6 References

1. Arenas F., Garcia-Ruiz C., and Fernandez-Checa J. C.. 2017. Intracellular cholesterol trafficking and impact in neurodegeneration. *Front. Mol. Neurosci.* 10: 382.
2. Fliesler S. J., and Bretillon L.. 2010. The ins and outs of cholesterol in the vertebrate retina. *J. Lipid Res.* 51: 3399–3413.
3. Athanasiou D., Aguila M., Bellingham J., Li W., McCulley C., Reeves P. J., and Cheetham M. E.. 2018. The molecular and cellular basis of rhodopsin retinitis pigmentosa reveals potential strategies for therapy. *Prog. Retin. Eye Res.* 62: 1–23.
4. Bowes Rickman C., Farsiu S., Toth C. A., and Klingeborn M.. 2013. Dry age-related macular degeneration: mechanisms, therapeutic targets, and imaging. *Invest. Ophthalmol. Vis. Sci.* 54: ORSF68–ORSF80.
5. Niven J. E., and Laughlin S. B.. 2008. Energy limitation as a selective pressure on the evolution of sensory systems. *J. Exp. Biol.* 211: 1792–1804.
6. Okawa H., Sampath A. P., Laughlin S. B., and Fain G. L.. 2008. ATP consumption by mammalian rod photoreceptors in darkness and in light. *Curr. Biol.* 18: 1917–1921.

7. Goldberg A. F., Moritz O. L., and Williams D. S.. 2016. Molecular basis for photoreceptor outer segment architecture. *Prog. Retin. Eye Res.* 55: 52–81.
8. Albert A., Alexander D., and Boesze-Battaglia K.. 2016. Cholesterol in the rod outer segment: a complex role in a “simple” system. *Chem. Phys. Lipids.* 199: 94–105.
9. Storti F., Raphael G., Griesser V., Klee K., Drawnel F., Willburger C., Scholz R., Langmann T., von Eckardstein A., Fingerle J., et al.. 2017. Regulated efflux of photoreceptor outer segment-derived cholesterol by human RPE cells. *Exp. Eye Res.* 165: 65–77.
10. Sene A., and Apte R. S.. 2014. Eyeballing cholesterol efflux and macrophage function in disease pathogenesis. *Trends Endocrinol. Metab.* 25: 107–114.
11. Sene A., Khan A. A., Cox D., Nakamura R. E., Santeford A., Kim B. M., Sidhu R., Onken M. D., Harbour J. W., Hagbi-Levi S., et al.. 2013. Impaired cholesterol efflux in senescent macrophages promotes age-related macular degeneration. *Cell Metab.* 17: 549–561.
12. Duncan K. G., Hosseini K., Bailey K. R., Yang H., Lowe R. J., Matthes M. T., Kane J. P., LaVail M. M., Schwartz D. M., and Duncan J. L.. 2009. Expression of reverse cholesterol transport proteins ATP-binding cassette A1 (ABCA1) and scavenger receptor BI (SR-BI) in the retina and retinal pigment epithelium. *Br. J. Ophthalmol.* 93: 1116–1120.
13. Ananth S., Gnana-Prakasam J. P., Bhutia Y. D., Veeranan-Karmegam R., Martin P. M., Smith S. B., and Ganapathy V.. 2014. Regulation of the cholesterol efflux transporters ABCA1 and ABCG1 in retina in hemochromatosis and by the endogenous siderophore 2,5-dihydroxybenzoic acid. *Biochim. Biophys. Acta.* 1842: 603–612.

14. Li S., Chen D., Sauve Y., McCandless J., Chen Y. J., and Chen C. K.. 2005. Rhodopsin-iCre transgenic mouse line for Cre-mediated rod-specific gene targeting. *Genesis*. 41: 73–80.
15. Lin J. B., Kubota S., Ban N., Yoshida M., Santeford A., Sene A., Nakamura R., Zapata N., Kubota M., Tsubota K., et al.. 2016. NAMPT-mediated NAD(+) biosynthesis is essential for vision in mice. *Cell Reports*. 17: 69–85.
16. Le Y. Z., Ash J. D., Al-Ubaidi M. R., Chen Y., Ma J. X., and Anderson R. E.. 2004. Targeted expression of Cre recombinase to cone photoreceptors in transgenic mice. *Mol. Vis*. 10: 1011–1018.
17. Westerterp M., Gourion-Arsiquaud S., Murphy A. J., Shih A., Cremers S., Levine R. L., Tall A. R., and Yvan-Charvet L.. 2012. Regulation of hematopoietic stem and progenitor cell mobilization by cholesterol efflux pathways. *Cell Stem Cell*. 11: 195–206.
18. Westerterp M., Murphy A. J., Wang M., Pagler T. A., Vengrenyuk Y., Kappus M. S., Gorman D. J., Nagareddy P. R., Zhu X., Abramowicz S., et al.. 2013. Deficiency of ATP-binding cassette transporters A1 and G1 in macrophages increases inflammation and accelerates atherosclerosis in mice. *Circ. Res*. 112: 1456–1465.
19. Zhou Z., Vinberg F., Schottler F., Doggett T. A., Kefalov V. J., and Ferguson T. A.. 2015. Autophagy supports color vision. *Autophagy*. 11: 1821–1832.
20. Mattapallil M. J., Wawrousek E. F., Chan C. C., Zhao H., Roychoudhury J., Ferguson T. A., and Caspi R. R.. 2012. The Rd8 mutation of the *Crb1* gene is present in vendor lines of C57BL/6N mice and embryonic stem cells, and confounds ocular induced mutant phenotypes. *Invest. Ophthalmol. Vis. Sci*. 53: 2921–2927.

21. Rajagopal R., Bligard G. W., Zhang S., Yin L., Lukasiewicz P., and Semenkovich C. F.. 2016. Functional deficits precede structural lesions in mice with high-fat diet-induced diabetic retinopathy. *Diabetes*. 65: 1072–1084.
22. Feodorova Y., Koch M., Bultman S., Michalakis S., and Solovei I.. 2015. Quick and reliable method for retina dissociation and separation of rod photoreceptor perikarya from adult mice. *MethodsX*. 2: 39–46.
23. Skaper S. D. 2012. Isolation and culture of rat cone photoreceptor cells. *Methods Mol. Biol.* 846: 147–158.
24. Santeford A., Wiley L. A., Park S., Bamba S., Nakamura R., Gdoura A., Ferguson T. A., Rao P. K., Guan J. L., Saitoh T., et al.. 2016. Impaired autophagy in macrophages promotes inflammatory eye disease. *Autophagy*. 12: 1876–1885.
25. Ding J. D., Salinas R. Y., and Arshavsky V. Y.. 2015. Discs of mammalian rod photoreceptors form through the membrane evagination mechanism. *J. Cell Biol.* 211: 495–502.
26. Aït-Ali N., Fridlich R., Millet-Puel G., Clérin E., Delalande F., Jaillard C., Blond F., Perrocheau L., Reichman S., Byrne L. C., et al.. 2015. Rod-derived cone viability factor promotes cone survival by stimulating aerobic glycolysis. *Cell*. 161: 817–832.
27. Saadane A., Mast N., Dao T., Ahmad B., and Pikuleva I. A.. 2016. Retinal hypercholesterolemia triggers cholesterol accumulation and esterification in photoreceptor cells. *J. Biol. Chem.* 291: 20427–20439.
28. Maguire M. G., Ying G. S., McCannel C. A., Liu C., and Dai Y.; Complications of Age-related Macular Degeneration Prevention Trial (CAPT) Research Group. 2009. Statin use and the

incidence of advanced age-related macular degeneration in the Complications of Age-related Macular Degeneration Prevention Trial. *Ophthalmology*. 116: 2381–2385.

29. Al-Holou S. N., Tucker W. R., Agr#xF3n E., Clemons T. E., Cukras C., Ferris F. L. III, and Chew E. Y.; Age-Related Eye Disease Study 2 Research Group . 2015. The association of statin use with age-related macular degeneration progression: the Age-Related Eye Disease Study 2 Report Number 9. *Ophthalmology* 122: 2490–2496.

30. Chen W., Stambolian D., Edwards A. O., Branham K. E., Othman M., Jakobsdottir J., Tosakulwong N., Pericak-Vance M. A., Campochiaro P. A., Klein M. L., et al.. 2010. Genetic variants near TIMP3 and high-density lipoprotein-associated loci influence susceptibility to age-related macular degeneration. *Proc. Natl. Acad. Sci. USA*. 107: 7401–7406.

31. Neale B. M., Fagerness J., Reynolds R., Sobrin L., Parker M., Raychaudhuri S., Tan P. L., Oh E. C., Merriam J. E., Souied E., et al.. 2010. Genome-wide association study of advanced age-related macular degeneration identifies a role of the hepatic lipase gene (LIPC). *Proc. Natl. Acad. Sci. USA*. 107: 7395–7400.

32. Allikmets R. 1997. A photoreceptor cell-specific ATP-binding transporter gene (ABCR) is mutated in recessive Stargardt macular dystrophy. *Nat. Genet*. 17: 122.

33. Quazi F., and Molday R. S.. 2013. Differential phospholipid substrates and directional transport by ATP-binding cassette proteins ABCA1, ABCA7, and ABCA4 and disease-causing mutants. *J. Biol. Chem*. 288: 34414–34426.

34. Cantuti-Castelvetri L., Fitzner D., Bosch-Queralt M., Weil M. T., Su M., Sen P., Ruhwedel T., Mitkovski M., Trendelenburg G., Lutjohann D., et al.. 2018. Defective cholesterol clearance limits remyelination in the aged central nervous system. *Science*. 359: 684–688.

4.7 Figures

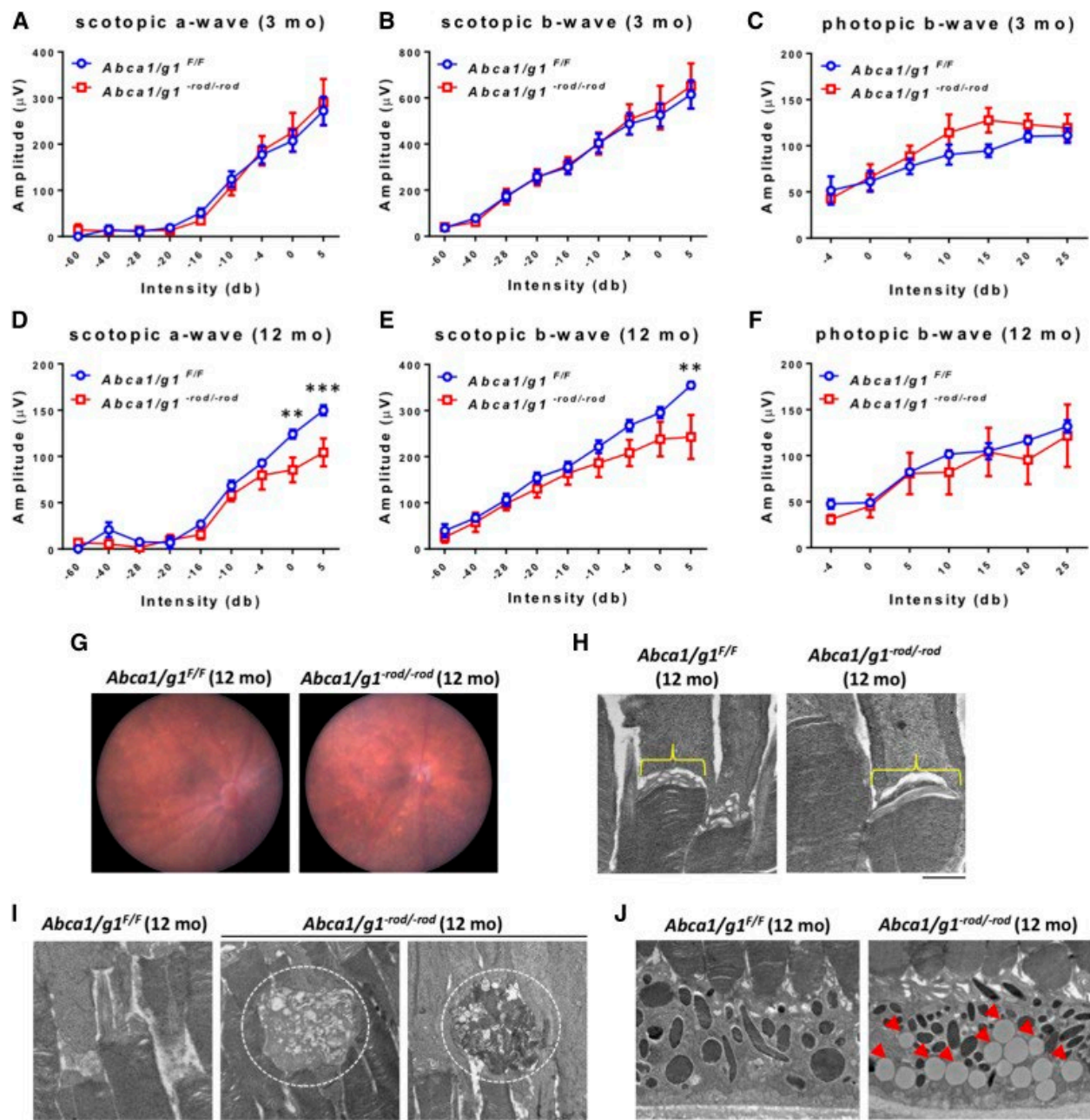


Figure 1. Aged (12 months) *Abca1/g1^{-rod/-rod}* mouse retinas show decreased scotopic responses and accumulation of lipids.

A–C: ERG of 3-month-old *Abca1/g1^{F/F}* and *Abca1/g1^{-rod/-rod}* mice. *Abca1/g1^{F/F}* (blue circles), $n = 7$; *Abca1/g1^{-rod/-rod}* (red squares), $n = 5$. A: Scotopic a-wave amplitude. B: Scotopic b-wave amplitude. C: Photopic b-wave amplitude. No significant difference was detected by two-way ANOVA. D–F: ERG of 12-month-old *Abca1/g1^{F/F}* and

Abca1/g1-rod/-rod mice. Abca1/g1F/F (blue squares), n = 5; Abca1/g1-rod/-rod (red squares), n = 5. D: Scotopic a-wave amplitude. E: Scotopic b-wave amplitude. F: Photopic b-wave amplitude. **P < 0.01 and ***P < 0.001 by two-way ANOVA with post hoc Bonferroni's multiple comparison test. G: Representative fundus images of 12-month-old Abca1/g1F/F and Abca1/g1-rod/-rod mouse retinas. H, I: Representative electron microscopy images of 12-month-old Abca1/g1F/F and Abca1/g1-rod/-rod mouse retinas. Scale bar: 1 μ m. H: Attenuation of vesicular structures at the rod inner and outer segment in Abca1/g1-rod/-rod mouse retinas. I: Dysmorphic change of outer segments of Abca1/g1-rod/-rod mouse retinas (dashed circle). J: Accumulation of large lipid droplets within the RPE (red arrowheads). Values are mean \pm SE.

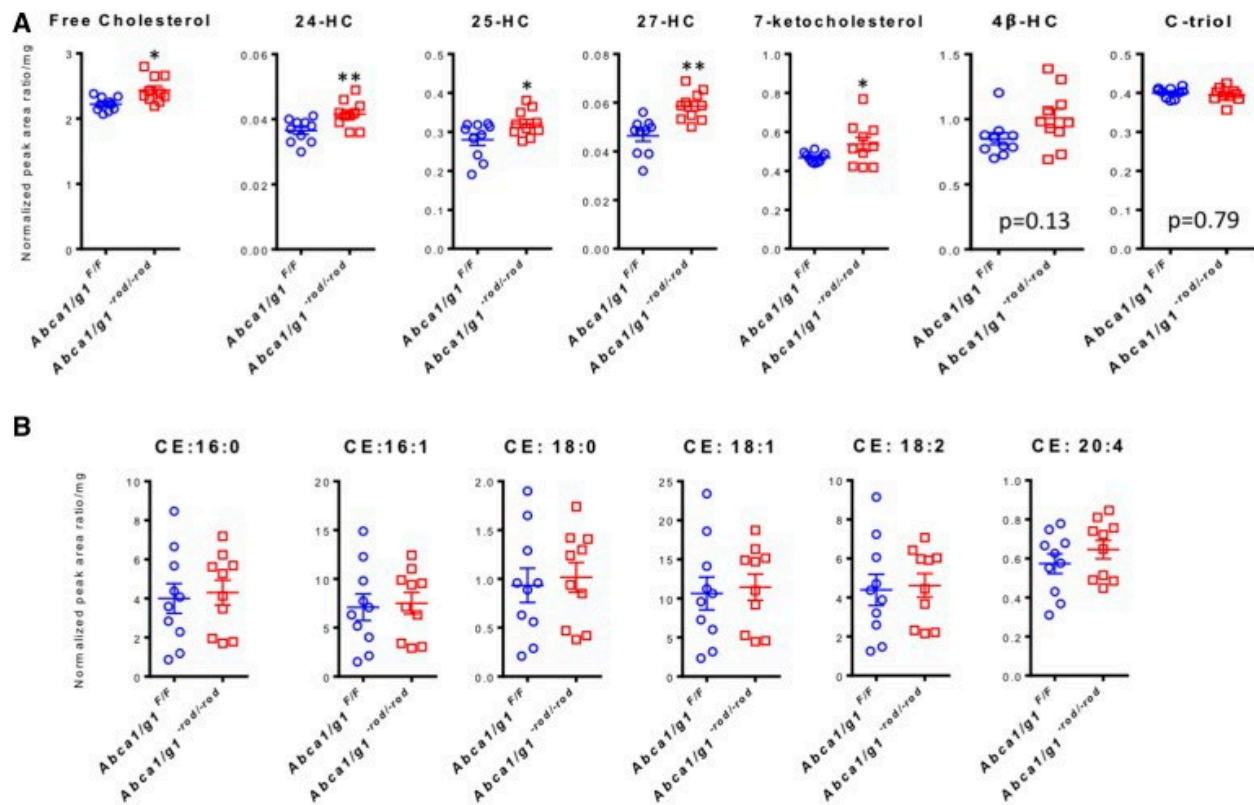


Figure 2. Lipid analysis of *Abca1/g1^{-rod/-rod}* mouse eyes at 12 months of age demonstrates accumulation of cholesterol metabolites.

A: Analyses of free cholesterol, 24-HC, 25-HC, 27-HC, and 7-ketocholesterol underneath the neurosensory retina in the RPE/choroid complex at 12 months of age (normalized peak area ratio per milligram wet tissue weight); n = 10 for each group. *P < 0.05 and **P < 0.01 by two-tailed unpaired t-test. B: Analyses of CEs underneath the neurosensory retina in the RPE/choroid complex at 12 months of age (normalized peak area ratio per milligram wet tissue weight); n = 10 for each group. No significant difference was detected by two-tailed unpaired t-test. Values are mean ± SE.

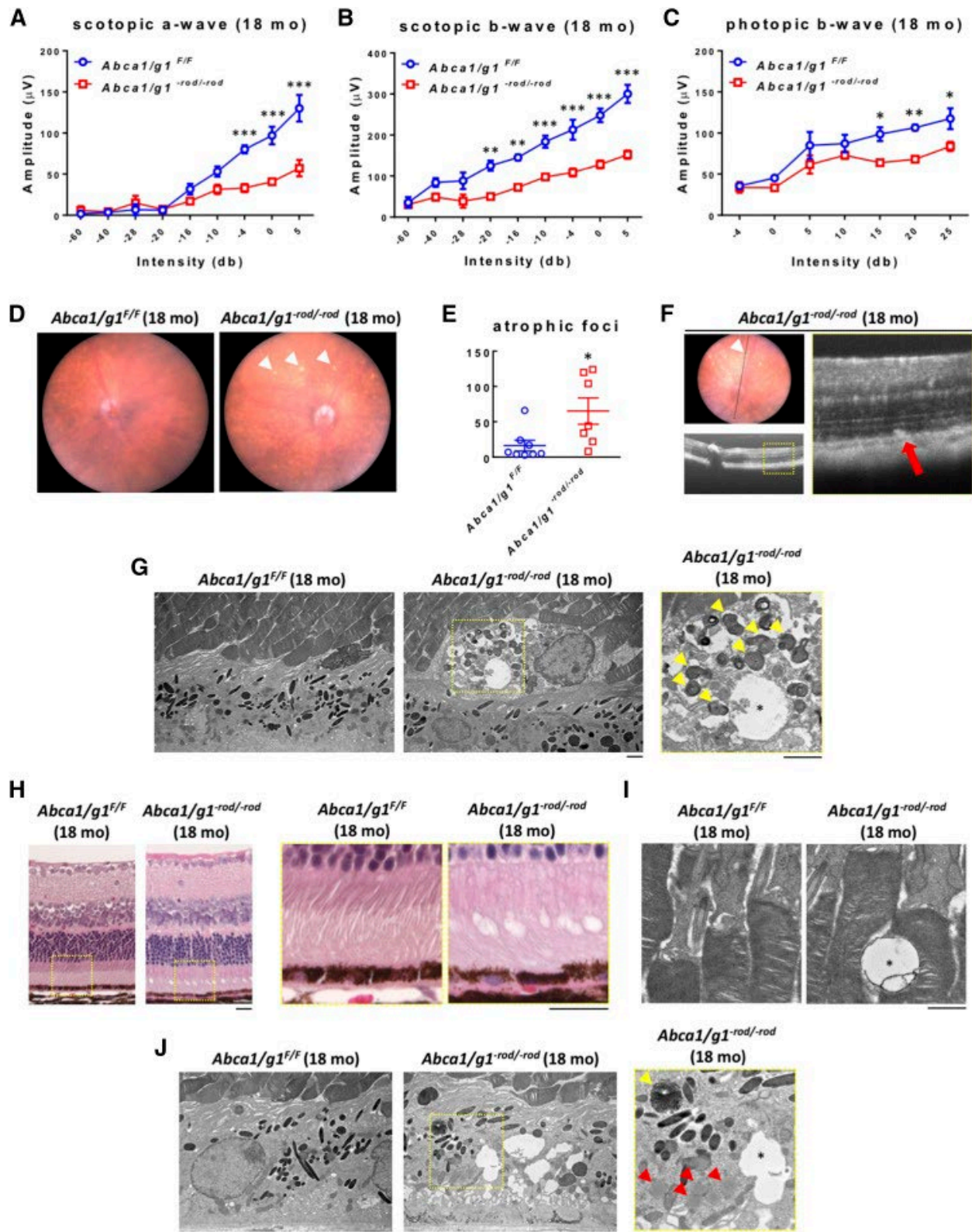


Figure 3. *Abca1/g1^{-rod/-rod}* mouse retinas (aged 18 months) show decreased scotopic and photopic responses and atrophic retinal neurodegeneration.

A–C: ERG of 18-month-old *Abca1/g1F/F* and *Abca1/g1-rod/-rod* mice. *Abca1/g1F/F* (blue circles), n = 4; *Abca1/g1-rod/-rod* (red squares), n = 4. A: Scotopic a-wave amplitude. B: Scotopic b-wave amplitude. C: Photopic b-wave amplitude. *P < 0.05, **P < 0.01, and ***P < 0.001 by two-way ANOVA with post hoc Bonferroni's multiple comparison test. D: Representative fundus images of 18-month-old *Abca1/g1F/F* and *Abca1/g1-rod/-rod* mouse retinas. Note the atrophic appearance of *Abca1/g1-rod/-rod* mouse retinas (white arrowhead). E: Quantification of retinal atrophic foci per field. *Abca1/g1F/F* (blue circles), n = 8; *Abca1/g1-rod/-rod* (red squares), n = 7. *P < 0.05 by two-tailed unpaired t-test. F: Representative optical coherence tomography images of 18-month-old *Abca1/g1-rod/-rod* mouse retinas. Note the subretinal hyper-reflective foci in *Abca1/g1-rod/-rod* mouse retinas (white arrowhead) corresponding to fundus atrophic appearance. G: Representative electron microscopy images of retinal atrophic foci in 18-month-old *Abca1/g1-rod/-rod* mouse retinas. Note the vacuoles (asterisk) and photoreceptor disk fragments (yellow arrowheads). Scale bar: 2 μ m. H: Representative H&E staining images of 18-month-old *Abca1/g1F/F* and *Abca1/g1-rod/-rod* mouse retinas. Note the degenerative vacuolization of the outer retina. Scale bar: 20 μ m. I, J: Representative electron microscopy images of 18-month-old *Abca1/g1F/F* and *Abca1/g1-rod/-rod* mouse retinas. I: Vacuoles in outer segment of *Abca1/g1-rod/-rod* mouse retinas (asterisk). Scale bar: 1 μ m. J: Accumulation of lipid globules (red arrowheads), undigested photoreceptor disk fragments (yellow arrowhead), and vacuoles (asterisk) within the RPE. Scale bar: 2 μ m. Values are mean \pm SE.

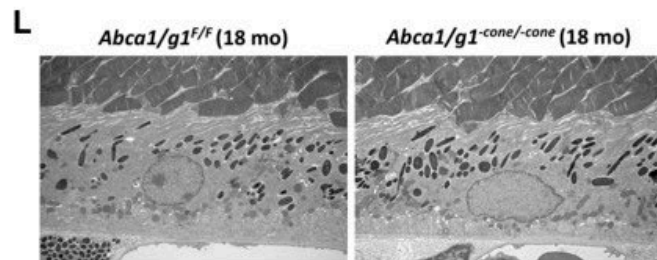
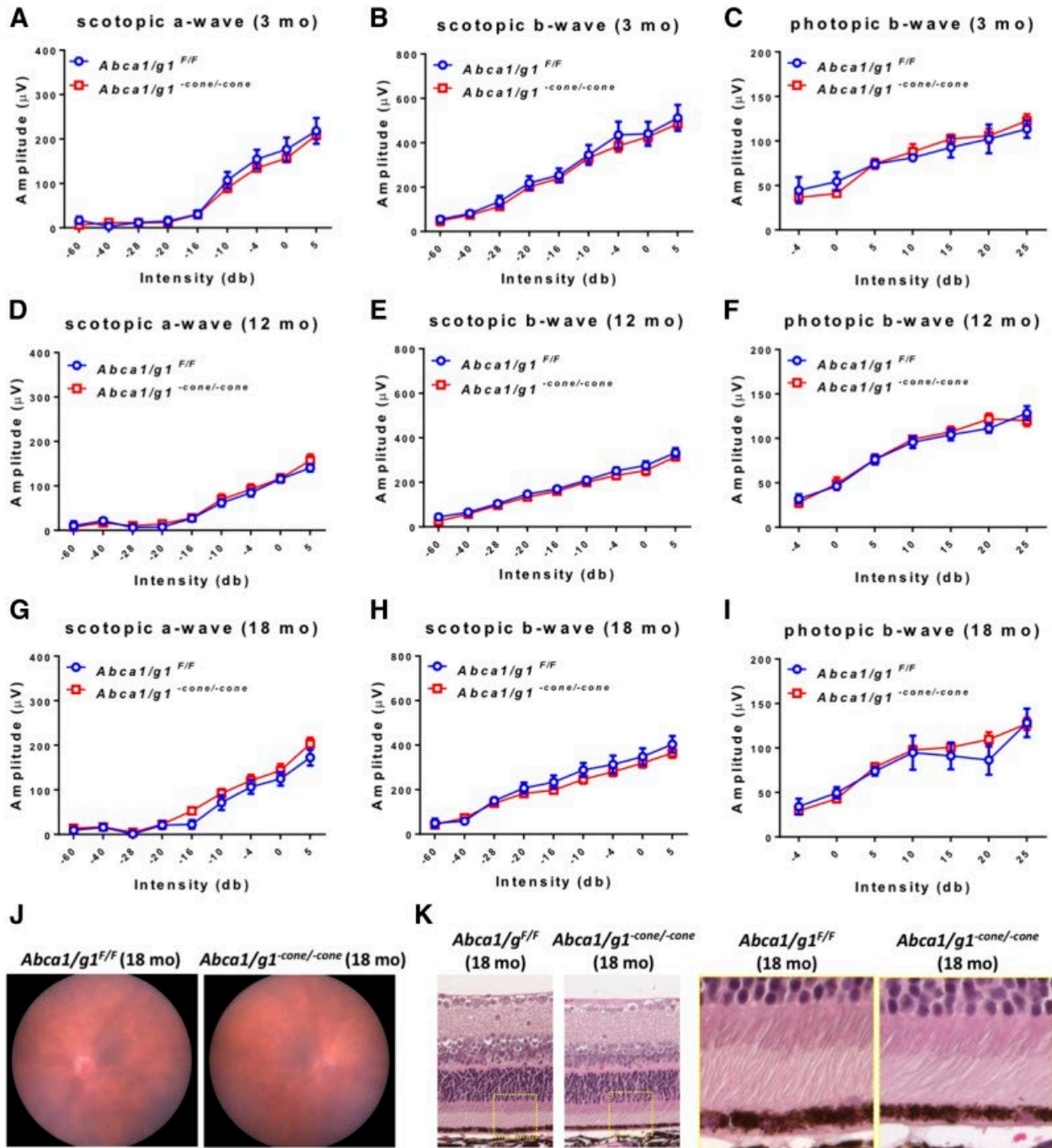


Figure 4. Deletion of *Abca1* and *Abcg1* in cone photoreceptors does not cause detectable neurodegeneration.

A–C: ERG of 3-month-old *Abca1/g1F/F* and *Abca1/g1-cone/-cone* mice. *Abca1/g1F/F* (blue circles), n = 5; *Abca1/g1-cone/-cone* (red squares), n = 6. A: Scotopic a-wave amplitude. B: Scotopic b-wave amplitude. C: Photopic b-wave amplitude. D–F: ERG of 12-month-old *Abca1/g1F/F* and *Abca1/g1-cone/-cone* mice. *Abca1/g1F/F* (blue circles), n = 7; *Abca1/g1-cone/-cone* (red squares), n = 7. D: Scotopic a-wave amplitude. E: Scotopic b-wave amplitude. F: Photopic b-wave amplitude. No significant difference was detected by two-way ANOVA. G–I: ERG of 18-month-old *Abca1/g1F/F* and *Abca1/g1-cone/-cone* mice. *Abca1/g1F/F* (blue circles), n = 4; *Abca1/g1-cone/-cone* (red squares), n = 6. G: Scotopic a-wave amplitude. H: Scotopic b-wave amplitude. I: Photopic b-wave amplitude. No significant difference was detected by two-way ANOVA. J: Representative fundus images of 18-month-old *Abca1/g1F/F* and *Abca1/g1-cone/-cone* mouse retinas. K: Representative H&E staining images of 18-month-old *Abca1/g1F/F* and *Abca1/g1-cone/-cone* mouse retinas. Scale bars: 20 μm . L: Representative electron microscopy images of 18-month-old *Abca1/g1F/F* and *Abca1/g1-cone/-cone* mouse retinas. Scale bars: 2 μm . Values are mean \pm SE.

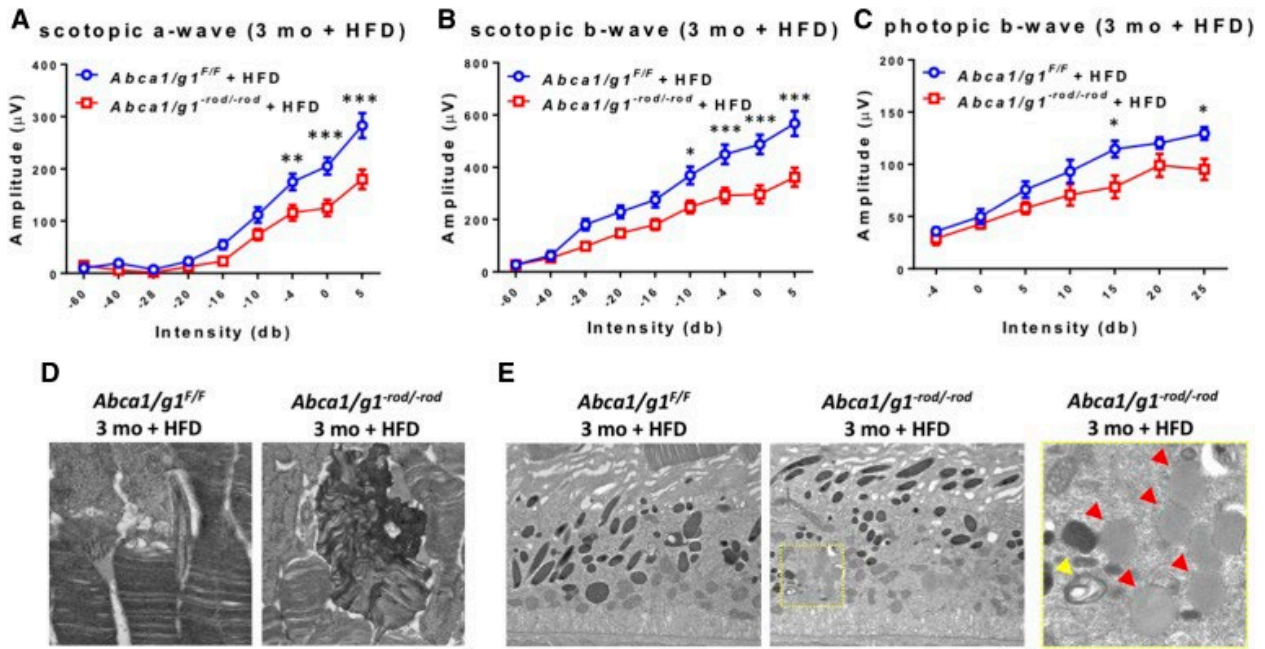
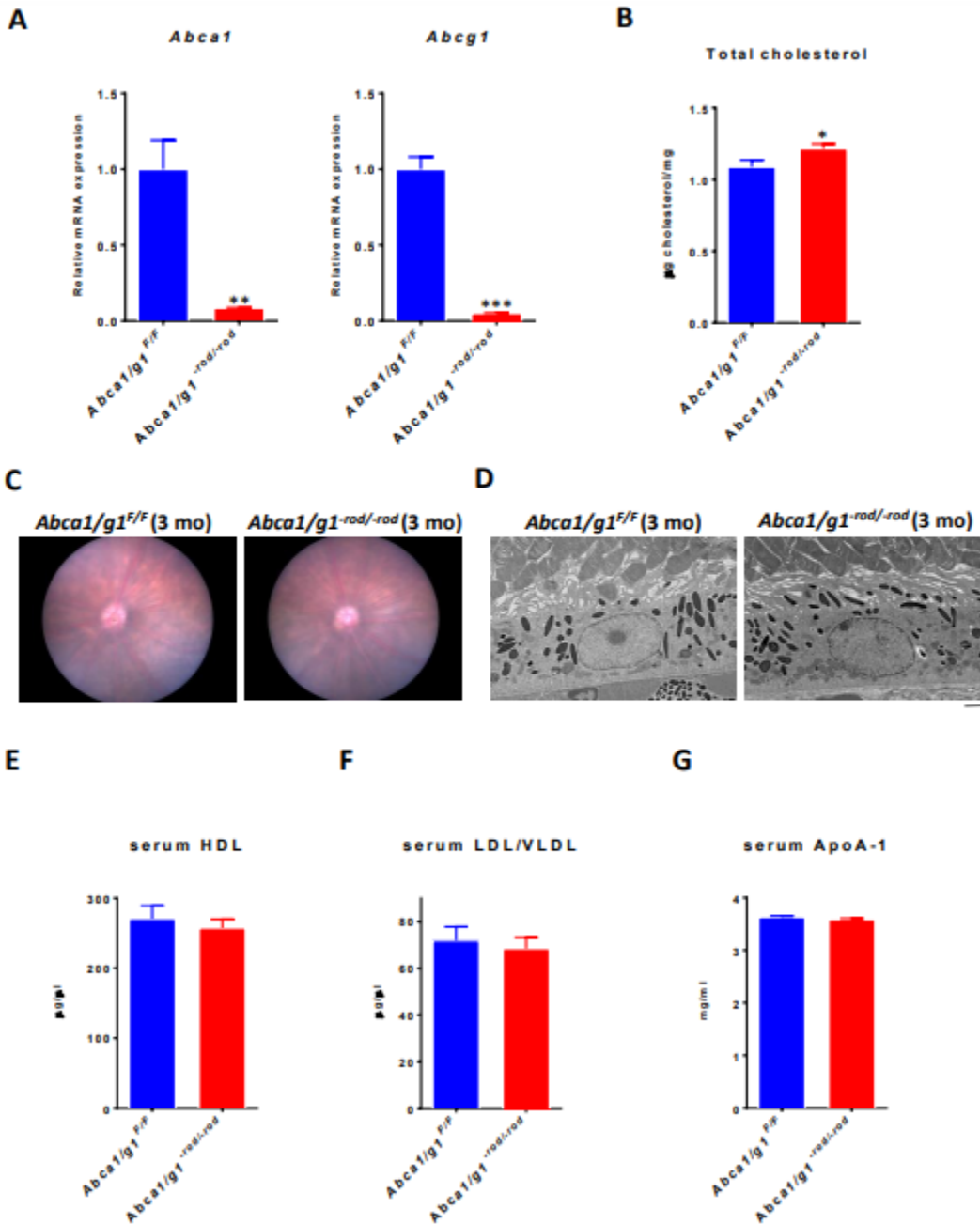


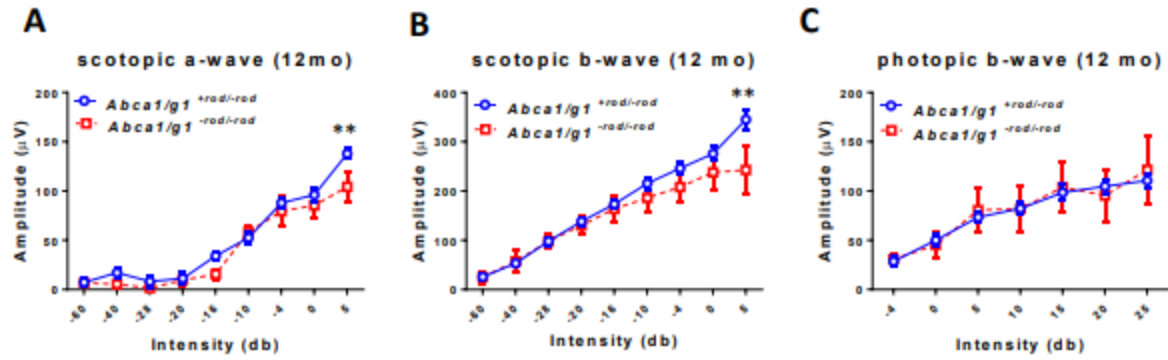
Figure 5. A HFD significantly accelerates retinal neurodegeneration in *Abca1/g1^{-rod/-rod}* mice. A–C: ERG of 3-month-old *Abca1/g1^{F/F}* and *Abca1/g1^{-rod/-rod}* mice on a HFD. *Abca1/g1^{F/F}* on a HFD (blue circles), $n = 6$; *Abca1/g1^{-rod/-rod}* on a HFD (red squares), $n = 9$. A: Scotopic a-wave amplitude. B: Scotopic b-wave amplitude. C: Photopic b-wave amplitude. * $P < 0.05$, ** $P < 0.01$, and *** $P < 0.001$ by two-way ANOVA with post hoc Bonferroni's multiple comparison test. D, E: Representative electron microscopy images of 3-month-old *Abca1/g1^{F/F}* and *Abca1/g1^{-rod/-rod}* mouse retinas on a HFD. D: Dysmorphic changes within outer segments of *Abca1/g1^{-rod/-rod}* mouse retinas on a HFD. Scale bar: 1 μm . E: Accumulation of lipid globules (red arrowheads) and undigested photoreceptor disk fragments (yellow arrowhead) in the RPE. Scale bars: 1 μm . Values are mean \pm SE.



Supplemental Figure S1. Deletion of *Abca1* and *Abcg1* in rod photoreceptors increases retinal cholesterol but does not affect the retina histopathologically in young mice

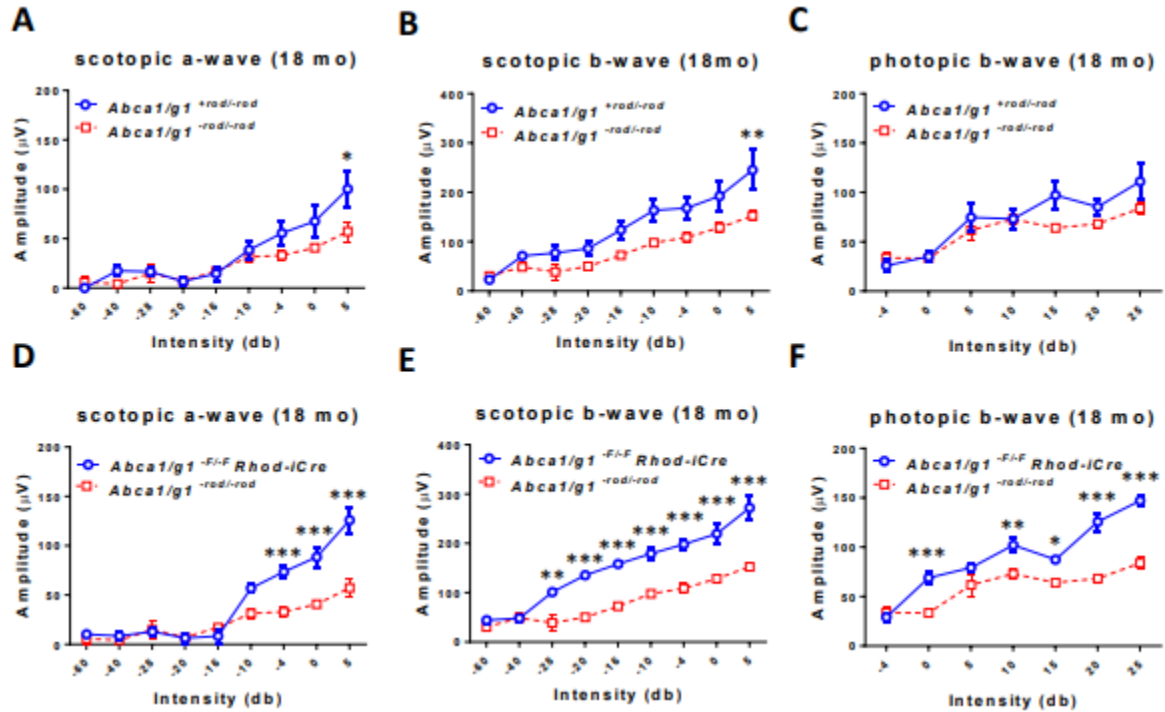
(A) *Abca1* and *Abcg1* expression in isolated rod photoreceptors from *Abca1/g1^{F/F}* and *Abca1/g1^{-rod/-rod}* mice (*Abca1/g1^{F/F}*: n=4, *Abca1/g1^{-rod/-rod}*: n=3). **p<0.01 and ***p<0.001 by two-tailed unpaired t-test. (B) Analysis of total cholesterol in the neurosensory retina (µg/mg wet tissue weight; *Abca1/g1^{F/F}*: n=9, *Abca1/g1^{-rod/-rod}*: n=11). *p<0.05 by two-tailed unpaired t-test. (C) Representative fundus images of 3-month-old *Abca1/g1^{F/F}* and *Abca1/g1^{-rod/-rod}* mice retinas. (D) Representative electron microscopy images of 3-month-old *Abca1/g1^{F/F}* and

Abca1/g1-rod/-rod mice retinas. Scar bars: 2 μ m. (E) Serum HDL concentration (Abca1/g F/F: n=6, Abca1/g1-rod/-rod: n=6). (F) Serum LDL/VLDL concentration (Abca1/g F/F: n=6, Abca1/g1-rod/-rod: n=6). (G) Serum ApoA1 concentration (Abca1/g F/F: n=6, Abca1/g1-rod/-rod: n=6). Values are mean \pm SE.



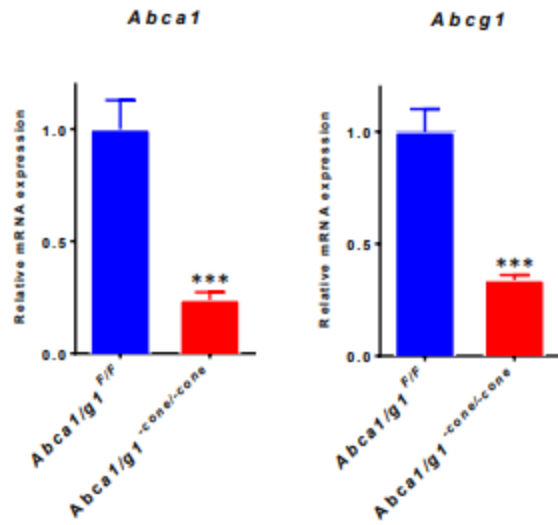
Supplemental Figure S2. Comparison of 12-month-old Abca1/g1-rod/-rod mice ERG with other controls.

(A-C) Electroretinography (ERG) of 12-month-old Abca1/g1+rod/-rod and Abca1/g1-rod/-rod mice; Abca1/g1+rod/-rod (blue circles with solid line): n=10, Abca1/g1-rod/-rod (red squares with dashed line): n=5. (A) Scotopic a-wave amplitude. (B) Scotopic b-wave amplitude. (C) Photopic b-wave amplitude. **p<0.01 by two-way ANOVA with post hoc Bonferroni's multiple comparison test. These experiments represent parallel sets of findings as in Fig. 1D-F for Abca1/g1-rod/-rod mice. Values are mean ± SE.



Supplemental Figure S3. Comparison of 18-month-old *Abca1/g1-rod/-rod* mice ERG with other controls.

(A-C) ERG of 18-month-old *Abca1/g1+rod/-rod* and *Abca1/g1-rod/-rod* mice; *Abca1/g1+rod/-rod* (blue circles with solid line): n=5, *Abca1/g1-rod/-rod* (red squares with dashed line): n=4. (A) Scotopic a-wave amplitude. (B) Scotopic b-wave amplitude. (C) Photopic b-wave amplitude. These experiments represent parallel sets of findings as in Fig. 2A-C for *Abca1/g1-rod/-rod* mice. (D-F) ERG of 18-month-old *Abca1/g1^{-F/-F} Rhod-iCre* and *Abca1/g1-rod/-rod* mice; *Abca1/g1^{-F/-F} Rhod-iCre* (blue circles with solid line): n=4, *Abca1/g1-rod/-rod* (red squares with dashed line): n=4. (D) Scotopic a-wave amplitude. (E) Scotopic b-wave amplitude. (F) Photopic b-wave amplitude. *p<0.05, **p<0.01, and ***p<0.001 by two-way ANOVA with post hoc Bonferroni's multiple comparison test. These experiments represent parallel sets of findings as in Fig. 2A-C for *Abca1/g1-rod/-rod* mice. Values are mean ± SE.



Supplemental Figure S4. Deletion of *Abca1* and *Abcg1* in cone photoreceptors in *Abca1/g1-cone/-cone* mice

Abca1 and *Abcg1* expression in isolated cone photoreceptors from *Abca1/g F/F* and *Abca1/g1-cone/-cone* mice (*Abca1/g F/F*: n=3, *Abca1/g1-cone/-cone*: n=4). ***p<0.001 by two-tailed unpaired t-test. Values are mean \pm SE.

**Chapter 5: ApoM-S1P Ameliorates Retinal Pigment
Epithelium Lipotoxicity as seen in Early Dry Age-related
Macular Degeneration**

This chapter is adapted from ongoing and unpublished work.

Lee TJ, Pitts K, Valenzuela Ripoll C, Terao R, Guo Z, Ozcan M, Santeford A, Christoffersen C,
Javaheri A, Apte RS.

5.1 Introduction

Age-related macular degeneration (AMD) is the leading cause of blindness in people over 50 years of age in the United States^{1–3}. Early/intermediate AMD is characterized by lipoprotein-rich deposits that form under the neurosensory retina, called sub-retinal drusenoid deposits (SDD), or under the retinal pigment epithelium (RPE), termed drusen^{4,5}. Vision loss in AMD occurs from progression to advanced disease. There are two forms of advanced AMD. One is called “wet” AMD, characterized by pathogenic angiogenesis called choroidal neovascularization (CNV) (20% of cases but about 80% of vision loss)⁶. In contrast, advanced “dry” AMD is characterized by atrophic neurodegeneration, also known as geographic atrophy (GA)⁷. Current therapies including anti-VEGF pharmacotherapy for neovascular AMD or complement pathway antagonists for geographic atrophy only address advanced disease⁸. The only recommended treatment for early/intermediate AMD is micronutrient supplementation^{1,9}. As such, there is a significant gap in our understanding of the molecular pathogenesis of early/intermediate dry AMD, and a treatment gap in how to prevent the progression to GA/CNV and subsequent vision loss. Current treatment for wet AMD is intravitreal injection of anti-VEGF agents. Anti-VEGF pharmacotherapy can reduce the chance of acute, catastrophic vision loss over the short term, but neurodegeneration associated with the underlying dry AMD can progress despite long-term therapy^{10–12}. Furthermore, an intravitreal complement C3 inhibitor was recently approved by the US FDA to treat GA. However, this treatment only modestly slows GA¹³. There are no curative treatments for early/intermediate dry AMD at any stage. Work from many laboratories, including our group, has identified the critical role of cholesterol accumulation as a root cause in the development and progression of AMD^{4,7,14}. Despite this

recent appreciation of lipid accumulation driving disease progression and vision-loss, no strategies exist for treating this root cause of AMD.

In AMD, there is thickening of the basement membrane of RPE cells (called Bruch's membrane), which is critical for the transport of lipoproteins^{5,15}. Lipid homeostasis in the RPE is maintained by the body's natural reverse cholesterol transport (RCT) system via high-density lipoprotein (HDL) particles¹⁶. The main protein component of HDL is apolipoprotein A-I (ApoA-I), which is critical for RCT and the removal of cholesterol from extrahepatic tissues. Impaired RCT with accumulation of lipoproteins underneath the retina is central to the AMD phenotype^{4,5}. Multiple genetic studies have shown that polymorphisms in the lipid pathway genes, including those involved in RCT, are associated with increased AMD risk^{17–19}. In addition, large clinical cohort studies have shown serum dyslipidemias in patients with AMD^{4,14,20,21}. These findings suggest that removal of cholesterol/lipid from the sub-retinal space/RPE/Bruch's membrane can prevent the development of drusenoid deposits in the early/intermediate stages of AMD²². As RPE cells highly express scavenger receptor class B type 1 (SRB-1) and ATP binding cassette subfamily A member 1 (ABCA1) cholesterol transporters^{23,24}, which recognize ApoA-I, targeting ApoA-I mediated pathways to promote reverse cholesterol transport is a potential therapeutic avenue for prevention of early AMD phenotypes. This is exemplified in a mouse model in which double knockout of *Abca1* and ATP binding cassette subfamily member G member 1 (*Abcg1*) in rod photoreceptors results in the development of a dry AMD-like phenotype, characterized by sub-retinal lipid deposits and impaired dark adaptation²⁵.

In addition to ApoA-I, other HDL-associated apolipoproteins may be important for reverse cholesterol transport, including apolipoprotein M (ApoM)²⁶. ApoM is produced primarily by the

liver, and to a minor degree by the kidney, and it binds directly to sphingosine-1-phosphate (S1P)²⁷, a bioactive lipid that activates G-protein coupled receptors (S1P receptors) expressed on multiple cell types, including RPE cells. Although ApoM is present in ~5% of HDL and <2% of low-density lipoprotein (LDL) particles, it binds 70% of circulating S1P^{28–30}. ApoM exerts multiple pleiotropic effects, including antioxidant and anti-atherogenic effects^{31,32}, regulation of inflammation, endothelial protection^{27,33}, and cell survival³⁴. Hepatocyte-specific overexpression of human APOM in mice (ApoMTG+) results in 3-5 fold increases in plasma ApoM and induces increase in plasma S1P³⁰, while ApoM knockout mice (ApoMKO-) exhibit 50% reduction in plasma S1P (with no S1P on HDL and normal amounts of S1P on albumin²⁷). ApoM has also been identified as a regulator of lysosomal function and autophagy in the murine heart³⁵.

Despite the background knowledge linking ApoM to RCT, lysosomal function, and autophagy, surprisingly little is known about the role of ApoM in AMD^{36,37}. Based on knowledge of ApoM, specifically its importance in cholesterol efflux (the first step in RCT) and interactions with S1P, which is itself critical for cholesterol efflux³⁸, we initially hypothesized that ApoM may be an unrecognized player in AMD. Utilizing plasma samples from individuals with AMD, we discovered significantly reduced levels of ApoM compared to controls. Administration of plasma from ApoM overexpressing mice, but not ApoM knockout mice, attenuated the development of AMD phenotypes in mice with *Abca1* and *Abcg1* double knockout in rod photoreceptors (*Abca1/Abcg1-Rhod/-Rhod*). Electron microscopy of the retina from these mice suggested that ApoM was stimulating lipophagy, as evidenced by a reduction in the number of lipid droplets, but increased numbers of lipid droplets interacting with melanosomes. Furthermore, the deletion of S1P receptor 3 (S1PR3), one of the key receptors for S1P,

recapitulated the AMD-like phenotype, with evidence of impaired lipid homeostasis on electron microscopy with increased lipid droplets in the RPE. Finally, knockout of lysosomal acid lipase (LAL), the key enzyme necessary for lysosomal cholesterol and triglyceride catabolism, phenocopied the dry AMD-like phenotype of *Abca1/Abcg1-Rhod^{-/-}Rhod* mice. Altogether, these results support the hypothesis that ApoM regulates S1P signaling to mediate lipid catabolism in the RPE and prevent dry AMD features.

5.2 Results

5.2.1 Older patients and patients with AMD have lower circulating levels of ApoM

To determine the relationship between circulating ApoM protein and AMD, we measured plasma ApoM in patients with and without AMD. We utilized a well-validated ELISA, which is the gold standard for measurement of ApoM^{39,40}. We first measured plasma ApoM in patients without AMD, and divided them by age under 50 (n = 299) and 50 and over (n = 635). The age of 50 is generally regarded to be when the risk of AMD presentation increases¹. We discovered that older patients have significantly lower levels of ApoM compared to younger patients (Figure 1A). We then measured plasma ApoM in patients without AMD (n = 328) and compared it to that of patients with diagnosed AMD (n = 53) (Figure 1B). Both groups were from patients over the age of 65. Patients with AMD notably had significantly decreased levels of ApoM compared to patients without AMD. These data suggest that patients with AMD have lower levels of ApoM, advocating that circulating ApoM may play a pivotal role in the development or progression of AMD.

5.2.2 ApoM plasma transfer ameliorates RPE functional deficits in a dry AMD-like mouse model

Our previous study established a dry AMD-like model using a conditional rod photoreceptor knockout of the cholesterol efflux transporters, *Abca1* and *Abcg1* (*Abca1/g1-rod/-rod*). After feeding mice a high-fat diet (60% kcal from fat, 25% kcal from carbohydrate, and 15% kcal from protein) for six weeks, we accelerated the neurodegenerative phenotype caused by aberrant accumulation of lipid in the RPE25. Of note, we considered using the conditional RPE knockout of *Abca1* and *Abcg1* model established by C. Grimm and colleagues24, but felt that the extremely accelerated neurodegeneration it presented did not represent the early features of dry AMD we wished to address.

We hypothesized that the high-fat diet fed *Abca1/g1-rod/-rod* phenotype could be ameliorated with concurrent plasma transfer from transgenic mice that overproduce ApoM (ApoMTG). Plasma transfer of ApoM is a validated strategy for ApoM delivery as previously utilized and published35. We isolated plasma from ApoM knockout mice (ApoMKO) as controls. Mice were injected with 120 μ L of either ApoMTG or ApoMKO plasma every other day (Figure 1C). Using the light bleach dark adaptation electroretinography technique41, we measured RPE function and found significant improvements in the ApoMTG treated mice by scotopic a-wave maximum measurements (Figure 1D). These findings suggest that the RPE of ApoMTG plasma treated mice functionally improved.

5.2.3 RPE lipid accumulation is reduced with ApoM plasma transfer

We next utilized electron microscopy to examine the ultrastructural effects of ApoM plasma transfer in the high-fat diet fed *Abca1/g1-rod/-rod* model. This model has been demonstrated to exhibit abnormal ultrastructure as evidenced by abnormal lipid droplet accumulation25. We discovered that ApoMTG treated mice appreciably had less lipid droplet accumulation in the RPE (Figure 1E and 1F). After quantification, the RPE of ApoMTG treated mice indeed had

significantly decreased lipid droplet counts compared to that of ApoMKO treated mice (Figure 1G). Another observation made was that there were significantly increased RPE melanosomes in ApoMTG treated mice (Figure 1H). As melanosomes are reportedly closely related to lysosomal function^{42–44}, we hypothesized that ApoMTG could potentially be ameliorating the RPE phenotype through lysosome-mediated lipid catabolism.

5.2.4 Rod photoreceptor function is improved with ApoM plasma transfer in high fat diet fed *Abca1/g1-rod/-rod* mice

We further hypothesized that rod photoreceptor function could be improved through RPE functional improvement as rod photoreceptor function is closely tied to RPE function⁴⁵. To measure rod photoreceptor function, we utilized full-field scotopic electroretinography to measure both the a-wave and b-wave amplitudes, which measure rod photoreceptor and inner retina function respectively⁴⁶ (Figure 1I and 1J). Scotopic a-wave and b-wave amplitudes were significantly improved in ApoMTG treated mice. These findings in tandem from the data in Figure 1D suggest the RPE of ApoMTG plasma treated mice functionally improved, leading to improved rod photoreceptor function.

5.2.5 Proper S1P binding of ApoM is necessary for amelioration of RPE lipid accumulation and rod photoreceptor function

The canonical binding partner of ApoM is sphingosine-1-phosphate (S1P)²⁷. We hypothesized that proper S1P binding of ApoM is necessary for functional rod photoreceptor and RPE improvement in the aforementioned *Abca1/g1-rod/-rod* model. To test this, we procured plasma from control mice (ApoMCtrl) and mice with a triple mutation in the ApoM binding site for S1P (ApoMTM)³⁵. ApoMTM produce mutated ApoM that is incapable of binding S1P. We then

used the same treatment paradigm as mentioned in Figure 1C to test if the binding mutation affected the extent of attenuation of the rod photoreceptor and RPE phenotype (Figure 2A). Compared to the control plasma treatment group, full-field scotopic electroretinography revealed a significant decrease in scotopic a-wave and b-wave amplitudes in ApoMTM-treated mice (Figure 2B and 2C). Hence, mutation of the ApoM binding site for S1P prevented any functional improvement in rod photoreceptors by plasma transfer.

In parallel with the functional electroretinography studies, we sought to investigate the structural effects of ApoMTM plasma transfer. We dissected and processed eyes of both the ApoMCtrl and ApoMTM treated mice for transmission electron microscopy to visualize the RPE and quantify lipid droplet and melanosome counts within the RPE (Figure 2D and 2E). Consistent with the photoreceptor phenotype, there were significantly increased lipid droplet counts in the ApoMTM treated RPE compared to those of ApoMCtrl treated RPE, even though the number of melanosomes were similar (Figure 2F and 2G). These data suggest that the ApoM binding site for S1P is necessary for both the structural amelioration of RPE lipid burden and functional improvement of rod photoreceptors.

5.2.6 S1PR3 knockout recapitulates features of RPE lipotoxicity

We sought to investigate which downstream effector of S1P is necessary for the ameliorative effects of ApoM-S1P plasma transfer therapy. We hypothesized that knocking out a key effector of S1P would be sufficient to recapitulate the RPE lipotoxicity features seen in high fat diet fed *Abca1/g1-rod/-rod* mice. After using publicly available bulk RNA sequencing data of human RPE cells (Supplemental Figure 1), we identified two S1P receptors to be much more highly expressed than all others: S1P receptor 1 (S1PR1) and S1P receptor 3 (S1PR3). We first generated RPE-specific conditional knockout mice of *S1pr1* (*S1pr1-RPE/-RPE*) and

administered high fat diet for six weeks to investigate whether they recapitulate RPE lipotoxicity features (Supplemental Figure 2A). We did not appreciate any functional changes between knockout and wild type mice (Supplemental Figure 2B and 2C).

We next generated germline *S1pr3* knockout mice (*S1pr3*^{-/-}) to test if they would recapitulate key features of RPE lipotoxicity after six weeks of high fat diet (Figure 3A). Light bleach dark adaptation electroretinography assessment of *S1pr3*^{-/-} RPE demonstrated significant functional reduction compared to that of wild type RPE (Figure 3B). Furthermore, structural assessment of RPE through transmission electron microscopy seemed to phenocopy RPE of high fat diet fed *Abca1/g1-rod/rod* (Figure 3C and 3D). Indeed, quantification of lipid droplets and melanosomes in *S1pr3*^{-/-} compared to wild types demonstrated significantly increased lipid droplet count and significantly decreased melanosome count (Figure 3E and 3F). Rod photoreceptor function assessed by full field scotopic electroretinography also showed significantly decreased scotopic a-wave and b-wave amplitudes in *S1pr3*^{-/-} (Figure 3G and 3H). These data suggest that *S1PR3* is the key effector of ApoM-S1P, and abrogation of *S1PR3* recapitulate distinguishing features of RPE lipotoxicity as seen in the *Abca1/g1-rod/rod* model.

5.2.7 ApoM overexpression does not rescue high fat diet induced *S1pr3*^{-/-} RPE lipotoxicity

Although *S1pr3* knockout with high fat diet was sufficient to provoke a RPE lipotoxicity phenotype, we sought to investigate if ApoM overexpression is sufficient to rescue the high fat diet induced *S1pr3*^{-/-} RPE lipotoxicity phenotype. We crossed *S1pr3*^{-/-} with ApoMTG mice to generate *S1pr3*^{-/-}/ApoMTG and administered high fat diet for 6 weeks (Figure 4A). Indeed, RPE function as measured by light bleach dark adaptation electroretinography demonstrated no significant differences between *S1pr3*^{-/-} and *S1pr3*^{-/-}/ApoMTG (Figure 4B). Structural assessment of RPE through transmission electron microscopy showed grossly similar features

between S1pr3^{-/-} and S1pr3^{-/-}/ApoMTG (Figure 4C and 4D). Lipid droplet quantification demonstrated no significant difference between S1pr3^{-/-} and S1pr3^{-/-}/ApoMTG (Figure 4E). However, melanosome quantification revealed significantly lower melanosome counts in S1pr3^{-/-}/ApoMTG, suggesting overexpression of ApoM may influence melanosome counts (Figure 4F). In corroboration with RPE functional data, rod photoreceptor functional assessment did not reveal any significant changes in scotopic a-wave and b-wave amplitudes through full-field scotopic electroretinography (Figure 4G and 4H). These data suggest ApoM-S1P acts through S1PR3 in RPE to ameliorate lipotoxicity.

5.2.8 ApoM-S1P does not change cholesterol efflux capacity in ARPE-19

Following the characterization of the in vivo effects of ApoM-S1P on RPE lipotoxicity, we sought to investigate how ApoM-S1P mechanistically ameliorates the lipotoxicity phenotype. We utilized the commercially available ARPE-19 cell line to feasibly elucidate these mechanisms. Using a previously outlined protocol to use ApoM-S1P in vitro³⁶, we tested if adding ApoM-S1P was sufficient to influence cholesterol efflux capacity according to a commercially available assay (Figure 5A). We utilized serum from ApoM knockout mice as cholesterol acceptors for both groups and added recombinant ApoM-S1P to one group to test if the addition of ApoM-S1P influences cholesterol efflux. Despite previous reports of ApoM influencing cholesterol efflux³⁸, we did not observe significant differences in cholesterol efflux capacity with the addition of ApoM-S1P. These data suggest that the effect of ApoM-S1P on cholesterol efflux could be cell type dependent, and its effect on ameliorating RPE lipotoxicity is not through manipulating cholesterol efflux.

5.2.9 Photoreceptor outer segment treatment of ex vivo RPE recapitulate features of in vivo RPE lipotoxicity

To further elucidate the mechanisms seen in RPE lipotoxicity, we sought to emulate cardinal features of lipotoxicity seen in the in vivo RPE models in in vitro and ex vivo models. We first utilized ARPE-19 cells to recapitulate lipid overburden as seen in the in vivo model by inundating cells with exogenous photoreceptor outer segments (Supplemental Figure 3). This model has been used previously to test RPE phagocytic and lipid processing capacity^{42,43,47,48}. Using commercially available bovine photoreceptor outer segments (POS), we first observed the amount of neutral lipid staining through BODIPY staining after treatment with a 10:1 and 20:1 POS to RPE ratio. The 10:1 ratio is what is recommended to observe normal phagocytic and processing behavior of RPE⁴⁷. As expected, we observed increased BODIPY staining with increased inundation with POS. We next investigated whether recombinant ApoM-S1P could reduce the amount of BODIPY staining seen after POS incubation. Indeed, we observed less BODIPY staining after incubation with ApoM-S1P. These data suggest ApoM-S1P may act similarly in ARPE-19 cells as in vivo RPE to ameliorate lipid burden.

We further sought to test if the lipid overburden phenotype could be appreciated in an ex vivo context. We dissected eyes from wild type mice, and removed the cornea, lens, and retinas to leave the RPE, choroid, and sclera complex intact. We then incubated the remaining eyecup in media with FITC-labelled POS to observe whether ex vivo RPE could still reliably phagocytose POS. Indeed, we observed increased FITC staining correlated with increased POS treatment in ex vivo RPE (Figure 5B).

5.2.10 Lipophagy abrogation recapitulate features of RPE lipotoxicity

Previous work has demonstrated ApoM to be a novel regulator of autophagy, and ApoM preserves lysosomal function³⁵. As lipophagy is a selective form of autophagy, it stands to

reason that ApoM could also enhance lipophagy. Based on in vitro data suggesting ApoM-S1P does not influence cholesterol efflux in RPE cells, we hypothesized that ApoM-S1P ameliorates RPE lipotoxicity by enhancing lipophagy. Supporting our observations of increased melanosome counts with ApoM treatment in *Abca1/g1-rod/-rod*, lipophagy was a candidate mechanism to explain how ApoM-S1P ameliorates lipotoxicity since melanosome and lysosomal function are closely associated^{42–44}. We therefore sought to investigate if abrogating lipophagy results in RPE lipotoxicity as seen in the aforementioned in vivo models.

Lysosomal acid lipase (LIPA) is an essential enzyme necessary for lipid catabolism through lipophagy to occur⁴⁹. We therefore generated germline lysosomal acid lipase knockout mice (*Lipa*^{-/-}) and placed them on high fat diet to test if they would develop RPE lipotoxicity (Supplemental Figure 4A). Transmission electron microscopy analysis showed structural intracellular changes in what may have been lipid droplets improperly processed (Supplemental Figure 4B and 4C). RPE functional analysis through light bleach dark adaptation electroretinography of *Lipa*^{-/-} demonstrated marginal decrease in scotopic a-wave recovery (Supplemental Figure 4D). Rod photoreceptor functional analysis through full field scotopic electroretinography revealed significantly reduced scotopic a-wave and b-wave amplitudes in *Lipa*^{-/-} (Supplemental Figure 4E and 4F). As LIPA is a largely ubiquitously expressed enzyme essential for lipid catabolism, the germline *Lipa* knockout model most likely suffers from deleterious effects from multiple cell types, including retinal cells such as photoreceptors.

To circumvent non-cell autonomous effects of *Lipa* knockout, we generated a conditional RPE knockout of *Lipa* (*Lipa*-RPE/-RPE) and placed the mice on a high fat diet (Figure 6A). *Lipa*-RPE/-RPE mice exhibited significantly decreased RPE function as measured by light bleach dark adaptation electroretinography (Figure 6B). Transmission electron microscopy analyses of *Lipa*-

RPE/-RPE RPE showed marked accumulation of lipid droplets along with undigested fragments of photoreceptor outer segments (Figure 6C and 6D). However, rod photoreceptor function as measured by full field scotopic electroretinography did not demonstrate significant differences (Figure 6E and 6F). This model recapitulates many features of the *Abca1/g1-rod/-rod* and *S1pr3-/-* models, but the advanced functional RPE deficits and accumulation of obvious undigested photoreceptor fragments suggest lipophagy abrogation does not comprehensively represent the mechanism of the dry AMD-like phenotype seen in the *Abca1/g1-rod/-rod* and *S1pr3-/-* models.

5.3 Discussion

In this study, we have investigated the role of ApoM as a potential therapeutic to ameliorate RPE lipotoxicity as seen in early dry AMD. We discovered older patients as well as patients with AMD had significantly lower levels of circulating ApoM as measured by ELISA. We demonstrated that the dry AMD-like model in the high fat diet fed *Abca1/g1-rod/-rod* paradigm could have improved RPE and subsequent rod photoreceptor function along with decreased RPE lipid droplet counts through ApoM plasma transfer therapy. We also demonstrated these ameliorative effects are contingent on proper binding of S1P by ApoM by using ApoM mutant binding plasma transfer therapy. Furthermore, we elucidated S1PR3 as a critical effector of ApoM as *S1pr3* knockout recapitulated the same dry AMD-like features seen in *Abca1/g1-rod/-rod* mice. This idea was further supported by the lack of rescue when *S1pr3* knockout mice were crossed with ApoM transgenic over expressing mice to generate *S1pr3* knockout ApoM overexpressing mice. In vitro assays using ARPE-19 cells showed ApoM-S1P does not influence cholesterol efflux, suggesting an alternate pathway for lipid elimination. Ex vivo eyecup treatment using POS demonstrated similar features as the in vivo models. Finally, the

characterization of lipophagy knockout mice suggested the mechanism of RPE lipotoxicity seen in *Abca1/g1-rod/-rod* and *S1pr3-/-* could be due to impaired lipophagy, but further investigation is warranted as complete abrogation of lipophagy lead to a more advanced disease phenotype.

As current approaches to treat AMD focus on the advanced stages, our study's approach was mainly concerned with discovering new therapeutic avenues for the early stages of the disease. As such, it was critical to model and treat a potential pathogenesis of the disease even before the appreciation of drusen. Many previous investigators have revealed different insights as to how drusen might develop¹, but an inevitable shared phenomenon in each of these theories is the dysfunction and compromise of RPE. In our initial high fat diet fed *Abca1/g1-rod/-rod* model, we leveraged the RPE's limitations in processing improperly loaded photoreceptor outer segments that lead to lipid overburden and dysfunction. As ABCA1 polymorphisms are a known risk factor for AMD¹⁸, we believe this model is a limited but accurate model for early AMD. Nonetheless, our approach to using ApoM-S1P to ameliorate RPE lipotoxicity remains to be validated as an appropriate therapeutic for other models of RPE lipid overburden.

As RPE lipotoxicity remains a central issue in the development of AMD, innovative approaches to alleviate lipid burden on RPE is essential to open new avenues of treatment. The RPE largely has two options for naturally eliminating lipids: efflux and catabolism^{48–50}. Surprisingly, our data showed that ApoM-S1P did not influence cholesterol efflux in ARPE-19. Therefore, our suspicion was that ApoM-S1P signaling promotes lipid catabolism in RPE. Furthermore, we suspected lipophagy to be a primary modality of lipid elimination as we observed significant changes in melanosome counts after ApoM plasma transfer. We did not observe a direct mechanistic effect of ApoM-S1P influencing lipophagy, but data from lipophagy knockout models suggest ApoM-S1P may be enhancing lipophagy and increasing melanosome counts.

Further investigation is warranted to fully connect a mechanism of ApoM-S1P signaling and enhancement of lipophagy.

Although S1PR1 and S1PR3 were the predominantly expressed S1P receptors according to human RPE bulk RNA sequencing data, other studies have shown S1PR2 may contribute to RPE function³⁶. Terao et al. demonstrated that S1PR2 is important in regulating inflammatory profiles of ARPE-19 cells, and intravitreal injection of a S1PR2-specific inhibitor in a laser-induced choroidal neovascularization model reduces choroidal neovascularization lesion size. These results suggest S1PR2 may regulate inflammatory and angiogenic factors in RPE, but the role of S1PR2 and even S1PR4 and S1PR5 although scantily expressed should be assessed in the context of early dry AMD models.

The endeavor to discover novel therapeutics to treat AMD, a leading cause of blindness, has made great strides despite the lack of ideal AMD models. It is evident that AMD pathogenesis is complicated by numerous genetic and environmental factors, so it is therefore critical to address and prevent the initial impetus that could cascade into catastrophic vision loss. Our study, specifically focused on addressing the initial impetus of RPE lipotoxicity, highlights a novel therapeutic use of ApoM-S1P to enhance RPE lipid elimination to prevent RPE lipotoxicity, which has the potential to become an effective method to delay or prevent onset of AMD.

5.4 Materials and Methods

Animals

All animal experiments were conducted in accordance with the ARVO Statement for the Use of Animals in Ophthalmic and Vision Research and Washington University School of Medicine in St. Louis Animal Care and Use guidelines and after approval by the Institutional Animal Care

and Use Committee (IACUC). Male and female mice between 8 and 12 weeks old (2-3 months of age) were used in this study. Mice were housed in a 12-hour light/dark cycle with free access to food and water. For high-fat diet (HFD) feeding experiments, only male mice were used. We used an adjusted-calorie diet (60% from fat, 25% kcal from carbohydrate, and 15% kcal from protein (ENVIGO, Indianapolis, IN) as a HFD, starting from 6 weeks old to the target age of analysis. We used Purina 4043 chow (13% kcal from fat, 62% kcal from carbohydrate, 25% kcal from protein) as the normal diet. ApoMKO, ApoMTG, ApoMTM, S1pr3^{-/-}, S1pr1-RPE^{-/-}RPE, Lipa^{-/-}, and Lipa-RPE^{-/-}RPE mice were all generated in house by the Javaheri and Apte laboratories. Mice with RPE conditional knockouts were crossed with mice carrying one copy of the Bestrophin1 (Best1-cre) transgene, which are available from Jackson Laboratories (017557). We confirmed that these mice did not carry the Crb1 gene rd8 mutation (data not shown). Mice were fully backcrossed to the inbred C57BL/6J background.

Sandwich ELISA for human unfolded plasma ApoM

Human plasma were collected from volunteer donors. An ELISA plate (Costar 3590 high binding) was coated with 50 μ l of capture antibody (clone 1G9) by diluting to 5 μ g/ml in TBS (pH 7.4) and incubated at room temperature overnight. The plate was blocked for 2 h with 200 μ l of 2% BSA in TBS (pH 7.4). Ten microliters of each plasma sample were mixed with 90 μ l of 50 mmol/l DTT, from Sigma-Aldrich, St. Louis, MO, in a 0.2 mol/l sodium phosphate buffer (pH 8.5). Disulfide bridges in apoM were broken by incubating samples at 30°C for 15 min. One hundred microliters of 0.6 mol/l iodoacetamide (Sigma-Aldrich) in a 0.02 mol/l sodium phosphate buffer (pH 8.0) were then added and samples were incubated for 1 h at room temperature in the dark to alkylate free cysteines in apoM and prevent reformation of disulfide bridges. After 1 h, the samples were diluted fifty times (variable for the standard curve) in TBS

(pH 7.4) containing 1% BSA and transferred to the ELISA plate for overnight incubation at room temperature. The plate was washed three times with TBS (pH 7.4) and incubated overnight at room temperature with 75 μ l of detection antibody (clone EPR2904) diluted to 125 ng/ml in TBS (pH 7.4) containing 1% BSA and 2% Triton-X 100. The plate was washed three times with TBS (pH 7.4) and 0.1% Triton-X 100 and incubated for 2 h with 75 μ l of HRP-conjugated anti-rabbit IgG antibody diluted to 125 ng/ml in TBS (pH 7.4) containing 1% BSA and 0.1% Triton-X 100. Finally, the plate was washed three times with TBS (pH 7.4) and 0.1% Triton-X 100, and apoM was detected by reading absorbance at 492 nm after incubation with 75 μ l o-phenylenediamine/hydrogen peroxide solution for 10 min followed immediately by addition of 75 μ l 1 mol/l H₂SO₄. The apoM concentration of measured samples was determined from the standard curve included in each assay run.

Plasma transfer

Plasma was obtained from either ApoMKO or ApoMTG mice from peripheral blood via the retro-orbital plexus under anesthesia. 120 μ L of either ApoMKO or ApoMTG plasma was intraperitoneally injected in Abca1/g1-rod/-rod starting at 6 weeks of age. High fat diet was implemented on the first day of injections. Mice were injected thrice weekly for 6 weeks.

Electroretinography

Full field scotopic ERG was performed as previously described⁴⁶. A UTAS BigShot System (LKC Technologies Inc.) was used. Mice were dark adapted overnight. Under red light illumination, mice were anesthetized with an intraperitoneal injection of 86.9 mg/kg ketamine and 13.4 mg/kg xylazine. Pupils were dilated with 1% tropicamide eye drops. Body temperature was maintained at 37°C with a heating pad. Contact lens electrodes were placed bilaterally with

appropriate reference and ground electrodes. The stimulus consisted of a full-field white light flash (10 μ s). Raw data were processed using MATLAB software (MathWorks). The amplitude of the a wave was measured from the average pretrial baseline to the most negative point of the average trace, and the b wave amplitude was measured from that point to the highest positive point.

For testing dark adaptation, we modified the protocol as previously described⁵¹. Briefly, we used a UTAS BigShot System (LKC Technologies Inc.) to get scotopic a-waves. A bright LED light (150,000 lux) was applied to both eyes for 15 seconds to photobleach an estimated 90% of the visual pigment. The recovery of the ERG responses was monitored at fixed post-bleach time points within 100 minutes after the bleach. The sensitivity was calculated as the ratio of dim flash response amplitude and the corresponding flash intensity in the linear range of the intensity-response curve. The post-bleach sensitivities were normalized to their dark-adapted prebleach level.

Transmission electron microscopy

We performed transmission electron microscopy as previously described⁴⁶. For ultrastructural analyses, eyecups were fixed in 2% paraformaldehyde (PFA)/2.5% glutaraldehyde (Polysciences Inc.) in 100 mM sodium cacodylate buffer, pH 7.2, for 2 hours at room temperature and then overnight at 4°C. Samples were washed in sodium cacodylate buffer at room temperature and postfixed in 1% osmium tetroxide (Polysciences Inc.) for 1 hour. Samples were then rinsed extensively in dH₂O prior to en bloc staining with 1% aqueous uranyl acetate (Ted Pella Inc.) for 1 hour. Following several rinses in dH₂O, samples were dehydrated in a graded series of ethanol and embedded in Eponate 12 resin (Ted Pella Inc.). Sections of 95 nm were cut with a Leica Ultracut UCT ultramicrotome (Leica Microsystems Inc.), stained with uranyl acetate and lead

citrate, and viewed on a JEOL 1200 EX transmission electron microscope (JEOL USA Inc.) equipped with an AMT 8 megapixel digital camera and AMT Image Capture Engine V602 software (Advanced Microscopy Techniques).

Cell culture

ARPE-19 was purchased from American Type Culture Collection (Manassas, VA, USA) and used for experiments. Dulbecco's Modified Eagle's Medium/F12 (Sigma-Aldrich, St. Louis, MO, USA) containing 1% penicillin/streptomycin (Sigma-Aldrich, St. Louis, MO, USA) and 10% fetal bovine serum was used for culture medium. Medium was changed every 2 days. Cells in the range of passages 3-16 were used for studies. All experiments were performed after serum starvation.

Preparation of ApoM-S1P

S1P was obtained from Enzo Life Sciences, inc. (Exeter, UK), and dissolved in methanol at 0.5 mg/mL. Before use in experiments, the methanol was evaporated using nitrogen gas. Human recombinant ApoM was obtained from R&D Systems (Minneapolis, MN, USA) and combined to create the ApoM-S1P complex as previously described³⁷. S1P was dissolved in ApoM, followed by 45 minutes of incubation at room temperature.

Preparation of FITC labelled POS

POS were labelled with FITC as previously described⁴⁷. Briefly, POS were incubated with fluorescein-t-isothiocyanate (FITC 'Isomer I') from ThermoFisher Scientific (Waltham, MA, USA) for 1 hour and washed thoroughly with PBS.

Treatment of ARPE-19 and ex vivo eyecups

To challenge RPE cells with photoreceptor outer segments, POS were obtained from InVision BioResources (Seattle, WA, USA). For ARPE-19, cells were allowed to adhere overnight in chamber slides from Ibidi (Germany). Media was exchanged for POS rich media at a 10:1 or 20:1 POS to RPE ratio as described previously⁴⁷. Cells were incubated for 4 hours at 37°C in a humidified cell culture incubator with 5% CO₂. After incubation, ApoM-S1P that was previously prepared was added and incubated for 1 hour at 37°C in a humidified cell culture incubation with 5% CO₂ after three washes with PBS. Cells were then washed thrice with PBS, fixed with 4% paraformaldehyde for 20 minutes at room temperature, and processed for analysis.

For ex vivo eyecups, mice were first sacrificed and enucleated. Eyes were carefully dissected to remove the cornea, lens, and retina. The remaining eyecup was placed in a 96-well U-bottom plate from Corning (Corning, NY, USA) with either control DMEM/F12 or media enriched with POS-FITC. The plate was then incubated for 2 hours at 37°C in a humidified cell culture incubator with 5% CO₂. After incubation, ApoM-S1P that was previously prepared was added and incubated for 1 hour at 37°C in a humidified cell culture incubation with 5% CO₂ after three washes with PBS. After three more PBS washes, eyecups were fixed for 20 minutes with 4% paraformaldehyde at room temperature. Eyecups were then immunohistologically stained and mounted onto a glass slide for imaging.

Immunohistochemistry

After fixing either ARPE-19 or eyecups, cells were stained with 1:500 DAPI (ThermoFisher Scientific, Waltham, MA, USA), 1:250 phalloidin-iFluor 594 (Abcam, Cambridge, UK), and 1:250 BODIPY 493/503 (ThermoFisher Scientific, Waltham, MA, USA) in PBS with 0.3% triton-X100 (Sigma-Aldrich, St. Louis, MO, USA) for 20 minutes at room temperature. Cells were then washed thrice with PBS before mounting and imaging.

Cholesterol efflux assay

Cholesterol efflux of ARPE-19 cells with addition of ApoM-S1P was assessed using the cholesterol efflux assay kit (ab196985) from Abcam (Cambridge, UK) according to the manufacturer's protocol. Briefly, ARPE-19 cells were allowed to adhere overnight in a 96-well tissue culture plate. Cells were loaded with fluorescently-labelled cholesterol before being treated with a cholesterol acceptor. Serum from ApoMKO mice were prepared as a cholesterol acceptor, so cells treated with ApoM-S1P had the complex mixed in with serum from ApoMKO mice. Fluorescence intensity of the supernatant and cell lysates were assessed with a microplate reader to then calculate a percentage of cholesterol efflux.

5.5 Acknowledgments

This work was supported by National Institutes of Health (NIH) grants R01 EY019287 (RSA) and P30 EY02687 (Vision Core Grant); The Retina Society (RSA); Jeffrey T. Fort Innovation Fund (RSA); Starr Foundation AMD Research Fund (RSA); Siteman Retina Research Fund (RSA); Carl Marshall and Mildred Almen Reeves Foundation (PAR and RSA); Retina Associates of St. Louis Research Fund (RSA); BrightFocus Foundation (RSA); a pilot project grant from the Washington University Genome Technology Access Center (RSA); an unrestricted grant from Research to Prevent Blindness to the John F. Hardesty, MD Department of Ophthalmology and Visual Sciences at Washington University School of Medicine in St. Louis. TL was supported by NIH Training Grant (1T32GM1397740-1) and Vitreoretinal Surgery Foundation Fellowship (VGR0023118).

The authors acknowledge Wandy L. Beatty, Molecular Microbiology Imaging Facility in Washington University School of Medicine, for electron microscopy analyses.

5.6 References

1. Apte RS. Age-Related Macular Degeneration. *N Engl J Med*. 2021;385(6):539-547.
doi:10.1056/NEJMcp2102061
2. Wong WL, Su X, Li X, et al. Global prevalence of age-related macular degeneration and disease burden projection for 2020 and 2040: a systematic review and meta-analysis. *The Lancet Global Health*. 2014;2(2):e106-e116. doi:10.1016/S2214-109X(13)70145-1
3. Rein DB, Wittenborn JS, Burke-Conte Z, et al. Prevalence of Age-Related Macular Degeneration in the US in 2019. *JAMA Ophthalmol*. 2022;140(12):1202-1208.
doi:10.1001/jamaophthalmol.2022.4401
4. Sene A, Khan AA, Cox D, et al. Impaired Cholesterol Efflux in Senescent Macrophages Promotes Age-Related Macular Degeneration. *Cell Metabolism*. 2013;17(4):549-561.
doi:10.1016/j.cmet.2013.03.009
5. Curcio CA. Antecedents of Soft Drusen, the Specific Deposits of Age-Related Macular Degeneration, in the Biology of Human Macula. *Invest Ophthalmol Vis Sci*. 2018;59(4):AMD182-AMD194. doi:10.1167/iovs.18-24883
6. Ferris FL III, Fine SL, Hyman L. Age-Related Macular Degeneration and Blindness due to Neovascular Maculopathy. *Archives of Ophthalmology*. 1984;102(11):1640-1642.
doi:10.1001/archopht.1984.01040031330019
7. Apte RS. Targeting Tissue Lipids in Age-related Macular Degeneration. *EBioMedicine*. 2016;5:26-27. doi:10.1016/j.ebiom.2016.02.003

8. Apte RS, Chen DS, Ferrara N. VEGF in Signaling and Disease: Beyond Discovery and Development. *Cell*. 2019;176(6):1248-1264. doi:10.1016/j.cell.2019.01.021
9. The Age-Related Eye Disease Study 2 (AREDS2) Research Group*. Lutein + Zeaxanthin and Omega-3 Fatty Acids for Age-Related Macular Degeneration: The Age-Related Eye Disease Study 2 (AREDS2) Randomized Clinical Trial. *JAMA*. 2013;309(19):2005-2015. doi:10.1001/jama.2013.4997
10. Yang S, Zhao J, Sun X. Resistance to anti-VEGF therapy in neovascular age-related macular degeneration: a comprehensive review. *Drug Des Devel Ther*. 2016;10:1857-1867. doi:10.2147/DDDT.S97653
11. Vishwakarma S, Kaur I. Molecular Mediators and Regulators of Retinal Angiogenesis. *Seminars in Ophthalmology*. 2023;38(2):124-133. doi:10.1080/08820538.2022.2152706
12. Khachigian LM, Liew G, Teo KYC, Wong TY, Mitchell P. Emerging therapeutic strategies for unmet need in neovascular age-related macular degeneration. *J Transl Med*. 2023;21:133. doi:10.1186/s12967-023-03937-7
13. Liao DS, Grossi FV, El Mehdi D, et al. Complement C3 Inhibitor Pegcetacoplan for Geographic Atrophy Secondary to Age-Related Macular Degeneration: A Randomized Phase 2 Trial. *Ophthalmology*. 2020;127(2):186-195. doi:10.1016/j.optha.2019.07.011
14. Cheung CMG, Gan A, Fan Q, et al. Plasma lipoprotein subfraction concentrations are associated with lipid metabolism and age-related macular degeneration. *J Lipid Res*. 2017;58(9):1785-1796. doi:10.1194/jlr.M073684

15. Danis RP, Lavine JA, Domalpally A. Geographic atrophy in patients with advanced dry age-related macular degeneration: current challenges and future prospects. *Clin Ophthalmol.* 2015;9:2159-2174. doi:10.2147/OPHTH.S92359
16. Martin SS, Qasim AN, Wolfe M, et al. Comparison of High-Density Lipoprotein Cholesterol to Apolipoprotein A-I and A-II to Predict Coronary Calcium and the Effect of Insulin Resistance. *Am J Cardiol.* 2011;107(3):393-398. doi:10.1016/j.amjcard.2010.09.033
17. Shen LL, Xie Y, Sun M, et al. Associations of systemic health and medication use with the enlargement rate of geographic atrophy in age-related macular degeneration. *British Journal of Ophthalmology.* 2023;107(2):261-266. doi:10.1136/bjophthalmol-2021-319426
18. Winkler TW, Grassmann F, Brandl C, et al. Genome-wide association meta-analysis for early age-related macular degeneration highlights novel loci and insights for advanced disease. *BMC Med Genomics.* 2020;13:120. doi:10.1186/s12920-020-00760-7
19. Strunz T, Kiel C, Sauerbeck BL, Weber BHF. Learning from Fifteen Years of Genome-Wide Association Studies in Age-Related Macular Degeneration. *Cells.* 2020;9(10):2267. doi:10.3390/cells9102267
20. Landowski M, Bowes Rickman C. Targeting Lipid Metabolism for the Treatment of Age-Related Macular Degeneration: Insights from Preclinical Mouse Models. *J Ocul Pharmacol Ther.* 2022;38(1):3-32. doi:10.1089/jop.2021.0067
21. Kelly UL, Grigsby D, Cady MA, et al. High-density lipoproteins are a potential therapeutic target for age-related macular degeneration. *J Biol Chem.* 2020;295(39):13601-13616. doi:10.1074/jbc.RA119.012305

22. Rudolf M, Malek G, Messinger JD, Clark ME, Wang L, Curcio CA. Sub-retinal drusenoid deposits in human retina: Organization and composition. *Experimental Eye Research*. 2008;87(5):402-408. doi:10.1016/j.exer.2008.07.010
23. Pfeffer BA, Fliesler SJ. Reassessing the suitability of ARPE-19 cells as a valid model of native RPE biology. *Experimental Eye Research*. 2022;219:109046. doi:10.1016/j.exer.2022.109046
24. Storti F, Klee K, Todorova V, et al. Impaired ABCA1/ABCG1-mediated lipid efflux in the mouse retinal pigment epithelium (RPE) leads to retinal degeneration. *eLife*. 8:e45100. doi:10.7554/eLife.45100
25. Ban N, Lee TJ, Sene A, et al. Disrupted Cholesterol Metabolism Promotes Age-Related Photoreceptor Neurodegeneration. *J Lipid Res*. Published online June 26, 2018;jlr.M084442. doi:10.1194/jlr.M084442
26. Wolfrum C, Poy MN, Stoffel M. Apolipoprotein M is required for pre β -HDL formation and cholesterol efflux to HDL and protects against atherosclerosis. *Nat Med*. 2005;11(4):418-422. doi:10.1038/nm1211
27. Christoffersen C, Obinata H, Kumaraswamy SB, et al. Endothelium-protective sphingosine-1-phosphate provided by HDL-associated apolipoprotein M. *Proc Natl Acad Sci U S A*. 2011;108(23):9613-9618. doi:10.1073/pnas.1103187108
28. Christoffersen C, Nielsen LB, Axler O, Andersson A, Johnsen AH, Dahlbäck B. Isolation and characterization of human apolipoprotein M-containing lipoproteins. *Journal of Lipid Research*. 2006;47(8):1833-1843. doi:10.1194/jlr.M600055-JLR200

29. Xu N, Dahlbäck B. A Novel Human Apolipoprotein (apoM)*. *Journal of Biological Chemistry*. 1999;274(44):31286-31290. doi:10.1074/jbc.274.44.31286
30. Liu M, Seo J, Allegood J, et al. Hepatic Apolipoprotein M (ApoM) Overexpression Stimulates Formation of Larger ApoM/Sphingosine 1-Phosphate-enriched Plasma High Density Lipoprotein. *J Biol Chem*. 2014;289(5):2801-2814. doi:10.1074/jbc.M113.499913
31. Elsåe S, Ahnström J, Christoffersen C, et al. Apolipoprotein M binds oxidized phospholipids and increases the antioxidant effect of HDL. *Atherosclerosis*. 2012;221(1):91-97. doi:10.1016/j.atherosclerosis.2011.11.031
32. Christoffersen C, Jauhiainen M, Moser M, et al. Effect of Apolipoprotein M on High Density Lipoprotein Metabolism and Atherosclerosis in Low Density Lipoprotein Receptor Knock-out Mice*. *Journal of Biological Chemistry*. 2008;283(4):1839-1847. doi:10.1074/jbc.M704576200
33. Christensen PM, Liu CH, Swendeman SL, et al. Impaired endothelial barrier function in apolipoprotein M-deficient mice is dependent on sphingosine-1-phosphate receptor 1. *FASEB J*. 2016;30(6):2351-2359. doi:10.1096/fj.201500064
34. Ruiz M, Okada H, Dahlbäck B. HDL-associated ApoM is anti-apoptotic by delivering sphingosine 1-phosphate to S1P1 & S1P3 receptors on vascular endothelium. *Lipids Health Dis*. 2017;16:36. doi:10.1186/s12944-017-0429-2
35. Guo Z, Valenzuela Ripoll C, Picataggi A, et al. Apolipoprotein M Attenuates Anthracycline Cardiotoxicity and Lysosomal Injury. *JACC Basic Transl Sci*. 2023;8(3):340-355. doi:10.1016/j.jacbts.2022.09.010

36. Terao R, Honjo M, Totsuka K, Miwa Y, Kurihara T, Aihara M. The role of sphingosine 1-phosphate receptors on retinal pigment epithelial cells barrier function and angiogenic effects. *Prostaglandins & Other Lipid Mediators*. 2019;145:106365.
doi:10.1016/j.prostaglandins.2019.106365
37. Terao R, Honjo M, Aihara M. Apolipoprotein M Inhibits Angiogenic and Inflammatory Response by Sphingosine 1-Phosphate on Retinal Pigment Epithelium Cells. *Int J Mol Sci*. 2017;19(1):112. doi:10.3390/ijms19010112
38. Vaidya M, Jentsch JA, Peters S, et al. Regulation of ABCA1-mediated cholesterol efflux by sphingosine-1-phosphate signaling in macrophages. *J Lipid Res*. 2019;60(3):506-515.
doi:10.1194/jlr.M088443
39. Chirinos JA, Zhao L, Jia Y, et al. Reduced Apolipoprotein M and Adverse Outcomes Across the Spectrum of Human Heart Failure. *Circulation*. 2020;141(18):1463-1476.
doi:10.1161/CIRCULATIONAHA.119.045323
40. Bosteen MH, Dahlbäck B, Nielsen LB, Christoffersen C. Protein unfolding allows use of commercial antibodies in an apolipoprotein M sandwich ELISA. *J Lipid Res*. 2015;56(3):754-759. doi:10.1194/jlr.D055947
41. Ban N, Lee TJ, Sene A, et al. Impaired monocyte cholesterol clearance initiates age-related retinal degeneration and vision loss. *JCI Insight*. 3(17). doi:10.1172/jci.insight.120824
42. Raposo G, Marks MS. The Dark Side of Lysosome-Related Organelles: Specialization of the Endocytic Pathway for Melanosome Biogenesis. *Traffic*. 2002;3(4):237-248.
doi:10.1034/j.1600-0854.2002.030401.x

43. Schraermeyer U, Peters S, Thumann G, Kociok N, Heimann K. Melanin Granules of Retinal Pigment Epithelium are Connected with the Lysosomal Degradation Pathway. *Experimental Eye Research*. 1999;68(2):237-245. doi:10.1006/exer.1998.0596
44. Kim IT, Choi JB. Melanosomes of retinal pigment epithelium--distribution, shape, and acid phosphatase activity. *Korean Journal of Ophthalmology*. 1998;12(2):85-91.
45. Tsin A, Betts-Obregon B, Grigsby J. Visual cycle proteins: Structure, function, and roles in human retinal disease. *J Biol Chem*. 2018;293(34):13016-13021. doi:10.1074/jbc.AW118.003228
46. Lee TJ, Sasaki Y, Ruzycski PA, et al. Catalytic isoforms of AMP-activated protein kinase differentially regulate IMPDH activity and photoreceptor neuron function. *JCI Insight*. Published online January 16, 2024. doi:10.1172/jci.insight.173707
47. Mazzoni F, Mao Y, Finnemann SC. Advanced Analysis of Photoreceptor Outer Segment Phagocytosis by RPE Cells in Culture. *Methods Mol Biol*. 2019;1834:95-108. doi:10.1007/978-1-4939-8669-9_7
48. Yako T, Otsu W, Nakamura S, Shimazawa M, Hara H. Lipid Droplet Accumulation Promotes RPE Dysfunction. *Int J Mol Sci*. 2022;23(3):1790. doi:10.3390/ijms23031790
49. Zhang S, Peng X, Yang S, et al. The regulation, function, and role of lipophagy, a form of selective autophagy, in metabolic disorders. *Cell Death Dis*. 2022;13(2):132. doi:10.1038/s41419-022-04593-3

50. Nolan ND, Jenny LA, Wang NK, Tsang SH. Retinal pigment epithelium lipid metabolic demands and therapeutic restoration. *Taiwan J Ophthalmol.* 2021;11(3):216-220.

doi:10.4103/tjo.tjo_31_21

51. Xue Y, Shen SQ, Corbo JC, Kefalov VJ. Circadian and light-driven regulation of rod dark adaptation. *Sci Rep.* 2015;5. doi:10.1038/srep17616

5.7 Figures

Figure 1

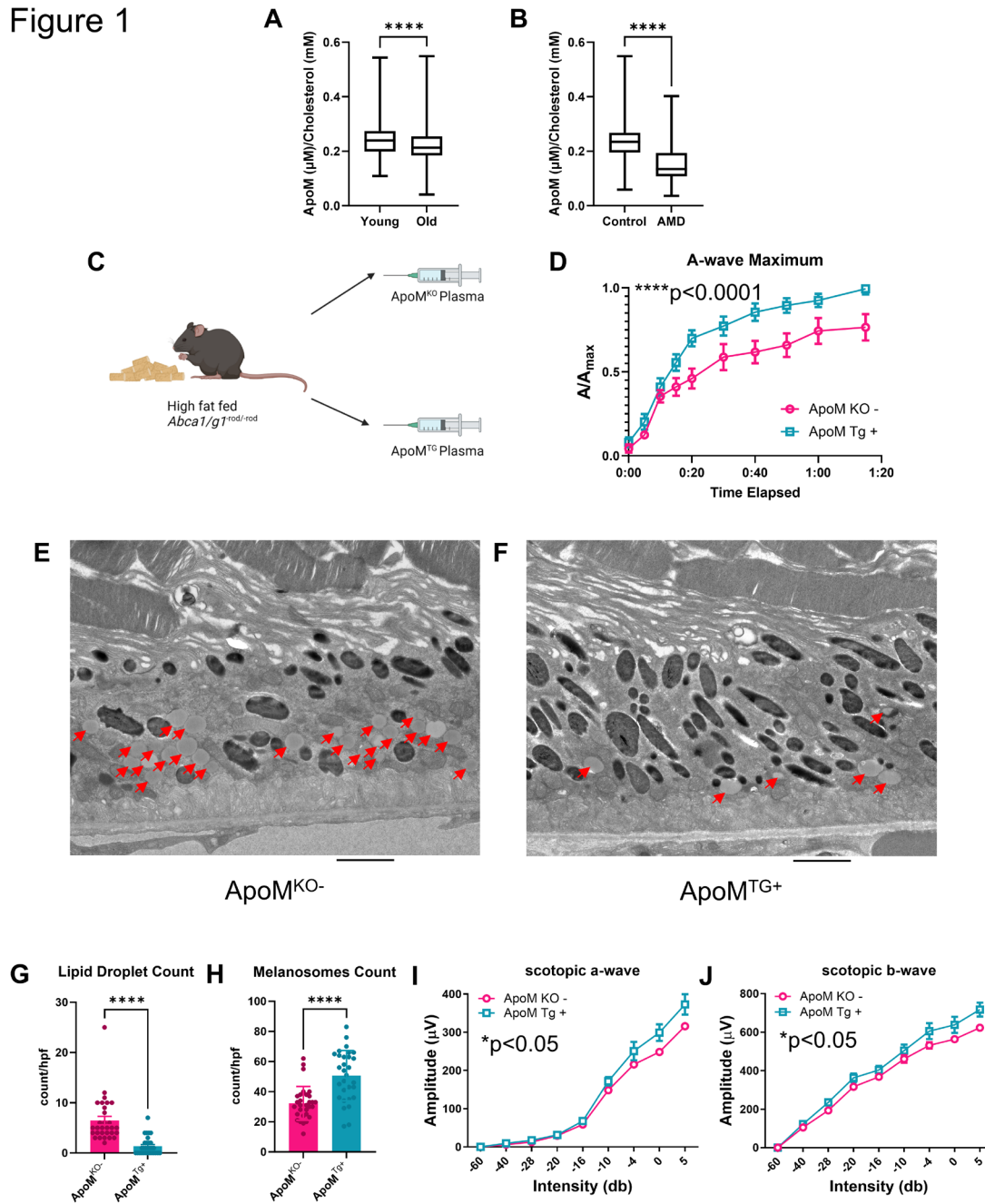


Figure 1. ApoM therapy ameliorates a dry AMD-like phenotype

(A) ApoM levels controlled to total cholesterol levels were measured in plasma of young ($n=299$) and old ($n=635$) patients using ELISA. Patients were considered young if aged 49 and under while old if aged 50 or over. Older patients had significantly lower levels of circulating ApoM compared to young patients (**** $p < 0.0001$, Welch's t-test). (B) ApoM levels controlled

to total cholesterol levels were measured in patients with (n=53) or without AMD (n=328) aged 65 and over. Patients with AMD had significantly lower ApoM levels compared to those without AMD (****p<0.0001, Welch's t-test). (C) High fat diet fed Abca1/g1-rod/-rod mice were treated with either ApoMKO or ApoMTG plasma. (D) RPE functional assessment using light bleach dark adaptation electroretinography (n=6) revealed significantly improved functional recovery in ApoMTG plasma treated mice (****p<0.0001, Two-way ANOVA). (E-F) Representative TEM imaging of RPE from either ApoMKO or ApoMTG plasma treated Abca1/g1-rod/-rod mice. Red arrows point to lipid droplets. (G) Quantitative assessment of lipid droplets per high-powered field within the RPE (n=30) revealed significantly reduced lipid droplets in ApoMTG plasma treated mice (****p<0.0001, Welch's t-test). (H) Quantitative assessment of melanosomes per high-powered field within the RPE (n=30) revealed significantly increased melanosomes in ApoMTG plasma treated mice (****p<0.0001, Welch's t-test). (I-J) Full-field scotopic electroretinography (n=6) demonstrated improved (I) rod photoreceptor (*p<0.05, Two-way ANOVA) and (J) inner retina (*p<0.05, Two-way ANOVA) function in ApoMTG plasma treated mice. Scale bar represents 2 μ m. Values are mean \pm SE.

Figure 2

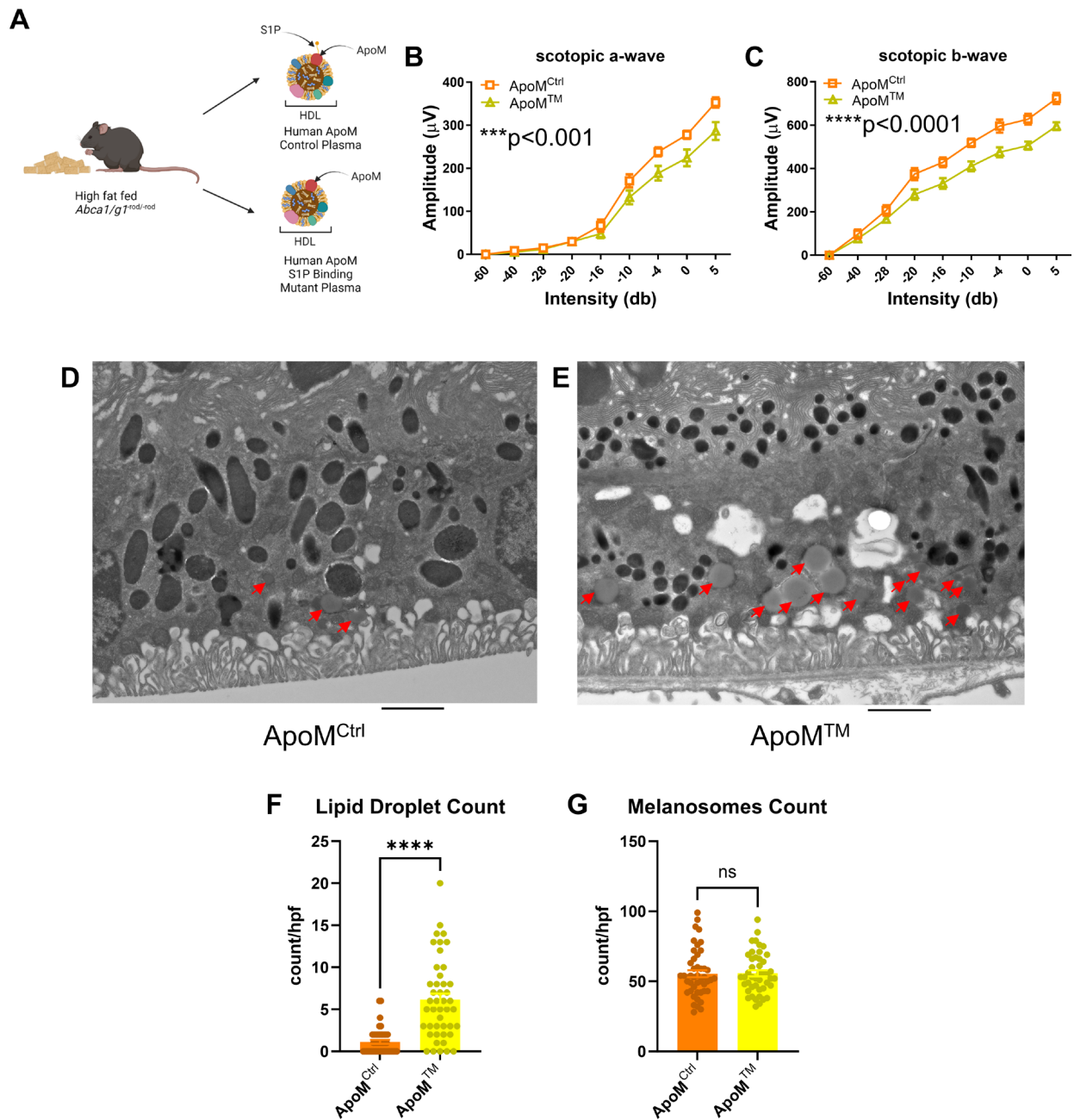


Figure 2. Proper binding of S1P by ApoM is necessary for RPE lipotoxicity amelioration

(A) High fat diet fed *Abca1/g1-rod/-rod* were treated with plasma from either control mice with human ApoM knocked in (ApoM^{Ctrl}) or mice expressing ApoM incapable of binding S1P (ApoMTM). (B-C) Full-field scotopic electroretinography (n=4) demonstrated significant reduction in (B) rod photoreceptor (*** $p < 0.001$, Two-way ANOVA) and (C) inner retina function (**** $p < 0.0001$, Two-way ANOVA) in ApoMTM treated mice. (D-E) Representative TEM imaging of RPE from either ApoM^{Ctrl} or ApoMTM plasma treated *Abca1/g1-rod/-rod*

mice. Red arrows point to lipid droplets. (F) Quantitative assessment of lipid droplets per high-powered field within the RPE (n=45) revealed significantly increased lipid droplets in ApoMTM plasma treated mice (****p<0.0001, Welch's t-test). (G) Quantitative assessment of melanosomes per high-powered field within the RPE (n=45) revealed no significant difference in melanosome counts between ApoMCtrl and ApoMTM plasma treated mice. Scale bar represents 2 μ m. Values are mean \pm SE.

Figure 3

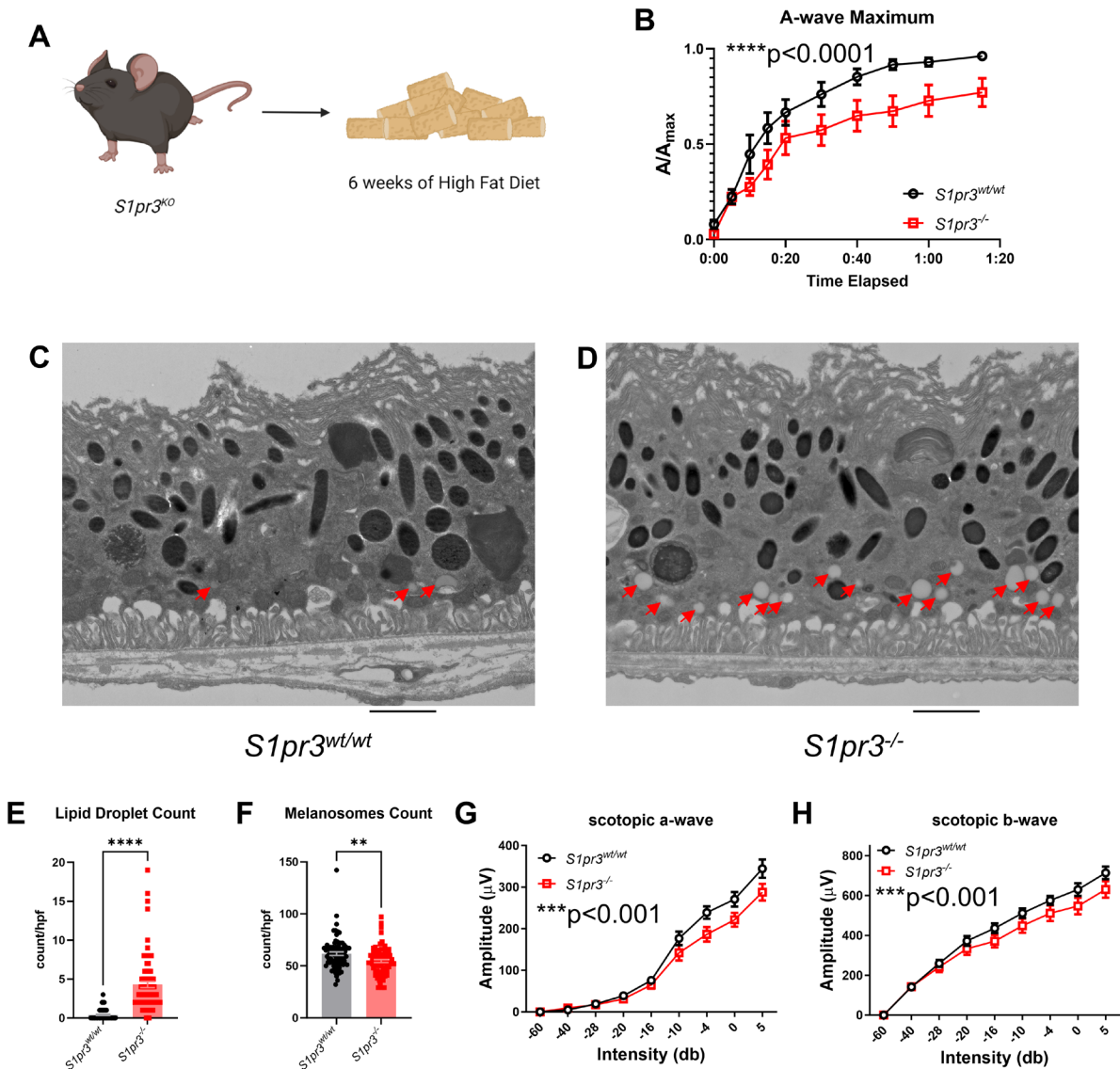


Figure 3. *S1pr3* knockout is sufficient to provoke a dry AMD-like RPE phenotype

(A) *S1pr3* germline knockout mice (*S1pr3^{-/-}*) were generated and placed on 6 weeks of high fat diet and subsequently assessed. (B) RPE functional assessment using light bleach dark adaptation electroretinography (n=10) revealed significantly reduced functional recovery in *S1pr3^{-/-}* mice compared to wild-type mice (**** $p < 0.0001$, Two-way ANOVA). (C-D) Representative TEM imaging of RPE from either wild-type or *S1pr3* knockout mice. Red arrows point to lipid droplets. (E) Quantitative assessment of lipid droplets per high-powered field within the RPE (n=80) revealed significantly increased lipid droplets in *S1pr3* knockout mice (**** $p < 0.0001$, Welch's t-test). (F) Quantitative assessment of melanosomes per high-powered field within the RPE (n=80) revealed significantly decreased melanosomes in *S1pr3* knockout mice (** $p < 0.01$, Welch's t-test). (G-H) Full-field scotopic electroretinography (n=8) demonstrated reduced (G) rod photoreceptor (*** $p < 0.001$, Two-way ANOVA) and (H) inner

retina (**p<0.001, Two-way ANOVA) function in S1pr3 knockout mice. Scale bar represents 2 μm . Values are mean \pm SE.

Figure 4

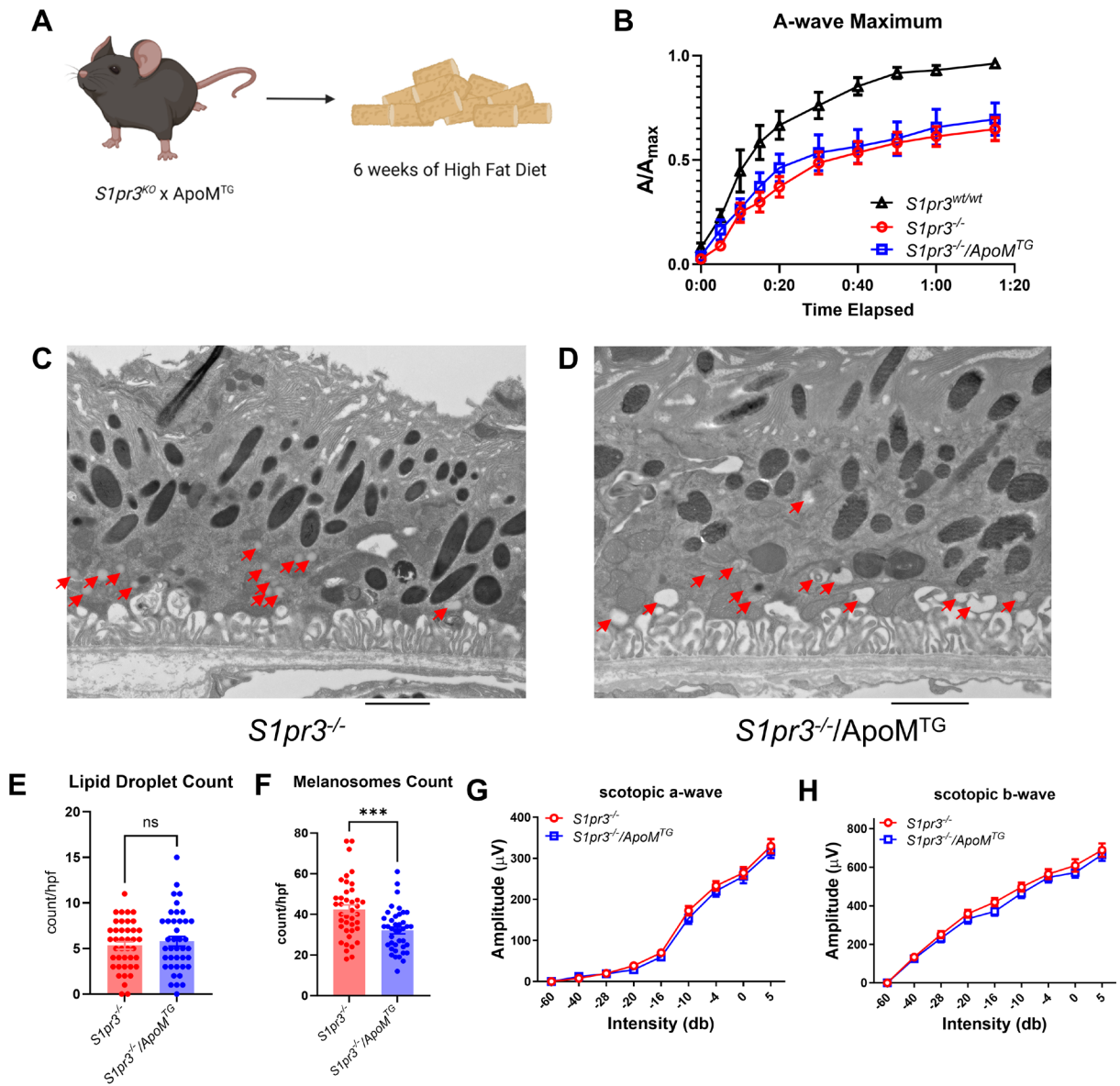


Figure 4. ApoM overexpression does not rescue S1PR3 deficiency induced RPE lipotoxicity

(A) *S1pr3* germline knockout mice (*S1pr3*^{-/-}) were crossed with ApoM overexpressing transgenic mice (ApoMTG) to generate *S1pr3*^{-/-}/ApoMTG mice and placed on 6 weeks of high fat diet and subsequently assessed. (B) RPE functional assessment using light bleach dark adaptation electroretinography (n=6) revealed no significant differences in functional recovery between *S1pr3*^{-/-} and *S1pr3*^{-/-}/ApoMTG mice. (C-D) Representative TEM imaging of RPE from either *S1pr3*^{-/-} or *S1pr3*^{-/-}/ApoMTG mice. Red arrows point to lipid droplets. (E) Quantitative assessment of lipid droplets per high-powered field within the RPE (n=42) revealed no significant differences between *S1pr3*^{-/-} and *S1pr3*^{-/-}/ApoMTG mice. (F) Quantitative assessment of melanosomes per high-powered field within the RPE (n=42) revealed significantly

decreased melanosomes in S1pr3^{-/-}/ApoMTG mice (***) $p < 0.001$, Welch's t-test). (G-H) Full-field scotopic electroretinography (n=8) demonstrated no significant differences in (G) rod photoreceptor and (H) inner retina between S1pr3^{-/-} and S1pr3^{-/-}/ApoMTG mice. Scale bar represents 2 μm . Values are mean \pm SE.

Figure 5

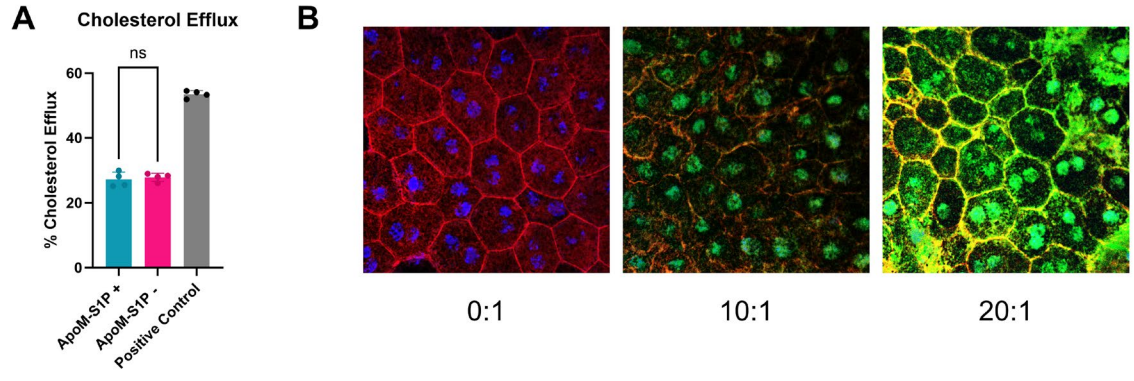


Figure 5. ApoM-S1P does not influence cholesterol efflux in ARPE-19

(A) The percentage of cholesterol efflux capacity in ARPE-19 cells were tested with the addition of ApoM-S1P. No significant differences were appreciated when ApoM-S1P was added to ARPE-19. (B) Ex vivo eyecups were treated with increasing dosages of FITC-labelled photoreceptor outer segments. RPE cells took in more POS according to dosage of POS. 20:1 ratio of POS to RPE cells represent lipid overburden as seen in aforementioned in vivo models.

Figure 6

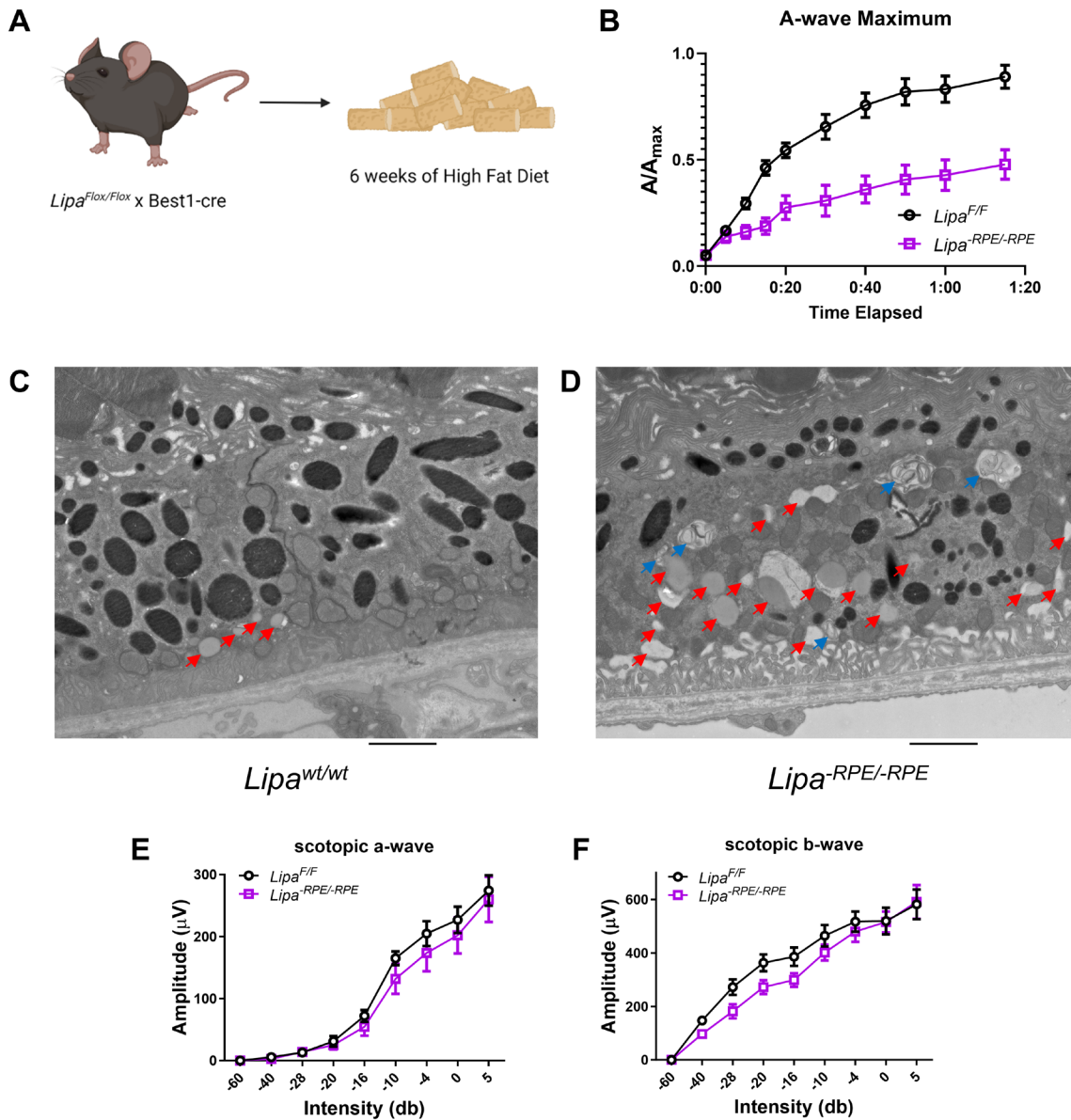
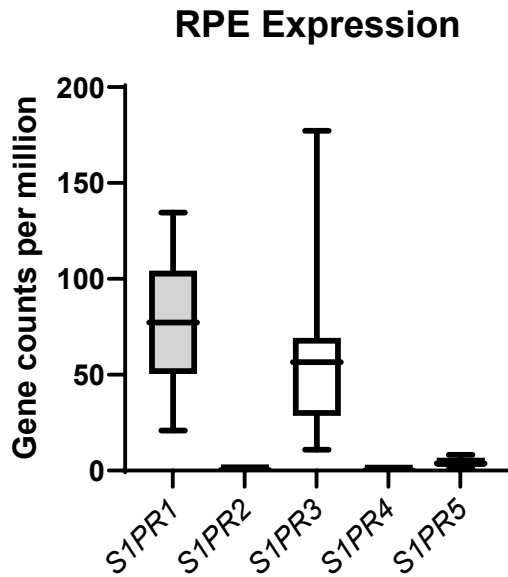
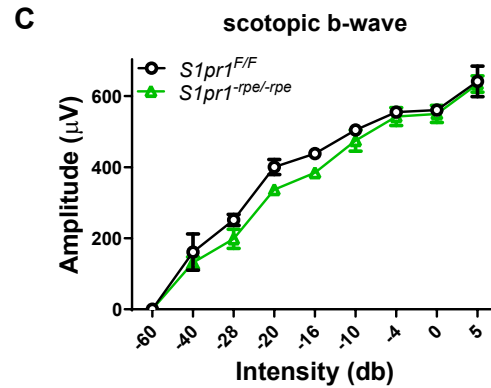
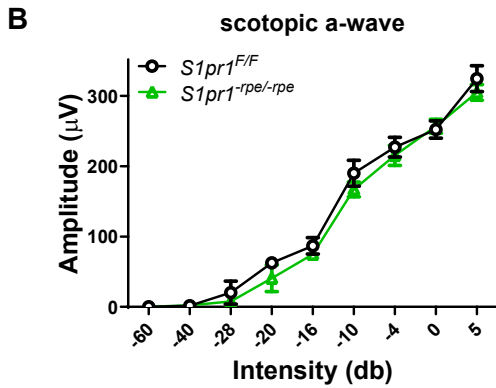
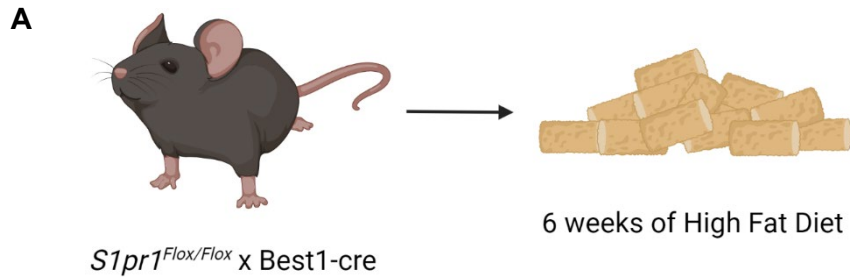


Figure 6. RPE-specific knockout of lipophagy recapitulate features of a dry AMD-like phenotype

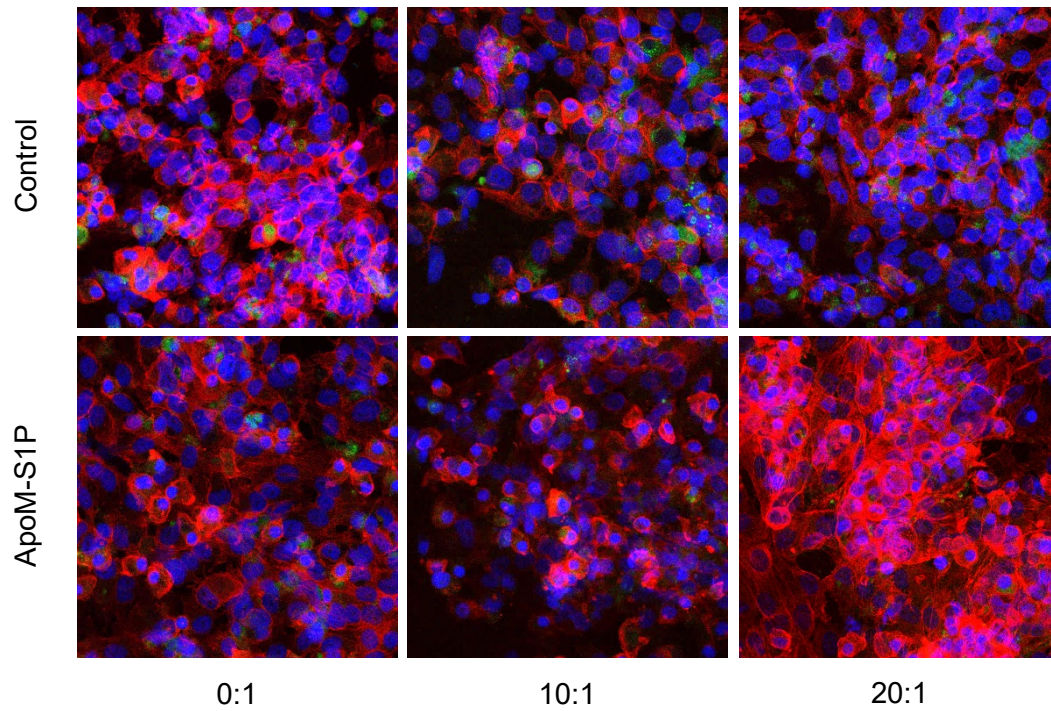
(A) RPE-specific lysosomal acid lipase conditional knockout mice (*Lipa*-RPE/-RPE) were generated and placed on 6 weeks of high fat diet and subsequently assessed. (B) RPE functional assessment using light bleach dark adaptation electroretinography (n=6) revealed significantly reduced functional recovery in *Lipa*-RPE/-RPE mice compared to wild-type mice (****p<0.0001, Two-way ANOVA). (C-D) Representative TEM imaging of RPE from either wild-type or *Lipa*-RPE/-RPE mice. Red arrows point to lipid droplets. Blue arrows point to dysmorphic structures with incompletely digest photoreceptor outer segments. (E-F) Full-field scotopic electroretinography (n=6) demonstrated no significant differences in (E) rod photoreceptor function but (F) inner retina (**p<0.01, Two-way ANOVA) function was significantly reduced in *Lipa*-RPE/-RPE mice. Scale bar represents 2 μ m. Values are mean \pm SE.



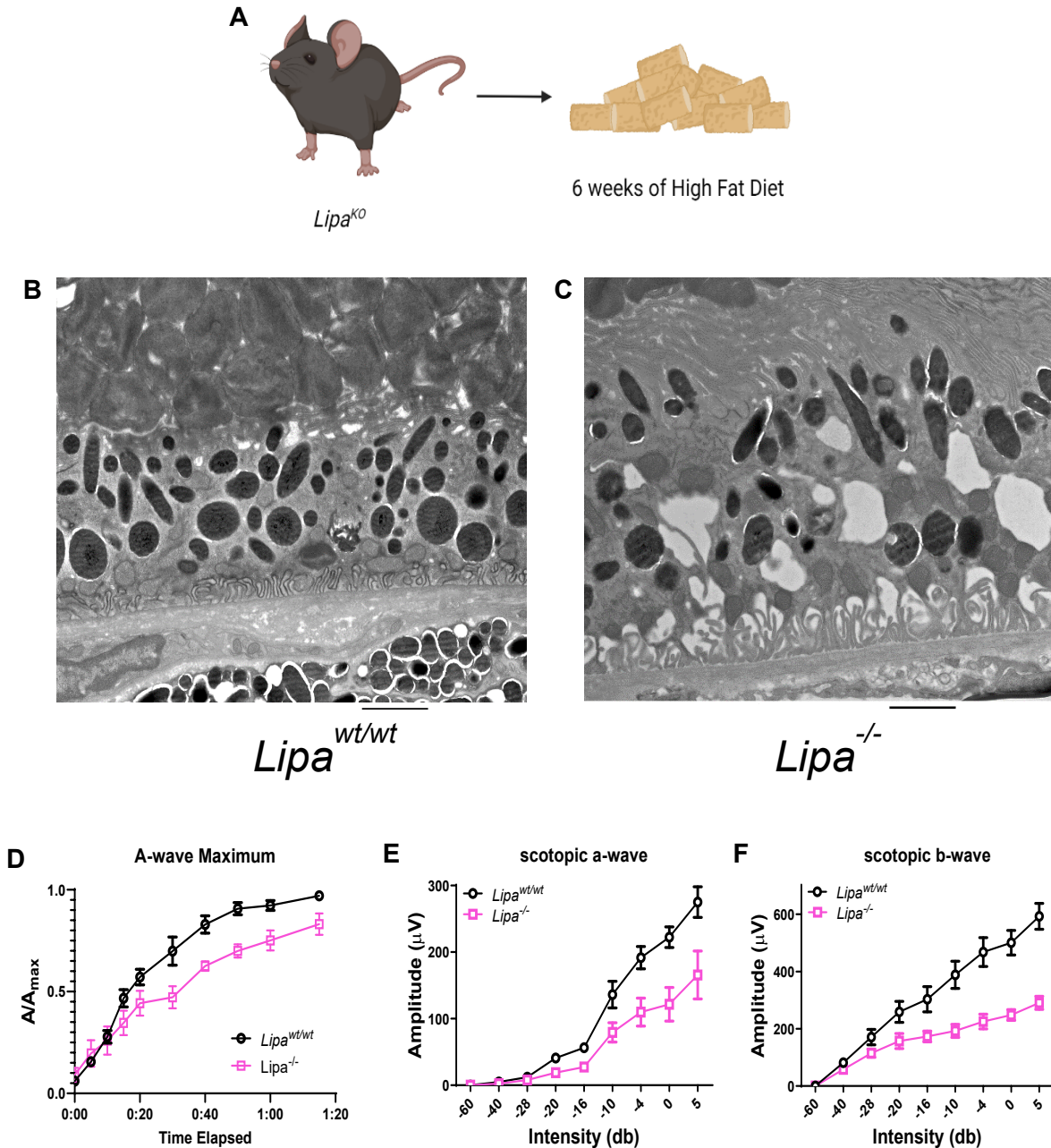
Supplementary Figure 1. *S1PR1* and *S1PR3* are the predominantly expressed S1P receptors in human RPE. According to publicly available bulk RNA sequencing data from humans, *S1PR1* and *S1PR3* are noticeably more expressed than other S1P receptors. There is therefore more rationale to investigate the roles of these S1P receptors in the mechanisms of RPE function. Values are mean \pm SE.



Supplementary Figure 2. RPE-specific conditional knockout mice of *S1pr1* do not show retinal deficits. (A) RPE-specific *S1pr1* conditional knockout mice (*S1pr1^{-RPE/-RPE}*) were generated and placed on 6 weeks of high fat diet and subsequently assessed. (B-C) Full-field scotopic electroretinography (n=8) demonstrated no significant differences in (B) rod photoreceptor and (C) inner retina between *S1pr1^{-RPE/-RPE}* and *S1pr1^{F/F}* mice. Values are mean ± SE.



Supplementary Figure 3. ApoM-S1P reduces neutral lipid staining in POS treated ARPE-19 cells. ARPE-19 cells were treated with increasing dosage of POS and with either no extra treatment or with recombinant ApoM-S1P. Blue staining represents DAPI+ nuclei staining; red staining represents Phalloidin+ actin staining; green staining represents BODIPY+ neutral lipid staining. The addition of ApoM-S1P seems to reduce the amount of BODIPY+ neutral lipid staining compared to control cells, even with increasing POS dosage.



Supplementary Figure 4. Germline lipophagy knockout results in widespread RPE and retinal dysfunction. (A) Lysosomal acid lipase germline knockout mice (*Lipa^{-/-}*) were generated and placed on 6 weeks of high fat diet and subsequently assessed. (B-C) Representative TEM imaging of RPE from either wild-type or *Lipa^{-/-}* mice. Gross structural changes and vacuole-like structures are appreciated in *Lipa^{-/-}* RPE. (D) RPE functional assessment using light bleach dark adaptation electroretinography (n=6) revealed significantly reduced functional recovery in *Lipa^{-/-}* mice compared to wild-type mice (****p<0.0001, Two-way ANOVA). (E-F) Full-field scotopic electroretinography (n=8) demonstrated reduced (E) rod photoreceptor (****p<0.0001, Two-way ANOVA) and (F) inner retina (****p<0.0001, Two-way ANOVA) function in *Lipa* knockout mice. Scale bar represents 2 µm. Values are mean ± SE.

Chapter 6: Summary and Future Directions

6.1 Summary

Visual acuity loss or blindness have a plethora of different etiologies, but none more devastating than retinal degeneration. Although our present understanding of the heterogeneous pathogenesis of different retinal diseases have immensely progressed with the advent of new and exciting technologies, the endeavor to comprehend the intricacies of cell metabolism and function in both homeostasis and disease will always persist. Throughout the dissertation, we have examined how both cell autonomous and non-cell autonomous effects can influence rod photoreceptor metabolism and function to yield new insights into how investigators can leverage rod photoreceptor metabolism to promote function and survival.

In chapter 1, we examined how the critical and ubiquitous nutrient sensing enzyme, AMPK, functions in rod photoreceptors. We specifically examined the catalytic isoforms of AMPK as AMPK is known to have heterogeneous effects across different tissues, and delineated a catalytic isoform specific effect from PRKAA2 that modulates rod photoreceptor metabolism. We discovered that PRKAA2 dysfunction, but not PRKAA1 dysfunction, leads to abnormal structure and function in rod photoreceptors. We discovered PRKAA2 dysfunction lead to increases in ATP, GTP, and cGMP which could partially be explained by the measured increased glycolysis. Unbiased phosphoproteomics revealed IMPDH as a potential downstream effector of PRKAA2 that may be dysregulated in *Prkaa2* knockout rod photoreceptors. Mechanistic studies of IMPDH function suggested PRKAA2 acts on IMPDH to inhibit IMPDH activity. In vivo inhibition of IMPDH in *Prkaa2* knockout rod photoreceptors by mycophenolate intravitreal injection recovered function of *Prkaa2* knockout rod photoreceptors. As AMPK is a critical enzyme in all tissues, it is essential that our understanding of AMPK function encompass tissue and

homeostasis context to develop targeted therapeutics for specific disease roles AMPK may play. Our findings suggest the AMPK-IMPDH axis is a therapeutically targetable phenomenon that may be applicable to other central nervous system cell types like rod photoreceptors.

Chapter 2 examined the role of NMNAT1 in photoreceptors. Similar to ATP homeostasis, NAD⁺ homeostasis has been well documented to be critical for survival and function across multiple tissues. LCA9 is associated with a mutation in the NAD⁺ biosynthesis enzyme NMNAT1, but is curiously known to only symptomatically affect the retina. We generated mouse models of *Nmnat1* knockouts in both germline and photoreceptor-specific *Nmnat1* knockouts that resulted in photoreceptor degeneration. These results demonstrated photoreceptors are uniquely vulnerable to degeneration due to NMNAT1 dysfunction. Mechanistic studies revealed SARM1 to be a critical mediator of NMNAT1-related photoreceptor degeneration. Germline knockouts of *Sarm1* concurrent with *Nmnat1* knockouts completely prevented photoreceptor degeneration suggesting SARM1 function is a direct cause of NMNAT1-related photoreceptor degeneration. This investigation revealed photoreceptors to uniquely rely on NMNAT1 for survival, but NMNAT1-related degeneration can be acutely prevented through inhibition of SARM1.

Beyond photoreceptor metabolism, this dissertation starting from chapter 3 also examined models and potential pathogenesis of AMD, a leading cause of blindness. These studies on AMD models demonstrate that there are non-cell autonomous factors that play into photoreceptor function. As the major cholesterol efflux transporter ABCA1 has been implicated in the pathogenesis of AMD, we examined the effect of cholesterol efflux abrogation in monocytes by selectively knocking out *Abca1* and *Abcg1* in monocytes. We discovered an age-related accumulation of sub-retinal deposits along with impaired dark adaptation and photoreceptor dysfunction, which are cardinal features of AMD. Through histological and gene

expression analyses, we revealed there is an aberrant accumulation of neutral lipids and monocytes in the sub-retinal space of monocyte-specific cholesterol efflux knockout mice. This study highlighted the significant role of innate immunity in the maintenance of healthy retina function, especially as it relates to lipid metabolism.

In chapter 4, we further explored the role of cholesterol efflux in rod photoreceptors. We generated *Abca1* and *Abcg1* rod photoreceptor-specific knockout mice and evaluated whether they develop any AMD-like phenotypes. With advanced age, these mice developed rod photoreceptor dysfunction and structural abnormalities appreciable on transmission electron microscopy. Closer structural examination revealed the RPE to accumulate lipid droplets in the advanced age knockouts. Furthermore, the administration of a high fat diet accelerated this phenotype, with appreciable phenotypic features after six weeks of diet and twelve weeks of age. This investigation elucidated an early dry AMD-like phenotype in which the RPE is overburdened with lipids, leading to rod photoreceptor dysfunction.

We lastly explored novel therapeutic pathways to treat the rod photoreceptor cholesterol efflux model in chapter 5. Proper lipid metabolism is key to maintaining function and integrity in RPE and rod photoreceptors as seen in chapter 4. We therefore hypothesized a novel way to enhance lipid metabolism in this model through ApoM therapy. By using plasma transfer, we were able to dramatically reduce the accumulation of lipids in RPE as well as recover both RPE and rod photoreceptor function. We also demonstrated that this effect relies on proper binding of ApoM to S1P. Mechanistic studies revealed S1PR3 as the major effector of the ApoM-S1P therapy as even ApoM overexpression does not rescue the RPE lipotoxicity phenotype in *S1pr3* knockouts. We also demonstrated that these effects in vivo can be recapitulated in vitro and ex vivo. Lastly, we hypothesized that lipophagy is the major lipid elimination pathway being utilized in ApoM-

S1P therapy. Our results from lipophagy knockout studies indicated that lipophagy could potentially be a mechanism for ApoM-S1P induced lipid elimination enhancement. ApoM-S1P therefore serves as a novel and potentially exciting therapeutic avenue to help treat early dry AMD.

6.2 Future Directions

As mentioned earlier, the endeavor to comprehend the intricacies of cell metabolism and function to discover new therapeutic avenues will continue to persist. The study discussed in chapter 1 was conducted within the context of homeostasis. It was nonetheless surprising that only PRKAA2 dysfunction lead to rod photoreceptor dysfunction despite adequate expression of both catalytic isoforms. Future directions to elucidate the roles of both isoforms in rod photoreceptors must include studying these in the context of disease. More specifically, it is known that metformin, a potent AMPK activator, is a mainline therapeutic for type II diabetes. A major complication of diabetes is diabetic retinopathy. However, scant is known about the roles of the different catalytic isoforms in the context of diabetic retinopathy. Thus, there is leeway in investigating what role AMPK contributes to the pathogenesis of diabetic retinopathy.

Ongoing studies are being conducted to target SARM1 to treat NMNAT1-related photoreceptor degeneration. Future studies include adeno-associated virus (AAV) therapies to acutely treat NMNAT1-related degeneration by knocking down SARM1. In addition, LCA9 is known to encompass multiple mutation in NMNAT1. Future directions involve elucidating how the different NMNAT1 mutations directly affect not only NMNAT1 function but also photoreceptor degeneration.

The study described in chapter 5 is the result of the findings from chapters 3 and 4. We aimed to discover new therapies to treat early dry AMD before the manifestation of deleterious symptoms. ApoM therapy serves as a promising candidate therapy; however, the specific mechanism leading to lipid elimination in RPE remains elusive. Thus, further investigation is warranted to confirm if lipophagy is indeed a major pathway involved in RPE lipid elimination by ApoM-S1P signaling. Clear elucidation of the downstream effectors of S1PR3 is also warranted as it is still unclear how S1PR3 activation molecularly leads to the observed lipotoxicity amelioration. Overall, there remains much to be done to not only illuminate our understanding of pathogenesis mechanisms, but to also practically translate these ideas into tangible therapeutics that can advance how we treat patients who suffer from blinding diseases.